DISSIMILAR FRICTION STIR WELDING OF LOW & HIGH MELTING POINT ALLOYS AND ITS NUMERICAL THERMAL & FLUID FLOW ANALYSIS

A thesis submitted in partial fulfillment of the requirements for the degree of

DOCTOR OF PHILOSOPHY

by

Pardeep Pankaj

(Roll No. 176103120)

Department of Mechanical Engineering

Indian Institute of Technology Guwahati

Guwahati-781039, Assam, India

August 2023

DEPARTMENT OF MECHANICAL ENGINEERING

INSTITUTE OF TECHNOLOGY GUWAHATI

GUWAHATI-781039, ASSAM, INDIA

DECLARATION

I declare that,

a. The work contained in this thesis is original and has been done by me under the guidance of my supervisor.
b. The work has not been submitted to any other institute for any degree or diploma.
c. I have followed the guidelines provided by the institute in preparing the thesis.
d. I have confirmed the norms the guidelines given in the ethical code of conduct of the institute.
e. Whenever I used material in the form of data, theoretical analysis, figures or text from other sources, I have given due credit to them by citing them in the text of the thesis and providing their detail in the references.

Pardeep Pankaj
Research Scholar
Department of Mechanical Engineering
Indian Institute of Technology Guwahati
Guwahati-781039, Assam, India

August 2023

DEPARTMENT OF MECHANICAL ENGINEERING

INSTITUTE OF TECHNOLOGY GUWAHATI

GUWAHATI-781039, ASSAM, INDIA

CERTIFICATE

This is to certify that the thesis entitled "**DISSIMILAR FRICTION STIR WELDING OF LOW & HIGH MELTING POINT ALLOYS AND ITS NUMERICAL THERMAL & FLUID FLOW ANALYSIS**" submitted by **Mr. Pardeep Pankaj (Roll No. 176103120)** to the Indian Institute of Technology Guwahati for the award of the Degree of Doctor of Philosophy has been carried out under my supervision in the Department of Mechanical Engineering, Indian Institute of Technology Guwahati. This work has not been submitted elsewhere for the award of any other degree or diploma.

Dr. Pankaj Biswas
Professor
Department of Mechanical Engineering
Indian Institute of Technology Guwahati
Guwahati-781039, Assam, India

August 2023

Dedicated to

My Beloved Parents

Mr. Kulwant Singh,

Mrs. Saroj Kumari

&

My Elder Brother

Mr. Sukhmeet Sonu

ACKNOWLEDGMENT

Undertaking this Ph.D. has been a truly life-changing experience for me and it would not have been possible without the help of many people. I would like to take this opportunity to thank them for their support, guidance, and instruction they provided me throughout my doctoral studies.

First of all, I would like to express my sincere gratitude to my esteemed supervisor ***Prof. Pankaj Biswas*** *for their consistent support and guidance during the running of this research work. His support, advice, and comprehensive insights in this field have made this an inspiring experience for me. The meetings and conversations with him inspired me to think from multiple perspectives to form a comprehensive and objective critique. Without his assistance and dedicated involvement in every step throughout the process, the research papers would have never been accomplished. His immense knowledge, motivation, and patience have given me more power and spirit to excel in research writing. He is my mentor and a better advisor for my doctorate study beyond the imagination.*

I am deeply grateful to my doctoral committee, including Prof. Swarup Bag, Prof. Chandan Das, and Dr. Prasenjit Khanikar for giving encouragement and sharing insightful suggestions. They all have played a major role in polishing my technical and research writing skills. Their endless guidance is hard to forget throughout my life.

I would like to extend my sincere gratitude to the Director, Deans, and other staff of IIT Guwahati, who offered me an astonishingly supportive research environment. My sincere gratefulness to the present HOD Prof. K. S. R. Krishna Murthy, and former HODs Prof S. Senthilvelan and Prof S. K. Dwivedi for providing the required research facilities to the department. I would like to acknowledge the Central Instruments Facility of IIT Guwahati for providing the required research facilities for the metallographic analysis. I also acknowledge the financial support provided by Naval Research Board, Govt. of India.

I am also highly grateful to the non-teaching staff of the mechanical department, particularly Mr. Pranjol Paul and Mr. Sanjib Sarma for helping in experimentation associated with metallography and mechanical testing. I am also pleased to say thank to the technical staff of the central workshop, particularly Mr. Nandan Kanan Das (Asst. Workshop Superintendent and Mr. Dilip Chetri for the experimental support related to the FSW machine and sample preparation.

Moving to my Lab, first, let me thank my seniors. I would not forget to express my gratitude to Dr. Avinish Tiwari and Dr. Tanmoy Medhi for their treasured support, which was really influential in shaping my experiment methods and critiquing my results. Their immense support actually guided me to rectify numerous things that could create major challenges in the acceptance of my paper. I also thank Dr. Sagar Pawar, Dr. Saurav Suman, and Mr. Utpal Kiran for giving their time to offer me valuable comments toward improving my work. I would like to extend my sincere thanks to all the Advanced Welding Technology lab members: Sanjay, Deepak, Lakshmi, and Ankan for their help and for being a constant source of encouragement throughout my project. It truly has been a very, very good time in this lab. I cannot forget my batchmates: Vivekananda, Viwek, and Sukant, who went through hard times together, cheered me on, and celebrated each accomplishment.

Finally, I would like to offer special thanks to my family for supporting me during the compilation of this dissertation. Without their tremendous encouragement, moral support, and motivation over the past few years, it would be impossible for me to accomplish the thesis work. This dissertation stands as a testament to their unconditional love and encouragement.

Pardeep Pankaj

ABSTRACT

Joining of dissimilar materials has received considerable attention in constructing lightweight hybrid structures in various industries, particularly in automotive, marine, and aerospace. Regardless of advancements in various joining techniques, green technology, namely friction stir welding (FSW) has emerged as a feasible industrial joining process for dissimilar materials, which are hard to weld by conventional fusion welding. There are still a number of significant obstacles that need to be overcome before it can be effectively implemented in a wide range of industries. A comprehensive understanding of metallography, heat generation, plastic deformation, and material flow/intermixing associated with the tool–workpiece intersection is required to substantially eradicate defects from the dissimilar joints. In this dissertation, an attempt was made to address the optimal dissimilar FSW process window through the experimental analysis, supported by the numerical modelling. The dissimilar material combination, i.e., shipbuilding grade DH36 steel & AISI 1008 steel, DH36 steel & 6061-T6 aluminum alloy (AA6061), and 304 stainless steel (304 SS) & AA6061 are chosen for the study.

In the experimental work, the weld joints were characterized based on the mechanical performance, macro/microstructural studies, and quantification of intermetallic compounds (IMCs) inside the stir zone (SZ). The compositions and phases of the IMCs at the Al/steel interface, SZ, and intercalated structure were confirmed through X-ray diffraction (XRD) analysis, atomic force microscope (AFM), field emission scanning electron microscope (FESEM), and transmission electron microscope (TEM) equipped with energy-dispersive X-ray spectroscopy (EDS). A dissimilar combination of DH36 steel and AISI 1008 steel plates were joined to investigate the influence of the rotational speed (ω), traverse speed (v_{weld}), and tool offset on welding temperature, axial force, microstructure, and mechanical properties of the joints. In the joining of dissimilar DH36 steel & AA6061 combination, the comprehensive effect of varying tool offset conditions on weld characteristics was examined. On the other hand, a detailed analysis was performed to obtain the optimal tool traverse speed during the FSW of dissimilar 304 SS & AA6061 joint.

From the experimental investigation of dissimilar steels joints, it is observed that the impact toughness and hardness are highly dependent on the grain size variation. The effect of pitch ratio (ω/v_{weld}) on temperature, microstructure, impact toughness, and hardness distribution is more as compared to tool offset. On the other hand, the study of dissimilar steel

& AA6061 revealed that the mechanical properties, particularly weld strength, ductility, and hardness are considerably influenced by steel fragments and IMCs formation apart from the microstructural variation. It is understood that the grain refinement and scattered IMCs (i.e., Al_3Fe) in the SZ could improve the hardness. However, the thicker IMC layer and larger area fraction of steel fragments and IMCs reduced the joint strength and ductility of the joints. The intercalated structure acted as the hardest zone due to the formation of IMCs, namely Al_2Fe, Al_3Fe, AlFe, and $AlFe_3$ at different welding conditions.

In the numerical work, the 3D transient thermal phenomenological models were established to compare the thermal history between FSW and plasma-assisted FSW (PAFSW) of dissimilar steels. The moving heat source models were embedded in a Fortran code and fed to Abaqus/CAE through the DFLUX subroutine. On the other hand, the steady-state multiphase thermal-fluid flow analysis based on computational fluid dynamics (CFD) by incorporating a modified analytical model was performed for steel & AA6061. The volume of fluid (VOF) method was implemented for the DH36 steel & AA6061 combination. A multi-species transport model (STM) coupled with a mixture model was established to simulate the dissimilar 304 SS & AA6061 joints for the first time, where the CFD solver transferred species mass fractions of the materials. The impact of rotational speed on the temperature and plasticized material flow associated with the tool–material interaction was investigated.

The thermal history obtained from the established models matched fairly well with the experimental results. The additional preheating source is significantly reduced axial force by 15% to 20%. The CFD simulation results revealed that the variation in rotational speed is significantly affected the temperature and material flow properties (i.e., flow velocity, dynamic viscosity, and strain rate) and material intermixing around the high-speed rotating tool. The velocity vectors are discontinuous in the advancing side at low heat input, whereas it is improved and becomes almost uniform at higher heat input conditions. The developed STM can capture the transversal/horizontal material flow features and embedded steel fragments/strips in the joints, which are also detected in macrographs from experiments under different welding conditions.

Keywords: Friction stir welding, Dissimilar materials, Computational fluid dynamics simulation, Finite volume model, Multi-species transport model, Intermetallic compound, Metallographic analysis, Mechanical characterization

TABLE OF CONTENTS

LIST OF FIGURES

LIST OF TABLES

NOMENCLATURE

Abbreviation

AS	Advancing side
AVG	Average grain size
CEL	Coupled Eulerian Lagrangian
CFD	Computational fluid dynamics
DRX	Dynamic recrystallization
FEM	Finite element method
FSW	Friction stir welding
HAZ	Heat-affected zone
HMPA	High melting point alloys
IMC	Intermetallic compound
LMPA	Low melting point alloys
MZ	Mixed zone
PAFSW	Plasma-assisted friction stir welding
PAZ	Pin-affected zone
RS	Retreating side
SAZ	Shoulder-affected zone
SEZ	Steel extruded zone
STM	Species transport model
SZ	Stir zone
TMAZ	Thermo-mechanically affected zone
VOF	Volume of Fluid
304 SS	304 stainless steel
6061-T6 aluminum alloy	AA6061

Roman letters

Representation	Description	Units
A	Material related constant	1/s
D	Diffusion coefficient	m^2/s
E	Energy	J
J	Diffusive flux	kg/m^2 s

P	Pressure	Pa
$\dot{Q}_a$	Activation energy	J/mol
$\dot{R}_{sh}$	Shoulder radius	m
$\dot{R}$	Gas constant	J/K mol
S	Reaction source	kg/m^3 s
T	Temperature	K
V	Preheating voltage	V
Z	Zener–Hollomon parameter	
c	Specific heat	J/kg K
d	Grain diameter	m
f	Heat fraction	%
e_h	Enthalpy	J/kg
$\dot{h}_c$	Convection coefficient	W/m^2 K
h_p	Pin height	m
k	Thermal conductivity	W/m K
$\dot{k}_r$	Rate constant	1/s
n	Material related constant	
p	Primary phase	
q	Heat flux	W/m^2
r_{pb}	Bottom pin radius	m
r_{pt}	Top pin radius	m
s	Secondary phase	
t_e	Exposer time	s
v_{matrix}	Velocity at the tool/matrix interface	m/s
v_{sp}	Slip velocity	m/s
v_{weld}	Welding velocity	m/s
x_t	IMC layer thickness	µm

Greek symbols

η	Thermal efficiency	%
σ_{fs}	Flow stress	MPa
σ_y	Yield stress	MPa
$\dot{\alpha}$	Material related constant	1/MPa

β	Steffen-Boltzmann coefficient	$W/m^2 K^4$
$\dot{\varepsilon}$	Strain rate	1/s
μ	Viscosity	kg/m s
ρ	Density	kg/m^3
Φ	Shear stress tensor	Pa
τ_{eff}	Effective stress tensor	Pa
ω	Angular rotational speed	rpm
μ_f	Coefficient of friction	
δ^*	Slip rate	
α	Mass fraction	
ε	Emissivity	

CHAPTER 1

INTRODUCTION AND LITERATURE REVIEW

Growing concerns about sustainability and environmental preservation increase the demand to construct new lightweight multi-material structures in several industries. The sophisticated hybrid constructional design can produce lightweight structures when lightweight materials replace some strengthened components. An economical and efficient lightweight multi-material structure allows a reduction of the overall weight of products and, subsequently, fuel consumption. For those kinds of applications, the successful joining of dissimilar materials is needed to manufacture the assemblies and components. Advanced joining technology is an integral part of the manufacturing processes of lightweight structures. A lot of effort has been expended to develop different joining procedures and evaluate their suitability for implementation in lightweight structures. Regardless of advancements in joining techniques, the versatile, energy-efficient, and environmentally friendly solid-state joining process has emerged as a feasible industrial joining technique for dissimilar materials. Among the several solid-state joining techniques, Friction stir welding (FSW) is the most suitable and emerging process for joining the dissimilar materials. This chapter is intended to summarize the recent progress in FSW of dissimilar materials. Particular attention has been paid to material flow behaviour, material intermixing, microstructural evolution, and mechanical performance of the dissimilar joints. Various experimental and numerical simulation results have been mentioned to compare weld characteristics. This chapter is ended with the main conclusions and opportunities for research in the field of dissimilar FSW.

1.1 MOTIVATION FOR THE PRESENT WORK

Nowadays, the manufacturing of higher efficient and lightweight constructions encourages engineers to create hybrid structures. Among the numerous kinds of hybrid structures, the structures made of dissimilar materials are highly prominent due to their wide-ranging applications in different industries [1]. An example of different material combinations in an automobile body structure is shown in Fig. 1.1(a). In the category of dissimilar alloys, researchers are paying attention to structural materials, especially copper (Cu), aluminum (Al), magnesium (Mg), and steel alloys.

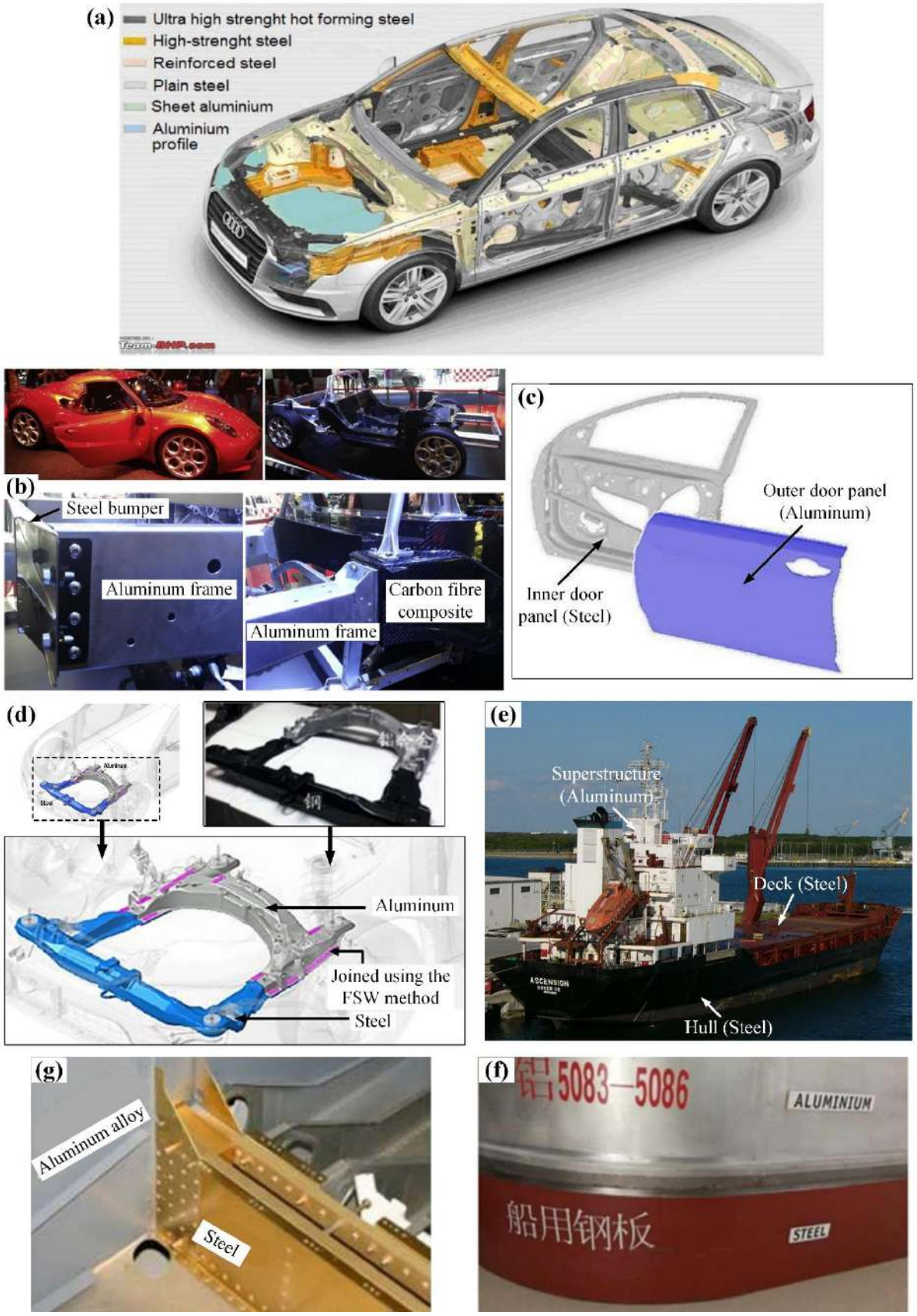

Fig. 1.1 *Multi-material design used in (a–d) automotive industry [2,3]; (e,f) ship industry [4]; and (g) aerospace industry [4]*

Each of these materials offers varying performance and characteristic advantages for individual components. Consequently, these materials may be employed simultaneously in multiple configurations to enhance mechanical performance for each application. However, many auxiliary issues, such as corrosion, formability, and production cost are just a few of the auxiliary problems with these materials that are being gradually resolved. However, the joining of appropriate material combinations remains an ongoing challenge since the several traditional joining procedures employed in the manufacturing sectors are incompatible with dissimilar materials. Accordingly, this section explains the efficient dissimilar material combinations and their joining techniques for the excellent performance of the hybrid structures.

1.1.1 Joining of Steel and Aluminum Alloys

The high corrosion resistance, low density, superior mechanical properties, and weldability of Al alloys make them more applicable in various aircraft, marine, and car industries. On the other hand, steel alloys are considered an attractive material in vehicle, aerospace, and marine industry applications due to their higher toughness and corrosion resistance [5,6]. Joining of aluminum (Al) with steel creates unique hybrid structures utilized in various aero, marine, railway, and automobile industries [1,7]. The joining of Al alloy with steel is considered an efficient way to raise productivity and reduce fuel consumption by reducing the overall weight of structures in shipbuilding, transportation, and automobile manufacturing industries [8,9]. In transportation industries, it is essential to develop a dissimilar joining of steel and Al alloys to reduce the gas emission and fuel consumption through weight-saving aspects [9]. For example, Fig. 1.1(b) shows the framework of the 2014 Alfa Romeo 4C design, which incorporates an Al frame for lightweight and suspension components with ultra-high-strength steel bumpers for crash resistance. Additionally, the major interior construction is a carbon fiber composite tub to keep the final vehicle mass below 900 kg [2]. The sophisticated hybrid constructional design can produce lightweight structures when Al substitutes some steel components, as shown in Fig. 1.1(c). A hybrid framework of aluminum and steel was constructed in the sub-frame of the new Accord product of Honda Motor Co., Ltd. for large-scale production, as shown in Fig. 1.1(d). In some instances, especially in structural sections of machinery, the high strength of the steel is irreplaceable. As a consequence, the need for steel-to-aluminum joining is increased. For example, the decks and hulls of most ships in the shipbuilding industries are composed of steel, as shown in Figs. 1.1(e) and 1.1(f), but the superstructures are made of aluminum to maintain the low centre of mass for proper stability and buoyancy [10]. A reliable technique is required to join the Al

superstructure with the steel decks and hulls. Fig. 1.1(g) shows some hybrid structures made up of Al/steel in the aerospace industry. The dissimilar Al alloy and steel joints are also applicable in cryogenics, where the cryogenic liquid is stored in Al alloy chambers and transferred through stainless steel pipeline [4].

1.1.2 Joining of Dissimilar Steels

Joining of dissimilar grade steels has wide applications, especially in ship parts, oil and gas industry, power plants, and chemical plants [11,12]. Their combination improves the fatigue behaviour, heat resistance, and corrosion resistance of ship parts and vessels in chemical and power plants. There is a lot of potential for expanding the usage of low-cost castings in many industrial applications through the successful joining of different carbon-content steel alloys [13]. In pressurized water reactors, stainless steel and low alloy steels are widely used in the primary system due to their excellent mechanical characteristics. For example, the primary branch lines in the Korean-designed OPR1000 and APR1400 plants are built of stainless steel to offer adequate strength and corrosion resistance, but the core primary coolant piping is composed of low alloy steels that are clad with stainless steel [14]. Typically, stainless steels are used for components operating at relatively high temperatures, while ferritic or carbon steels are used for components at lower temperatures. As a result, the joining of stainless steel to other grades of steel can be economically sustainable in some conditions. In the automobile sector, dissimilar steel joining is used to attain the stability between the weight, ductility, stiffness, and strength [15]. However, the formation of brittle microstructural features like martensite and bainite in the joints as well as hydrogen cracking and solidification cracking provide specific technical and metallurgical problems [16]. Consequently, the selection of the different grade steels as well as their joining techniques are crucial for the excellent mechanical performance of the joints.

1.1.3 Materials

Steel, one of the essential materials in the contemporary world, is available in a wide range of grades and sizes. It is basically an iron alloy with a small carbon percentage (up to 2.1 wt.%). Carbon steels are utilized in a variety of industrial applications since their ability to modify the mechanical properties by varying the carbon content. Furthermore, structural steel is a form of steel that is employed in construction. It is designed with a good strength/weight ratio (also known as specific strength) and at a reasonable price for use as a structural element

in structures such as buildings, roads, bridges, etc. Mild steels with less than 0.25% carbon content have good weldability and can be joined without extra safeguards. Similar to structural steel, it is a ferrous metal containing iron and carbon. Mild steel is extensively employed in structural applications because of its superior mechanical qualities, affordability, and dependability. Thus, it can be joined using the current welding processes. For gas turbine applications, it is essential for the joint structure of mild steel to exhibit adequate tensile strength and creep resistance [17]. Therefore, it is crucial to rigorously examine the microstructure and mechanical performance since it affects the reliability of the joint sections. Upon joining by fusion-based welding techniques like arc, metal inert gas (MIG), and tungsten inert gas (TIG), mild steel becomes viable for automotive applications [18].

One type of high-strength shipbuilding grade DH36 steel certified by the American Bureau of Shipping (ABS) is low alloy steel utilized in various industries, including the European shipbuilding and offshore industries. DH36 steel with good qualities is created by regulating rolling and normalising [19]. The primary structural components of ships, such as the hull, bulkheads, and deck are made of structural steel. It is based on C-Mn steel and alloyed with Nb, V, and Ti elements. Structural steel has excellent toughness, high corrosion resistance, processing, and welding qualities. From a metallographic perspective, DH36 steel has a greater average carbon content than D-grade steel. As a result, a higher pearlite concentration decreases its ductility and makes it more resistant to distortion [20]. Joining of structural steel via solid-state welding technique becomes economically and technically viable for introduction in the shipbuilding sector; hence it must develop into a competitive procedure with traditional fusion welding techniques [19].

Stainless steels are essential industrial materials, and their wide range of applications are growing steadily. Particularly for working under corrosive environments, their applications are expanding in the chemical, food, mechanical, medical, nuclear, aerospace, offshore, and food processing industries [21]. Amongst the different categories of stainless steel, 304 and 316 austenitic chromium-nickel (Cr-Ni) stainless steel possess excellent corrosion resistance and good formability. The major alloying component of stainless steels that gives them their stainless nature is chromium. Chromium assists in the formation of a chromium oxide layer that prevents corrosion on the surface of stainless steel. The primary function of the nickel is to stabilize the austenitic structure of the steel at both high and low temperatures.

In recent years, the use of aluminum alloys for automotive purposes has greatly expanded as a result of the growing focus on fuel efficiency and environmental issues. Among the

different series of aluminum alloys, the 1xxx, 3xxx, and 5xxx series are non-heat treatable and strain hardenable only. The 2xxx, 6xxx, and 7xxx series are heat treatable, and the 4xxx series consists of heat-treatable and non-heat-treatable alloys. The heat-treatable 6xxx-series aluminum alloys containing magnesium and silicon as primary alloying constituents are of specific interest due to their appealing combinations of properties as structural materials for aerospace and automotive applications. A substantial portion of the world's total aluminum production is made up of the 6xxx-series aluminum alloy. This aluminum series has medium strength, good formability, high strength & stiffness-to-weight ratios, corrosion resistance, fatigue resistance, and comparatively low cost [22]. These characteristics of 6xxx alloys have emerged as essential requirements for their usage in low-weight military vehicles, rockets, aircraft, missiles, and cars used for both military and domestic purposes [23].

1.1.4 Joining Technique

In recent years, a variety of techniques for joining dissimilar materials has been established by researchers. The differences in melting point temperature, physical/mechanical properties and the compositions of materials make the welding of dissimilar materials more challenging than a similar metal welding process. A mechanical joining technique, self-piercing riveting technology, is employed to join the steel and aluminum alloy [24,25]. Arc brazing is proposed to achieve metallurgical bonding and prevent the formation of brittle IMCs [4]. The base material (BM) is not melted and solidified during this joining process, which avoids the IMCs formation in the joint. However, some drawbacks include a lack of metallurgical bonding, insufficient joint strength, poor airtightness, and particularly poor fatigue performance, which restrict its applicability. On the other hand, welding is a well-known technique for joining the dissimilar components when fasteners, adhesives, or self-piercing rivets are prohibitively expensive. Many conventional fusion welding techniques (i.e., tungsten inert gas welding, plasma arc welding, laser, and electron beam welding) are proposed for joining the dissimilar materials. One of the more noticeable issues is that conventional fusion welding methods produce a wider heat-affected zone and a heterogeneous microstructure. This leads to the type-IV cracking at the base material/heat-affected interface region during creep exposure [26]. Furthermore, the coarse grain structure of a conventional fusion weld joint produces poor weld properties. To resolve these issues, the weld joints are frequently repaired or subjected to some post-welding treatments. The solid-state joining technique is one of the most effective alternatives to conventional fusion welding techniques, which can eliminate the fusion related defects (i.e., porosity, slag inclusions, and spatter).

Furthermore, it has the capability to reduce the IMCs formation, residual stress, and residual deformation in the welded joints. The elimination of arc flash, splatter, and toxic fumes makes the work environment safe for the workers. Overall, the solid-state welding technique is a desirable, environmentally friendly welding option that finds widespread use in a variety of sectors, including the maritime, railroad, aerospace, and automobile. Many solid-state joining methods, namely diffusion bonding [27,28], friction welding [29,30], ultrasonic joining [31,32], and explosive welding [33,34] have attracted attention to improve the weldability of dissimilar joints. Among these welding methods, the friction-based joining process, namely friction stir welding (FSW) is an appropriate and rapidly growing technique for joining the dissimilar materials [3,35]. The Honda Motor company provided an example of the industrial application of dissimilar FSW by lap-joining of aluminum and steel in engine cradles [4]. However, there are still a number of significant obstacles to overcome before it can be effectively implemented in a wide range of industries. Therefore, a better understanding of the behaviour of FSW joints is required to ensure their efficiency, and reliability.

1.2 INTRODUCTION TO FSW

Over a century ago, a US patent mentioned the use of frictional heat for solid-phase welding and forming. Then, it took another 50 years before friction technology was substantially developed, specifically a British patent in 1941 that introduced friction surfacing. Yet another 50 years went by before friction stir welding (FSW) was patented in 1991 by Thomas et al. at The Welding Institute, UK [4]. The friction technique can now achieve continuously welded seams for plate manufacturing, especially in light metals, thanks to this comparative innovation [36]. FSW is a "green" technique because of its energy efficiency, environmental friendliness, and versatility. It is regarded as the most significant advancement in metal joining in the last ten years. FSW uses a significant amount less energy than traditional welding techniques. The technique is environmentally friendly because no cover gas or flux is employed. Any aluminum alloy can be welded without worrying about the compatibility of the composition since no filler metal is used in the joining process. The peak temperature during the welding remains around 0.6–0.9 of the melting point of materials in degrees or Kelvin [2].

1.2.1 Process Description

FSW tool consists of a rotating shoulder connected to a pin (probe). As illustrated in Fig. 1.2, the welding occurs mainly in three phases, each one can be characterized as a period of

time during which the tool and the workpiece are moved in relation to one another. In the initial phase, i.e., the plunge phase, the revolving tool is pushed vertically into the weld line of the two rigidly clamped plates on a backing plate. Localized plastic deformation takes place in the joint section as a result of frictional heat. Subsequently, the tool is permitted to stir down the joint surface in the welding direction. After that, the dwelling phase is the time when a tool rotates exclusively in one location during the tool plunge process, until the point at which the shoulder makes contact with the work surface. The heat is generated by friction and plastic deformation due to the mechanical interaction of the tool and workpiece. Also, heat dissipation occurs in the neighbouring material, which promotes temperature growth and subsequent material softening. After these two preliminary phases, the welding phase begins by moving the workpiece or the tool along the weld line relative to each other.

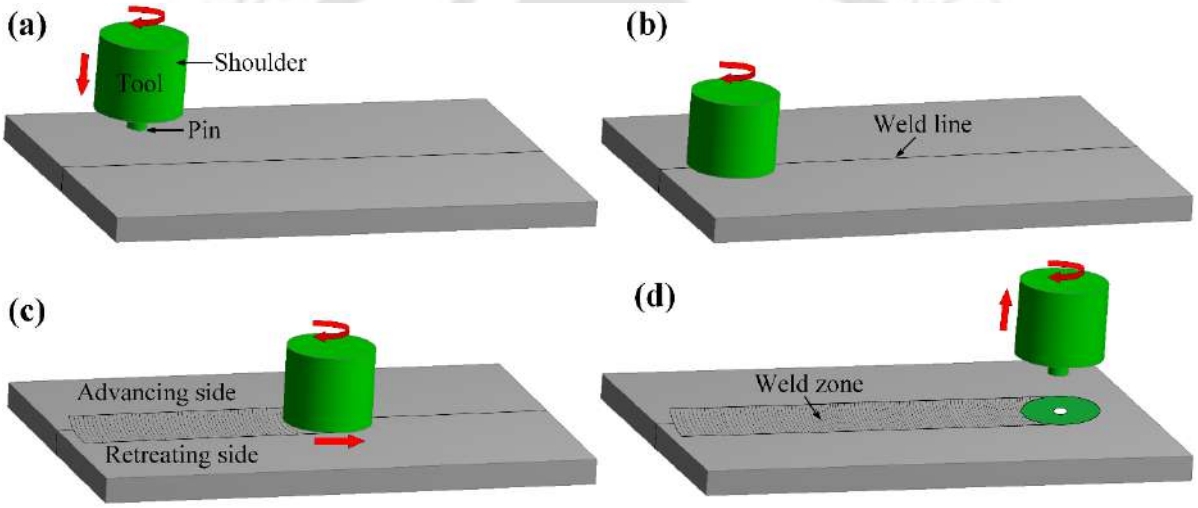

Fig. 1.2 *Different phases during the FSW process (a) plunging phase; (b) dwelling phase; (c) welding phase; and (g) tool retraction*

Intense plastic deformation and plasticized material flow occur when the rotating tool moves along the welding direction. As follows, the material transfers from the front of the tool (leading side) to the behind (trailing side), where it is forged into a joint. Lastly, the tool is dragged out of the material after completing its traverse motion and arriving at its terminal location. As the pin is removed from the workpiece, a hole is left behind, known as the exit hole or pin hole. Numerous researchers are working on ways to close this exit hole because it is considered a defect in the process. The weld has two regions, i.e., the advancing side (AS) and the retreating side (RS). The welding direction and the tangential component of the tool rotation are similar in the AS. In the RS, the tool traverse and rotation directions are opposite.

1.2.2 Process Parameters

FSW involves complex multi-physical phenomena in plastic deformation, heat generation, material movement, and intermixing. The tool geometry, welding parameters, and joint design are significantly impact the temperature distribution and material flow/mixing, which subsequently influence the mechanical performance and macro/microstructural evolution of the joint. Therefore, the optimum combination of the welding parameters is needed to produce the sound quality welded joints by controlling heat generation and material flow characteristics. Fig. 1.3 shows the FSW processing parameters. This section addresses the only crucial parameters affecting the FSW process.

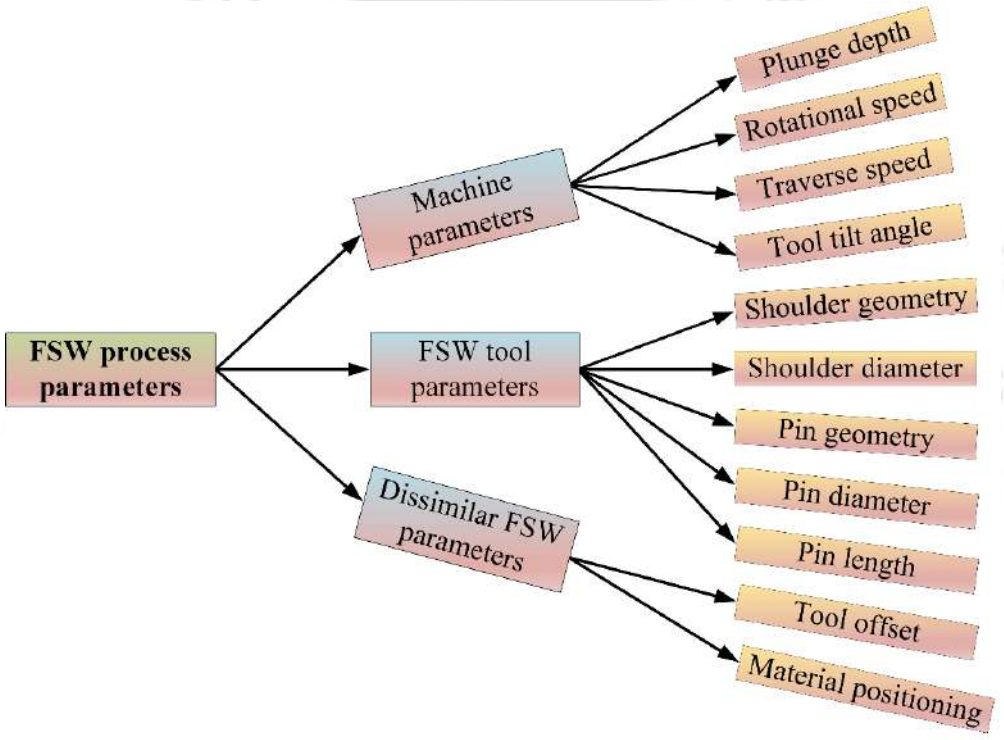

Fig. 1.3 *FSW process parameters*

Tool rotational speed (ω) and traverse speed or welding speed (v_{weld}): In the FSW, tool rotational speed (clockwise or counter clockwise direction) and tool traverse speed along the weld line are very essential parameters. During the welding process, the tool rotation causes the material around the pin to be stirred and mixed, and the tool translation transfers the stirred material from the front to the back of the pin. These parameters can monitor the heat generation and material flow, as well as regulate the evolution and growth of the IMC layer. The severe plastic deformation at higher rotational speed and lower traverse speed can lead to extensive IMCs formation with a subsequent reduction in the joint strength. Conversely, insufficient heat input at a low rotational speed and higher traverse speed can generate voids, tunnels, and micro-

cracks due to improper material flow. Therefore, the optimum rotational speed and traverse speed are needed to produce the sound quality welded joints by controlling heat generation and material flow characteristics.

Tool geometry: Tool geometry is the most prominent feature of process development. FSW tool features generally consist of shoulder & pin shape, shoulder & pin diameters, and pin length. The heat generation, material flow, and traverse rate for the welding are governed by the tool geometry. The tool has two primary functions: localized heat generation and material movement. The friction at the workpiece/shoulder interface is responsible for the major component heat generation. The relative size of the pin and shoulder is crucial from a heating perspective; however, other design features are not essential. Additionally, the shoulder confines the more heated volume of plasticized material than the pin. The stirring and movement of the material is the second function of the tool. Besides this, the tool design monitors the uniformity of microstructure, characteristics, and process loads.

Tool offset: The tool offset is an essential parameter, especially in dissimilar FSW of high melting point alloys (HMPA) like steel/titanium with low melting point alloys (LMPA) like aluminum. It controls the heat generation and mixing of both materials, which significantly effects the IMCs formation inside the SZ and weld quality. In dissimilar FSW, the tool from the weld line is shifted towards the LMPA to avoid the tool degradation and overheating of the LMPA. It is introduced as the distance between the tool axis and the weld line or faying surface of the two materials, as shown in Fig. 1.4.

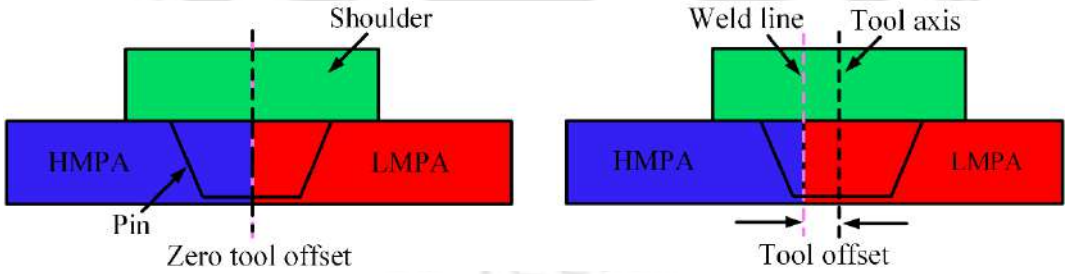

Fig. 1.4 *Tool offsetting during the dissimilar FSW process*

Material positioning: In the FSW of dissimilar materials, the critical issue is the material positioning concerning the tool rotation direction, which can provide superior tensile properties and defect-free welded joints. The similar direction of the tangential component of the rotating tool and tool traverse direction in the AS produces additional frictional heat compared to the RS, where the tool rotation direction is opposite to that of the tool traverse direction [37]. Similar to the significance of the rotational speed and the traverse speed, the positioning of

dissimilar materials turns into an essential parameter due to complex material flow during the FSW process. Some of the researchers were performed an experimental study to understand the effect of material positioning during FSW of dissimilar materials. Kim et al. [38] investigated the impact of material positions on the mechanical characterizations of dissimilar friction stir (FS) welded A5052 and A5032 Al alloys. They were obtained the highest tensile strength when the high-strength A5032 Al alloy was clamped at the RS and A5052 Al alloy at the AS. During dissimilar FSW of Al–Zn–Mg/Al–Mg–Si Al alloys, Yan et al. [39] obtained the highest tensile strength as the high strength Al–Zn–Mg Al alloy was clamped at the RS and Al–Mg–Si Al alloy at the AS. Anbukkarasi et al. [40] reported the formation of defects when the soft material (Al) was positioned at the AS and hard material (Cu) at the RS during dissimilar FSW of AA2024 Al and pure copper. Park et al. [41] performed the FSW of dissimilar Al alloys to understand the effect of material locations on the mechanical characterizations of the welds. They were found that the material flow improved by locating the 5052-H32 Al alloy at the AS and 6061-T6 aluminum alloy at the RS. During the dissimilar joining of Al-Mg, Fu et al. [42] and Firouzdor et al. [43] reported that defect-free materials intermixing could be obtained by positioning the soft material (Mg) at the AS than that of positioning at the RS. Sadeesh et al. [44] reported that the weld strength could be improved by placing the harder material at the AS and the softer material at the RS. Mehta [45] reported that better material flow and intermixing could be obtained by keeping the steel at the AS and Al at the RS during dissimilar FSW of Al and steel.

1.2.3 FSW Microstructure

The complex interaction at the tool/workpiece interface occurs due to the simultaneous thermo-mechanical action during the welding process. These interactions affect the plastic deformation, material flow, heating & cooling rates, dynamic recrystallization, and subsequently, the mechanical performance of the joint. The thermo-mechanical action by the tool produces the different microstructural zones in the joint. Generally, the FS weld joints contain three distinct zones based on a microstructural characterization of grains and precipitates. These zones are the stir zone (weld nugget), thermo-mechanically affected zone, and heat-affected zone, as shown in Fig. 1.5.

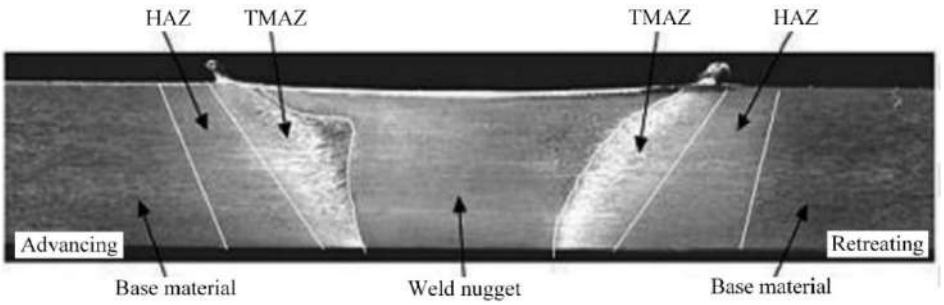

Fig. 1.5 *Different microstructure zones in the FSW process* [46]

Stir zone (SZ): The extensive deformed region that roughly signifies the location of the tool pin (probe). The SZ exhibits the fine-grained microstructure due to the dynamic recrystallization during the welding process.

Thermo-mechanically affected zone (TMAZ): This zone is not directly influenced by the tool pin; however, the thermal history and plastic deformation adjacent to the SZ effect the TMAZ. A rotating tool pin produces the elongated grains due to a lack of dynamic recrystallization under insufficient heat and deformation in the TMAZ.

Heat-affected zone (HAZ): This zone commonly exists in all welding processes; however, in FSW, it is subjected to only a thermal cycle without any material deformation. It is located between the base material and TMAZ and exhibits a microstructure approximately similar to the base materials.

1.2.4 Process Advantages and Disadvantages

FSW is a "green" technique because of its energy efficiency, environmental friendliness, and versatility; hence it is regarded as the most significant advancement in metal joining in a decade. FSW consumes significantly less energy as compared to conventional welding methods. The technique is environmentally friendly because no flux or cover gas is used. Any aluminum alloy can be joined without concern for composition compatibility because there is no usage of a filler metal during the joining process. The key benefits of FSW with some drawbacks are summarized in Table 1.1.

Table 1.1 *Advantages and disadvantages of the FSW process*

Advantages	Disadvantages
• No solidification cracking and porosity defects. • Lower residual stress and residual deformation. • Less brittle IMCs formation and IMC layer thickness. • SZ (weld nugget) contains a fine recrystallized microstructure. • Post-weld operations like the removal of slag and surface cleaning are not required. • No welding fumes, harmful gases, such as carbon monoxide, carbon dioxide, and undesirable radiations are generated. • Dissimilar materials can be easily welded. • Tailor-welded blanks can be easily manufactured. • Joint preparation is more flexible. • Good repeatability and dimensional stability.	• Exit hole left when the tool is withdrawn. • Higher process forces are required with heavy-duty clamping fixtures. • Less flexible than manual and arc welding processes. • Tool wear is the key issue during the welding of high-strength materials.

1.3 FSW OF DISSIMILAR STEELS

FSW technique was firstly employed to join the aluminum alloys, which are very difficult to be welded by fusion welding techniques. Later it becomes highly usable for joining high-temperature/high-strength alloys like titanium, nickel, steels, and dissimilar metals [37]. However, tool wear is an important issue during FSW of these high melting point alloys, despite some alternative tool materials being used to overcome this issue. FSW tool materials, namely tungsten (W) based alloys, polycrystalline cubic boron nitride (PCBN), and refractive materials (i.e., rhenium and iridium) are suggested for welding of such higher melting point

alloys [47,48]. FSW process has the potential to produce defect (i.e., blowholes, porosity, and solidification cracking) free weld joints due to solid-state in nature [16]. Moreover, low heat input during the FSW process is expected to minimize the microstructural change in the HAZ and limit the residual stress and distortion in steel joints as compared to fusion welding techniques [16,49]. FSW process often provides the fine dynamically recrystallized grain in the stir zone (SZ) and improved mechanical properties [16]. These benefits of the FSW process attract considerable attention in the manufacturing industries for joining similar or dissimilar steels. The differences in mechanical properties, carbon content, and the compositions of alloying elements make the welding of dissimilar steels more challenging than a similar metal welding process [50]. In previously published experimental findings, FSW successfully joined carbon steels without any welding defects from mild steels with low carbon content to ultrahigh carbon steels with carbon concentration above 1.2 wt.% [13,51]. Furthermore, FSW has shown the capability to solve the majority of problems that occurs during the fusion welding of mild steels, DH36 steel, and stainless steels as well as carbon steels with carbon levels up to 1.02 wt.% [52].

Unlike the conventional fusion welding techniques, the research in FSW of dissimilar steel alloys is still in its infancy and continuing to develop. In recent years, the researchers used FSW tools made up of tungsten carbide–molybdenum hard alloy [53], polycrystalline boron nitride (PCBN) [11,13], tungsten carbide–cobalt [16,50] and tungsten–rhenium [26] to join the dissimilar steels. Logan et al. [11] reported that the dissimilar metals were chemically bonded with the diffusion of alloying elements, i.e., Ni, Cr, and Mo into DSS at AS and Cr at the RS during FSW of low alloy structural steel (S275) and duplex stainless steel sheets (DSS). Tiwari et al. [50] studied the effect of tool pin offset, and rotational speed on microstructure and mechanical properties of FS welded mild steel and stainless steel sheets. They were obtained the non-uniform hardness distribution in the SZ and TMAZ due to complex intermixing of the dissimilar metals on the AS. Rahimi et al. [54] investigated the crystallographic texture and microstructure during dissimilar FSW of S275 steel and duplex stainless steel (DSS). They were observed the strain partitioning into the ferrite phase and fine equiaxed grains in the SZ, HAZ, and TMAZ of both materials. Cheng et al. [53] joined the low carbon steel and ferritic ductile iron and investigated the degradation of mechanical properties due to the formation of martensite and fine pearlite in the stir zone. Choi et al. [13] evaluated the mechanical properties and microstructure of dissimilar FS welded high carbon steel (SK85) and low carbon steel (SPHC). They were reported the maximum hardness in SZ due to the formation of fine

martensite and ferrite phase due to dynamic recrystallization and phase transformation. Jafarzadegan et al. [16] investigated the mechanical properties and microstructure of FS welded st37 steel and 304 stainless steel. SZ of st37 steel exhibited fine ferrite and pearlite along with Widmanstatten ferrite and martensite. However, the SZ of 304 stainless steel contained fine austenite grains. Tang et al. [26] were obtained the maximum hardness from 350 HV to 450 HV in the SZ of China low activation martensitic (CLAM) steel with 316 L stainless steel welded joint. They achieved the maximum tensile strength by clamping the 316 L stainless steel at the RS and maximum temperature of 1130 ℃ in the SZ. Figs. 1.6(a) and 1.6(b) show the TEM images of the weld interface when the 316 L is placed at the AS. The EDS spot analysis and diffraction patterns results revealed that no chromium carbides were formed at the weld interface, as shown in Figs. 1.6(c–e).

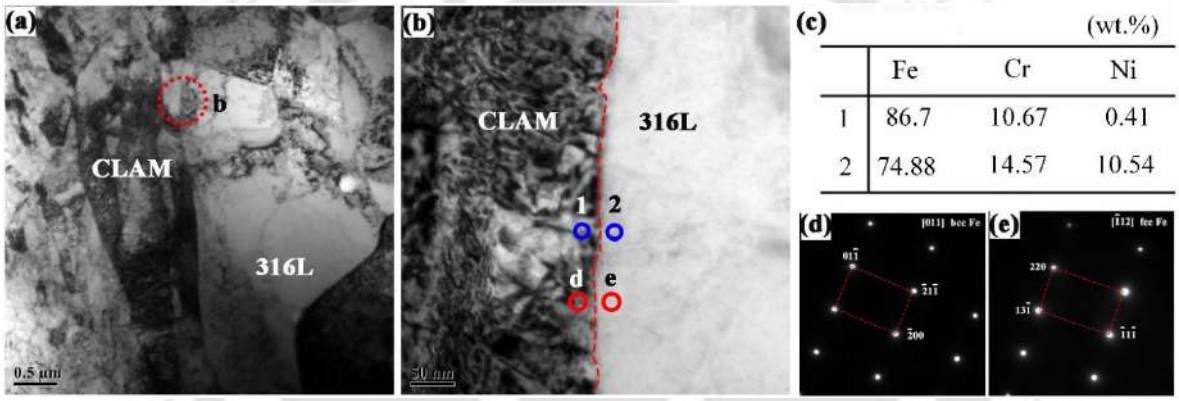

Fig. 1.6 *(a,b) TEM images of weld interface; (c) EDS results of blue points; and (d,e) diffraction patterns of red points [26]*

Tiwari et al. [55] characterized the tungsten carbide tool wear performance using weight measurement, profile measurement, X-ray diffraction, and microstructure analysis before and after the FSW of DH36 steel. Fujii et al. [56] studied the influence of phase transformation on the microstructure, and mechanical properties of the FS welded three-carbon steels, namely S12C, IF steel, and S35C. They were observed that the strength of S12C and S35C steel joints increased by increasing the tool traverse speed. G. Ipekoglu et al. [57] reported the presence of ferrite phase and Widmanstatten ferrite (WF) in the SZ of St52 and St37 dissimilar steels. They achieved the maximum tensile strength value between St52 and St37 base material strength. D Sunilkumar et al. [47] conducted a comparative study on activated-gas tungsten arc welding and FSW of AISI 316LN SS and P9 steel. They were found that the FSW process produced better mechanical properties without any W-La_2O_3 tool wear as compared to GTAW process. Table 4 summarizes the optimum welding conditions for dissimilar FSW of the different graded steels.

Table 1.2 *Summary of the parameters and joint strength of dissimilar steel joints*

Dissimilar steels		Thickness (mm)	Tool material	Tool geometry	ω (rpm)	v_{weld} (mm/min)	Strength (MPa)	Ref.
304 SS	st37	3	WC-Co	CS + TP	800	50	442	[16]
316 L SS	CLAM	3.5	W-25 wt.% Re alloy	CVS+TP	250	80	897	[26]
SK85	SPHC	4	PCBN	CXS+TP	400	200	360	[13]
2205 grade DSS	S275	6	MegaStir Q70 PCBN with W-Re	-	200	100	451	[11]
SK5	SPHC	4	PCBN	CXS+TP	800	200	-	[51]
Ductile iron	Low carbon	3	WC-Mo	CS+CP	982	72	160	[53]
St37	St52	4	WC	CS + TP	630	65	389	[57]
St 37	St 44	4	WC	CS + TP	630	55	385	[58]
SS304	Q235	3	WC-Co	CS + TPS	475	47.5	493	[59]
SS304	UNS G10080	4	WC	CS + TP	875	90	341.54	[50]
Structural	Ferritic stainless	3	WC	CS + TP	508	20	475.1	[60]
F82H	SUS304	1.5	WC	CS+CP	100	100	610	[61]
P9	316LN SS	3	W-La_2O_3	CS+CP	400	30	652	[47]

Notes: *If many welds were performed, the welding parameters providing the maximum strength are reported. DSS: duplex stainless steel, SS: Stainless steel, SPHC: Steel pickle hot-rolled coil, CLAM: China low activation martensitic, SUS: Steel use stainless, St: Steel, CS: Cylindrical shoulder, TP: Tapered pin, CVS: Concave shoulder, CXS: Convex shoulder, CP: Cylindrical pin, TPS: Truncated pyramid shape.*

1.4 FSW OF STEEL AND ALUMINUM ALLOYS

Joining steel and aluminum alloys is one of the essential requirements in the marine, aero, automotive, and railway industries; hence it is appropriate to review the joining of these materials using the FSW technique. Joining of Al/steel is challenging because of significant dissimilarity in mechanical/physical properties and melting point temperature of the base materials [62]. In fusion welding techniques, the higher heat input produces a thick IMC layer at the interface between Al and steel, which is detrimental to the weld joint strength [63]. In addition, aluminum has some distinctive characteristics, including higher reflectivity, lower molten viscosity, and inherent oxide layer formation, which induce hot cracking and unsuccessful joining with traditional fusion welding techniques [64]. On the other side, many solid-state joining methods attracted attention to improve the weldability of Al/steel joints. Among these welding methods, the friction-based joining process, namely friction stir welding (FSW) is an appropriate and rapidly growing technique for joining dissimilar materials, such as steel and Al alloys [1,63]. The thermodynamically solid-state chemical reactions under low heat input in the FSW process is capable to enhance the mechanical performance of the welded joints by reducing the IMC layer thickness [1]. According to the binary phase diagram shown in Fig. 1.7, the atomic percentage of aluminum that monitors the most forms of IMCs, namely $AlFe_3$, Al_3Fe_2, AlFe, Al_5Fe_2, Al_2Fe, and Al_3Fe ($Al_{13}Fe_4$).

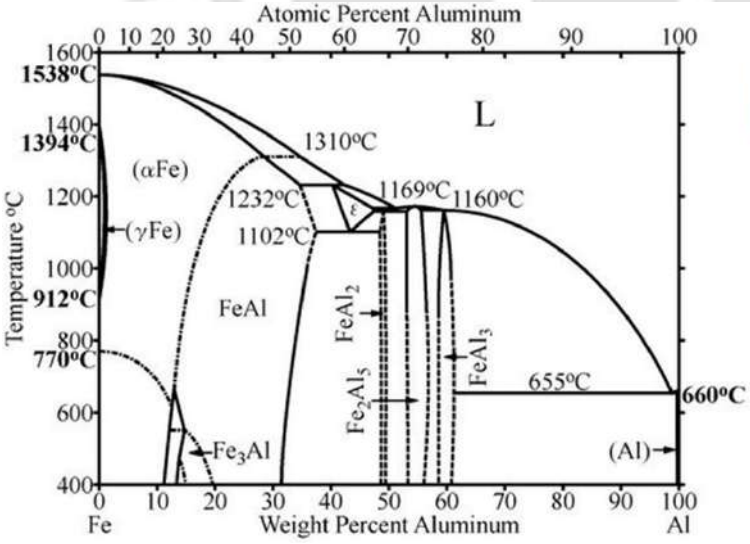

Aluminum percentage (at.%)	IMCs phases
25	Al_3Fe_2
50	AlFe
63	Al_3Fe_2
66–67	Al_2Fe
69.7–73.2	Al_5Fe_2
74–76	Al_3Fe ($Al_{13}Fe_4$)

Fig. 1.7 *AlFe binary phase diagram [65] and atomic percentage of the IMCs phases [3]*

In recent years, several researchers employed the FSW technique to join the different grades of steels and Al alloys. Mostly, the researchers were focused on the optimization of welding parameters, such as rotational speed [63,65–68], welding speed [63,67,69,70], tool

offset [63,65], tool tilt angle [71], and tool geometry [69,72,73] on the material and mechanical characterization of the joints. Experimental methods, namely the particle image velocimetry (PIV) technique [74] and X-ray radiography [75] were used to find the material flow movement during the FSW process. Lee et al. [76] investigated that the hexagonal close-packed (HCP) Al_4Fe compound was formed in the dissimilar FSW of stainless steel and Al alloy joints. Zhou et al. [77] employed friction stir lap welding to join Q235 steel and Al alloy 6061 using Al as the interlayer, which was fabricated on the steel by the friction surfacing process. This technique replaced the IMC layer with the diffusion layer at the Al/steel interface, which improved the atomic migration and interfacial bonding. Coelho et al. [78] joined high-strength steels, i.e., DP600 and HC260LA with AA6181-T4 Al alloy at a traverse speed of 8 mm/sec and rotational speed of 1600 rpm with tool pin offset of 1 mm towards the Al alloy. The Al/Fe interface consisted of fine equiaxed α-ferrite grains and a thin layer of Fe_2Al_5 IMC. Murugan et al. [66] joined the Al and 304 stainless steel sheets using the FSW technique at a traverse speed of 60 mm/min, rotational speed of 200–1000 rpm and tool offset of 1.25 mm towards the Al side. They were observed that the brittle IMCs produced the maximum hardness value at the Al/steel interface. Liu et al. [65] were observed that the IMC layer thickness increased by increasing the rotational speed and decreasing the traverse speed during dissimilar FSW of TRIP 780/800 high strength steel and 6061-T6 Al alloy. Their welded joints exhibited the maximum tensile strength of 240 MPa, which was about 85% of the base Al alloy. Zhaoa et al. [72] investigated the effect of traverse speed, rotational speed and tool offset on microstructure and mechanical performance of FS welded TRIP 780/800 steel and Al6061-T6511 Al alloy. The higher cooling and heating period reported on the Al side compared to steel, which could be attributed to the higher thermal conductivity of Al and the higher contact surface between the tool shoulder and Al sheet. Thaiping Chen [67] optimized the process parameters using the Taguchi technique for dissimilar FSW of A6061 Al alloy and SS400 steel. They achieved the maximum tensile strength (i.e., 76% of the Al) at a rotational speed of 550 rpm and welding speed of 1.2 mm/sec. Dehghani et al. [69] performed the FSW to join the Al5186 Al alloy and mild steel to investigate the influence of process parameters, i.e., tool tilt angle, traverse speed, plunge depth, and tool pin geometry on the microstructure of weldments. In their work, the harder material, i.e., steel provided the resistance to deformation and produced the tunnel defect at the RS. Pourali et al. [70] studied the effect of varying welding speed and rotational speed on the IMCs formation during the FSW of St37 steel and Al1100 Al alloy. They were found iron-rich IMCs, namely FeAl and Fe_3Al at the joint interface. Bang et al. [79] carried out the gas tungsten arc welding (GTAW) assisted dissimilar hybrid FSW to improve the strength of

stainless steel alloy (STS304) and Al alloy (Al6061) joints. They were found the minimum hardness in SZ about 50% of Al alloy due to the softening phenomena created by the hybrid FSW. Torres Lopez et al. [80] studied the impact of different tool offset values during the FSW of SAE 1020 steel and Al alloy 6063-T5 at low heat input conditions. In their study, the TEM analysis of different grains confirmed that some elements from the recrystallized stage persist in the SZ, such as low-angle grain boundaries, as shown in Figs. 1.8(a–c). However, the dynamic recovery in the SZ adjacent to the TMAZ-Al produced the cellular structure inside the grains, as shown in Figs. 1.8(d–f).

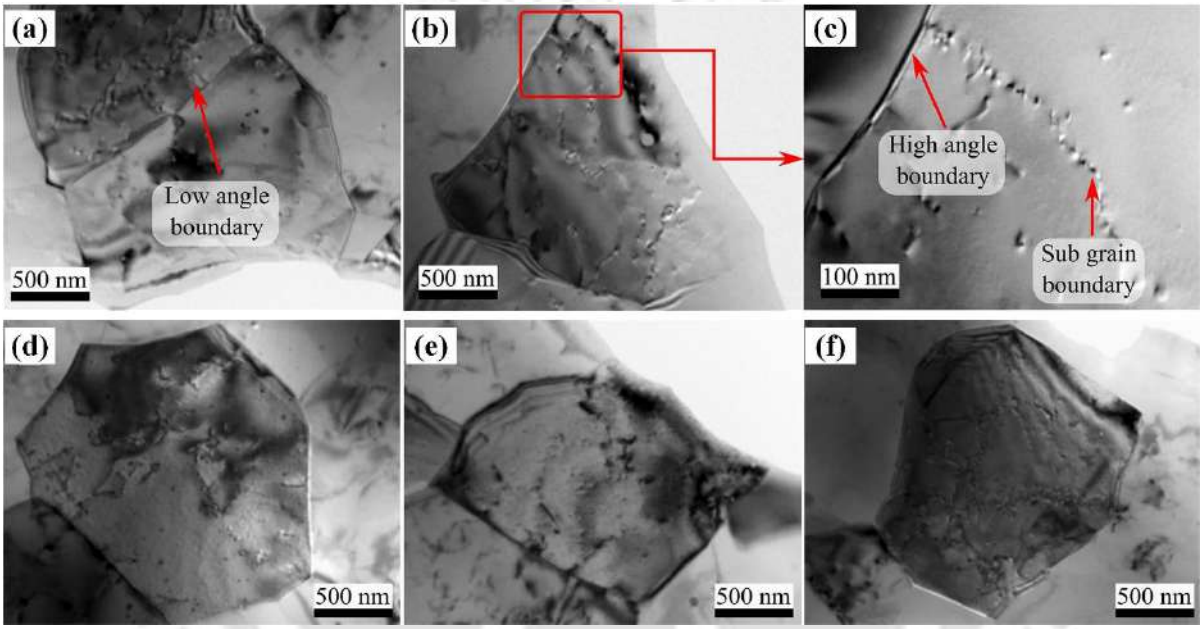

Fig. 1.8 *TEM analysis of (a–c) SZ; and (d–f) SZ adjacent to the TMAZ-Al [80]*

Yazdipour et al. [81] examined the effect of traverse speed, tool rotation direction, and tool offset in dissimilar FSW of 316L stainless steel and Al 5083–H321. They reported that shifting the tool pin towards the steel side enhanced the tensile strength. However, the large value of pin offset decreased the tensile strength caused by the formation of voids and coarse steel fragments in the Al matrix. Anaman et al. [82] joined the DP1200 steel to 5052-H32 Al alloy at a rotational speed of 2000 rpm, traverse speed of 75 mm/min, and tool offset of 0.5 mm towards the steel. They investigated that the complex mixed layer experienced higher hardness due to the presence of FeAl solid solutions and IMCs, namely FeAl, $FeAl_2$, and Fe_2Al_3. Ramachandran et al. [83] investigated that the taper angle of tool pin was significantly influenced the composition and thickness of the IMC layer during dissimilar FSW of HSLA steel (IRSM42-93) and AA5052 Al alloy. The formation of IMCs, namely $FeAl_3$, Fe_2Al_5 and FeAl was reported at a taper angle of 10°, 20°, and 30°, respectively. Kaushik et al. [84]

investigated the influence of the different tool pin profiles on the weld strength and microstructural characterization of the dissimilar mild steel and 5052 Al alloy joints. They were observed that the tool pin with a tapered cylindrical profile produced additional heat due to the excessive rubbing of steel. Habibnia et al. [5] studied the impact of FSW process parameters on the joining of 304 stainless steel with 5050 Al alloy sheets. They were obtained excellent weld quality at a rotational speed, traverse speed, and tool offset of 500 rpm, 80 mm/min, and 1.5 mm, respectively. Picot et al. [85] identified the Al-rich IMC, namely $FeAl_3$ at the 5083 Al alloy/316L stainless steel interface in the FS lap joint. Rafiei et al. [86] joined the 5083 Al alloy and A316L austenitic stainless steel to understand the impact of FSW parameters on the mechanical and microstructural behaviour of welded joints. They were observed that the traverse velocity had a considerable effect on the formation of the IMC layer and tunneling defects since it extended the elevated temperature during the welding process. The optimum welding conditions and tool materials for joining of Al-steel are summarized in Table 1.3.

Table 1.3 *Summary of the feasible parameters and joint strength of Al & steel joints*

Al alloy	Steel	Tool material	Plate thickness	Tool offset (mm)	ω (rpm)	v_{weld} (mm/min)	Strength (MPa)	Ref.
Al6181	DP600	Tungsten-RheniumWRe25	1.5	1	1600	480	211	[78]
Al5186	St52	-	3	1.3	355	56	246	[69]
Al5052	HSLA	WC	3	2	500	45	188	[83]
Al1050	S235	-	4	3.25	900	100	80	[87]
Al6016	Mild steel	WC-CO	1.12	3	900	250	210	[88]
Al6061	TRIP	WC-CO	1.5	1.63	1800	90	240	[65]
Al7075	Mild steel	-	3	1.6-1.7	500	100	333	[35]
Al6061	304 SS	WC	3	1.75	710	30	260	[89]
Al6061	SS	AISI 4140	6	2.8–2.9	550	54–72	225–240	[67]
Al1100	A441 steel	WC	3	1.3	800	63	80	[63]
Al5083	Mild steel	Tool steel	2	0.8	250	25	237	[68]
AA7075	Q235	W-25Re	2	1.6	650	30	100	[90]
Al5052	Mild steel	WC	3	2	386	40	195	[84]
3003-H18	St 52	-	3	2.7	450	12	146	[91]
Pure Al	IF steel	WC	3	~0.5	600	100	123	[92]

Notes: *If many welds were performed, the welding parameters providing the maximum strength are reported. HSLA: High-strength low-alloy steels, TRIP: Transformation induced plasticity, IF: Interstitial Free, St: Steel, SS: Stainless steel*

1.5 AUXILIARY ENERGY ASSISTED FSW

Tool wear and larger axial force are critical issues during the FSW of high temperature/high strength alloys, even though some alternate methods, i.e., auxiliary energy-assisted FSW or hybrid FSW (HFSW) and different tool materials used to overcome this problem [93]. Thermal-assisted hybrid FSW is the most convenient way to apply an additional preheating source before the FSW tool, as shown in Fig. 1.9(a). This extra thermal assistance softens the material in front of the tool before the stirring action, which can minimize the welding power consumption & welding forces and improve tool life & weld quality [93–95]. Preheating temperature can improve the material flow and recover the heat lost during the FSW process [96]. The main preheating source involves induction heating [97], electric arc heating [79,98], laser heating [94,99], and plasma heating [79,93]. Figs. 1.9(b–e) show the experimental setup of different preheating sources for the hybrid FSW process. Among the possible preheat sources, the plasma arc offers a unique combination of concentrated energy density, higher thermal efficiency, high arc stability, and low equipment cost [79].

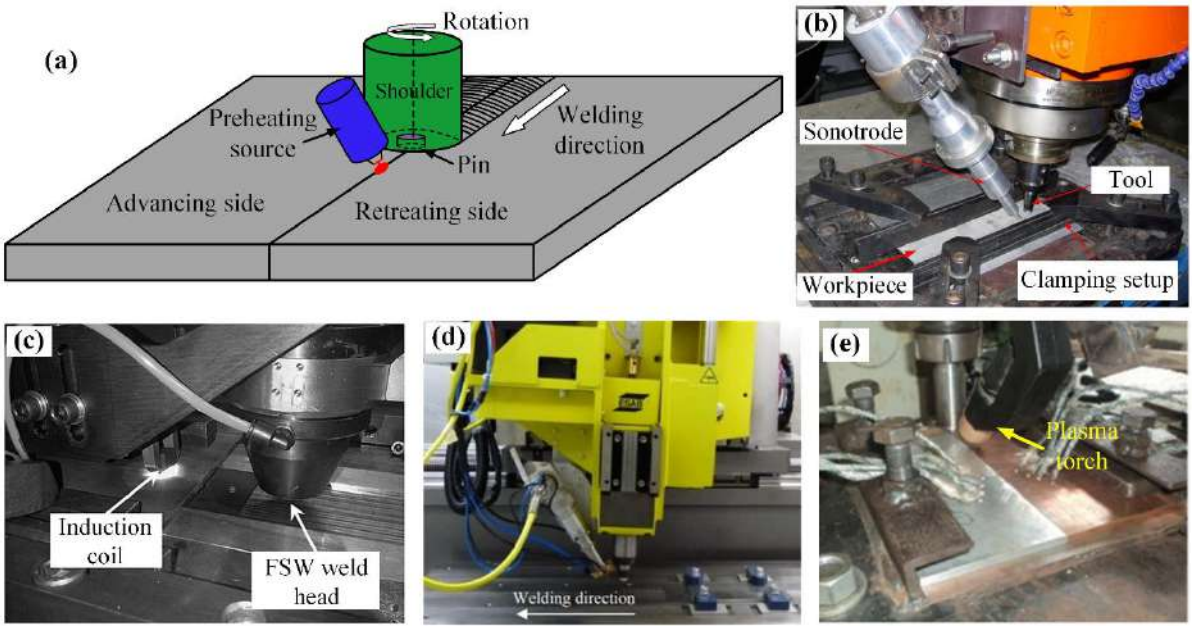

Fig. 1.9 *(a) Schematic illustration of the hybrid FSW process; (b) ultrasonic-assisted FSW [100]; (c) induction-assisted FSW [97]; (d) laser-assisted FSW [101]; and (e) plasma-assisted FSW [93]*

The researchers used various hybrid FSW processes to improve the weld quality and reduce the tool wear. Yaduwanshi et al. [93] established the 3D heat transfer model for plasma-assisted dissimilar FSW of pure copper and AA1100. In their study, the peak temperature was enhanced by applying the preheating source on hard material in front of the FSW tool, which

reduced the tool wear and made the materials weld easily. Song et al. [94] performed the laser-assisted FSW of Inconel 600 to evaluate the microstructure and mechanical properties of welded specimens. They reported that the grain refinement due to preheating improved the tensile strength and microhardness by 10% and 30%, respectively. Ahmad et al. [99] developed the three-dimensional FE model based on the coupled Eulerian-Lagrangian approach to optimize the laser-assisted FSW of DH36 steel. They reported that laser assistance improved the tool life by reducing the reaction force on the tool pin to 55% compared to that of normal FSW. Bang et al. [79] improved the weld strength using the gas tungsten arc as additional preheating assistance in dissimilar hybrid FSW of aluminum (Al6061) and stainless steel (STS304). They were observerd the grain refinement in the SZ of hybrid friction stir welds due to temperature increment and severe plastic deformation. Bang et al. [98] used the tungsten inert gas (TIG) as a preheating source to reduce the plunging force and improve the plastic flow during dissimilar hybrid FSW of DP590 high-strength steel and Al5052 Al alloy. Yaduwanshi et al. [95] reported the enhancement in material flow and reduction in plunging force during the plasma-assisted FSW (PAFSW) of Al alloy. They were found that the PAFSW reduced the grain size, uniformly distributed the hardness, and enhanced the tensile strength by about 8% higher than conventional FS welded joints. Merklein et al. [102] performed the dissimilar hybrid FSW of steel and Al using a laser as a preheating source to reduce the tool wear and improve the weld quality. Sundqvistv et al. [103] established the 3D Eulerian model to analyze the laser-assisted dissimilar FSW of SS AISI 304 L and Ti–6Al–4V. They were observed that the laser preheating reduced the forces on the FSW tool due to the high temperature field around the tool. Yaduwanshi et al. [104] improved the weld quality and welding efficiency using plasma as an additional heat source in the FSW of AA1100 with pure copper. Increasing the preheating current enhanced the material flow, which reduced the formation of voids in the welded specimens. Alvarez et al. [97] conducted a comparative study of induction-assisted FSW (IA-FSW) and normal FSW of duplex stainless steel. They were observed that IA-FSW produced the dynamic recrystallized refined grains in the SZ, which resulted in the higher strength of the welded joints. Bilgin et al. [105] reported that the open-flame heating system improved the plastic deformation and reduced the generation capacity of welding defects during the heat-assisted dissimilar FSW of AZ31B magnesium with AA7075-T6 aluminum alloy. Furthermore, the mechanical properties deteriorated with a decrease in the temperature caused by increasing the axial & feed forces during the FSW process.

1.6 MATERIAL FLOW INTERPRETATION

The schematic model of material transportation around the FSW tool is shown in Figs. 1.10(a) and 1.10(b). FSW process involves different forces, such as axial force from the shoulder, contact force from the pin, and extrusion force from the backing plate. The tool section is divided into quadrants: advancing/leading, advancing/trailing, retreating/leading, and retreating/trailing. The advancing/leading quadrant initiates the shearing of plasticized material adhered to the tool surface, and then it is transported and accumulated across the retreating/leading quadrant. Finally, the accumulated material is deposited layer by layer on the trailing side, and the cycle is repeated as the rotating tool pin traverses through the workpiece simultaneously.

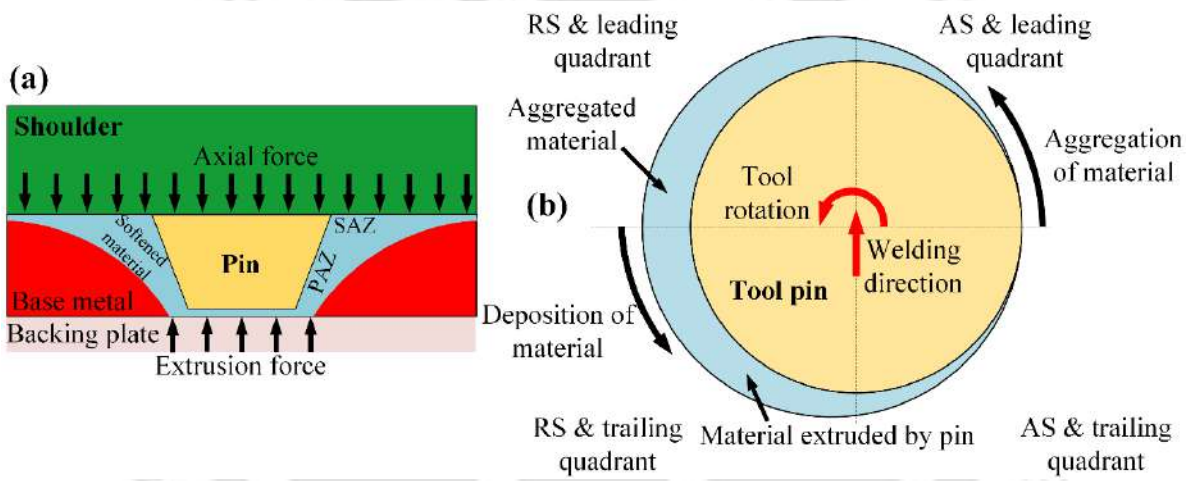

Fig. 1.10 *(a,b) Schematic illustration of material movement around the FSW tool*

The top section of the welded region can be designated as the shoulder-affected zone (SAZ) because the shear and extrusion of the tool shoulder generate the primary driving force for the material flow in this zone. The middle and the lower sections can be defined as the pin-affected zone (PAZ), where the driving force for the material flow originates mainly from the shear of the tool pin side.

Understanding in-process material flow around the tool is essential since it is critical in governing fundamental processes, such as heat generation and dynamic recrystallization, which subsequently impact the microstructure and weld characteristics [106]. Sometimes, the material movement leads to improper mixing under insufficient heat generation with subsequent generation of defects, such as cracks and voids in welded joints.

The proper material flow can remove/minimize defects by choosing the right combination of the welding parameters. In the FSW, the process parameters, i.e., tool rotational speed and traverse speed are crucial parameters that can monitor the heat generation and material flow, as well as regulate the evolution and growth of the IMC layer [3]. The severe plastic deformation at higher heat generation can lead to extensive IMCs formation with a subsequent reduction in the joint strength. Conversely, insufficient heat input at a low rotational speed may generate voids, tunnels, and micro-cracks due to improper material flow [8]. Therefore, the optimum parameters are needed to produce the sound quality joints by controlling heat generation and material flow characteristics.

1.7 PROCESS MODELLING AND SIMULATION

The FSW process simulation is a complex problem involving massive deformations, strain rates in the stirring zone around the rotating tool, and physical couplings between mechanics and heat transfer. Numerical methods can be an excellent alternative to costly and time-consuming experiments to understand these complex phenomena. The estimation of many process parameters, including tool geometry and speeds, is possible through numerical simulation of the FSW processes. However, the simulation is not a simple task because it involves the interaction of thermal and mechanical phenomena. Some well-known numerical modelling methods were established to clarify and evaluate crucial aspects of the process physics related to the FSW. The FSW simulations cover a wide range of complexities, starting with the basic conduction heat transfer models [107,108] to the material flow models [109–111] and the fully thermo-mechanical coupled models [112–114]. These heat transfer & viscoplastic flow-based models evaluate the thermal history, material flow properties, and residual stress distributions. Some other simplified numerical models were also implemented to reveal numerous aspects of the complex thermo-mechanical phenomena related to the FSW. Overall, the numerical analysis can be very helpful for describing and assessing important FSW process characteristics. Numerical modelling can be used to identify the development of a thermo-mechanical environment and material flow behaviour under standard conditions during the welding process. For that reason, this section summarizes some of the recent numerical advances made in the field of conventional FSW process.

1.7.1 Thermal Modelling

The heat generation between the workpiece and tool is the primary element that acts as a driving force for the FSW technique. Compared to experimentation, the numerical methods are cost & time effective for computing the heat generation in the FSW process. Two kinds of thermal models for the FSW process are developed. The first model assumes only the sliding condition based on the frictional heat, and the second model assumes sliding & sticking conditions based on both frictional heat and plastic deformation [115]. The thermal models based on frictional heat (sliding condition) and constant friction coefficient were successfully developed and verified for FSW of aluminum alloys [116–118]. The sophisticated numerical model for the FSW process increases interest since the effect of different process parameters can be studied comprehensively [115]. The maximum temperature generated by the heat flux must be high enough to soften the material for stirring action by pin. Still, it should be low enough, so the material does not liquefy. The weld quality, shape, and size of a weld, residual stress and deformation in the FS welded specimen, tool life, and efficiency can be depicted by the extent of the heat conducted into the workpiece material [119]. The microstructural variation across the cross-section significantly influences the mechanical characterization of the welded joint. The microstructural changes can be strongly controlled by the thermal heat input, which further depends on the welding and rotational speed [117]. The shoulder diameter is also an essential factor in FSW tool geometry, which significantly influences the material softening during the welding process [120]. Tool wear is an important issue during the joining of high-temperature/high-strength alloys, i.e., titanium, nickel, and steel. Insufficient heat input may lead to wear of the tool pin due to lack of softening, which results in inadequate plastic deformation of the material [121]. Therefore, the development of the finite element (FE) thermal model for FSW is necessary to measure and optimize the thermal history concerning process parameters, such as tool traverse speed, rotational speed, and tool geometry.

Many previous researchers established 3D heat transfer models to determine the thermal history during the FSW process. Nandan et al. [122] investigated the thermal history and material flow behaviour for FSW of AISI 1018 steel. They reported the asymmetry in temperature distribution around the tool region due to the rotating and traversed action of the tool. Riahi and Nazari [118] established the 3D thermo-mechanical model to determine the temperature history for the FSW of AA6061. They were observed the non-symmetric temperature distribution nearby the weld center line and validated the numerical results with the experimental observations. Das et al. [123] developed the FE thermal model for FSW of

AA6061 plates to obtain the temperature distribution. In the FE model, sticking and sliding phenomena were assumed between the tool and the workpiece. Their established heat source model was confirmed with the experiments with a percentage error of 5% for maximum temperature. Moussawi et al. [124] used the CFD technique to develop the numerical model to predict the strain rate, material flow, and temperature field during FSW of DH36 steel. The heat generation was divided into three parts, i.e., shoulder, pin side surface, and the tip of the pin. It observed that the cooling rate and peak temperature increased by increasing the traverse speed and rotational speed, respectively. Ahmad et al. [119] established the finite element (FE) model for FSW of DH36 steel using the coupled Eulerian-Lagrangian (CEL) approach in Abaqus/Explicit FE software package. Their developed FE model investigated the plastic strain, temperature distribution, and flash generation in welded specimens during three stages of the FSW process, i.e., plunging, dwelling, and traverse phase. They were also observed that the maximum flash produced on the workpiece surface at the slower weld model (200 rpm & 120 mm/min) than the faster weld model (700 rpm & 500 mm/min), as shown in Fig. 1.11.

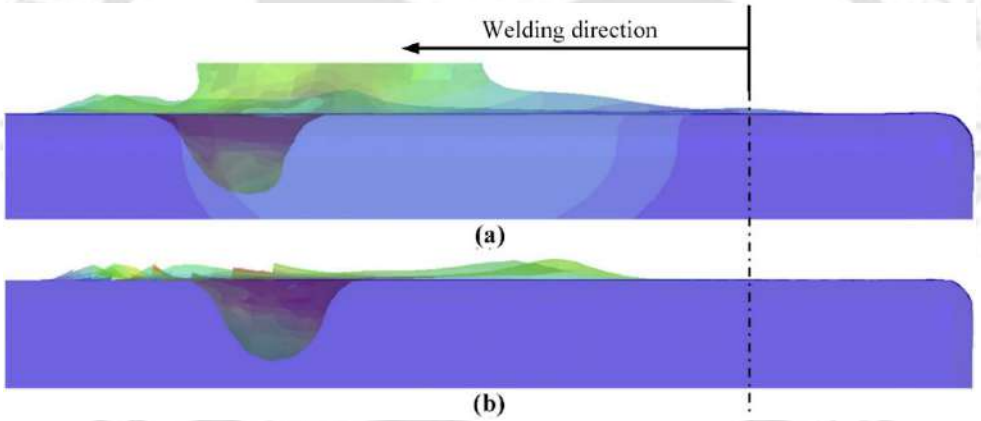

Fig. 1.11 *Visualisation of flash and weld from the side view in the (a) slower weld model; and (b) faster weld model [119]*

Ma et al. [115] developed two kinds of FE thermal models to measure the thermal history during the welding process. The first model was developed based on heat generation due to friction only. However, the second model assumed heat generation by the combined action of friction as well as plastic deformation. Yau et al. [125] developed the nonlinear computational model based on frictional heat generation for measuring the temperature distribution during the FSW of Al2024-T3 alloy. In the developed FE model, they assumed the constant coefficient of friction and neglected the heat loss during the plunging and retracting phase of the tool. Darvazi et al. [126] numerically measured the thermal history and residual stress by considering the mechanical and pin effects in FSW of 304L stainless steel. They reported that

the heat generation from plastic deformation and heat convection coefficient considerably influenced the temperature distribution. Hernandez et al. [127] compared the transient and steady-state models through the measurement of stress, streamlines, and temperature distributions during the dissimilar FSW of AISI 1078 and AISI 1008 steels. They reported that a steady state could provide faster results than a transient state. The asymmetric temperature distribution was observed in the SZ due to the different thermal properties of the steels. Zhu et al. [128] performed the nonlinear thermal FE analysis to measure the time-temperature field in the FSW of 304L stainless steel. They were obtained the highest temperature at the welding line and surrounded by the tool shoulder. The maximum temperature difference was lesser than 100 ^{o}C concerning the rotational speed of 300 rpm and 500 rpm. Selvaraj et al. [129] proposed the 3D FE thermal model based on the slip factor to predict the influence of welding parameters on the peak temperature during the FSW of 304L stainless steel. They were observed that the peak temperature increased with an increase in rotational speed and a decrease of traverse speed. Camilleri et al. [130] developed the thermos-elastoplastic numerical model to predict the thermal history, deformation, and thermal stresses in the FSW of DH36 steel. It was found that heat loss into the machine bed and tool significantly influenced the cooling rates and magnitude of the peak temperatures. Nandan et al. [131] measured the temperature history in the FSW of 304 stainless steel through momentum, mass, and energy conversation equations solved by the 3D viscoelastic model. Zhang et al. [132] used the Abaqus software FE package to develop the thermal-structural model for FSW of AA2024-T3 with different thicknesses. They were obtained the higher material flow in the RS due to lesser slipping rates and large heat fluxes in the AS. Buffa et al. [133] used the DEFORM-3DTM software to develop the FE model for FSW of AA7075 Al alloy to determine the thermal history in the SZ and HAZ. Their model considered the FSW tool as a rigid body and workpiece as a rigid viscoplastic behaviour.

1.7.2 Multiphase Flow Modelling

Experimentally, it is difficult to determine the heat and material flow characteristics around the high-speed rotating FSW tool, which is subjected to complex physical interaction with the workpiece materials. Numerical methods are reported as cost-effective and convenient ways to understand the complex physics involved in the heat and material flow during the welding process [134]. Therefore, a three-dimensional (3D) fully coupled thermal-mechanical model needs to be established to understand the material flow characteristics, such as velocity components, viscosity variation, and strain rate. In the simulation, the three major challenges

generally occur in solving the FSW process [135]. Primarily, the severe plastic deformation of the material may easily cause element distortion and consequent simulation divergence. Secondary, inaccuracy to a certain degree due to the material behaviour under combined environments of higher temperature and strain rate. Tertiary, the difficulty in defining the thermal and mechanical conditions at the workpiece/backing plate interface and tool/workpiece interface. On the other hand, the dissimilar joining process experiences very complex multi-physical phenomena in heat generation, material flow, material mixing, and plastic deformation compared to similar joining [136]. In the similar FSW, the material movement generally occurs in the two main regions, i.e., beneath the FSW tool shoulder and around the tool pin [137]. However, the material flow in the dissimilar FSW occurs at the additional interfaces between the two materials, which controls reaction-diffusion between the elements and, subsequently, the IMCs formation [137]. Therefore, the simulation of dissimilar joints has been an exciting topic for industries and academic researchers due to the complexity & difficulty of equations and boundary conditions, particularly at base material contacts. For that reason, fully coupled thermo-mechanical models need to be established to better comprehend the process variables, such as heat generation, strain distribution, material flow, and material intermixing.

Nowadays, the two kinds of thermo-mechanical modelling techniques for numerical simulation, namely CFD and computational solid mechanics (CSM) are used. Regarding solid mechanics, two main methods, arbitrary Lagrangian-Eulerian (ALE) method and coupled Eulerian–Lagrangian (CEL) method have been utilized. The ALE method is utilized to retain a good mesh quality during the calculation of the FSW process [138]. However, the greater stirring impact of the FSW process led to excessive mesh distortion and, subsequently, premature interruption of the simulation using the ALE method [139]. To resolve the drawbacks of the ALE method, the CEL method has been utilized to deal with extreme material deformation during the FSW process. The extensive mesh distortion can be avoided using this method since the Lagrangian formulation is used to model the tool, and the workpiece domain is described by the Eulerian formulation [138]. However, the CEL method is based on explicit integration strategies, which include a very small step size, a large number of increments, and a substantial computational time [140]. A mass scaling strategy was used in the CEL method to increase computational efficiency [139,140]. On the other hand, the improper selection of the mass scaling factor can produce quantitatively incorrect results [141]. For that reason, the majority of the FSW simulations were performed for a short computational time (plunging and

dwelling phase) [142–144]. Furthermore, the computational cost for the CEL modelling of the complex friction stir process is yet another serious issue [145].

The CFD method is the other most widely used approach to examine the intricate nonlinear material flow and heat transfer in the FSW process. Apart from the capability to prevent mesh distortion caused by severe plastic deformation, CFD-based models are more compatible than CSM in dealing with complex tool geometries [146]. During the development of the ALE model, it is necessary for the tool pin to penetrate the workpiece to prevent computational misconvergence. As a result, a significant variation exists between the actual conditions and simulation results, which can be reduced by employing CFD method [147]. Furthermore, the CFD method significantly reduces computational time and cost [146]. This is because the CFD-based thermo-mechanical analysis simplifies the governing equation by ignoring the elasticity conditions, and the calculation of stress is only dependent on the velocity gradient [146]. In recent years, CFD-based models have been widely established for simulating the FSW process due to their precise estimation of the heat generation, thermal history, material flow behaviour, and defect formation [148,149]. Jiang et al. [150] developed the multiphase flow model based on the volume of fluid (VOF) approach to determine the material flow and mixing in the dissimilar FSW of Al/Mg alloys. Their model assumed materials as an incompressible non-Newtonian viscous fluid and analyzed the material flow under quasi-steady state heat transfer conditions using mass, momentum, and energy conservation equations. The model was successfully validated by comparing the measured and calculated mixed zone width, thermomechanically affected zone (TMAZ) boundary, and temperature distribution at the tool/workpiece interface. Sadeghian et al. [134] performed heat transfer and CFD-based simulation to investigate the materials flow behaviour during the dissimilar FSW of 5083 Al alloy and 304 stainless steel. They were observed that the distribution of the steel particle in SZ enhanced by increasing the rotational speed, leading to the initiation of cracks and defects. Nandan et al. [151] developed the numerical model based on the mass, momentum, and energy equations to determine the temperature fields during the FSW of 6061 Al alloy. In their study, the heat generation was calculated from rotational speed, tool geometry, and yield shear stress, whereas non-Newtonian viscosity was computed based on the strain rate, temperature, and material properties. Eyvazian et al. [1] used the VOF approach to investigate the materials flow, intermixing, and temperature profile in the dissimilar underwater FSW of AA5182 Al alloy and AISI 1010 steel. In their research, it was observed that the thickness of the IMC layer continuously increased by decreasing the tool traverse velocity and increasing

the rotational speed due to higher heat input. Yang et al. [136] considered the dissimilar materials as functionally graded materials (FGM) to build the model for understanding the materials flow characteristics during the dissimilar FSW of Mg alloy (AZ31BeH24) and 6061-T4 Al alloy. Gotawala and Shrivastava [137] and Kadian and Biswas [110] applied the VOF method to investigate the material movement during the dissimilar FSW of Al and copper. They were observed that the rotational tool speed and welding speed directly affected the mixing of plasticized materials. Derazkola and Khodabakhshi [152] developed the 3D thermo-mechanical model to examine the nucleation and growth of the IMC layer during the FSW of AA5005-O Al-Mg alloy and St-52 steel. They were found that the higher peak temperatures enhanced the material flow patterns and growth kinetics of IMC layer formation. Liu et al. [135] developed the coupled thermal-mechanical model based on the volume of fluid method for the dissimilar FSW of 6061 Al Alloy and TRIP steel. Their developed model can capture the material features around the high-speed rotating tool. The chunk of steel pieces was extruded from the bulk steel region and deposited in the bulk aluminum region at the RS under different tool offset conditions, as shown in Figs. 1.12(a) and 1.12(b).

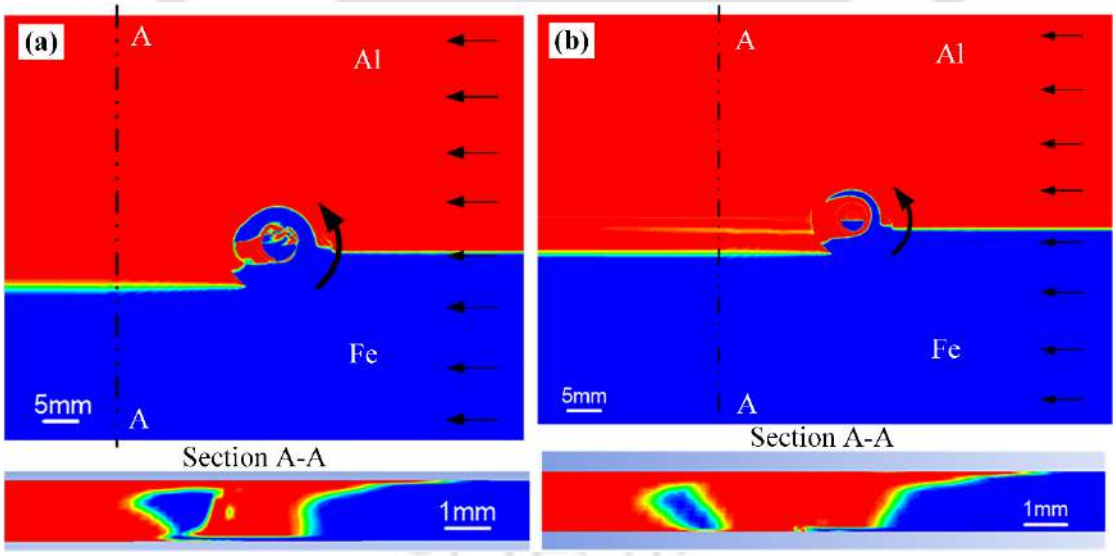

Fig. 1.12 *Material distribution at a tool offset of (a) 1.03 mm; and (b) 1.63 mm [135]*

Tang and Shen [153] used the finite volume model to investigate the consequence of preheating technique on the temperature and material flow in steel and Al alloy FS welded joints.

In the CFD-based model, multi-species transport is also a suitable approach for predicting phase flow by calculating the changes in thermo-physical properties of dissimilar materials. In the STM, the primary governing equations, i.e., mass, momentum, energy, and species conservation equations describing convection, diffusion, and reaction sources are

solved for each individual species assigned in the mixture. Nandwani et al. [154] studied the flow of multiple phases in a porous bed using this mixture model, which took into account the mass transfer of the surfactant into the oil and water phases. This method was used by Lin et al. [155] to study the heat and mass transfer characteristics of a condensed combustion flue gas inside a cross-flow transport membrane tube bundle. Zhang et al. [156] and Lee and Dimenna [157] established the species transport model to simulate the gas mixing process under thoroughly turbulent flow conditions. Furthermore, Mansour et al. [158] and Thomas et al. [159] used the species transport model to compute the mixing between the two different fluids by considering a laminar fluid flow. Likewise, the dissimilar FSW process involves complex multi-physical phenomena in terms of heat generation, flow, and intermixing of different materials. Accordingly, the STM can be a convenient way of addressing the physics associated with heat transfer and material flow in terms of mass transfer during the welding process.

1.8 SUMMARY

The welding industry has been revitalized with the development of dissimilar joining using traditional, unconventional, as well as hybrid welding technologies. Dissimilar welding has enormous potential to reduce manufacturing cost, production time, and overall structure weight, especially in the shipbuilding, aerospace, and automotive industries. Friction stir welding, a solid-state welding technology, provides many advantages over conventional welding techniques to join dissimilar materials with substantially different physical, thermal, and mechanical properties. There are still a number of significant obstacles to overcome before it can be effectively implemented for joining dissimilar materials in a wide range of industries. Therefore, a better understanding of the behaviour of FSW joints is required to ensure their safety, efficiency, and reliability.

In view of that, this chapter comprises the research activities and progress to date in the advancement of experimental and numerical analysis of FSW of dissimilar materials, especially al-steel & steel-steel, with an emphasis on their applicability to the manufacturing of components. Firstly, an experimental investigation of the influence of welding conditions on weldability is discussed; then, different kinds of numerical methods and modelling techniques are presented. Numerical analyses of the FSW process can accurately predict the major process variables, which can eliminate the number of experimental trials, speeds up the design procedures, and decreases the expense of variable optimization.

According to the literature survey, the biggest problem during the FSW of similar/dissimilar steels is larger axial force and tool wear. Some alternate methods, i.e., hybrid friction stir welding (HFSW) and different tool materials were used to overcome this problem. Accordingly, the research area can be expanded in the field of the development of a durable, long-lasting, and cost-effective tool material. Previous research was conducted using WC-CO based tools, while the PCBN base tools are not recommendable due to their high cost. From the weld characteristics perspective, the review shows that most research was focused on improving the weld strength, and a few works were concentrated on improving the tool life. The hybrid FSW technique is reported as a convenient way to improve the tool life as well as the weld quality. Consequently, more research on the hybrid FSW technique is required to reduce the joining cost and enrich the commercialization of FSW for high-strength alloys.

The literature survey on the FSW of steel and Al alloy reveals that a smooth gradient of grain size, a thin Fe-riched IMC layer, and smaller defect-prone steel fragments in the weld zone can be favourable to the joint performance. The IMCs formation in the FSW is a major issue similar to conventional welding techniques. A literature survey exposed many of the parameters, i.e., rotational speed, traverse speed, and tool offset, that can control the formation and growth of IMCs. The heat generation and plastic deformation have a significant effect on IMCs thickening, phase transformation, and, subsequently, the weld quality.

Experimentally, it is also difficult to analyze extensive material deformation and heat generation during the welding process. On the other hand, numerical modelling assists in understanding the effects of various weld parameters (including tool design) and boundary conditions on the fundamental behaviour of weldments without the need for expensive experimentation. The finite element method (FEM) is the most popular technique for the numerical analysis of FSW. Numerical techniques, such as the finite difference method, particle method, and fluid mechanics method must be used to prevent these challenging or problematic processes. An appropriate numerical method is essential to develop computational FSW process models that are efficient, robust, and bidirectional. Currently, the CFD-based volume of fluid (VOF) method is convenient for dealing with complex material flow through coupled thermal-fluid flow analyses in dissimilar FSW models. Furthermore, the species transport model (STM) can be a suitable technique for addressing the physics associated with heat transfer and material flow in terms of mass transfer during the welding process.

CHAPTER 2

RESEARCH OBJECTIVES AND THESIS OUTLINES

From the previous chapter, the overview and literature survey of existing work reveals that FSW is the most convenient technique to join the dissimilar material. There are still a number of significant obstacles to overcome before it can be effectively implemented for dissimilar joining in a wide range of industries. Therefore, a better understanding of the behavior of dissimilar FSW joints is required to ensure their safety, efficiency, and reliability. In this dissertation, an attempt is made to find the optimum welding conditions through experimental investigation supported by numerical modelling. This chapter summarizes the main objectives followed by the thesis organization based on the research gap in the field of dissimilar FSW process.

2.1 RESEARCH GAP

Despite the promising results in the field of dissimilar FSW, a comprehensive investigation for the joining of dissimilar materials, especially for dissimilar steels, and steel to Al alloy is still lacking. The previous studies were mainly concerned with the joining of dissimilar Al alloys, Al alloys to Cu alloys, and Al alloys to Mg Alloys. The following research gap from the literature survey on the experimental and numerical study of dissimilar FSW can be summarized.

2.1.1 Experimental Study

- The literature survey on the joining of dissimilar steels shows that very few published literature is available on the FSW of structural steel sheets. The fundamental knowledge of the FSW for joining the dissimilar steel plates is relatively limited.
- There is a lack of in-depth analysis of the impact of processing parameters (i.e., rotational speed, traverse speed, tool offset, and plunge depth) on thermal history, axial force, macro/microstructure, and mechanical performance of the dissimilar steel joints.
- There is no literature found on dissimilar FSW of DH36 shipbuilding steel and AISI 1008 steel.

- Regarding the dissimilar FSW of Al alloy and steel, most of the studies in the existing literature were focused on optimizing tool pin geometry, rotational speed, and traverse speed. Only a few studies were conducted on varying tool offsets by keeping the other parameters constant. Comprehensive research on the effect of varying tool offsets on the IMCs formation, macro/microstructure, and mechanical performance of Al/steel joints is still lacking.
- The wide-ranging research on the coinciding effect of tool traverse speed on the volume fraction of steel fragments and IMCs, metallographic behaviour, and mechanical performance of joints is still missing.
- An experimental investigation on the dissimilar FSW of 6061-T6 aluminum alloy to DH36 steel & 304 stainless steel is not explored.

2.1.2 Numerical Study

- The literature survey on hybrid FSW reveals that various numerical and experimental studies were performed on the hybrid FSW. These studies were concerned with similar materials and low melting temperature alloys, such as aluminum alloys. Very few researchers worked on hybrid FSW of high melting temperature alloys like steel.
- The literature review shows the lack of in-depth analysis of thermal history under varying welding & preheating parameters during the PAFSW of dissimilar steels.
- There is a lack of understanding of the flow behaviour of dissimilar materials (especially for Al alloy and steel) from a physical basis, which is otherwise difficult to compute through simple experiments. Numerical methods are reported as convenient ways to understand the material flow behaviour around the FSW tool. However, the numerical modelling of the material flow is one of the yet least defined phenomena during the dissimilar joining of steel and Al alloy.
- It is well known that the CSM method has some constraints when addressing complicated material movement and nonlinearities induced by severe plastic deformation in the FSW. Another important approach is the CFD method, which has the capability to generate highly accurate results in the heat transfer and material flow modelling of dissimilar FSW process. Furthermore, the numerical technique, i.e., the multi-species transport method coupled with the mixture model suits the multiphase thermal-fluid flow dynamics reasonably well. However, this technique was not yet applied to predict the material flow in the FSW process.

2.2 RESEARCH OBJECTIVES

Based on the research gap in existing literature, the overall objective of the thesis work is to determine the feasible processing parameter for defect-free weld joints. It is achieved by comprehensive experimental analysis supported by numerical modelling. Accordingly, the primary objective is divided into the following research objectives for the accomplishment.

- To optimize the welding process parameters during the dissimilar FSW of shipbuilding grade steel, i.e., DH36 steel and AISI 1008 steel.
- To investigate the optimum process parameters for successfully joining the DH36 steel and 6061-T6 aluminum alloy.
- To identify the feasible parameters domain to produce the sound quality weld joints of 304 stainless steel and 6061-T6 aluminum alloy.
- To develop the three-dimensional finite element-based thermal models for the comparative thermal history between conventional and hybrid FSW processes for dissimilar steels, i.e., DH36 steel and AISI 1008 steel.
- To build up the volume of the fluid-based multiphase CFD model by incorporating a modified analytical model for dissimilar FSW of DH36 steel and 6061-T6 aluminum alloy.
- To establish the steady-state CFD-based multi-species transport model for dissimilar FSW of 6061-T6 aluminum alloy and 304 stainless steel.
- To perform the comprehensive experimental characterization of the dissimilar weld joints based on the mechanical performance, welding forces, macro/micrographs, material flow features, quantification of steel fragments and IMCs, and phase/composition analysis of IMCs.
- To conduct the comprehensive numerical investigation of the temperature distribution and material flow properties, i.e., material flow velocity, strain rate, dynamic viscosity, and material intermixing by triggering material flow associated with the high-speed rotating tool during the dissimilar FSW process.

2.3 SCOPE OF THE PRESENT WORK

The focus of the current work was to produce the sound quality friction stir weld joints of dissimilar material combinations, i.e., DH36 steel & AISI 1008 steel, DH36 steel & 6061-T6 aluminum alloy, and 304 stainless steel & 6061-T6 aluminum alloy. The main goal of the current work is to identify the feasible domain of the welding parameters through experimental

investigation supported by the numerical modelling. Accordingly, the proposed experimental work has a huge scope to investigate the effect of different welding parameters (i.e., rotational speed, traverse speed, and tool offset) on the thermal history, welding forces, metallographic behaviour, IMCs formation, and their corresponding effect on the mechanical performance of dissimilar joints. Numerically, there is a huge scope of proposed 3D heat transfer modelling to better understand the effect of welding & preheating parameters on thermal history during the conventional and hybrid FSW processes. On the other hand, the CFD models based on the volume of fluid and multi-species transport approach are capable to find the effect of welding process parameters on thermal history, material flow properties (i.e., material flow velocity, viscosity, pressure, and strain rate) and material intermixing around the high-speed rotating tool.

Regarding potential industrial applications, the dissimilar material combinations chosen for the present work can be more applicable in industrial construction and manufacturing sectors like marine, aerospace, and automotive. Increased use of dissimilar combinations for engineering applications is growing because of special performance requirements for corrosion resistance, high strength to weight ratio, optimal mechanical performance, cost-effectiveness, and value addition. The sophisticated hybrid constructional design can produce the lightweight structures where the low-density materials like Al alloys replace some steel parts. In the shipbuilding sector, the joints of the Al superstructure with decks and hull (made of steel) maintain the lower centre of mass for proper stability and buoyancy. In the automotive sector, the category of dissimilar alloys like different graded steels and steel-Al alloys can reduce the overall weight of the vehicle and, subsequently, improve the fuel efficiency.

2.4 LIMITATION OF THE THESIS

The present research is based on the identified technical gaps from the existing literature on the dissimilar FSW process. Accordingly, this thesis includes both comprehensive experimental analysis supported by numerical modelling for dissimilar FSW process. This thesis focuses on the specific dissimilar material combinations, i.e., DH36 steel & AISI 1008 steel, DH36 steel & 6061-T6 aluminum alloy, and 304 stainless steel & 6061-T6 aluminum alloy. Due to time and resource constraints, this thesis does not explore the effect of different IMCs on the corrosion behaviour of Al-steel joints. Numerically, the proposed heat transfer and CFD models were subjected to certain assumptions and simplifications as a consideration

of realistic results. Furthermore, the numerical stability in simulations and convergence can be computationally demanding and might require substantial computational resources.

2.5 ORGANIZATION OF THE THESIS

This thesis is organized into ten chapters with references and appendices. Each chapter ends with a summary outlining the achievements and findings obtained through experimental investigation or numerical simulations. Fig. 2.1 shows the plan of the thesis work organized into the different interrelated sub-objectives.

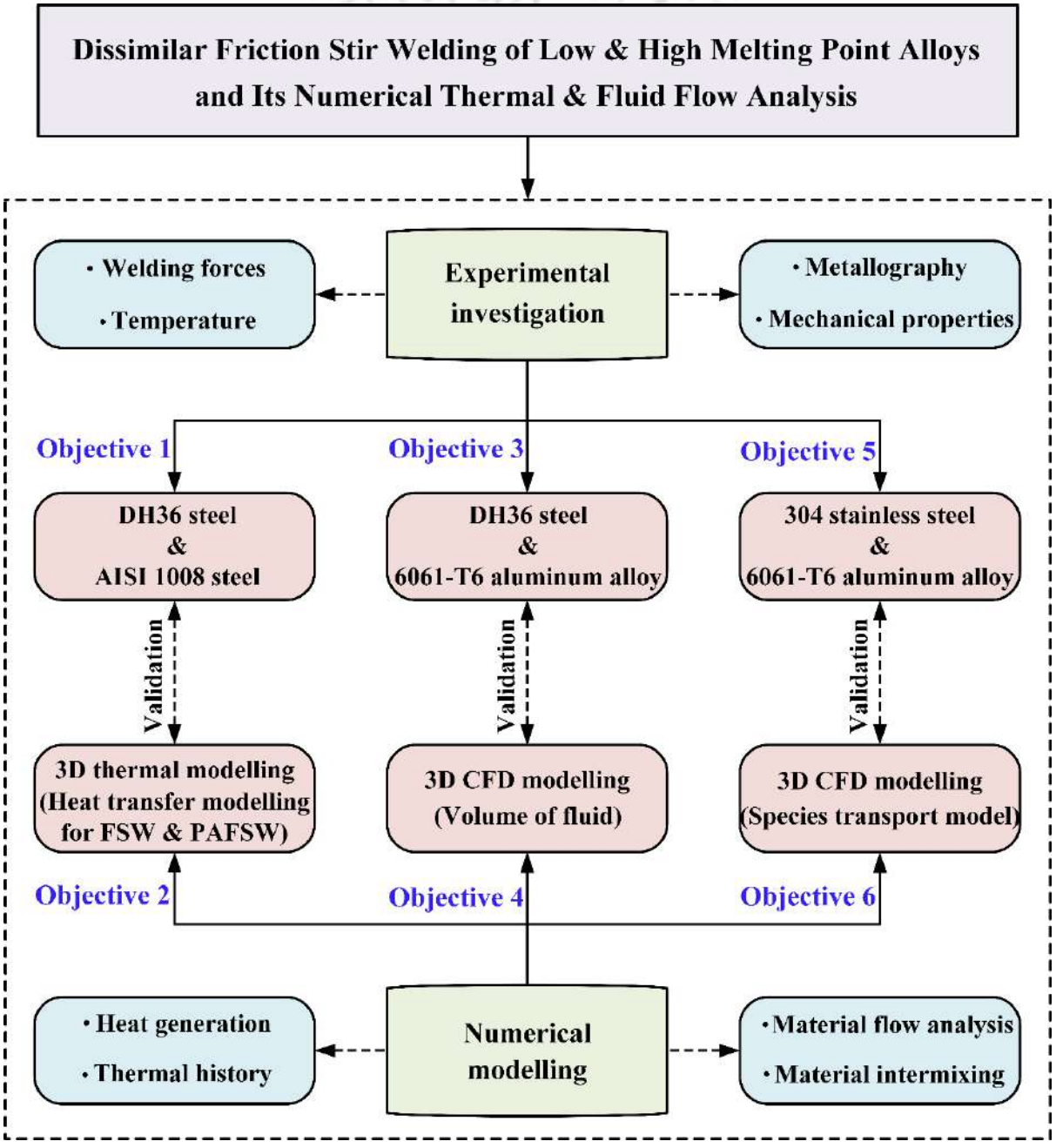

Fig. 2.1 *Plan of the work to accomplish the objectives*

Chapter 1 provided an overview of FSW, a literature survey on experimental and numerical analysis of dissimilar FSW process, and the motivation for the present work.

Chapter 2 (current chapter) discusses the thesis outlines followed by primary objectives based on the research gap from the literature survey. The remaining part of the thesis is organized as follows:

Chapter 3 includes the experimental and numerical methodologies adopted in the present work. Also, the modified mathematical formulation to develop the FE-based three-dimensional numerical models is discussed.

Chapter 4 deals with the joining of dissimilar steels, i.e., DH36 steel and AISI 1008 steel. This chapter discusses the influence of the rotational speed, traverse speed, and tool offset on temperature distribution, axial force, microstructure, and mechanical performance (i.e., tensile properties, impact toughness, and hardness distribution) of the weld joints.

Chapter 5 deals with the comparative study of the thermal history between FSW with PAFSW of dissimilar steels, such as DH36 steel and AISI 1008 steel. The 3D transient thermal moving heat source models for FSW are PAFSW are successfully established. For a reliable comparative study, the consequence of FSW and preheating parameters on the thermal history is investigated.

Chapter 6 explores the experimental investigation to find the feasible tool positioning for the successful joining of DH36 steel with 6061-T6 aluminum alloy. The tool pin is shifted towards AA6061 at various distances with constant tool rotational speed and traverse speed. The tool offset conditions are analyzed based on the macro/microstructure, mechanical properties, and IMCs formation in various regions of the weld joints.

Chapter 7 discusses the VOF-based multiphase CFD simulation by incorporating a modified analytical model for dissimilar FSW of DH36 shipbuilding steel and 6061-T6 aluminum alloy. The impact of different rotational speeds on the temperature distribution and plasticized material flow properties associated with the tool–material interaction is investigated.

Chapter 8 presents the experimentation to find the optimum tool traverse speed for successfully joining the 304 stainless steel with 6061-T6 aluminum alloy. For this purpose, five different traverse speeds are considered. The composition/phase analysis of IMCs, quantification of steel fragments & IMCs is performed, and their subsequent influence on the mechanical performance of the weld joints is investigated.

Chapter 9 explores the material flow behaviour during the dissimilar FSW of 304 stainless steel and 6061-T6 aluminum alloy. A novel steady-state multi-species transport model (STM) coupled with a mixture model is established for the first time, where the CFD solver transported species mass fractions of materials in the FSW process.

Chapter 10 represents the main finding & conclusions from the present work, and future scopes in the field of experimental/numerical analysis of dissimilar FSW process. The outcomes of the current work in the form of journal papers, book chapters, and conferences are reported at the end of this chapter.

Finally, the thesis is ended with a list of corresponding references and appendices.

CHAPTER 3

RESEARCH METHODOLOGY

The previous chapter discussed the objectives, followed by thesis outlines based on the research gap. To accomplish the objectives, this chapter provides a concise overview of the methodologies employed for both experimental investigation and numerical simulation. Firstly, the experimental setup for the dissimilar FSW process is highlighted. Then, the experimental strategy for temperature measurement, welding forces measurement, mechanical tests, and metallographic analysis is described. After that, the numerical procedure, solution strategy, and mathematical formulation employed for the thermal modelling and multiphase CFD modelling is presented. In the numerical simulation, thermal modelling is performed to conduct a comparative study of the thermal history between the FSW and PAFSW for dissimilar steels. At the same time, the multiphase CFD modelling is employed to determine the thermal history and material flow behavior during the dissimilar FSW of steel and AA6061.

3.1 EXPERIMENTAL PROCEDURE

In this study, the experiments were conducted on a semiautomatic position-controlled FSW machine with 25 kW spindle drive motor power. A hydraulic power pack system is connected to the machine, which can provide a maximum axial force of 55–58 kN in working conditions. The machine frame is robust, so it does not reflect during the experiments. The available rotational and traverse speeds are in the range of 20 mm/min–300 mm/min, and 300 rpm–1200 rpm, respectively. The adjustable fixture was designed, which can restrict the lateral and transverse movement of the workpiece. In this study, both FSW and hybrid FSW, i.e., PAFSW were performed. The following subsections include the experimental procedure for both techniques.

3.1.1 FSW Setup

The schematic illustration and experimental setup for the joining of the dissimilar materials are shown in Figs. 3.1(a) and 3.1(b). A tungsten carbide (WC-10wt.%Co) tool with a cylindrical shoulder and cylindrical tapered pin was used, and its dimensions are shown in Fig. 3.1(c).

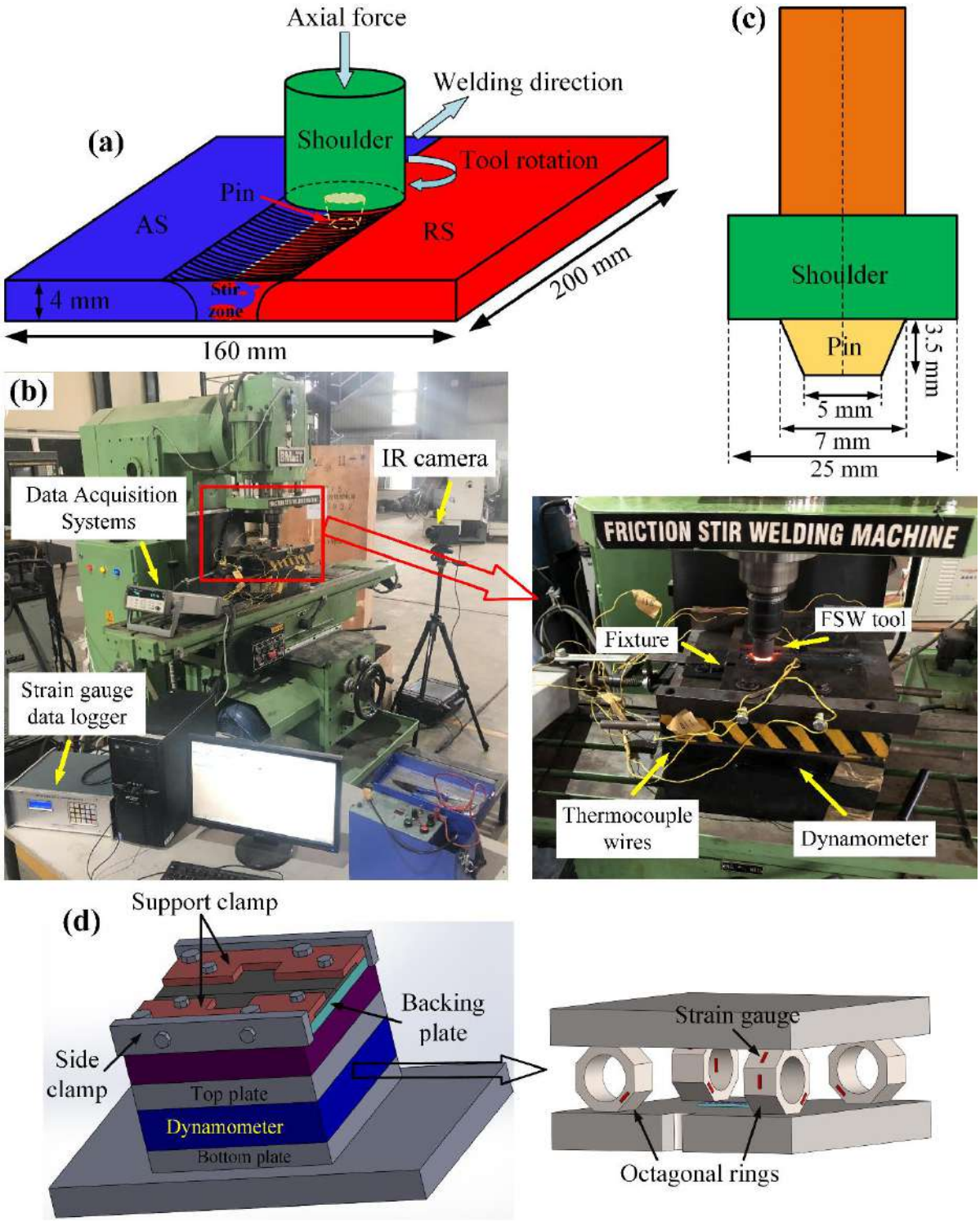

Fig. 3.1 *(a) Schematic illustration of the dissimilar FSW process; (b) experimental setup; (c) tool geometry with dimensions; and (d) schematic diagram of the dynamometer with fixture*

The temperature measurements were performed at both top and the bottom surfaces of the workpiece. In this study, a non-contact infrared (IR) thermal imaging camera (Testo 868 thermal imager) with a measurement range from -30°C to 650°C was used to obtain the isotherm, overall peak welding temperature, and the top surface temperature. Before measuring

the temperature, the IR camera was calibrated by heating the worksheets to specific temperature limits and adjusting the emissivity setting until the measured temperature of the camera matched the reference temperature. The calibration range of the thermographic system was set as 300 K–900 K since the maximum welding temperature remains below the melting point of AA6061, which is about 855 K [160]. The IR camera has a ±2% measurement error. After the temperature measurements, Testo IRSoft software was used to conveniently process and analyze the captured images on a computer. To measure the temperature at the bottom surface, the K-type thermocouples were inserted at the bottom of the workpiece through the drilled hole (2 mm diameter). The multi-channel data acquisition system was used to record the readings from the thermocouples.

Nowadays, a challenging issue during the FSW of the high strength material like steel is the development of the force & torque measuring dynamometer, which is capable of supporting the higher loads as well as the higher temperatures generated during the welding process. In the present work, a strain gauge-based dynamometer was designed, developed, and calibrated to monitor the vertical force, traverse force, and torque during the FSW of steel. A 3D finite element (FE) analysis was performed to detect the suitable positions for mounting the strain gauges on the octagonal ring members for different real time loading conditions (i.e., axial force, traverse force, and torque). Analytical methods were used to estimate the mechanical responses, i.e., stress, strain, and vibration frequency of the octagonal ring members. When the load was acting on the octagonal members during the welding process, the data acquisition system recorded the induced strain in the octagonal members. The data acquisition system was connected to the developed dynamometer with the essential software and hardware to record the strain data automatically on a computer during welding. After completing the construction, the dynamometer was tested by performing the FSW on DH36 steel and AISI 1008 steel plates in similar and dissimilar combinations. The results showed that the developed dynamometer could be suitable for measuring the real time vertical force, traverse force, and torque during the FSW of low carbon steels. Fig. 3.1(d) shows the assembled view of a strain gauge-based developed dynamometer with a mechanical fixture. The detailed procedure of design, development, and calibration of the dynamometer is described in our published article [161].

3.1.2 PAFSW Setup

In the PAFSW, the additional heating source, i.e., plasma torch was employed in front of the tool with an angle of 60° normal to the workpiece surface. Figs. 3.2(a) and 3.2(b) show the

schematic illustration of the PAFSW for dissimilar steels. The experiment setup of PAFSW is shown in Fig. 3.2(c). The plasma offset of 8 mm away from the tool shoulder surface was applied. The plasma torch was fitted in the DH36 steel side by 5 mm in the transverse direction, and the radius of the plasma arc was 4 mm. The argon was used as a shielding gas to prevent the surface oxidation during preheating.

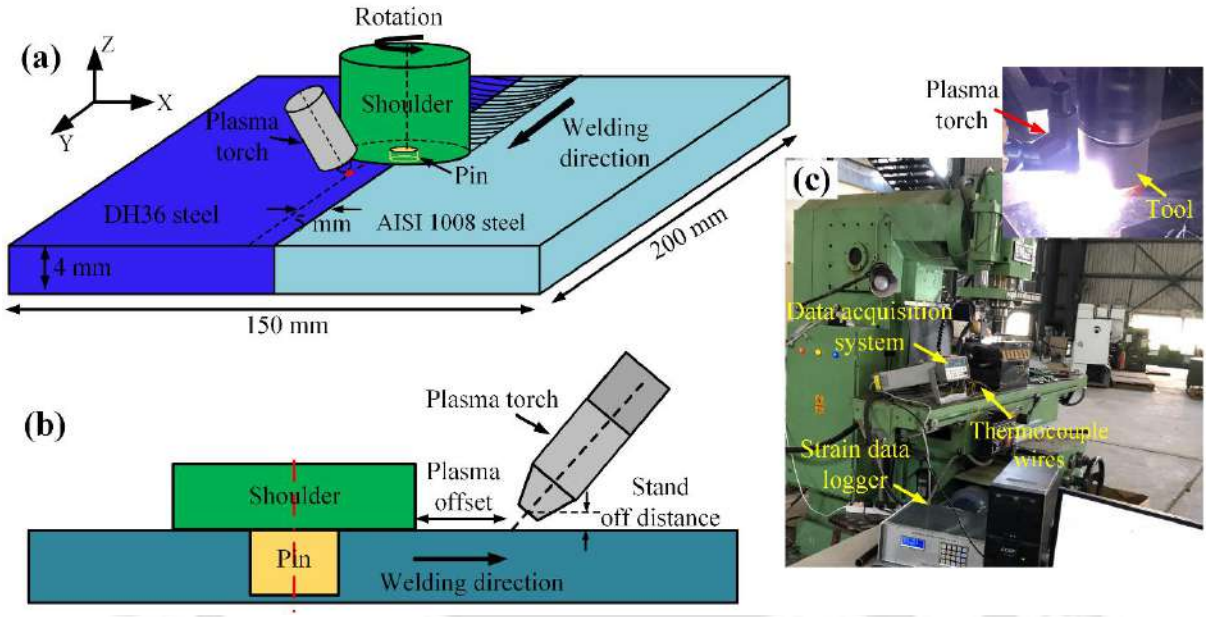

Fig. 3.2 *(a) Schematic illustration of the PAFSW; (b) cross-sectional view of the PAFSW in welding direction; and (c) experimental setup of PAFSW*

3.1.3 Materials and Processing

In the experimental study, DH36 steel, AISI 1008 steel, 304 stainless steel (304 SS), and 6061-T6 Al alloy (AA6061) were used as base materials. The 6061-T6 Al alloy is a solution heat-treated, artificially aged, and precipitation hardened with magnesium and silicon as major alloying elements. The T6 temper condition is generally obtained through solution heat treatment at around 530 °C–550 °C followed by the artificial ageing at a temperature of approximately 170 °C–200 ºC [162]. The five measurements for chemical composition and mechanical properties of base materials were taken using the EDX system and universal tensile testing machine at room temperature. Table 3.1 shows the nominal chemical composition and average values of mechanical properties of base materials. FSW technique was applied to produce the DH36 steel & AISI 1008 steel, DH36 steel & AA6061 sheets, and 304 SS & AA6061 joints.

Table 3. 1 *Chemical composition and mechanical properties of the base materials*

Materials	Chemical composition (wt.%)							
AA6061	Si	Mg	Mn	Cu	Fe	Zn	Ti	Cr
	0.64	0.95	0.08	0.28	0.49	0.15	0.1	0.21
DH36 steel	C	Cu	S	Mn	Ti	V	Si	Nb
	0.17	0.53	0.027	1.68	0.52	0.14	0.44	0.04
304 SS	C	Cr	Ni	Mn	P	S	Si	Cu
	0.064	18.52	8.42	1.05	0.03	0.01	0.34	0.12

	Mechanical properties			
	UTS (MPa)	Yield Strength (MPa)	% Elongation	Hardness (HV)
AA6061	272.56	232.34	12	64.2
DH36 steel	514.62	384.83	16	140.3
304 SS	561.9	264.2	56.3	168.5

As discussed in the literature survey, material positioning is the critical issue during the dissimilar FSW. Accordingly, preliminary experiments were conducted to find the effect of material positioning in the joining of DH36 steel and AA6061. The comprehensive outcomes of this work are described in our published article [163]. A typical weld surface appearance is shown in Fig. 3.3. The dissimilar materials are adequately mixed and joined without any surface defects when DH36 steel is positioned at the AS, as shown in Fig. 3.3(a).

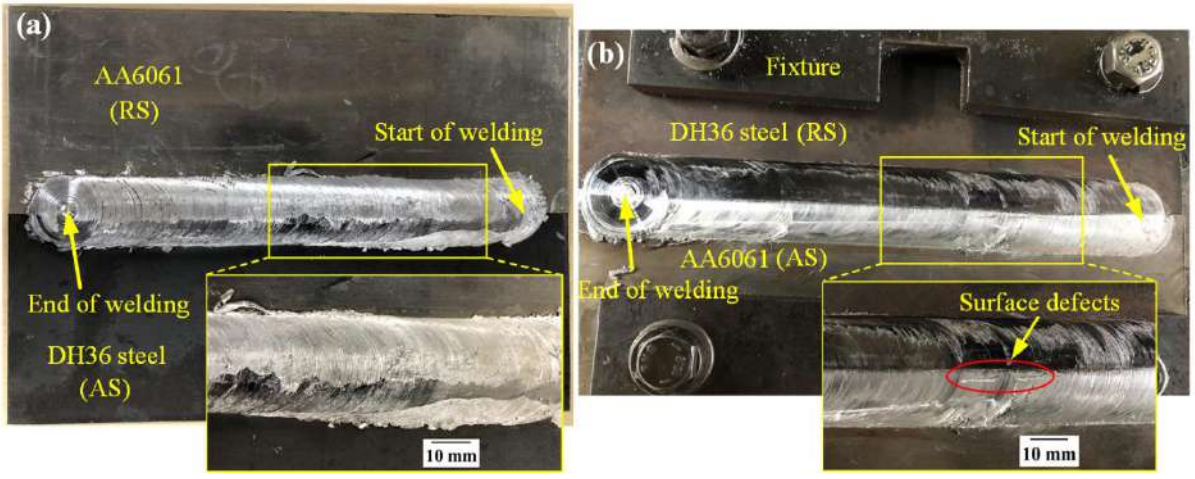

Fig. 3.3 *Top weld surface appearance when (a) DH36 steel at AS; and (b) AA6061 at AS*

On the other hand, when AA6061 is positioned at the AS, the lack of mixing generated the surface defects, such as cracks on the weld surface, as shown in Fig. 3.3(b). It is also observed that the joint efficiency improved by placing the AA6061 at the RS and DH36 steel

at the AS. However, reverse positioning led to the scattering of steel particles inside the AA6061 matrix, which deteriorated the joint efficiency due to the formation of cracks and voids. This is attributed to the tangential velocity of the rotating tool surface at the AS, which is parallel to the tool traverse direction causing more frictional heat in the AS. Therefore, the harder material can move easily from AS to RS due to high heat generation, which can lead to uniform material flow and proper mixing of dissimilar materials. Accordingly, the harder material, i.e., DH36 steel was clamped at the AS in DH36 steel & AISI 1008 steel and DH36 & AA6061 combinations, and 304 SS in 304 SS & AA6061 combination.

3.1.4 Measurements

The accuracy of the welding process was verified by performing two experiments for each tool offset condition. Once the experiments were completed, three tensile samples, two impact test samples, two samples for metallurgical analysis, and two samples for hardness measurement were extracted from each weld joint, as shown in Fig. 3.4. Electro-discharge machining was used to extract the transverse tensile samples from the different locations by keeping the weld region in the middle of the samples. All the tensile tests were performed as per the ASTM E8 standard at a 0.5 mm/min crosshead speed under room temperature conditions. The impact test was carried out at room temperature on the Charpy Impact test machine (IT-30 Make: FIE) as per the ASTM E-23 terms by keeping the V notch at the centre of the weld. Vickers microhardness measurements were conducted across the weld cross-section at an interval of 0.25 mm by applying a load of 500 g for 15 s dwell time. The hardness test was repeated three times to obtain the average values for each specimen.

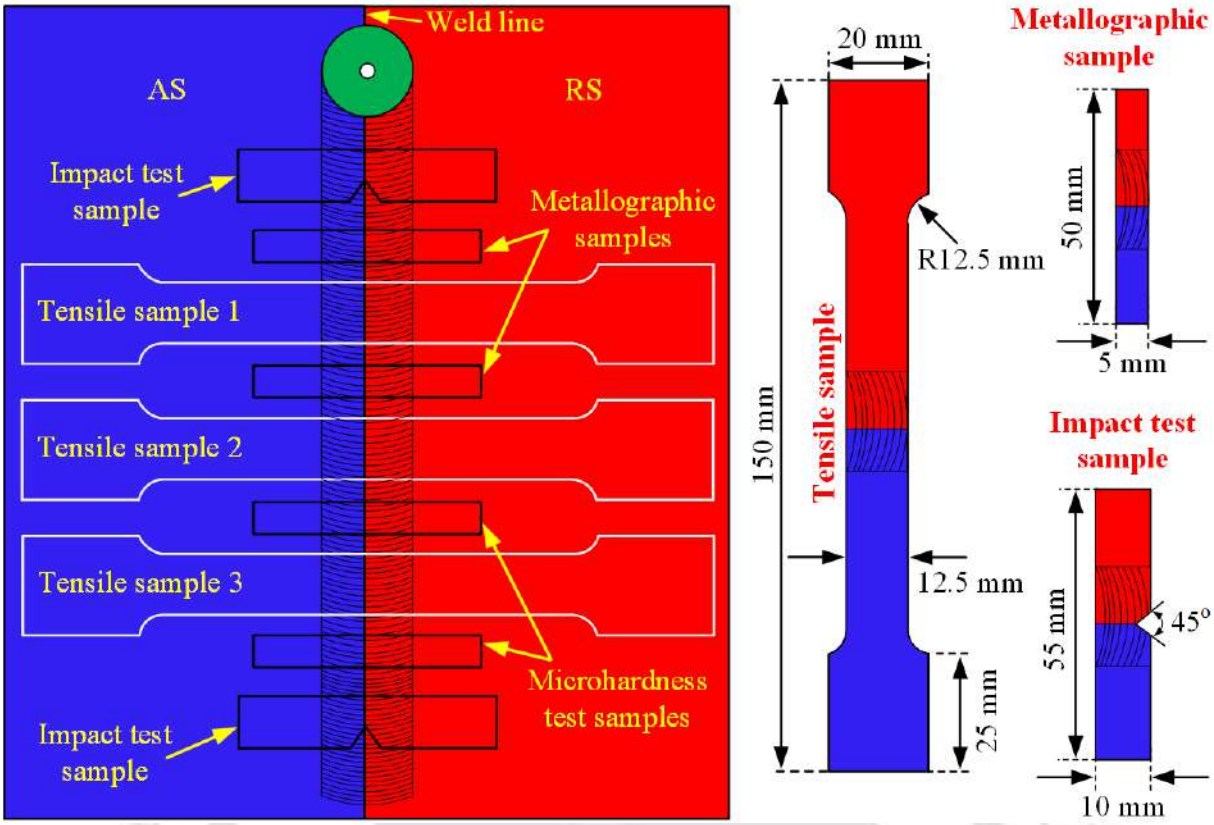

Fig. 3.4 *Extraction of the test samples from the weldment*

3.1.4 Metallographic Analysis

The metallographic analysis was conducted using an optical microscope, X-ray diffraction (XRD), field emission scanning electron microscope (FESEM), and transmission electron microscope (TEM) equipped with an energy dispersive spectroscopy (EDS) system. For the comprehensive metallographic analysis, samples were taken from the weld cross-sections transverse to the welding direction as shown in Fig. 3.4; then, these samples were mirror-polished using 1 µm diamond suspension followed by the polishing on 200, 400, 800, 1000, 1200, 1500, 2000 and 2500 emery papers. Finally, the metallographic samples were etched using Keller's reagent (1 ml HCl, 1.5 ml HNO_3, 2.5 ml HF and 95 ml H_2O), 2% nital solution, and Glyceregia (5 ml HNO_3, 10 ml HCl and 15 ml glycerol) for revealing the microstructure of AA6061, DH36 steel, and 304 SS, respectively. The flow behaviour, grain size, and grain distribution under different magnifications were detected using an optical microscope. The grain size in different zones of the weld cross-section was measured using the line intercept and area counting technique. The XRD and EDS analysis were performed to investigate the composition of the SZ, IMC layer, and mixed regions. Based on microstructural observation using SEM, the IMC layer thickness was averaged over 40 points with an interval of 2 µm at the Al/steel interface. TEM samples were cut into thin slices (200–250 µm) using

the diamond wafering blade. Then, they were mechanically lapped/polished to less than 100 µm. The thin slices were punched to a diameter of 3 mm for the TEM specimen holder, and the final thinning was done with a twin-jet electro-polishing machine.

Image analysis was performed to quantify the IMCs and steel fragments inside the SZ. The cross-sectional area of the tool pin was taken into account for the total area of the SZ. Based on the total numbers and mean area of the particles, the entire area covered by the IMCs and steel fragments inside the SZ is investigated. The minimum particle size for steel fragments and IMCs was kept as 0.001 mm^2 and 0.001 μm^2 for thresholding, respectively.

For the in-depth metallographic study, atomic force microscopy (AFM) analysis was performed at dry ambient conditions. It was conducted in non-contact mode to examine the surface topography of the SZ, including the steel fragments and IMCs. The cross-sectional samples with the dimension of 50 µm × 50 µm were extracted from the interface region and SZ because the AFM method is not ideally suited to a scale larger than 30 µm. Then, the samples were mechanically wet polished using the velvet cloth and 0.05 µm alumina slurry, washed with ethanol, followed by ultrasonic cleaning to avoid contamination. The ultrasonic cleaning of the samples was done again and finally dried with hot air blow just before the analysis. The dual-scan mode with a scan frequency rate of 2.5 Hz was performed to acquire the surface mapping during analysis. Gwyddion 2.45 software was used to visualize the captured mapping data and perform a three-dimensional surface topography assessment.

3.2 NUMERICAL MODELLING

In the numerical simulation, the three-dimensional CFD modelling was performed to determine the thermal history and material flow behavior during the dissimilar FSW of steel and AA6061. At the same time, heat transfer modelling was performed to conduct a comparative study of the thermal history between the FSW and PAFSW for dissimilar steels. The computer configuration used to perform the numerical analysis is the processor: Intel(R) Core (TM) i7-9750H CPU @ 2.60GHz @ 2.59 GHz, RAM: 16 GB. The time step of 0.1 s was used for the heat transfer modelling. On the other hand, the double precision solver was used to solve the governing equations in the CFD modelling. Accordingly, the computing time for the heat transfer modelling was about 5 hours, and 9 hours for the CFD modelling. The following subsections include the detailed numerical procedure for both modelling techniques

3.2.1 CFD Modelling

In multiphase CFD-based modelling, the materials were assumed as an incompressible and non-Newtonian viscoplastic fluid. The fluid flow was considered to behave as a laminar flow, and the coherence variance was evaluated as a temperature and strain rate function. For the simplification of the model, the following assumptions were made.

i. The angle of tool tilt was considered to be zero.
ii. The volumetric heat generation due to plastic deformation in the shear layer was neglected.
iii. The coefficient of friction and reference temperature were considered as constant values.
iv. The quasi-static steady-state welding stage was assumed in the Eulerian formulation.

The interior computation domain was allowed to move by providing the two different material inlets at their respective sides, i.e., AA6061 inlet and steel inlet, as shown in Fig. 3.5. However, the opposite sides of the plates were assigned as pressure outlet walls with zero constant pressure to avoid the reverse flow of fluids. The reference temperature (T_{ref}) of 300 K was considered. The welding speed (v_{weld}) was equivalent to a material flow velocity, but the material movement direction was opposite to the welding direction. FSW tool was inserted as a tool wall inside the workpiece at 100 mm from the inlet and outlet walls. It was shifted from the weld line at 1.5 mm towards the AA6061 side. The origin was fixed in the middle of the weld line at bottom of the workpiece. The full dimensions of the plates in the simulations were the same as those in the actual experiments, i.e., 200 mm × 160 mm × 4 mm. The solution of fluent simulations was converged as the continuity, velocity, and energy residual fell below the values of 0.001, 0.001, and 10^{-6}, respectively. The pressure-velocity coupling algorithm was applied to efficiently solve the energy and the flow equations (i.e., continuity and momentum equations were solved in a coupled manner) in the non-linear physical model. The mass fraction was calculated using the third-order QUICK methodology, whereas the momentum and energy equations were solved using the second-order upwind method. Numerical calculations were executed using the popular CFD package Fluent 19.2.

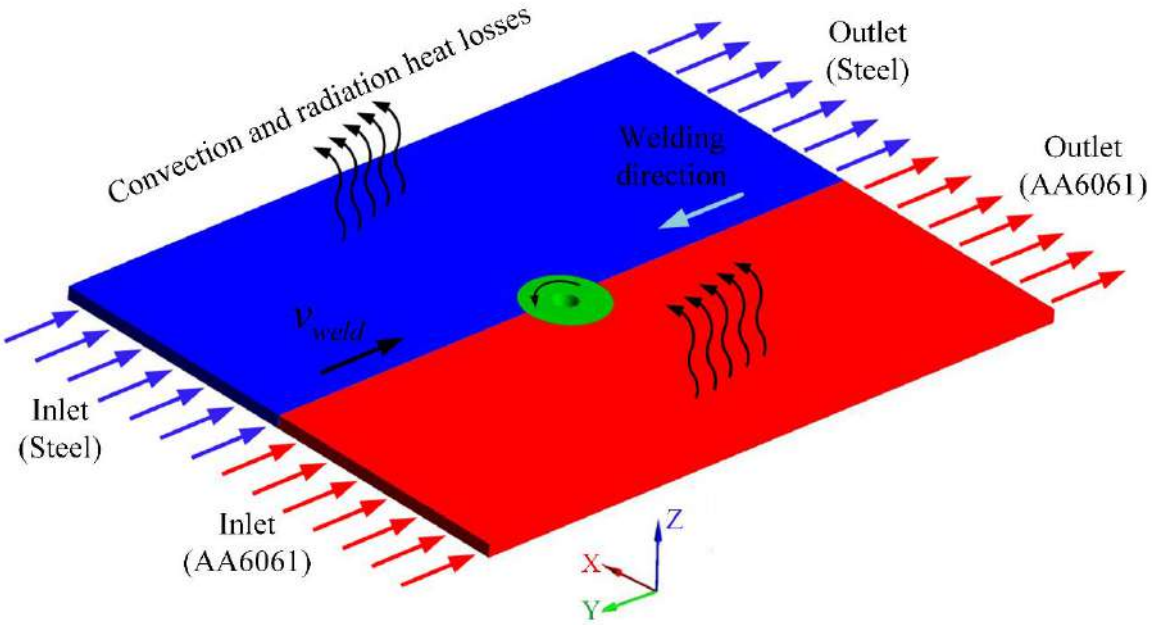

Fig. 3.5 *CFD model for the dissimilar FSW*

Fig. 3.6(a) shows the tool geometry considered in the numerical model, which contained dimensions similar to the tool used in the experiments. The developed CFD models were meshed using 3D tetrahedral elements. Apart from the element type, the element size plays an important role in determining the accuracy and suitable computational time. Finer mesh leads to higher computation time, whereas coarse meshing produces inaccurate results. Therefore, mesh optimization is essential for maintaining the accuracy of results with less computation time. Accordingly, mesh sensitivity analysis was performed by varying the mesh size to maintain a balance between accuracy and computation time. The non-dimensional parameter ($T_{peak}/T_{reference}$) based on the computed temperature is compared with four different mesh sizes, as shown in Table 3.2. It is observed that no significant variation occurred in the peak temperature by increasing the number of elements from 1100000 to 1200000 for DH36 steel & AA6061, and 600000 to 700000 for 304 SS & AA6061 combination. Based on the mesh sensitivity analysis, the total number of the elements on worksheets was selected as 1124614 for DH36 steel & AA6061, and 657977 for 304 SS & AA6061 combination. The fine meshing was applied at the tool wall to achieve a more accurate thermal history and material flow behavior. Whereas coarse meshing was applied away from the tool wall, as shown in Fig. 3.6(b).

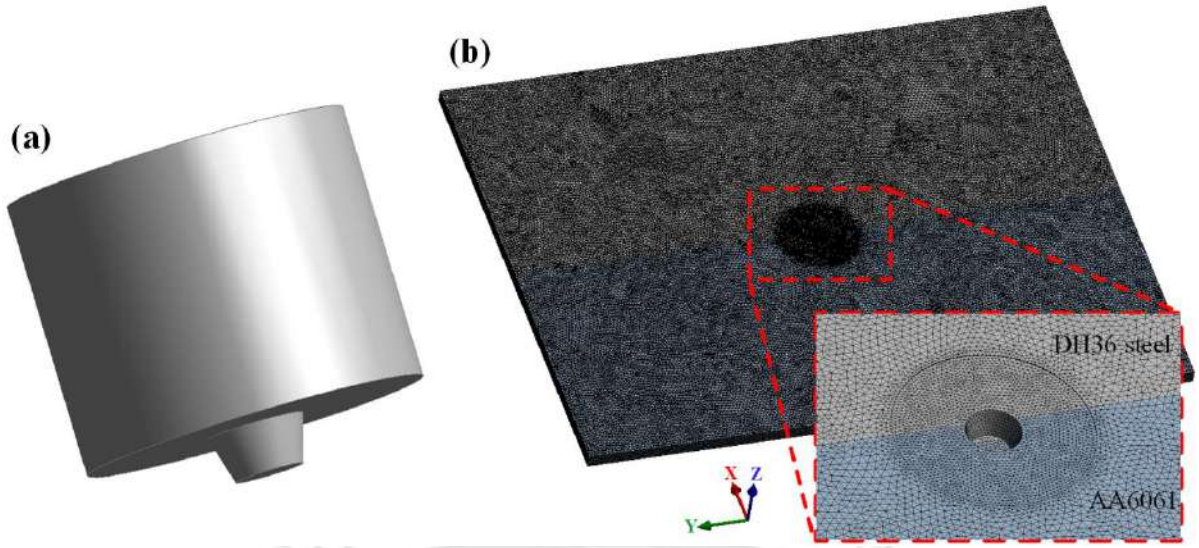

Fig. 3.6 *(a) FSW tool; and (b) meshing of the workpiece*

Table 3.2 *Non-dimensional temperature factor (T_{peak}/T_{ref}) with four different mesh sizes for CFD modelling*

DH36 steel & AA6061		304 SS & AA6061	
No. of elements	T_{peak}/T_{ref}	No. of elements	T_{peak}/T_{ref}
867000	2.021	347000	2.010
1020000	2.130	530000	2.091
1104000	2.244	617000	2.155
1194000	2.250	698000	2.158

3.2.1.1 Material Properties

The temperature-dependent material properties (i.e., thermal conductivity and specific heat) were taken from the published literature for DH36 steel [119], 304 SS [164], and AA6061 [109]. The constant density of the materials was considered in CFD simulation, i.e., 7850 kg/m^3 for DH36 steel [165], 7406 kg/m^3 for 304 SS [166], and 2700 kg/m^3 for AA6061 [109]. The FSW tool was assumed as a solid rigid body, and the properties of the WC-Co were taken from the published work [167]. The important aspect, i.e., dynamic viscosity needs to be quantified correctly in the CFD modelling for the FSW process since the material experiences a severe strain rate and plastic deformation. Therefore, this model considered the temperature & strain rate-dependent viscosity of the non-Newton fluid. The following relationship represents the material viscosity (μ) as a function of flow stress (σ_{fs}) and strain rate ($\dot{\varepsilon}$).

$$\mu = \frac{\sigma_{fs}}{3\dot{\varepsilon}} \qquad \therefore \sigma_{fs} = \frac{1}{\dot{\alpha}} \arcsin h\left(\frac{Z}{A}\right)^{\frac{1}{n}} \tag{3.1}$$

where A, $\dot{\alpha}$, and n indicate the material-related constants. The temperature & strain rate dependent Zener–Hollomon parameter (Z) is represented as:

$$Z = \dot{\varepsilon} \exp\left(\frac{\dot{Q}_a}{\dot{R}T}\right) \tag{3.2}$$

where $\dot{Q}_a$, and $\dot{R}$ indicate the activation energy, and gas constant, respectively. The following equation represents the effective strain rate.

$$\dot{\varepsilon} = \sqrt{\frac{2}{3}\varepsilon_{ij}\varepsilon_{ij}} \qquad \therefore \varepsilon_{ij}(\text{strain tensor}) = \frac{1}{2}\left(\frac{\partial v_j}{\partial x_i} + \frac{\partial v_i}{\partial x_j}\right) \tag{3.3}$$

The material-related constants for AA6061 and 304 SS are shown in Table 3.2.

Table 3.3 *Material-related parameters*

Material	Parameters			
	A	$\dot{\alpha}$	n	$\dot{Q}_a$
AA6061 [109]	1.63×10^{13} s^{-1}	0.0165 MPa^{-1}	5.33	191 kJ mol^{-1}
304 SS [168]	2.14×10^{17} s^{-1}	0.008 MPa^{-1}	6.1	446 kJ mol^{-1}

The material-related constant A as a function of carbon percentage ($\%C$) for DH36 steel is represented as [165]:

$$A = 1.8\times10^{6} + 1.74\times10^{8}(\%C) - 6.5\times10^{8}(\%C)^{2} \tag{3.4}$$

$\dot{Q}_a$ = 371 kJ/mol was considered for DH36 steel [169]. $\dot{\alpha}$, and n as a function of temperature is represented as:

$$\dot{\alpha} = 1.07 + 1.7\times10^{-4}T - 2.81\times10^{-7}T^{2} \tag{3.5}$$

$$n = 0.2 + 3.966\times10^{-4}T \tag{3.6}$$

The above equations were applied in the ANSYS Fluent 14.5 software using a user-defined function (UDF). The formation and the effect of IMCs were ignored in the fluent model to minimize the computational time/complexity and improve the convergence.

3.2.1.2 Volume of Fluid

In the dissimilar FSW process, the volume of fluid (VOF) is considered as the most convenient method to solve the complex multiple-phase flow modelling through volume fraction (V_{frac}) equations at the interface of parent materials. In the present study, the VOF method was employed to simulate the dissimilar FSW of AA6061 and DH36 steel. In this multiphase interaction model, V_{frac} of phase b is introduced by the variable α_b to describe the

phase distribution. The different phases are shared by the temperature (T), velocity (v), and pressure (P) fields. The averaged values based on the α_h in each unit cell are considered to evaluate the material properties. Consequently, the mass, momentum, and energy equations are calculated in the following form [170]:

$$\text{Mass: } \nabla\cdot\left(\alpha_b\rho_b v\right)=\sum_{g=1}^{2}\left(\dot{m}_{gb}-\dot{m}_{bg}\right) \tag{3.7}$$

$$\text{Momentum: } \bar{\rho}\left(v\cdot\nabla\right)v=-\nabla P+\nabla\cdot\Phi \tag{3.8}$$

$$\text{Energy: } \nabla\cdot\left[\left(\sum\alpha_b\rho_b c_b\right)T\underset{\sim}{v}\right]=-\nabla\cdot\underset{\sim}{\bar{q}}+\nabla\cdot\left[\left(\Phi-PI\right)\cdot v\right] \tag{3.9}$$

where ∇ denotes the spatial vector differential operator, and ρ_b indicates the density of phase b. The mass conservation equation is used to calculate the V_{frac} of different phases in each domain element. The mass transfer rate from phase g to b is described by $\dot{m}_{gb}$, whereas the switched condition corresponds to $\dot{m}_{bg}$. This modelling involved only two phases hence the V_{frac} of either steel or Al needs to be calculated. In the momentum equation, the averaged material density ($\bar{\rho}$) based on the volume fraction and shear stress tensor (Φ) is represented as:

$$\bar{\rho}=\sum_{b=1}^{2}\alpha_b\rho_b \tag{3.10}$$

$$\Phi=\bar{\mu}\left(\nabla\otimes v+\nabla\otimes v^{\mathrm{T}}\right),\qquad \text{where } \bar{\mu}=\sum_{b=1}^{2}\alpha_b\mu_b \tag{3.11}$$

where μ_b indicates the viscosity of each phase, and the symbol $\otimes$ denotes the tensor product operation.

The specific heat capacity in the energy equation is specified as c_b for phase b. Heat flux ($\underset{\sim}{\bar{q}}$) as a function of average thermal conductivity and temperature gradient is represented as:

$$\underset{\sim}{\bar{q}}=-\bar{k}\nabla T;\qquad \text{where } \bar{k}=\sum_{b=1}^{2}\alpha_b k_b \tag{3.12}$$

where k_h indicates the thermal conductivity of phase b.

3.2.1.3 Species Transport Model

The dissimilar FSW process involves very complexity of the multi-physical phenomena. Accordingly, a relatively primitive multi-species transport model was also developed for the first time to simulate heat and mass transfer during the welding process. The STM solves an

additional scalar transport equation with continuity and momentum equations to obtain the mass fraction of distinct species. The interaction between the two phases was calculated using source terms of mass, energy, momentum, and species concentrations. In this study, AA6061 and 304 SS were assigned as primary phase (*p*) and secondary phase (*s*) for the STM, respectively. During the simulation of species transport in multiphase flow, the Ansys Fluent FE software package calculates the following conservation equations for the local mass fraction of each i^{th} phase [154,155]. To calculate the mass fraction of the species, the convection-diffusion equation is represented as:

$$\nabla \cdot \left(\rho_m M_i \vec{v}_m \right) = -\nabla \vec{J}_i + S_i \tag{3.13}$$

where ρ_m is the density of the mixture (*m*), $\vec{v}_m$ is the velocity of the mixture, M_i is the local mass fraction of i^{th} phase, J_i is the diffusive flux of i^{th} phase, and S_i is the reaction source of i^{th} phase. The governing conservation equation of energy is calculated as:

$$\nabla \cdot \left(\vec{v}_m \left(\rho_m E + P \right) \right) = \nabla \cdot \left(k_{eff} \nabla T - \sum_i e_{h,i} \vec{J}_i + \left(\tau_{eff} \cdot \vec{v}_m \right) \right) + V_h \tag{3.14}$$

where k_{eff} indicates the effective thermal conductivity, τ_{eff} is the effective stress tensor, *P* is the pressure, *T* is the temperature, $e_{h,i}$ is the enthalpy of i^{th} phase, and V_h includes the heat by mixing reaction and additional volumetric heat source terms. The transmission of enthalpy related to species diffusion in multiphase mixing flow is denoted as $\nabla \cdot \left[\sum_{i=1}^{q} e_{h,i} J_i \right]$. The total mechanical energy (*E*) is represented as:

$$E = e_h - \frac{P}{\rho_m} + \frac{v_m^{\,2}}{2} \tag{3.15}$$

The enthalpy (e_h) for incompressible fluid flow is represented as:

$$e_h = \sum_i M_i e_{h,i} + \frac{P}{\rho_m}; \qquad \text{where } e_{h,i} = \int_{T_{ref}}^{T} c_{p,i} dT \tag{3.16}$$

where $c_{p,I}$ indicates the specific heat of i^{th} phase, and T_{ref} indicates the reference temperature. The diffusive flux $\vec{J}_i$ of different species in a laminar flow using mass diffusion coefficients is calculated as:

$$\vec{J}_i = -\rho D_{i,m} \nabla M_i - D_{T,i} \frac{\nabla T}{T} \tag{3.17}$$

where $D_{i,m}$ is the diffusion coefficient of i^{th} phase in the mixture, and $D_{T,i}$ is the thermal diffusion coefficient. The transmission of enthalpy related to species diffusion in multiphase mixing flow is represented as $\nabla \cdot \left[\sum_{i=1}^{q} e_{h,i} J_i \right]$. The governing conservation equation of continuity is calculated as:

$$\nabla \cdot \left(\rho_m \vec{v}_m \right) = 0 \tag{3.18}$$

The governing conservation equation of momentum is calculated as:

$$\rho_m \left(\vec{v}_m \cdot \nabla \right) \vec{v}_m = -\nabla P + \nabla \cdot \left[\mu_m \left(\nabla \vec{v}_m + \nabla \vec{v}_m^{\,T} \right) \right] \tag{3.19}$$

where $\vec{v}_m = \frac{\sum_{i=1}^{n} \alpha_i \rho_i \vec{v}_i}{\rho_m}$, $\rho_m = \sum_{i=1}^{n} \alpha_i \rho_i$, α_i is the volume fraction of i^{th} phase, and μ_m is the viscosity of the mixture written as $\sum_{i=1}^{n} \alpha_i u_i$. Likewise, the mass fraction for the secondary phase based on the continuity equation is represented as:

$$\nabla \cdot \left(\alpha_s \rho_s \vec{v}_m \right) = \nabla \cdot \left(\alpha_s \rho_s \vec{v}_{ds} \right) + \sum_{p=1}^{n} \left(m_{sp} - m_{ps} \right) \tag{3.20}$$

where the drift velocity of secondary phase (s) is represented as $\vec{v}_{ds} = \vec{v}_{sp} - \sum_{i=1}^{n} \left(\frac{\alpha_i \rho_i}{\rho_m} . \vec{v}_{pi} \right)$. The mass transfer rate from phase s to p corresponds to m_{sp}, whereas the switched condition is denoted by m_{ps}. The slip velocity ($\vec{v}_{sp}$) of a secondary phase relative to the primary phase is represented as $\vec{v}_{sp} = \vec{v}_p - \vec{v}_s$.

3.2.1.3 Heat Generation Model

In this study, the modified analytical expression of heat flux based on the heat generation at the rotating tool/stationary workpiece contact interface is established, which was applied to the tool wall in the CFD model. Consequently, the heat generation was estimated separately on the three main contact surfaces of the tool, i.e., shoulder surface, tool pin side surface, and tool

pin tip surface. Fig. 3.7(a) shows the schematic illustration of the FSW tool, where Q_{sh}, Q_{p1}, and Q_{p2} are the heat generation by the tool shoulder, tool pin side, and tool pin tip, respectively.

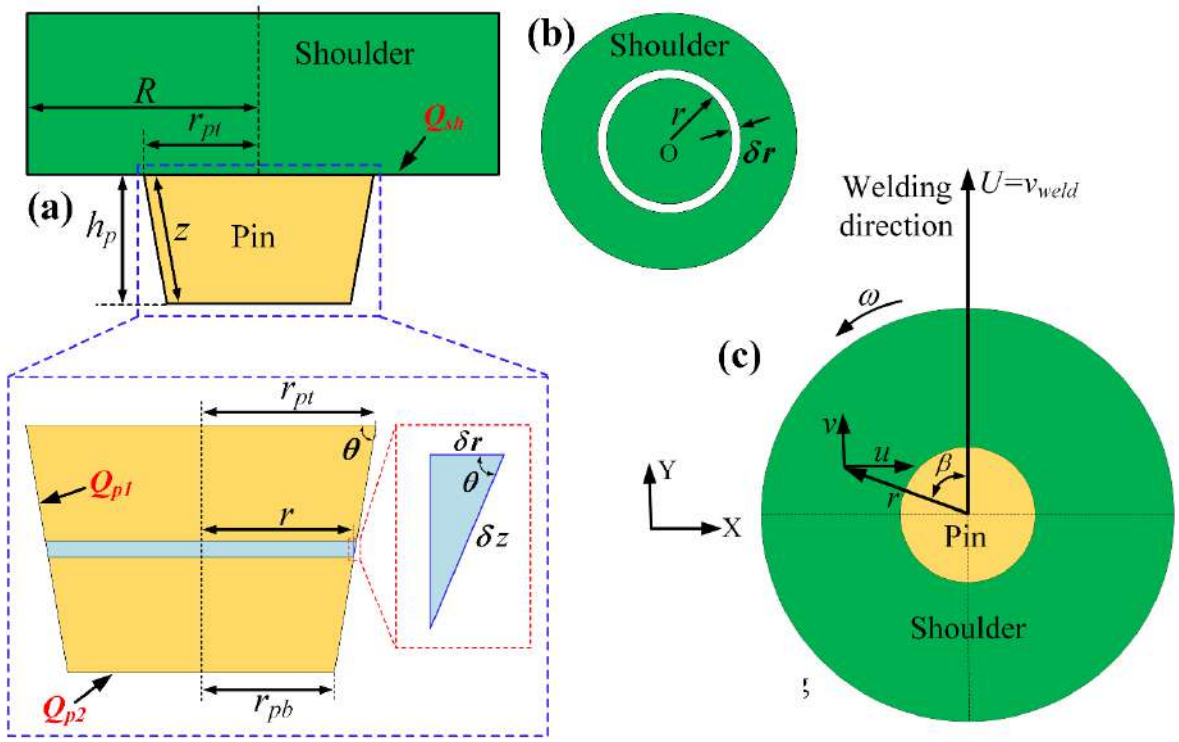

Fig. 3.7 *(a) FSW tool terminology and different heat generation regions; (b) shoulder surface; and (c) velocity boundary conditions at the tool surface*

Accordingly, the total heat generation by the FSW tool is expressed as $Q_{FSW} = Q_{sh} + Q_{p1} + Q_{p2}$. The general equation for heat generation at each contact surface is represented as:

$$\delta Q = \omega \delta M = \omega r \delta F = \omega r \tau_{contact} \delta A \tag{3.21}$$

where F indicates the force, M is the moment, A is the contact area, and ω is the angular rotation speed. The following expressions are analytical estimations of heat generation based on the tool/workpiece contact conditions.

(i) Heat generation from the shoulder (Q_{sh})

The surface area for the heat generation in the shoulder is shown in Fig. 3.7(b). Considering the small elemental ring with the thickness of δr at a distance of r from the centre, the area of this smaller elemental ring is indicated as $\delta A = 2\pi r \delta r$. Hence, the heat generation from the elemental ring is represented as:

$$\delta Q = 2\pi\omega r^2 \tau_{contact} \delta r \tag{3.22}$$

The total heat generation through the elemental ring is represented as:

$$Q_{sh} = 2\pi\omega\tau_{contact}\int_{r_{pt}}^{R} r^2 \delta r \tag{3.23}$$

Therefore, the following equation represents the total heat generation from the cylindrical shoulder.

$$Q_{sh} = \frac{2}{3}\pi\omega\tau_{contact}\left(\dot{R}_{sh}^{\ 3} - r_{pt}^{\ 3}\right) \tag{3.24}$$

(ii) Heat generation from the pin (Q_{pin})

The heat is generated from the pin at the two main regions, such as Q_{p1} from the side surface and Q_{p2} from the tip surface. The small elemental ring with thickness δr and slant thickness δz on the curved surface area of the pin at a distance of r from the centre is shown in Fig. 3.7(a).

$$\cos\theta = \frac{r_{pt} - r_{pb}}{z};\ z = \sqrt{\left(r_{pt} - r_{pb}\right)^2 + h_p^{\ 2}} \tag{3.25}$$

The elemental area for the heat generation is represented as:

$$\delta A = 2\pi r \delta z \tag{3.26}$$

The total heat generation through the elemental area is represented as:

$$\delta Q_{p1} = 2\pi\omega\tau_{contact} r^2 \delta z = \frac{2\pi\omega\tau_{contact} r^2}{\cos\theta}\delta r \tag{3.27}$$

Integrating both sides of Equation (3.27):

$$Q_{p1} = \frac{2\pi\omega\tau_{contact}}{\cos\theta}\int_{r_{pb}}^{r_{pt}} r^2 \delta r = \frac{2\pi\omega\tau_{contact}}{3\cos\theta}\left[r_{pt}^{\ 3} - r_{pb}^{\ 3}\right] \tag{3.28}$$

$$Q_{p1} = \frac{2}{3}\pi\omega\tau_{contact}\left(\sqrt{\left(r_{pt} - r_{pb}\right)^2 + h_p^{\ 2}}\right)\left(r_{pt}^{\ 2} + r_{pb}^{\ 2} + r_{pt} r_{pb}\right) \tag{3.29}$$

In the case of a flat pin tip, integration of Equation (3.22) across the surface of the pin tip provides the heat generation as:

$$Q_{p2} = 2\pi\omega\tau_{contact}\int_{0}^{r_{pb}} r^2 \delta r = \frac{2}{3}\pi\omega\tau_{contact} r_{pb}^{\ 3} \tag{3.30}$$

The following equation represents the total heat generation through the conical pin.

$$Q_{pin} = \frac{2}{3}\pi\omega\tau_{contact}\left(\sqrt{\left(r_{pt} - r_{pb}\right)^2 + h_p^{\ 2}}\right)\left(r_{pt}^{\ 2} + r_{pb}^{\ 2} + r_{pt} r_{pb}\right) + \frac{2}{3}\pi\omega\tau_{contact} r_{pb}^{\ 3} \tag{3.31}$$

Therefore, the total heat generation by the FSW tool (Q_{FSW}) with a cylindrical shoulder and a conical pin is represented as:

$$Q_{FSW} = Q_{sh} + Q_{pin} \tag{3.32}$$

$$Q_{FSW} = \frac{2}{3}\pi\omega\tau_{contact}\left[\left(\dot{R}_{sh}^{\ 3} - r_{pt}^{\ 3}\right) + \left(r_{pt}^{\ 2} + r_{pb}^{\ 2} + r_{pt}r_{pb}\right)\sqrt{\left(r_{pt} - r_{pb}\right)^2 + h_p^{\ 2}} + r_{pb}^{\ 3}\right] \tag{3.33}$$

In the case of the cylindrical shoulder with a cylindrical pin (i.e., $r_{pt} = r_{pb}$), the total heat generation equation is simplified as:

$$Q_{FSW} = \frac{2}{3}\pi\omega\tau_{contact}\left[\dot{R}_{sh}^{\ 3} + 3h_p r_{pt}^{\ 2}\right] \tag{3.34}$$

This expression is well correlated with the heat generation model developed by Schmidt et al. [108] and Essa et al. [171] for a tool with the cylindrical shoulder and cylindrical pin.

(iii) Contact Conditions

The contact condition is the most critical aspect in the numerical modelling of the FSW process. The heat generation in the FSW process is governed by the contact conditions, namely sliding and sticking at the tool/workpiece interface. The pure sliding condition causes the heat generation by friction only since it assumes the shear at the contact interface. The pure sticking assumes shearing in the workpiece material layer close to the contact surface, and the heat generation occurs by the plastic deformation. The above heat generation equations are generally based on the contact shear stress ($\tau_{contact}$) that varies according to the sliding or sticking condition. For a sliding condition, the contact shear stress is described by Coulomb's friction law as $\tau_{contact} = \dot{\mu}_f P_N$, whereas, for the sticking condition, it is described in terms of yield stress (σ_y) of the material as $\tau_{contact} = \frac{\sigma_y}{\sqrt{3}}$. By inserting the value of $\tau_{contact}$ in Equation (3.33), the total heat generation under pure sliding ($Q_{FSW,sliding}$) and sticking ($Q_{FSW,sticking}$) conditions is represented as:

$$Q_{FSW,sliding} = \frac{2}{3}\pi\omega\dot{\mu}_f P_N\left[\left(\dot{R}_{sh}^{\ 3} - r_{pt}^{\ 3}\right) + \left(r_{pt}^{\ 2} + r_{pb}^{\ 2} + r_{pt}r_{pb}\right)\sqrt{\left(r_{pt} - r_{pb}\right)^2 + h_p^{\ 2}} + r_{pb}^{\ 3}\right] \tag{3.35}$$

$$Q_{FSW,sticking} = \frac{2\sigma_y}{3\sqrt{3}}\pi\omega\left[\left(\dot{R}_{sh}^{\ 3} - r_{pt}^{\ 3}\right) + \left(r_{pt}^{\ 2} + r_{pb}^{\ 2} + r_{pt}r_{pb}\right)\sqrt{\left(r_{pt} - r_{pb}\right)^2 + h_p^{\ 2}} + r_{pb}^{\ 3}\right] \tag{3.36}$$

where $\dot{\mu}_f$ is the coefficient of friction, ω is the angular rotational speed, P_N is the normal pressure at the contact interface, r_{pt} is the top pin radius, r_{pb} is the bottom pin radius, $\dot{R}_{sh}$ is the shoulder radius, and h_p is the pin height.

FSW process in the actual condition exhibits the heat generation under the partial sliding/sticking condition at three contact surfaces (i.e., Q_{sh}, Q_{p1}, and Q_{p2}), which is simply a combination of pure sliding and sticking conditions. The workpiece material remains in a solid condition at the start of the FSW process. As a result, the tool slides over the workpiece material and induces a sliding condition at the tool-workpiece contact. As the welding progresses, the cohesive strength of the workpiece material reduces with an increase in temperature. The plastic deformation occurs since the portion of material sticks to the tool, which leads to a sticking condition at the tool-workpiece contact. The total heat generation under combined sliding and sticking ($Q_{FSW,sliding/sticking}$) is generally specified in terms of slip rate (δ^*), which expresses the consequence of slipping in the heat generation through the velocity difference between the FSW tool and material movement. The value of δ^* is generally set as 0 for pure sliding condition, 1 for pure sticking condition, and 0 to 1 for partial sliding/sticking condition [172]. In this study, it was taken as 0.58 [110,173]. The modified total heat generation based on the combined sticking and sliding condition is expressed as:

$$Q_{FSW,sliding/sticking} = \delta^* Q_{sticking(al/steel)} + \left(1-\delta^*\right) Q_{sliding(al/steel)} \qquad \therefore \delta^* = \frac{v_{matrix}}{v_{tool}} \tag{3.37}$$

$$Q_{sliding(al/steel)} = \frac{2}{3}\pi\omega P_N \left(\left(\dot{R}_{sh}{}^3 - r_{pt}{}^3\right) + \psi + r_{pb}{}^3\right)\left[\varphi \overset{A}{\dot{\mu}}_f + (1-\varphi)\overset{S}{\dot{\mu}}_f\right] \tag{3.38}$$

$$Q_{sticking(al/steel)} = \frac{2}{3\sqrt{3}}\pi\omega\left(\left(\dot{R}_{sh}{}^3 - r_{pt}{}^3\right) + \psi + r_{pb}{}^3\right)\left[\varphi \overset{A}{\sigma}_y + (1-\varphi)\overset{S}{\sigma}_y\right] \tag{3.39}$$

where $\psi = \left(r_{pt}{}^2 + r_{pb}{}^2 + r_{pt}r_{pb}\right)\sqrt{\left(r_{pt}-r_{pb}\right)^2 + h_p{}^2}$, v_{tool} is the position-dependent tool velocity of $\omega\dot{r}$ ($\dot{r}$ indicates the distance from the rotational axis to the calculated point, ω is the angular velocity), v_{matrix} is the velocity of contact points at the tool/matrix interface, φ is the ratio of tool wall area towards the AA6061 plate to the total area of the tool wall, $\overset{A}{\dot{\mu}}_f$ is the friction coefficient of Al, and $\overset{S}{\dot{\mu}}_f$ is the friction coefficient of steel. This study considered the constant coefficient of friction, i.e., 0.3 for DH36 steel [119], and 0.4 for AA6061 and 304 SS [131,174]. The normal pressure (P_N) was estimated based on the average axial force during the welding phase. $\overset{A}{\sigma}_y$ and $\overset{S}{\sigma}_y$ are the temperature-dependent yield strength of AA601 and steel, respectively. It was taken from the literature for AA6061 [118], DH36 steel [124], and 304 SS

[129]. The total heat generation equation was further divided by the total area of the tool wall to obtain the surface heat flux.

3.2.1.4 Boundary Conditions

The boundary conditions for the surface flow region are expressed as:

$$\dot{u} = 0; \quad \dot{v} = v_{weld}; \quad \dot{w} = 0 \tag{3.40}$$

where $\dot{u}$, $\dot{v}$, and $\dot{w}$ indicate the velocity magnitudes in the *x*, *y*, and *z* directions, respectively. From Fig. 3.7(c), the velocity at the tool periphery is represented as:

$$\dot{u}_i = \omega \dot{r} \cos\beta; \dot{v}_i = \omega \dot{r} \sin\beta + v_{weld}; \dot{w}_i = 0 \tag{3.41}$$

where $\dot{u}_i$, $\dot{v}_i$, and $\dot{w}_i$ indicate the velocity vectors in the *x*, *y*, and *z* directions, respectively. β indicates the angle between the horizontal direction vector from the tool axis to any point on the cylindrical surface.

The boundary conditions for heat exchange between the top and bottom surfaces of the plates include both convective and radiation heat transfer, which are represented as:

$$k \frac{\partial T}{\partial z}\Big|_{Top} = q_1 = \dot{h}_{ct}(T - T_{amb}) + \beta\varepsilon\left(T^4 - T_{amb}{}^4\right) \tag{3.42}$$

$$\dot{h}_{ct} = 0.0668T \quad \therefore T < 500^{\circ}\mathrm{C} \tag{3.43}$$

$$k \frac{\partial T}{\partial z}\Big|_{Bottom} = q_2 = \dot{h}_{cb}(T - T_{amb}) \tag{3.44}$$

where T is workpiece temperature, $\dot{h}_c$ is the convection coefficient, β is the Stefan–Boltzmann constant, and ε is the emissivity of the workpiece. The top and side surfaces were exposed to the ambient air; therefore, the convection coefficient ($\dot{h}_{ct}$) of 25 W/m^{2}K was applied for DH36 steel and AA6061. According to Sadeghian et al. [134], the convection coefficient for top and side surfaces ($\dot{h}_{ct}$) of 304 SS was applied by Equation (3.43). On the other hand, the influence of the backing plate was taken into account by using high convection coefficient at the lower surfaces. Tiwari et al. [169] reported the range of convection coefficient as 1000–2000 W/m^2 K for the FSW of steel. Chao et al. [121] considered the coefficient of 350 W/m^{2}K when the bottom surface of the Al plate was in contact with the steel backing plate. Accordingly, in this CFD modelling, the convection coefficient ($\dot{h}_{cb}$) of 1500 W/m^2 K and 350 W/m^2 K were considered at the bottom surfaces of DH36 steel and AA6061 to compute realistic

results, respectively. The convection coefficient ($\dot{h}_{cb}$) for 304 SS bottom surface was taken ten times larger than the upper surface.

3.2.2 Thermal Modelling

The heat transfer models for FSW & PAFSW were established using Abaqus/Explicit (Trademark and copyright with Dassault Systèmes, France) to measure the thermal history during the joining of dissimilar steels i.e., AISI 1008 steel and DH36 steel. The additional heat source, namely the plasma arc was modelled using the Gaussian distribution of heat flux. In this study, the following assumptions were made to develop and reduce the complexity of the 3D heat transfer models.

i. The linear relationship was considered between heat input and distance from the FSW tool centre.
ii. The only frictional heat generation (i.e., sliding condition) was considered at the interface of the tool and workpiece.
iii. The coefficient of friction and ambient temperature were considered as constant values.
iv. Heat loss during the plunging and retracting phase of the tool was not considered.

The entire FE analysis was carried out in two steps, i.e., the welding phase and the cooling phase. During the welding phase, the heat source traveled from one end to another along the weld centre line. The heat source was deactivated during the cooling period to cool the welded plates up to the ambient temperature. The DFLUX user subroutine was used in Abaqus to simulate a moving heat source at the top of the plates. The temperature-dependent thermal properties of DH36 steel and AISI 1008 steel, i.e., specific heat, thermal conductivity, and coefficient of thermal expansion were taken from the published literature [119,127]. A constant coefficient of friction, i.e., 0.3 for both steels was used [119,122]. The surrounding temperature, i.e., 30 °C was considered ambient temperature.

The developed FE model was meshed using 8-node linear heat transfer DC3D8 brick elements. The full dimensions of the worksheets in the models were the same as used in the experiments, i.e., 200 mm × 150 mm × 4 mm. A mesh sensitivity analysis was implemented to predict the optimum meshing parameters such as element size and the number of elements. The analysis was performed based on the peak temperature with different mesh sizes. As shown in Table 3.4, it is observed that no significant variation occurred in the peak temperature by increasing the number of elements from 474000 to 655000. Therefore, the number of elements was selected as 475000.

Table 3.4 *Non-dimensional temperature factor (T_{peak}/T_{ref}) with four different mesh sizes for thermal modelling*

No. of elements	196000	326000	474000	655000
T_{peak}/T_{ref}	35.162	35.573	36.153	36.233

Accordingly, the uniform fine mesh size of 0.4 mm × 0.4 mm was chosen for the weld zone. To reduce the simulation time, the coarse biased mesh was applied away from the weld zone with the minimum and maximum sizes of 0.4 mm and 3 mm, respectively. Five number of the equidistance elements were taken in the thickness direction. The meshing of the FE model is shown in Fig. 3.8.

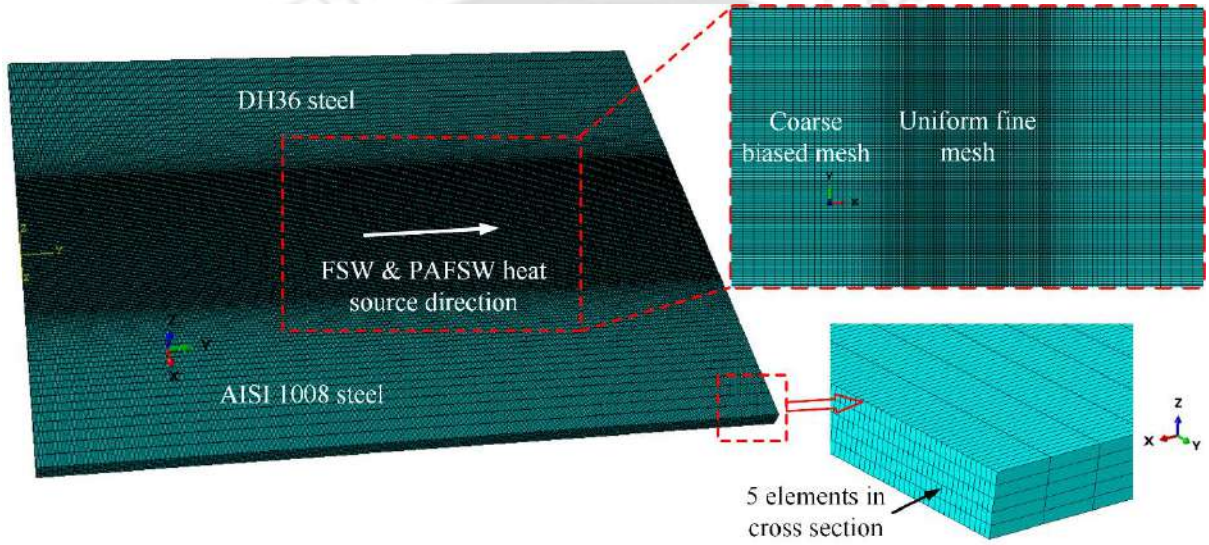

Fig. 3.8 *Mesh model for thermal simulation of the dissimilar steels*

3.2.2.1 Heat Generation Model

In moving heat source thermal modelling of FSW, the heat generation was considered by the sliding interaction condition at the workpiece/tool interface. The sliding friction is designated by pressure (P_N) and the frictional coefficient (μ_f). The heat input based on the heat generation from the shoulder and tool pin was applied as heat flux, as represented in Fig. 3.9. The shear strength of the material is represented by τ^* at about 0.8 times the liquidus temperature of the material. Accordingly, the total heat generation by the cylindrical shoulder (Q_{sh}) and cylindrical pin (Q_{pin*}) is represented as:

$$Q_{FSW*} = Q_{sh} + Q_{pin*} \tag{3.45}$$

$$Q_{FSW*} = \frac{2}{3}\pi\omega\mu_f P_N\left(\dot{R}_{sh}^{\ 3} - r_p^{\ 3}\right) + \left(\frac{2}{3}\pi\omega\mu_f P_N r_p^{\ 3} + 2\pi\omega\tau^* r_p^2 h_p\right) \tag{3.46}$$

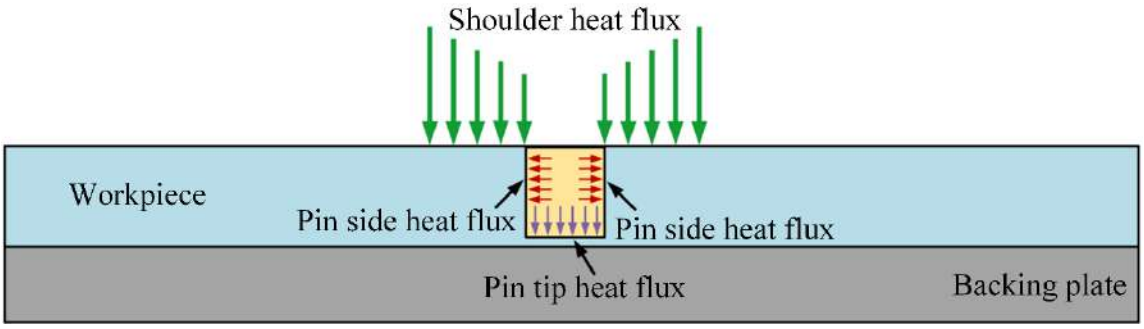

Fig. 3.9 *Heat applied to heat transfer model*

where r_p = 3.5 mm is the pin radius. In this modelling, it was assumed that heat generation in the shoulder varied linearly to the distance from the axis of the tool. The heat flux (q_{sh}) at the interface of the workpiece and shoulder surface as a function of radius (r) is represented as:

$$q_{sh} = \frac{3Q_{sh}r}{2\pi(\dot{R}_{sh}^{3} - r_p^{3})} \tag{3.47}$$

The heat generation from the pin side and pin tip was considered in the thermal model. The heat generation from the pin was applied as volumetric heat flux in the form of a cylinder. Consequently, the volumetric heat flux distribution (q_p) at the interface of pin/workpiece is represented as:

$$q_p = \frac{Q_{pin*}}{\pi r_p^{2} h_p} \tag{3.48}$$

In the moving heat source thermal modelling of PAFSW, the thermal heat source model was a combination of heat generation due to the FSW tool and plasma arc. During the traverse phase, the plasma arc through the moving heat source was applied on the DH36 steel side (harder material) in front of the FSW tool. The net heat input in the PAFSW process is calculated as:

$$Q_{PAFSW} = Q_{FSW*} + Q_{Plasma} \tag{3.49}$$

The plasma arc based on the Gaussian distribution heat flux is expressed as:

$$q_p(r) = \frac{3Q_{plasma}}{\pi r_o^{2}} \exp(-\frac{3r_a^{2}}{r_o^{2}}) \tag{3.50}$$

$$Q_{Plasma} = \eta VI \tag{3.51}$$

where Q_p is the plasma arc power (W), η is the thermal efficiency considered as 0.53 [175], I is the preheating current (A), V is the preheating voltage, r_a is the arc radius, and r_o is the radius at which heat flux is applied.

3.2.2.2 Boundary Conditions

During the FSW process, the transient heat transfer analysis is described by the following governing equation.

$$\frac{\partial}{\partial x}\left[k\frac{\partial T}{\partial x}\right]+\frac{\partial}{\partial y}\left[k\frac{\partial T}{\partial y}\right]+\frac{\partial}{\partial z}\left[k\frac{\partial T}{\partial z}\right]+Q_{gen}=\rho c_p\frac{\partial T}{\partial t} \tag{3.52}$$

where k is the thermal conductivity, ρ is the density of the material, T is the temperature, c_p is the specific heat, t is the time, and Q_{gen} is the heat generation.

(i) Initial condition

The entire elements of the developed heat transfer model subjected to the initial temperature can be represented as:

$$T = T_{amb} \text{ at } t = 0 \text{ sec} \tag{3.53}$$

where T_{amb} is the ambient temperature (i.e., 30 ºC).

(ii) First boundary condition

A significant amount of the heat is transferred to the FSW tool made up of tungsten due to its higher thermal conductivity, i.e., approximately four times greater than steel [124]. Hence the following fraction (f) is used to partition the extent of the heat transferred at the shoulder-workpiece interface.

$$f = \frac{\dot{J}_{Workpiece}}{\dot{J}_{Workpiece}+\dot{J}_{Tool}} \text{ in range of } r_p \le r \le \dot{R}_{sh} \tag{3.54}$$

$$\dot{J} = \sqrt{\rho c_p k} \tag{3.55}$$

where $\dot{J}$ represents the effusivity of the material or conduction of the heat at the shoulder-workpiece interface, f denotes the heat fraction at the workpiece/tool interface, and ρ is the material density. In the present study, the fraction (f) of 39.52% was calculated using the inverse analysis method to obtain a better agreement between numerically and experimentally measured temperature distribution during dissimilar FSW of AISI 1008 steel & DH36 steel.

(iii) Second boundary condition

Convection and radiation are responsible for heat loss (q_1) over the surface, which can be signified as:

$$q_1 = \dot{h}_{ct}(T - T_{amb}) + \beta\varepsilon\left(T^4 - {T_{amb}}^4\right) \tag{3.56}$$

where $\dot{h}_c$ is the convection coefficient, β is the Stefan–Boltzmann constant, T is workpiece temperature during welding, and ε is the emissivity of the workpiece. The effect of the backing plate was considered by applying the higher value of the convection coefficient at the bottom surface of the workpiece, which can be represented as:

$$q_2 = \dot{h}_{cb}(T - T_{amb}) \tag{3.57}$$

In the present model, the convection coefficient of 25 W/m^2 °C was considered for entire surfaces excluding the bottom surface. However, the higher convection coefficient (i.e., 2000 W/m^2 °C) was applied at the bottom surface to achieve realistic results [124].

CHAPTER 4

EXPERIMENTAL STUDY ON THE JOINING OF DISSIMILAR STEELS

The previous chapter covered the experimental procedures, including the FSW setup, materials and processing, and methods for measurements and metallographic examination. With the support of that experimental procedures, this chapter covers the outcomes of the first objective, i.e., experimental findings on dissimilar FSW of DH36 steel and AISI 1008 steel at different welding parameters. The influence of the rotational speed, traverse speed, and tool offset on temperature distribution, axial force, microstructure, and mechanical properties of the welded specimens is discussed. The primary objective of this study was to evaluate feasible welding parameters that can eliminate defects and produce sound quality weld joints. The metallographic analysis was conducted to understand the underlying mechanisms at the macro/micro levels using an optical microscope and SEM equipped with the EDS system. The complex relationship between the pitch ratio (ω/v_{weld}), heat generation, plastic deformation, microstructure, and mechanical properties of the dissimilar joints is established. Finally, this section points out the major conclusions from the experimental study on the dissimilar steels.

4.1 PROCESS PARAMETERS

In this experimental study, DH36 steel and AISI 1008 steel sheets are joined. The trial and error procedure was used to choose the best combination of the welding process parameters (i.e., rotational speed, traverse speed, and tool offset) that can produce sound quality weld joints. The welding was performed by shifting the tool pin towards the AISI 1008 steel from the weld line. Initially, experiments were performed to obtain the optimum rotational speed with fixed traverse speed and tool offset. After the macrographs and visual inspection of the initially tested weld joints, further experiments were carried out by changing the traverse speed and tool pin offset with constant rotational speed. The tool tilt angle was kept constant at 0° during the FSW process. The chosen working range of the welding parameters with a constant plunge depth of 0.2 mm is represented in Table 4.1.

Table 4.1 *FSW parameters with clockwise tool rotation direction*

Sample no.	Process parameters		
	Rotational speed (rpm)	Traverse speed (mm/min)	Tool offset (mm)
S_1	300	90	2
S_2	450	90	2
S_3	600	90	2
S_4	850	90	2
S_5	600	50	2
S_6	600	70	2
S_7	600	132	2
S_8	600	90	0.5
S_9	600	90	1
S_{10}	600	90	1.5
S_{11}	600	90	2.5

4.2 VISUAL INSPECTION AND JOINT OBSERVATIONS

A typical weld surface appearance of welded samples S_1, S_4, S_5, S_7, and S_9 are shown in Figs. 4.1(a–e). Semi-circular patterns are observed on the crown of welded joints. The rubbing of the FSW tool shoulder on the sheets leads to the formation of these patterns. Ceschini et al. [176] reported the formation of these patterns in the FSW process as a wake effect. The tool shoulder geometry is responsible for this type of crown appearance. Many numbers of trial runs were conducted to establish the proper welding parameters. Some of the observations due to improper welding parameters are shown in Figs. 4.1(f–j).

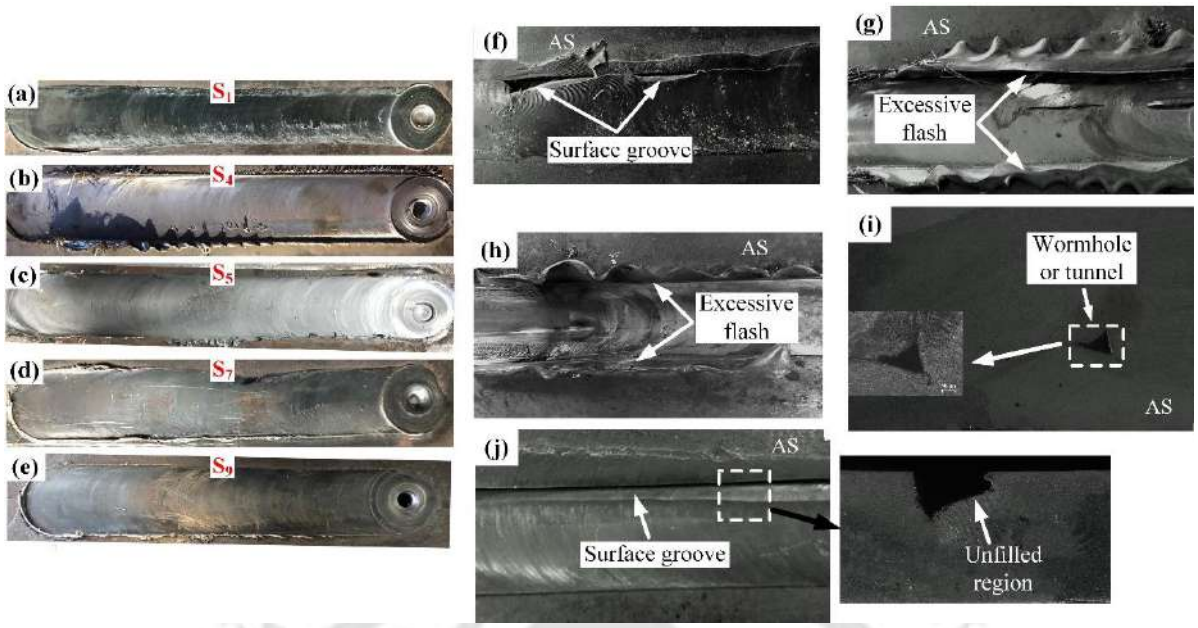

Fig. 4.1 *(a–e) Surface-appearance of the welded samples; defects at improper parameters (f) rotational speed < 300 rpm; (g) rotational speed > 850 rpm; (h) traverse speed < 50 mm/min; (i) traverse speed > 132 mm/min; and (j) plunge depth < 0.2 mm*

Improper parameters generated the defects like an excessive flash, wormhole, and surface groove, as shown in Figs. 4.1(f–j). The surface grove defect is observed on the AS at low rotational speed (i.e., below 300 rpm) due to inadequate material flow at low heat input, as shown in Fig. 4.1(f). The excessive flash is generated at the higher rotational speed and lower traverse speed due to material softening by the excess frictional heat generation, as shown in Figs. 4.1(g) & 4.1(h) respectively. The excessive flash deteriorated the strength of the welded joints due to the reduction of the plasticized weld metal volume. The higher plunging depth (i.e., above 0.2 mm) also generated the excessive flash due to higher frictional heat. The wormhole or tunnel is a volumetric type defect in which a continuous hole is created inside the SZ of welded specimens. These defects exhibit sharp corners, which act as stress raisers in the weld region and significantly deteriorate the strength of the welded joints. Fig. 4.1(i) shows the wormhole or tunnel defect in the advancing side of the SZ at the higher tool traverse speed due to a lack of material stirring during the welding process. This is attributed to the fast cooling rate of the material before mixing the stirred material at a higher traverse speed. The lower plunge depth (i.e., below 0.2 mm) generated the defect like a surface groove or surface lack of fill due to insufficient material flow across the top surface of the weld, as shown in Fig. 4.1(j).

4.3 TEMPERATURE DISTRIBUTION

The friction between the workpiece and tool shoulder generates extensive heat through plasticized material flow during the FSW process, which strongly affects the strength of the welded specimens. Accordingly, the proper selection of the FSW parameters is essential to achieve a sufficient weld temperature that can eliminate the defects in welded specimens. In the present study, to measure the transient thermal history, eight k-type thermocouples were attached to the workpiece at various positions on the AS (i.e., Ta1, Ta2, Ta3, and Ta4) and RS (i.e., Tr1, Tr2, Tr3, and Tr4), as shown in Fig. 4.2.

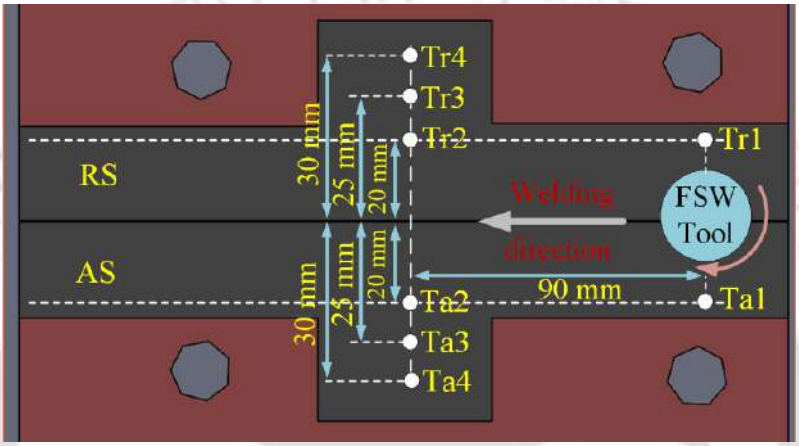

Fig. 4.2 *Position of the thermocouples in the workpiece*

To measure the thermal history during the plunging & dwelling period, Ta1 and Tr1 thermocouples were attached at 20 mm away from the start point on the AS and RS, respectively. To measure the thermal history during the traverse phase, thermocouples (Ta2, Ta3, Ta4) and (Tr2, Tr3, Tr4) were away from the middle section of the specimen in AS and RS, respectively. After the welding process was completed, the workpiece was allowed to cool down to near about the ambient temperature. The measured transient temperature distribution at 300 rpm and 850 rpm is shown in Figs. 4.3 and 4.4, respectively.

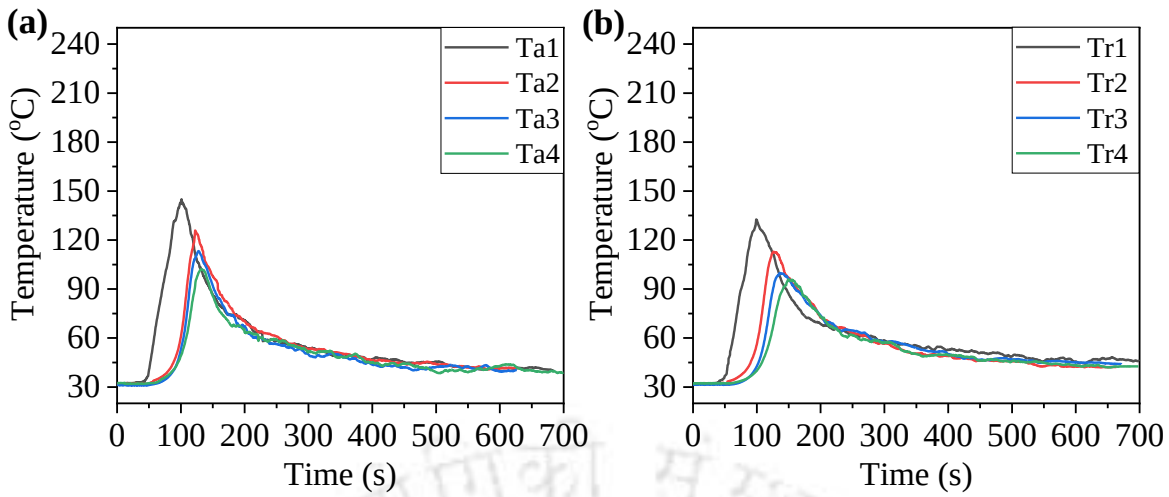

Fig. 4.3 *Transient thermal profiles of samples S_1 at (a) advancing side; and (b) retreating side*

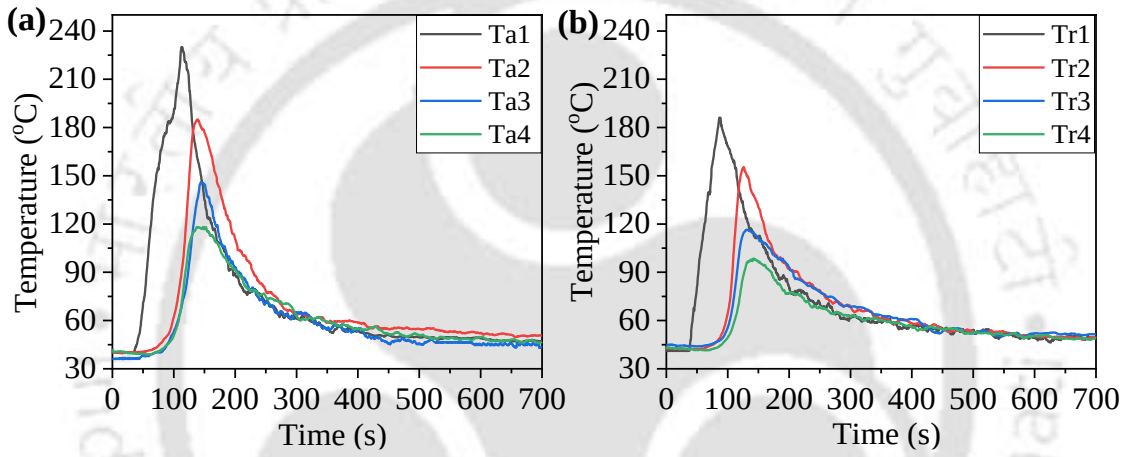

Fig. 4.4 *Transient thermal profiles of samples S_4 at (a) advancing side; and (b) retreating side*

It is observed that increasing the distance away from the weld line decreased the temperature due to the heat loss by conduction to the backing plate, convection, and radiation to the atmosphere. The thermocouples Ta1 and Tr1 exhibited the temperature higher than the other thermocouples because these thermocouples are located at the starting position, which led to more contact time between the tool and workpiece during the plunging and dwelling periods and generated excessive frictional heat compared to the traverse period. At a rotational speed of 300 rpm, Ta1, Ta2, Ta3, Ta4, Tr1, Tr2, Tr3, and Tr4 exhibited the peak temperatures, i.e., 144.4 °C, 125.7 °C, 113.2 °C, 101.8 °C, 132.5 °C, 112.6 °C, 99.8 °C and 95 °C, respectively, as shown in Fig. 4.3. With an increase in the rotational speed from 300 rpm to 850 rpm, these peak temperature values enhanced, i.e., 229.8 °C, 184.3 °C, 145.4 °C, 118.4 °C, 187.4 °C, 154.5 °C, 116.8 °C and 99.6 °C at Ta1, Ta2, Ta3, Ta4, Tr1, Tr2, Tr3, and Tr4, respectively, as shown in Fig. 4.4. The temperature in the AS is higher than the RS due to the same direction of tool traverse and the tangential component of the tool rotation, which generated the more frictional heat in the AS than the RS. Another reason behind the higher

temperature in the AS is the low thermal conductivity of DH36 steel [189] compared to AISI 1008 steel [127]. Figs. 4.5(a–c) represents the influence of varying parameters, i.e., rotational speed, traverse speed, and tool offset on peak temperature at Ta2 and Tr2.

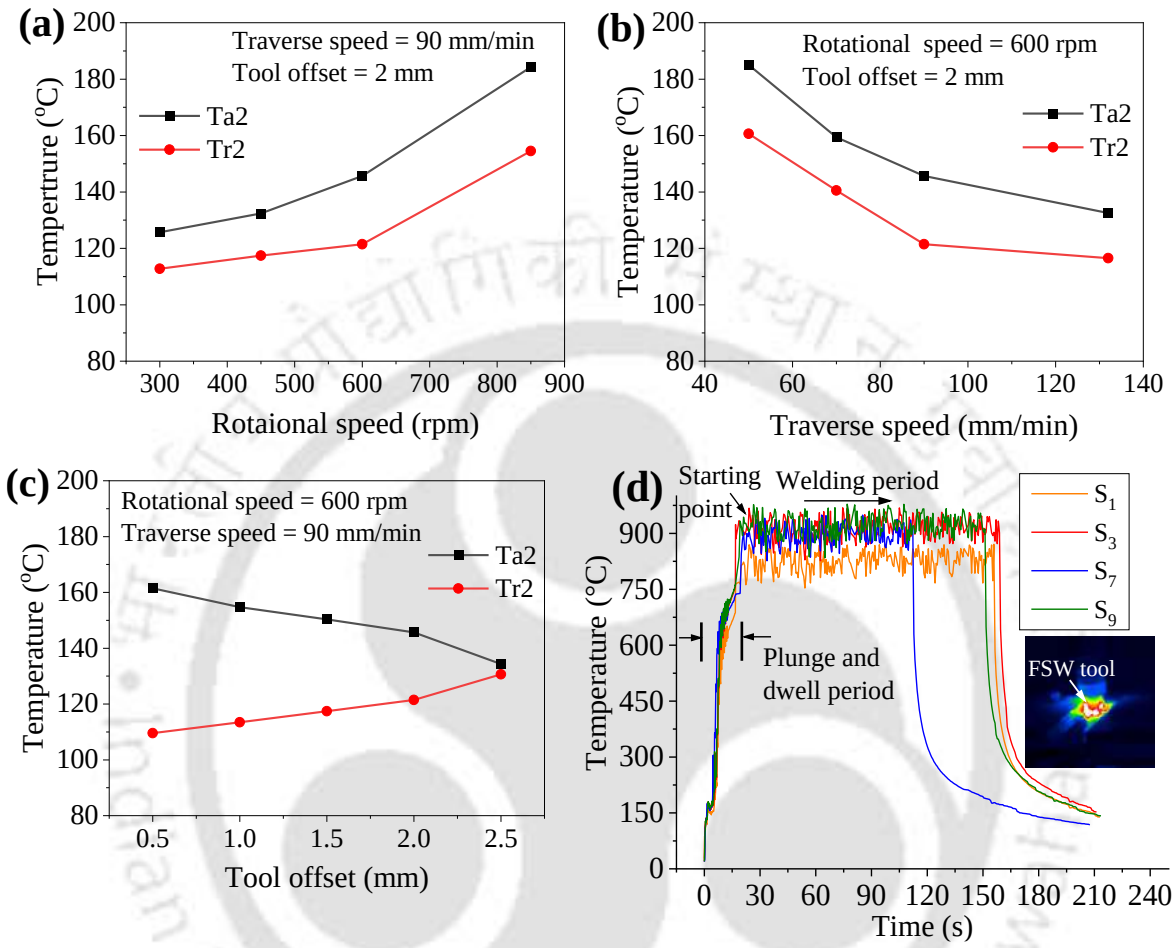

Fig. 4.5 *Peak temperature distribution at varying (a) rotational speed; (b) traverse speed; (c) tool offset; and (d) transient thermal history using IR camera at different welding conditions*

The temperature variation strongly depends upon the rotational speed and traverse speed. The temperature of thermocouples (i.e., Ta2, Ta3, Ta4, Tr2, Tr3, and Tr4) increased with an increase in rotational speed and a decrease in the traverse speed. A significant variation in the peak temperature is observed by varying the pin offset. Increasing the rotational speed from 300 rpm to 850 rpm increased the peak temperature by 58.6 ºC and 42 ºC in AS and RS, respectively, as shown in Fig. 4.5(a). Fig. 4.5(b) shows that the peak temperature increased to 52.5 ºC and 44 ºC by decreasing the traverse speed from 132 mm/min to 50 mm/min in AS and RS, respectively. The varying tool offset towards AISI 1008 steel side slightly increased the peak temperature in RS and decreased in AS, as shown in Fig. 4.5(c). The higher surface contact between the shoulder and AISI 1008 steel, which led to high frictional heat in the RS.

The thermal history is directly correlated to heat generation due to friction between the tool and the workpiece. Saeid et al. [52] reported that heat input during the FSW process is represented as:

$$Q = \frac{4}{3}\pi^2 \frac{\eta \dot{\mu}_f \omega P_N \dot{R}_{sh}^{\ 3}}{v_{weld}} \tag{4.1}$$

where Q represents the heat input, $\dot{\mu}_f$ is the coefficient of friction, η is the heat input efficiency, P_N is the pressure, $\dot{R}_{sh}$ is the shoulder radius, ω is the rotational speed, and v_{weld} is the traverse speed. By assuming the constant efficiency (η) and coefficient of friction ($\dot{\mu}_f$) in Equation (4.1), it can be concluded that increasing the rotational speed or decreasing the traverse speed increases the value of heat input. In this study, the non-contacting infrared (IR) camera was used to measure the transient thermal history of the tool during the welding process, as shown in Fig. 4.5(d). The average temperature of the FSW tool at a rotational speed of 600 rpm was 87 °C higher than 300 rpm during the welding period. From the temperature profiles, it is observed that the average temperature decreased by 22 °C with an increase in the traverse speed from 90 mm/min to 132 mm/min. The temperature slightly changed by varying the tool offset from 1 mm to 2 mm towards AISI 1008 steel side.

4.4 AXIAL FORCE

The temperature variation by welding parameters changes the yield/flow stress of the material, which is the cause of axial force variation during the welding process. Fig. 4.6 shows the axial force variation with the time at varying welding parameters.

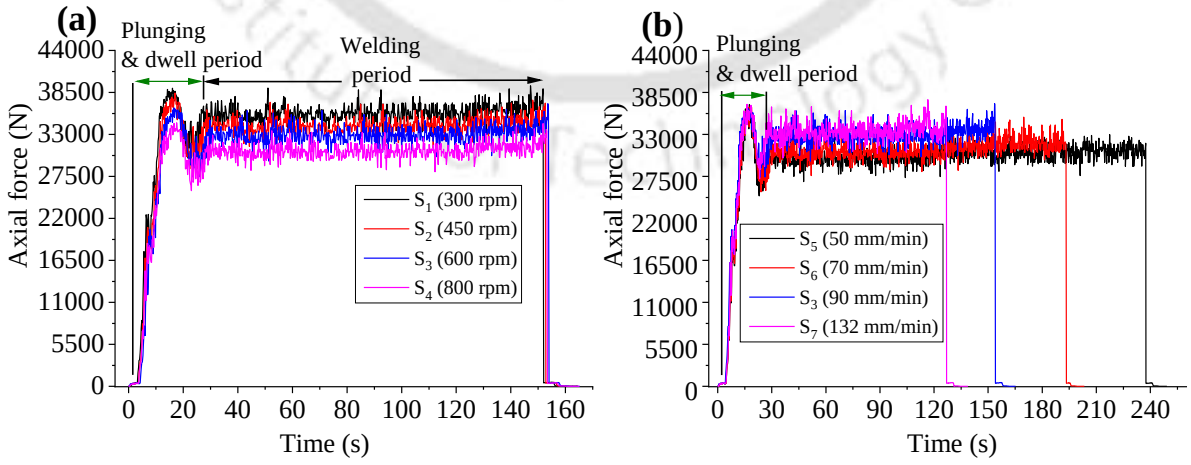

Fig. 4.6 *Variation of axial force with time at varying (a) rotational speed; and (b) traverse speed*

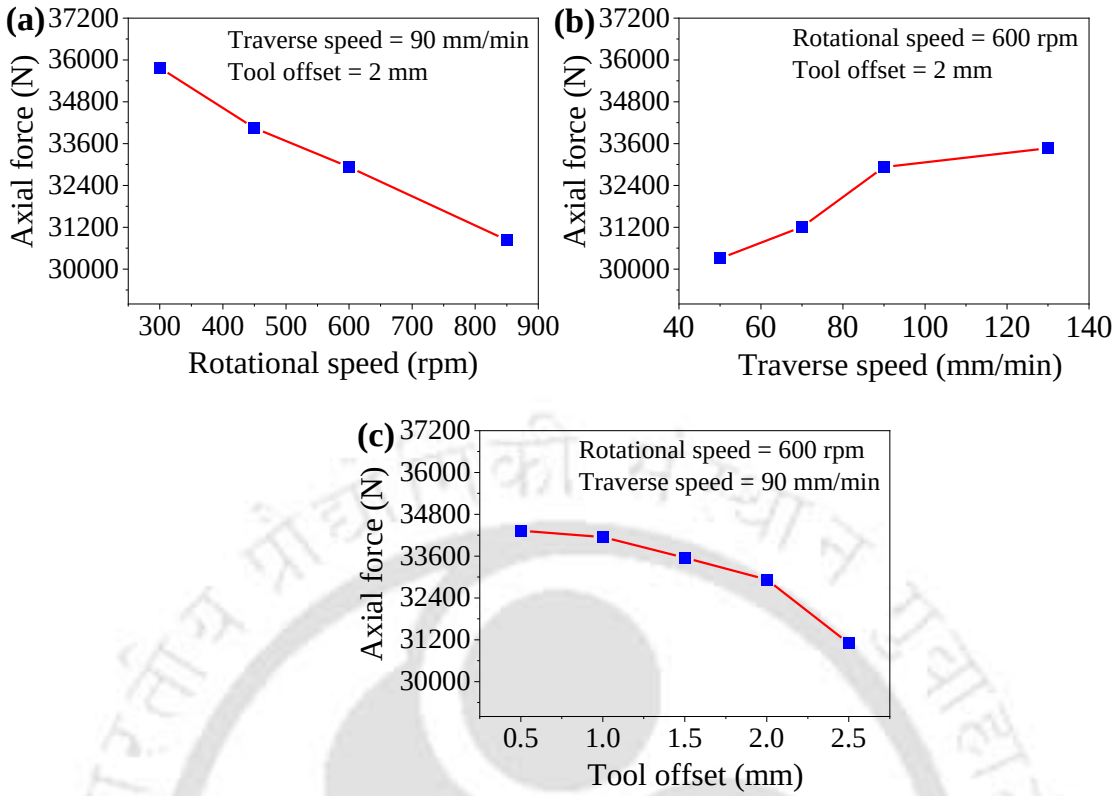

Fig. 4.7 *Average axial force during welding period at varying (a) rotational speed; (b) traverse speed; and (c) tool offset*

The maximum variation and peak value in the axial force achieved during the plunging period due to the lack of thermally softened material and then it reduced significantly due to the increased frictional heat in the dwelling period. After this, it remained steady during the traverse stage because adjacent material was sufficiently softened in this period, as shown in Fig. 4.6. The axial force decreased with an increase in the tool rotational speed, as shown in Fig. 4.7(a). This is attributed to the thermally softening of the material due to higher temperatures at a high rotational speed. The higher temperature reduces the yield/flow stress of the material, which decreases the axial force. The axial force increased with an increase in traverse speed, as shown in Fig. 4.7(b). The less heat input at a higher traverse speed reduced the thermal softening of the material, which increased the axial force. Increasing the rotational speed from 300 rpm to 850 rpm and decreasing the traverse speed from 132 mm/min to 50 mm/min reduced the average axial force during the welding period by 13.8% and 9.7%, respectively. Increasing the tool offset from 0.5 mm to 2.5 mm towards the AISI 1008 steel side decreased the axial force by 9.4%, as shown in Fig. 4.7(c). The higher tool offset increased the contact area between the tool and low-flow stress material (i.e., AISI 1008 steel), which softened the material easily and decreased the axial force.

4.5 MACRO/MICROSTRUCTURE

The dissimilar FSW of DH36 steel-AISI 1008 steel revealed the different regions in macrostructure, such as base AISI 1008 steel, base DH36 steel, heat affected zone (HAZ) in the DH36 steel, HAZ in the AISI 1008 steel, thermo-mechanically affected zone (TMAZ) in the DH36 steel, TMAZ in the AISI 1008 steel, and stir zone (SZ), as shown in Fig. 4.8.

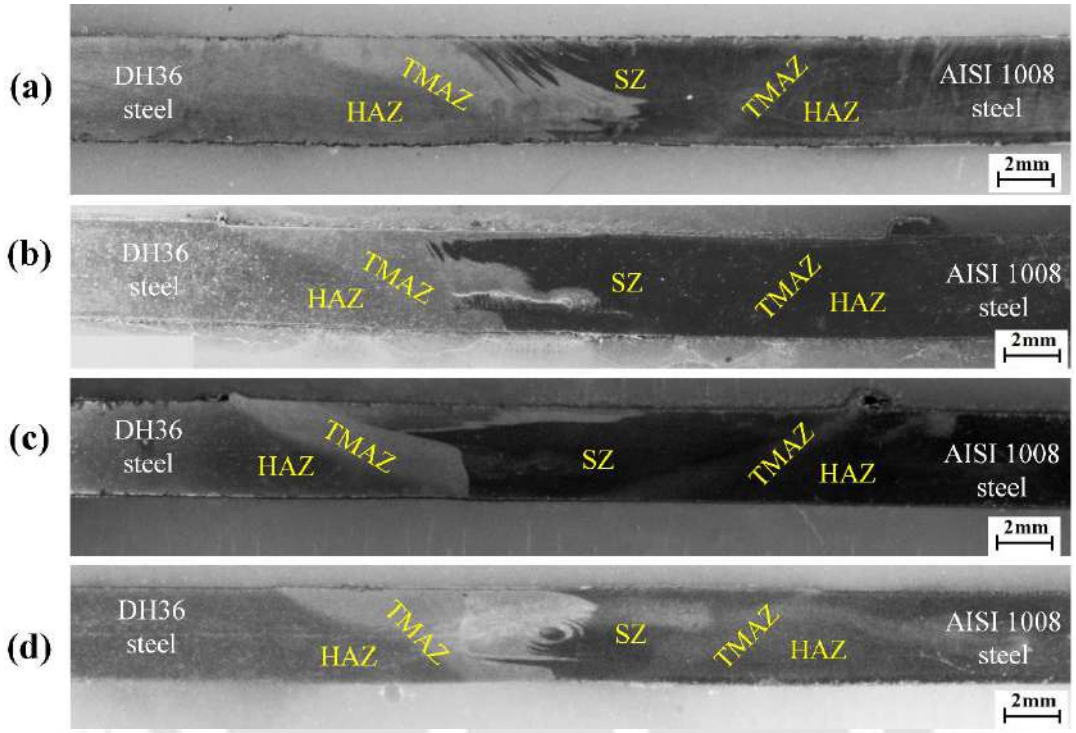

Fig. 4.8 *Macrostructure of the dissimilar welded sample (a) S_1; (b) S_5; (c) S_7; and (d) S_9*

The macrostructure of the welded samples shows the flow of material from DH36 steel to AISI 1008 steel. The ‘‘basin shape’’ weld cross-section profile appeared due to high deformation and frictional heat at the top surface by contact between the tool shoulder and the workpiece. However, the heat conducted from the bottom surface to the backing plate leads to a narrow bottom region of SZ. Fig. 4.9 shows the microstructure of the mixed mechanical region in the SZ at different welding parameters.

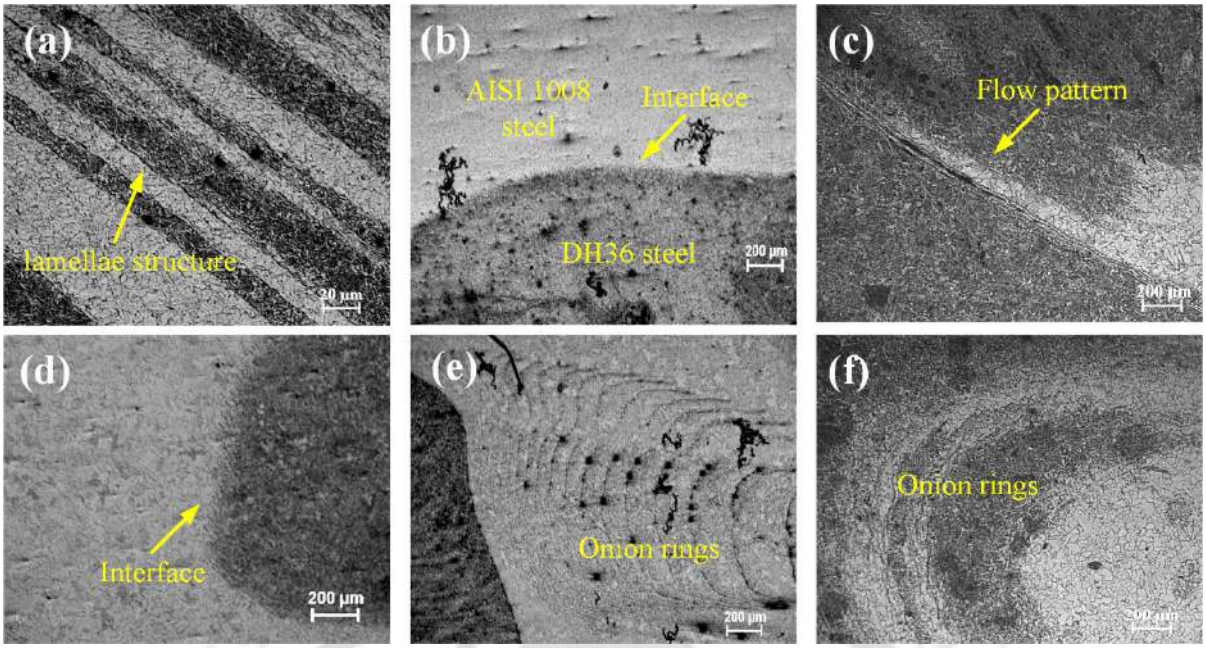

Fig. 4.9 *Microstructure of mechanically mixed regions in the SZ of sample (a) S_1; (b) S_3; (c) S_4; (d) S_5; (e) S_7; and (f) S_{10}*

The unmixed region exhibited fine grain structure in the SZ resulting from the dynamic recrystallization during the FSW process. However, the dissimilar metals are mechanically mixed and contain the microstructure of both metals in the mixed region, as shown in Fig. 4.9. This region exhibited the microstructure of different lamellae of both the steels, and complex vortex flow pattern. The stirring action of the tool creates the chaotic intercalation patterns in the mixed region due to the intense plastic deformation of materials. The lamellae structure formed due to the deposition of alternating layers of dissimilar materials. The onion-ring pattern is also observed in the stir zone (SZ) consisting of DH36 and AISI 1008 steel. K.N. Krishnan [177] investigated that the rotation and traverse movement of the tool extrudes the metal to the retreating side, which generates the frictional heat leading to the formation of onion rings. Fig. 4.10 shows the microstructure of both base materials. The microstructure of DH36 base material exhibited the banded coarse-grained ferrite and pearlite with 15.9 µm average grain size (AVG) of ferrite, as shown in Figs. 4.10(a) and 4.10(b). The equiaxed ferrite phase along with the pearlite structure with the AVG of 29.25 µm is observed in AISI 1008 steel base material, as shown in Figs. 4.10(c) and 4.10(d). Fig. 4.11 shows the optical microstructure of various regions in the S_4 welded sample.

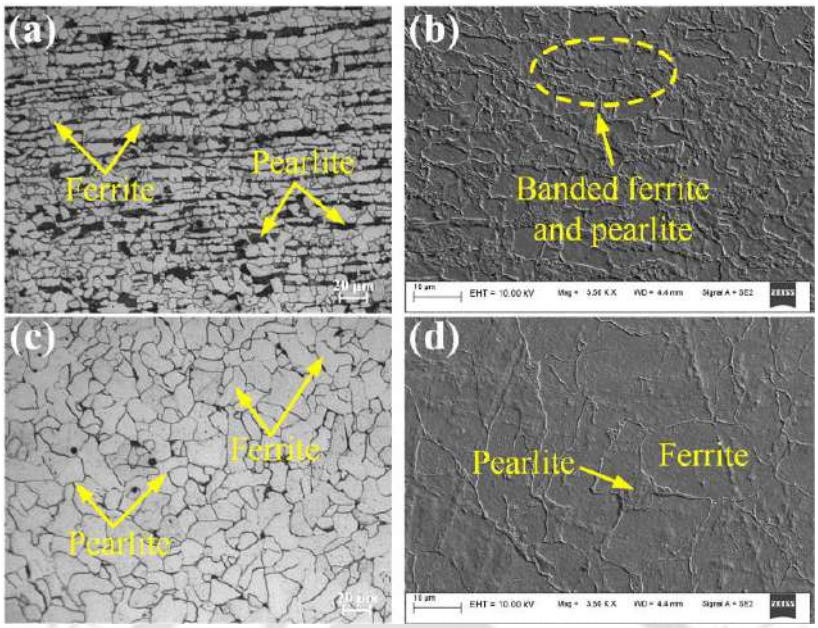

Fig. 4.10 *Optical and SEM Microstructure of (a,b) DH36 steel; and (c,d) AISI 1008 steel*

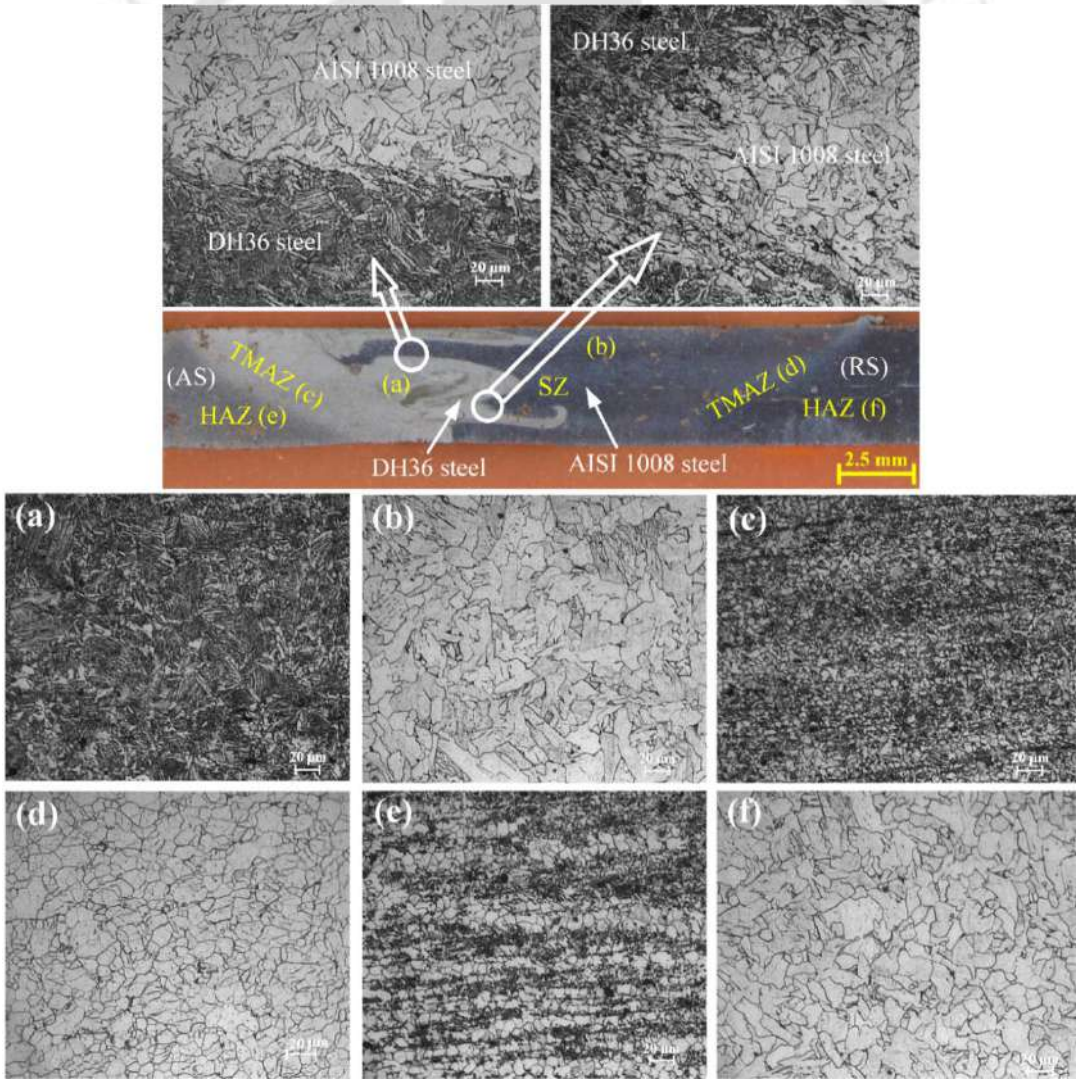

Fig. 4.11 *Microstructure in various zones*

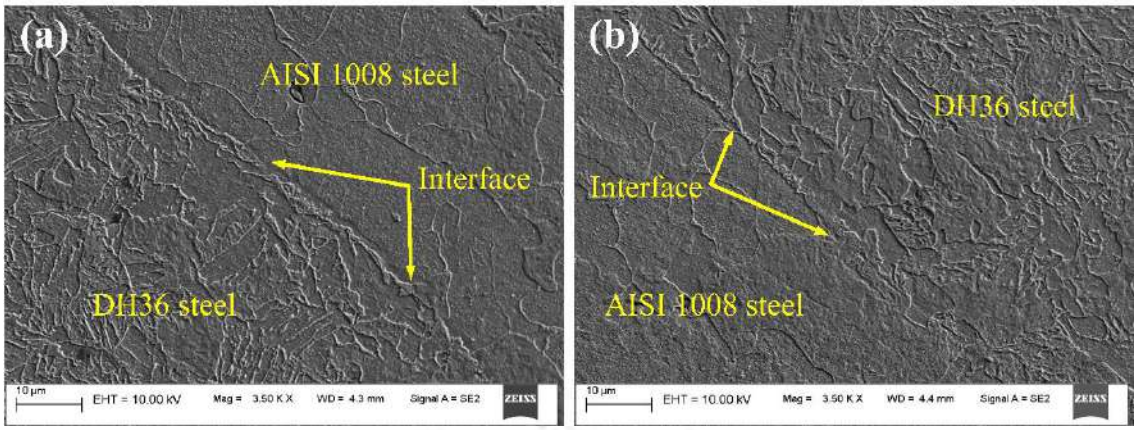

Fig. 4.12 *SEM microstructure of interface between both steels in the SZ*

In the FSW, the SZ exhibits dynamic recrystallization, which signifies the location of the pin. TMAZ adjacent to the SZ is subjected to plastic deformation and thermal cycle due to the friction and the movement of the stirring tool. SZ experienced not only the axial force and frictional force due to the rotating shoulder but also the friction force as well as the shear force of the rotating pin, which led to the elongation of the coarse grains and then divided into finer grains. The finer grains produced dynamic recrystallization due to excessive heat generation and plastic deformation. SZ in the DH36 steel side contained the fine acicular-shaped randomly mixed grains of bainitic ferrite, as shown in Fig. 4.11(a). The microstructure in the SZ is similar to that reported by McPherson et al. [178]. The stir zone in AISI 1008 steel side consisted of Widmanstatten ferrite grains, as shown in Fig. 4.11(b). The TMAZ in the DH36 steel side exhibited grain refinement with finer ferrite grains as a result of mechanical deformation and recrystallization, as shown in Fig. 4.11(c). Significant grain size reduction is also observed in TMAZ of AISI 1008 steel, as shown in Fig. 4.11(d). Lienert et al. [49] mentioned that the thermal cycles transformed the pearlite to austenite during heating and then refined the ferrite and pearlite during the cooling phase in TMAZ during FSW of 1018 mild steel. HAZ existed between the TMAZ and base material. HAZ in DH36 steel contained the slightly fine banded equiaxed ferrite grains with pearlite compared to the base material, as shown in Fig. 4.11(e). In AISI 1008 steel, this zone also contained ferrite grains slightly finer than the base material, as shown in Fig. 4.11(f). HAZ exhibited the coarse grain microstructure compared to SZ and TMAZ because this zone is subjected to heat only but not experiences mechanical deformation during the welding process. Interface separating both steels in SZ with acicular-shaped bainitic ferrite and Widmanstatten ferrite grained SEM microstructure is clearly visible in Fig. 4.12.

During the FSW process, the grain size in the SZ is affected by two phenomena, namely dynamic recrystallization (DRX) and heat generation. These two phenomena compete with

each other, and the dominating phenomenon controls the grain size during the welding process. In the FSW, the extreme plastic deformation of the base material leads to dynamic recrystallization, which includes the nucleation of new strain-free grains and their subsequent growth by grain boundary migration. Samanta et al. [179] reported that the dislocation density difference, i.e., the difference in strain energy stored across the grain boundary induces the driving force, which promotes the grain growth through the boundary migration. According to Asadi et al. [180], the nucleation of new grains happens at the preferential sites during the DRX. Subsequently, the grain growth initiates due to enough heat and the dislocation density difference, which continues as long as the driving force acts for the grain boundary migration. As the deformation progresses, the driving force for the grain growth reduces as the dislocation density within the grain increases, and finally, the growth of recrystallized grains stops. Furthermore, the DRX grain boundaries again turn into nucleation sites at a higher plastic deformation when its dislocation density reaches the critical value for nucleation. Meanwhile, heat generation due to friction in the FSW process leads to the annealing phenomenon, which causes the grain size to increase. Fig. 4.13 shows that the grain size in the SZ and TMAZ is considerably reduced with an increase in rotational speed and a decrease in traverse speed, respectively, which was also reported in the dissimilar FSW of Al & steel [1]. The degree of plastic deformation increases with an increase in rotational speed and a decrease in traverse speed. The lower traverse speed causes more contact time between the rotating tool and the workpiece, which enhances the plastic deformation by the stirring action of the tool. As a result, in this study, dynamic recrystallization under extreme plastic deformation could be considered the determinative phenomenon for grain size variation. Eyvazian et al. [1] also reported that the more refined grains at the lower traverse speed could be attributed to the formation of nucleates under extensive shear deformation. Therefore, the grain size variation strongly depends on the pitch ratio (w/v_{weld}). Dynamic recrystallization is increased by enhancing the pitch ratio due to higher plastic deformation, which reduces the grain size [181]. TMAZ in DH36 steel and AISI 1008 steel exhibited the finer average grain size, which is 20.7% and 32.13% lesser than the respective base material. SZ in DH36 steel and AISI 1008 steel contained the average grain size (AVG) slightly coarser than the TMAZ. It is 23% and 38.2% less than DH36 steel and AISI 1008 steel base material, respectively. The influence of heat input on HAZ showed no significant variation in AVG compared to base materials.

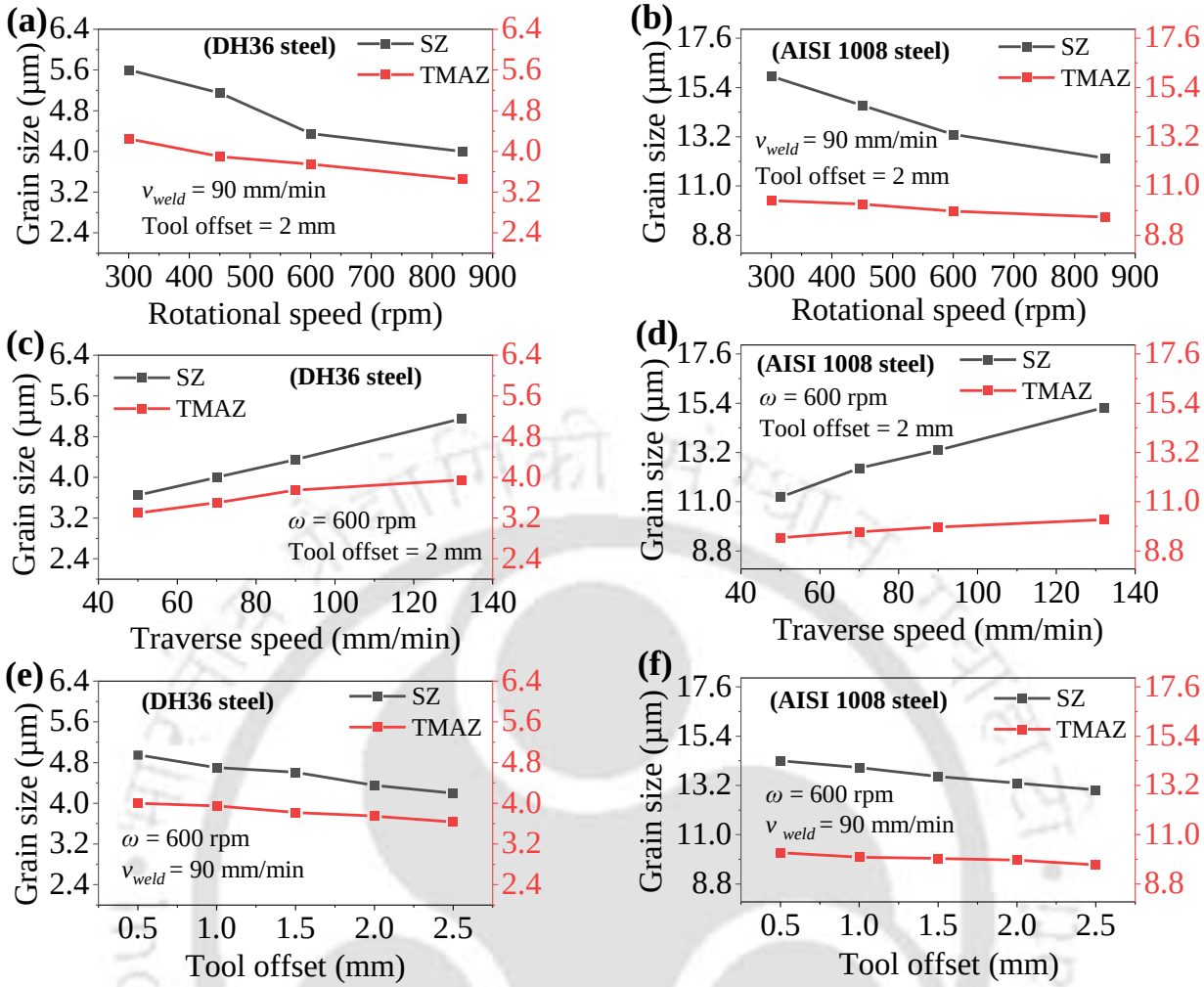

Fig. 4.13 *Average grain size variation in SZ and TMAZ of welded samples at varying (a,b) rotational speed; (c,d) traverse speed; and (e,f) tool offset*

Furthermore, the variation of AVG at varying parameters was significant between DH36 steel and AISI 1008 steel, as shown in Fig. 4.13. The AVG in TMAZ exhibited considerably lower than the SZ at varying welding parameters for both steels. It is observed that the AVG decreased by increasing the rotational speed and decreasing the traverse speed. Increasing the rotational speed from 300 rpm to 850 rpm reduced the AVG in SZ by 28.6% and 23% in DH36 steel and AISI 1008 steel, respectively. Reducing the traverse speed from 132 mm/min to 50 mm/min decreased the AVG in SZ by 29% and 26.3% in DH36 steel and AISI 1008 steel, respectively. The coarse grain structure is observed at the low rotational speed (i.e., 300 rpm), as shown in Figs. 4.13(a) and 4.13(b). The higher traverse speed also exhibited the coarse-grained microstructure, as shown in Figs. 4.13(c) & 4.13(d). Insufficient plastic deformation at low rotational speed and higher traverse speed led to a lack of grain refinement in SZ and TMAZ. At lower traverse speed (i.e., 50 mm/min), the very fine grain size is observed in TMAZ of DH36 steel (i.e., 3.3 µm) and AISI 1008 steel (i.e., 9.4 µm).

The contact time between the tool and workpiece is higher at low traverse speed, which results in high plastic deformation and grain refinement by the recrystallization process. Increasing the tool offset towards soft material produced not much variation in AVG, as shown in Figs. 4.13(e) and 4.13(f). The grain size variation directly affects the mechanical properties (i.e., impact toughness and microhardness) of the welded samples discussed in the next section.

4.6 MECHANICAL PROPERTIES

Tensile tests and impact tests were carried out up to the final failure of the specimens to determine the mechanical properties of the joints. The impact test was performed to investigate the energy absorbed by the welded specimens. Fig. 4.14 shows the fractured tensile samples of welded joints, tensile strength, and impact toughness of welded samples. It is observed that the tensile samples fractured in the AISI 1008 steel (weaker material), as shown in Fig. 4.14(a). The UTS values are at least on the level of the weaker material strength. Sample S_5 exhibited the maximum tensile strength of 356.45 MPa, as shown in Fig. 4.14(b). Fig. 4.14(c) shows that sample S_1 exhibited the minimum impact toughness due to inadequate stirring of plasticized material and grain coarsening in SZ and TMAZ at a lower rotational speed. The maximum impact toughness is obtained at the lower traverse speed (sample S_5) due to grain refinement. The impact toughness of the welded joints increased with an increase in the tool rotational speed up to 600 rpm, as shown in Fig. 4.14(d). Further increasing the tool rotational speed decreased the impact toughness. At higher tool rotational speed, high frictional heat generated more flash, which reduced plasticized weld metal volume and deteriorated the impact toughness of the welded joints**.** With an increase in the traverse speed, impact toughness followed the decreasing trend, as shown in Fig. 4.14(e). The decreasing trend can be due to two reasons: (1) grain coarsening and (2) less heat input which led to the insufficient stirring of plasticized material due to the shorter contact time between tool and workpiece. The impact toughness showed a slight variation by changing the tool pin offset with constant rotational speed and traverse speed, as shown in Fig. 4.14(f). It increased gradually up to 2 mm pin offset due to grain refinement in SZ and TMAZ. As the tool pin completely shifted towards the AISI 1008 steel, the improper mixing of both steels deteriorated the impact toughness of the welded joints. From Fig. 4.14, it can be concluded that sample S_5 is the best choice since its toughness is even better than the base material. The strength of the joint is comparable to all other results, and base material AISI 1008 steel is the limiting strength factor of the joint.

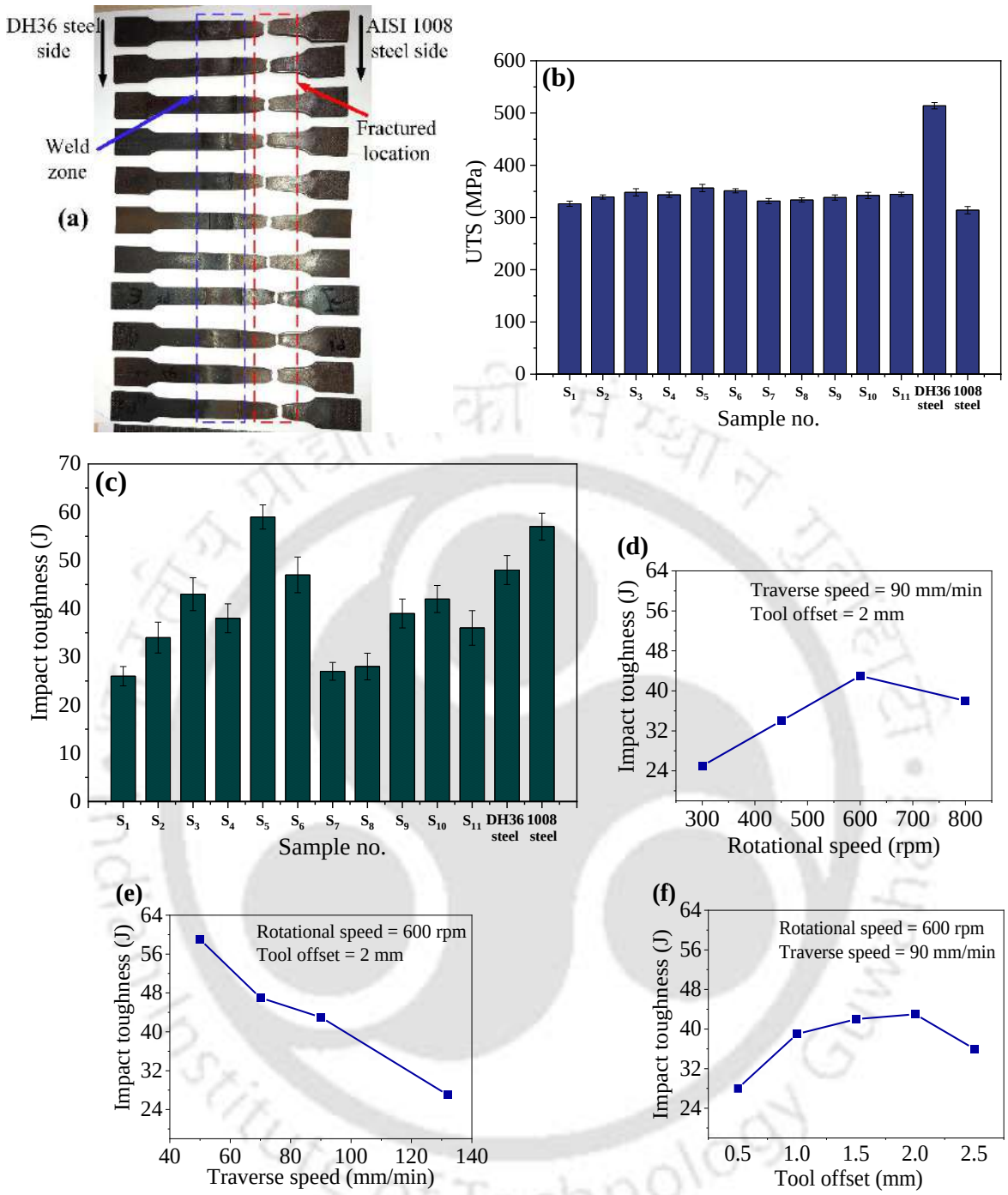

Fig. 4.14 *(a) Fractured tensile test samples; (b) tensile strength; (c) impact toughness of welded samples; impact energy of welded samples at varying (d) rotational speed; (e) traverse speed; and (f) tool offset*

In this section, a brief study on hardness distribution across the cross-section of welded samples is performed. The microhardness was measured at the three lines, i.e., 1 mm, 2 mm, and 3 mm from the top surface in the transverse direction to the weld centreline. Fig. 4.15 shows the microhardness contours across the cross-section of welded samples at varying welding parameters.

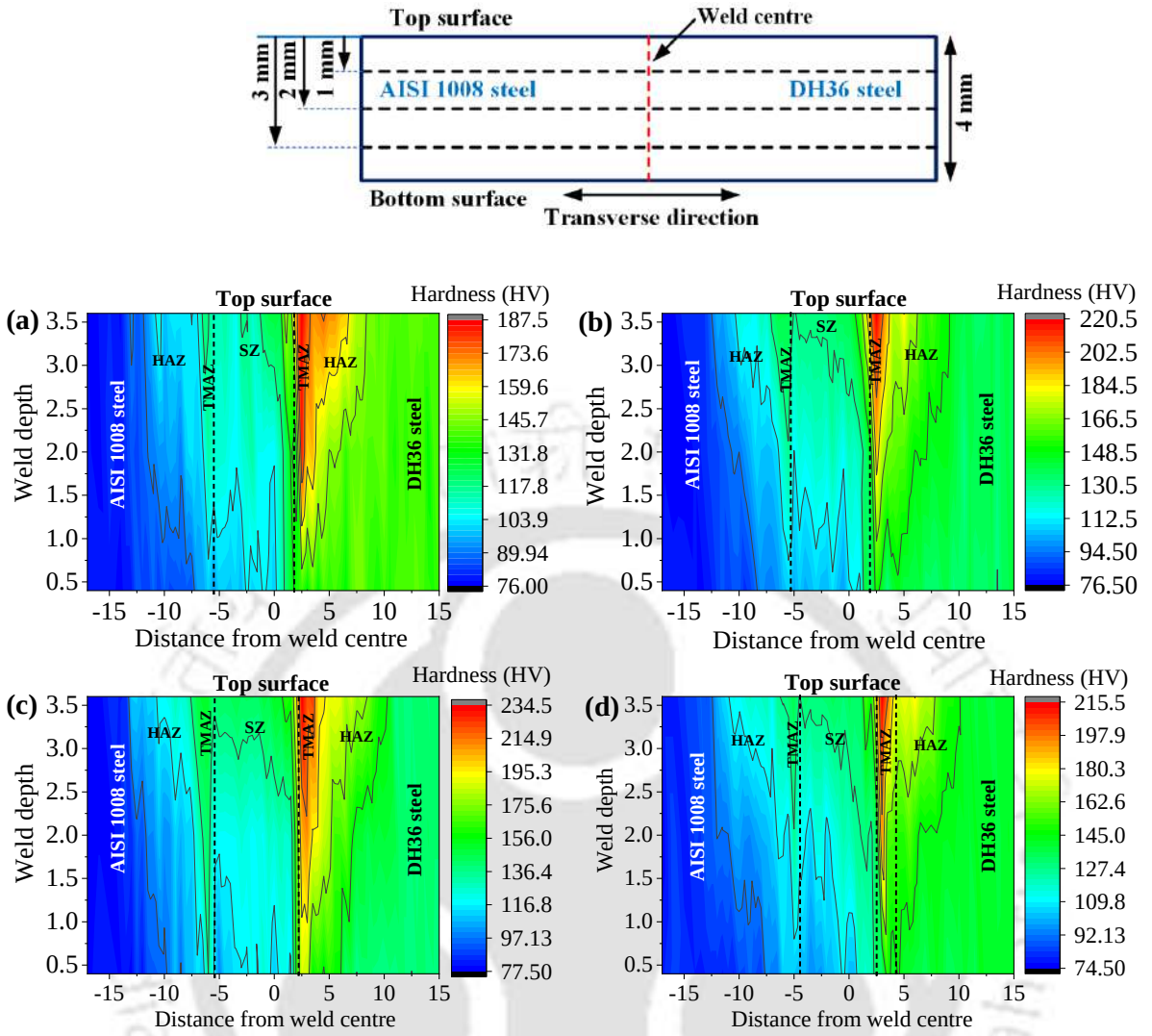

Fig. 4.15 *Microhardness contour throughout the cross-section of sample (a) S_1; (b) S_3; (c) S_5; and (d) S_9*

The hardness values at the DH36 steel side are much higher than the AISI 1008 steel side, as shown in Fig. 4.15. The hardness contours show that the AISI 1008 steel is the softest part of the joints as it exhibited the lowest hardness value, which resulted in the fracture of the tensile samples in the AISI 1008 steel base material. The top surface exhibited hardness values higher than the bottom surface. The top surface is subjected to high strain relative to the bottom surface due to more frictional heat between the tool shoulder and workpiece, which leads to fine grains and higher hardness [49]. SZ contained the hardness lower than TMAZ due to the presence of coarse-grained acicular-shaped bainitic ferrite in DH36 steel and Widmanstatten ferrite in AISI 1008 steel, but TMAZ experienced the grain refinement. The inhomogeneous hardness distribution is observed in the SZ due to finer recrystallized grains caused by intense plastic deformation. The fluctuation in hardness distribution can be attributed to the formation of different alignments of the grains and onion rings in the SZ. Cho et al. [182] reported that

the highest hardness in the SZ (central TMAZ) was due to the formation of an acicular-shaped bainitic ferrite microstructure. The hardness values in HAZ of DH36 steel varied from 190.7 HV to 151 HV, which is lower than that of the TMAZ and base materials. Due to fine-grain microstructure, the rotational speed of 600 rpm produced higher hardness (i.e., 220.5 HV) than 300 rpm (187.5 HV), as shown in Figs. 4.15(a) and 4.15(b). The traverse speed strongly affected the microstructure, which led to significant variation in microhardness distribution. Due to higher grain refinement, the maximum hardness of 234.2 HV in TMAZ of DH36 steel is obtained at a lower traverse speed, i.e., 50 mm/min as compared to 90 mm/min, as shown in Figs. 4.15(b) and 4.15(c). In published literature [16], it is also reported that the fine-grain microstructure is responsible for higher hardness, followed by the Hall-Petch relationship. In fine-grained microstructure, the grain boundaries act as an obstacle to dislocation movement, which results in higher hardness and impact toughness. Similar to the impact toughness, hardness showed little variation by changing the tool pin offset, which could be attributed to grain size variation, as shown in Figs. 4.15(b) and 4.15(d).

4.6.1 Fracture Morphology

The fractured surfaces of the impact test samples were examined using a scanning electron microscope (SEM). The fractured surfaces are covered with a large number of dimples and voids varying in shape and size, as shown in Fig. 4.16. The fracture surface also contained the inhomogeneous distribution of the dimples. The dimples in the fractured surface generally act as voids which leads to the ductile fracture mode by nucleation and growth. Accordingly, the fracture of all the dissimilar welded joints occurred in a ductile manner, followed by the coalescence of voids.

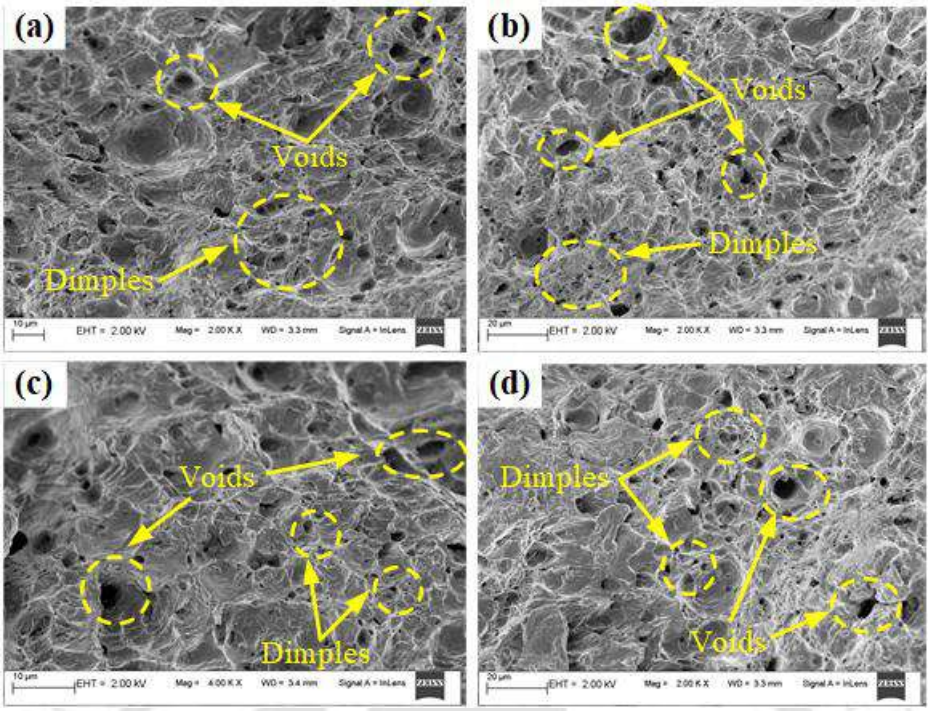

Fig. 4.16 *SEM morphologies of impact fractured surface of sample (a) S_1; (b) S_5; (c) S_7; and (d) S_{10}*

4.7 SUMMARY

This chapter discussed the joining of DH36 steel and AISI 1008 steel sheets using the FSW process. In this work, the influence of the rotational speed, traverse speed, and tool offset on temperature distribution, axial force, microstructure, and mechanical properties of the welded samples was investigated. The microstructure revealed the acicular-shaped bainitic ferrite in DH36 steel and Widmanstatten ferrite grains in AISI 1008 steel. It is observed that the rotational speed and traverse speed significantly influenced the temperature, microstructure, impact toughness, and hardness distribution in welded joints as compared to tool offset. The impact toughness and hardness are highly dependent on the grain size variation. Fig. 4.17 shows the influence of average grain size on impact toughness and average hardness values in the SZ at varying rotational speed and traverse speed.

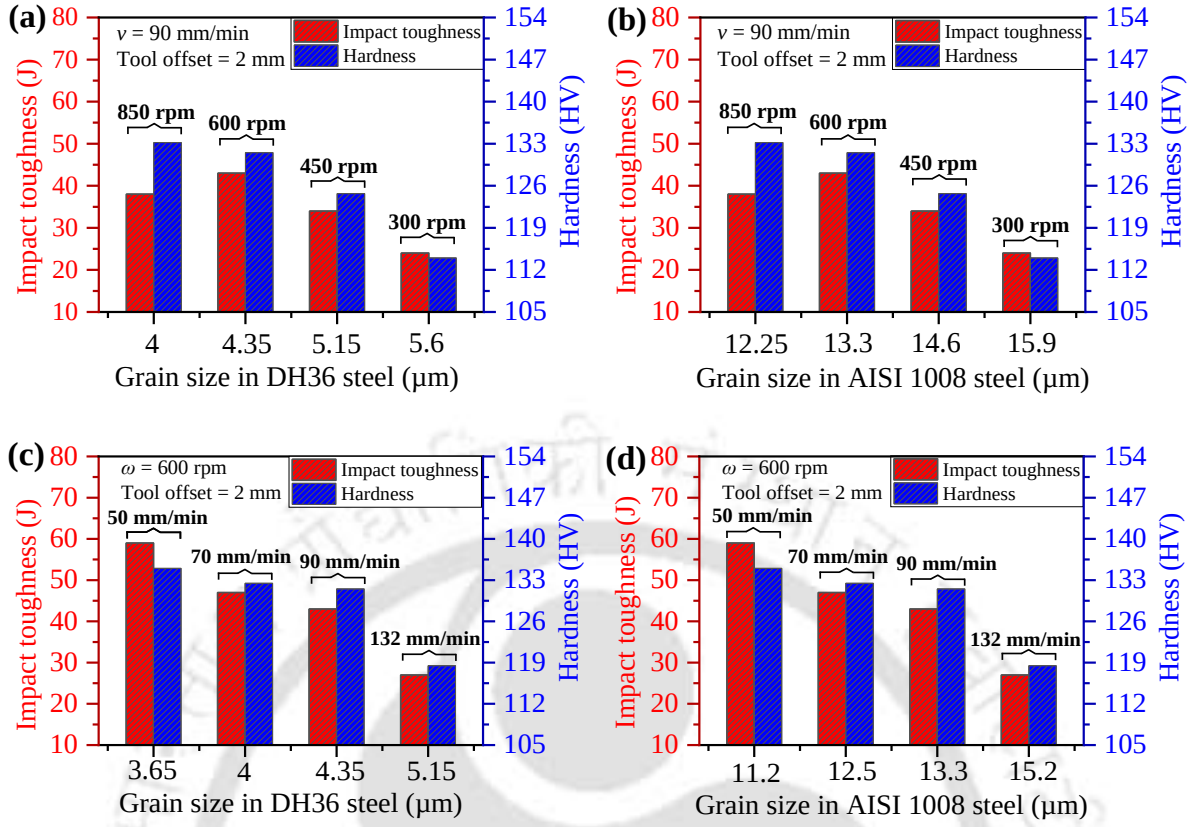

Fig. 4.17 *Influence of average grain size in SZ on impact toughness and hardness at varying (a,b) rotational speed; and (c,d) traverse speed*

It is observed that the AVG is reduced by increasing the rotational speed from 300 rpm to 850 rpm and decreasing the traverse speed from 132 mm/min to 50 mm/min, which led to improvement in the hardness values, as shown in Fig. 4.17. However, impact toughness increased with the decrease of AVG up to 4.35 µm in DH36 steel and 13.3 µm in AISI 1008 steel at a rotational speed of 600 rpm. Further increasing the rotational speed, i.e., 850 rpm generated the flash due to higher heat generation, which led to local thinning at the weld region. The local thinning effect is the dominating factor compared to fine grain size, which decreased the impact toughness value. Similarly, the impact toughness and hardness reduced due to grain refinement in the SZ with a decrease in traverse speed. At a lower traverse speed of 50 mm/min, the maximum impact toughness and hardness are obtained due to the minimum AVG of 3.65 µm in DH36 steel and 11.2 µm in AISI 1008 steel. By correlating the results of temperature, axial force, and mechanical properties, it can be concluded that lower axial force and high temperature increased the impact toughness and hardness. This is attributed to the enhancement of the plastic deformation in the SZ by increasing the tool rotational speed and reducing the traverse speed.

CHAPTER 5

NUMERICAL STUDY ON THE JOINING OF DISSIMILAR STEELS

The previous chapter included the experimental investigation of the FSW of dissimilar steels. The thermal history, axial force, metallographic behavior, and mechanical performance of the joints were discussed in detail. In the joining of high temperature alloys like steel, thermal-assisted hybrid FSW is the most convenient way to reduce the axial force and improve the tool life & weld quality. This chapter addresses the numerical investigation for comparing the thermal history between FSW and plasma-assisted FSW (PAFSW) of dissimilar steels, i.e., DH36 steel and AISI 1008 steel. The 3D transient thermal phenomenological models were established for FSW and PAFSW. The additional plasma arc heat source was modelled based on Gaussian heat flux distribution for PAFSW. Initially, the temperature distribution during the FSW at different process parameters was examined. Then, the consequence of FSW parameters (i.e., traverse speed and rotational speed) and preheating parameters (i.e., plasma offset and preheating current) on thermal history was investigated for a reliable comparative study. Based on the experimentally obtained feasible welding parameters, the calculated SZ isotherms and the transient thermal profiles were validated with experimental results. Furthermore, the effect of the preheating temperature on the axial force, microstructure, and mechanical properties (i.e., tensile strength, impact toughness, and hardness) was examined. The key outcomes drawn from this study are summarized at the end of this chapter.

5.1 THERMAL ANALYSIS OF THE FSW

The 3D heat transfer thermal modelling was performed to measure the thermal history during FSW of dissimilar steels, i.e., AISI 1008 steel and DH36 steel. The heat source is a critical aspect in measuring the thermal history during the FSW operation**.** In the present heat transfer FE model for FSW, the heat input based on the heat generation was applied as heat flux from the tool pin and tool shoulder. Table 5.1 represents the welding parameters, which are considered to predict their effect on thermal history during the FSW process.

Table 5.1 *Process parameters for the thermal modelling of the FSW process*

Sr. no.	Rotational speed (rpm)	Traverse speed (mm/min)	Shoulder diameter (mm)
1	300	70	
2	450	70	
3	600	70	25
4	450	50	
5	450	90	
6	450	130	
7	450	90	22
8	450	90	28

5.1.1 Temperature Distribution

The thermal simulation was performed in the two steps, such as the welding phase and the cooling phase. Fig. 5.1 shows the temperature contour of the dissimilar welded steels on the top surface at a rotational speed of 450 rpm with the traverse speed of 50 mm/min.

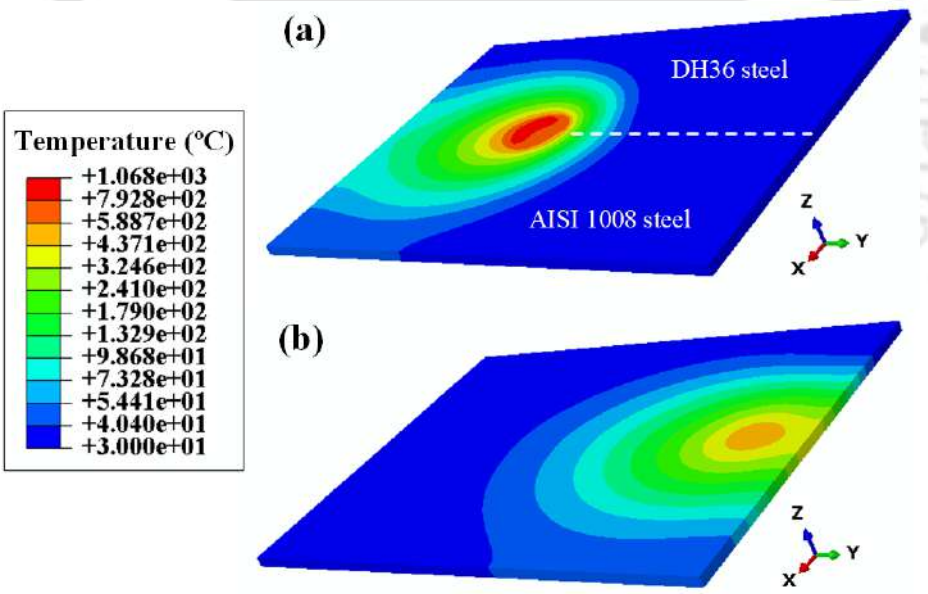

Fig. 5.1 *Temperature contour during (a) welding phase; and (b) cooling phase*

It was observed that the maximum temperature reached about 1068 °C during the welding phase, which was lesser than the melting point temperature of DH36 steel [183] and AISI 1008 steel [184]. Hence it is confirmed that the FSW is a solid-state welding process. The temperature decreased as going far from the weld centre line. Due to different thermo-physical properties, the temperature difference between the DH36 steel side and AISI 1008 steel side is observed. The heat generation is found higher in the trailing side of the DH36 steel side as

compared to the AISI 1008 steel. The heat dissipation in the AISI 1008 steel side is much faster than the DH36 steel side. Hence the thermal contours of the AISI 1008 steel side are wider than the DH36 steel side. A significant temperature difference between the top and bottom surface is observed, and the temperature starts to decrease as moving away from the weld centre line. To obtain the detailed thermal history during FSW, the temperature measuring points and line are shown in Fig. 5.2. Fig. 5.3 shows the peak temperature variation perpendicular to the welding direction at varying traverse speed with a constant rotational of 450 rpm.

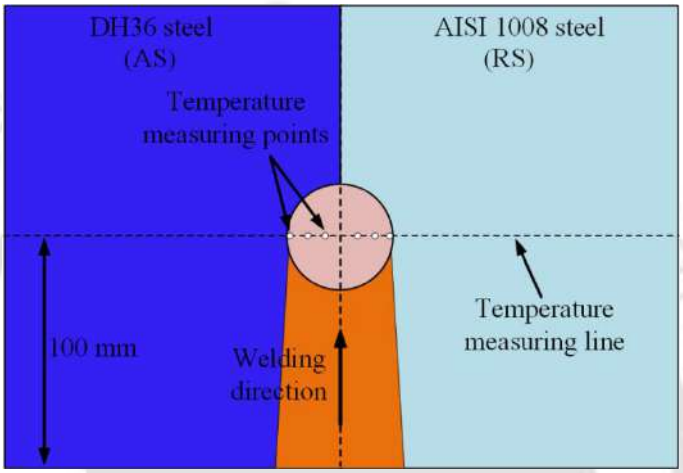

Fig. 5.2 *Temperature measuring positions on the top surface*

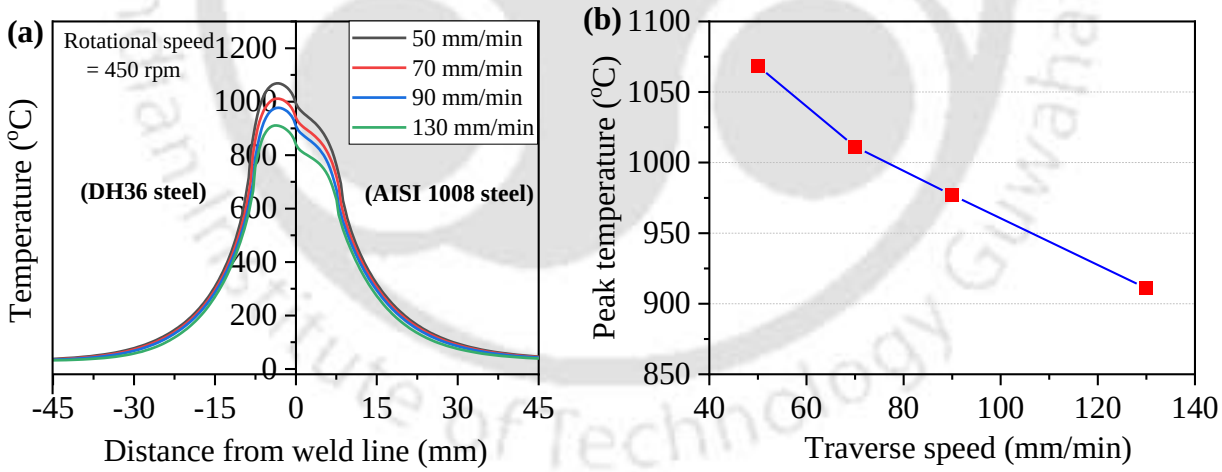

Fig. 5.3 *Influence of varying traverse speed on (a) peak temperature variation away from the weld centre line; and (b) peak temperature*

The asymmetric temperature distribution is observed in DH36 steel and AISI 1008 steel due to the different thermal properties of both steels, as shown in Fig. 5.3(a). The fastest temperature increment is obtained in the DH36 steel side due to its low thermal conductivity in comparison to the AISI 1008 steel. Consequently, the maximum temperature is observed on the DH36 steel side. It is also observed that increasing the traverse speed decreased the peak temperature, as shown in Fig. 5.3(b). This is caused by heat dissipation over a wider section of

the workpiece and lesser heat input at a higher traverse speed. Generally, the lower traverse speed reduces the vertical force subjected to the FSW tool due to the softening of the stirring material at a higher temperature. However, at the higher traverse speed, the tool generally stirs a comparatively harder material due to low heat in front of the tool, which results in a higher vertical force acting on the tool. Therefore, the thermal history is the essential aspect of the life of the FSW tool [55]. The maximum temperature at the same locations in the DH36 steel was 149.5 °C and 129.7 °C higher than AISI 1008 steel at 50 mm/min and 130 mm/min, respectively. The highest temperature increased by about 17.3% by reducing the traverse speed from 130 mm/min to 50 mm/min. Fig. 5.4 shows the transient temperature distribution at varying traverse speed in the AS and RS. The temperature is increased rapidly during the heating phase. As the heat source is moved far from the measuring locations, it starts to decrease gradually during the cooling step in transient thermal profiles, as shown in Fig. 5.4.

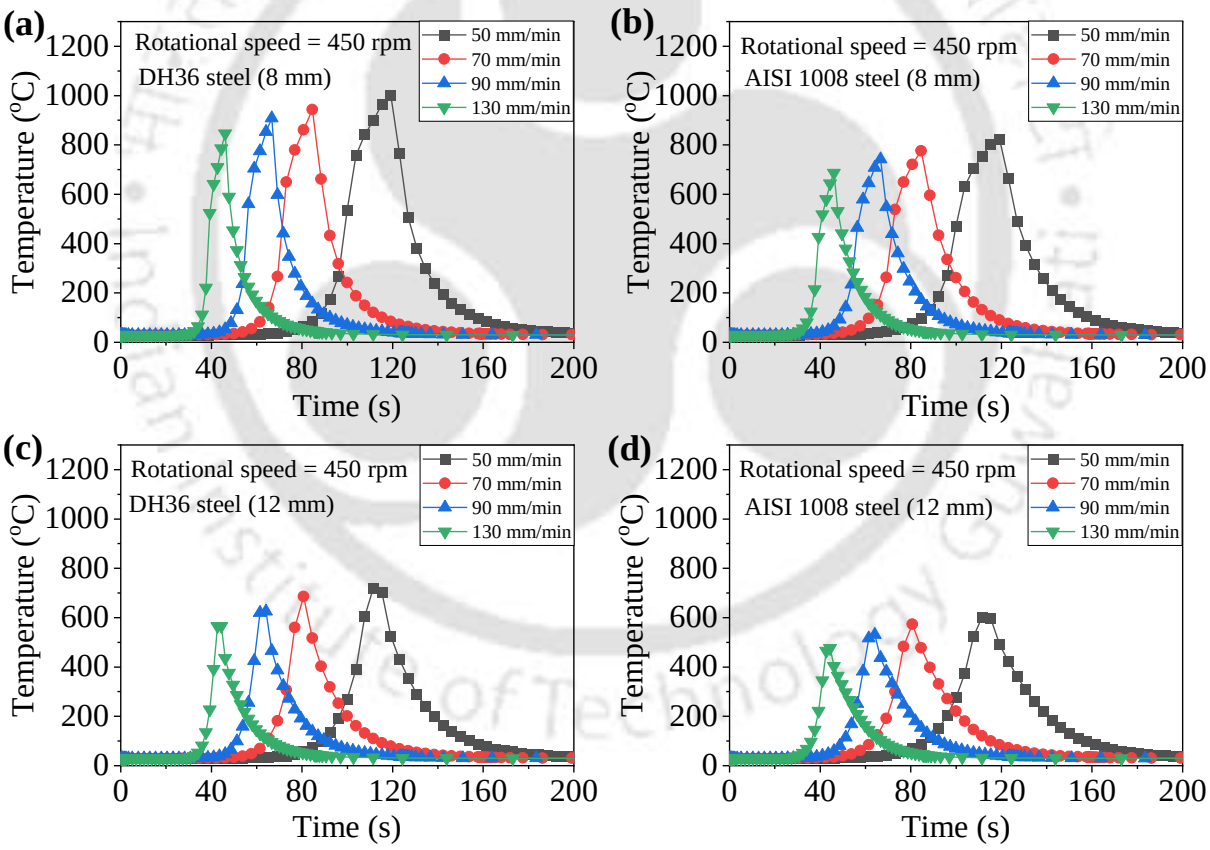

Fig. 5.4 *Transient temperature variation away from weld centre line at varying traverse speed at a distance of (a) 8 mm in DH36 steel; (b) 8 mm in AISI 1008 steel; (c) 12 mm in DH36 steel; and (d) 12 mm in AISI 1008 steel side*

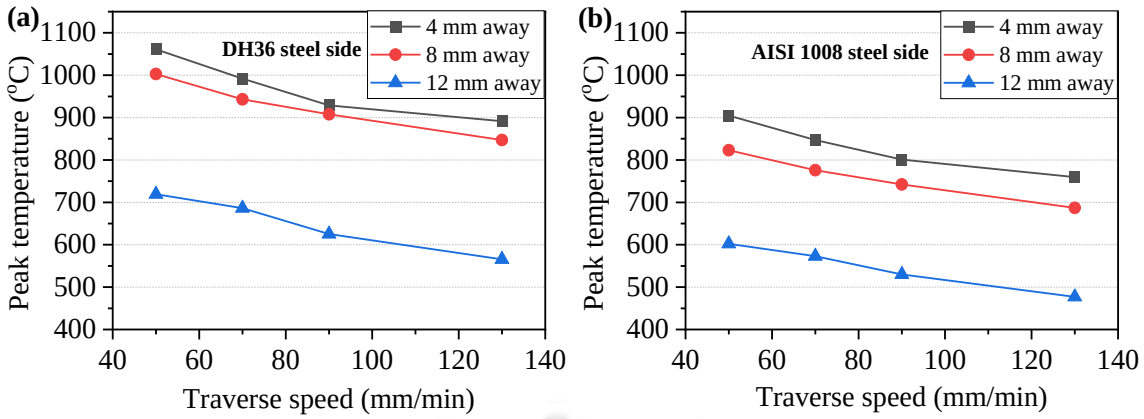

Fig. 5.5 *Influence of varying traverse speed on peak temperature in (a) DH36 steel; and (b) AISI 1008 steel side*

The higher traverse speed led to faster temperature change during the heating and cooling period. At the traverse speed of 50 mm/min, the DH36 steel side exhibited the peak temperatures of 1061.1 °C, 1002.8 °C, and 719.2 °C at 4 mm, 8 mm, and 12 mm far from the weld centre line, respectively, as shown in Fig. 5.5(a). However, the AISI 1008 steel side exhibited the peak temperatures lower than the DH36 steel side, i.e., 905 °C, 823 °C and 602.3 °C at 4 mm, 8 mm, and 12 mm away from the weld line, respectively, as shown in Fig. 5.5(b). The temperature values are significantly decreased by increasing the measuring distance from 8 mm to 12 mm. Fig. 5.6 shows the peak temperature distribution transverse to the weld interface at varying rotational speed with a constant traverse speed of 70 mm/min.

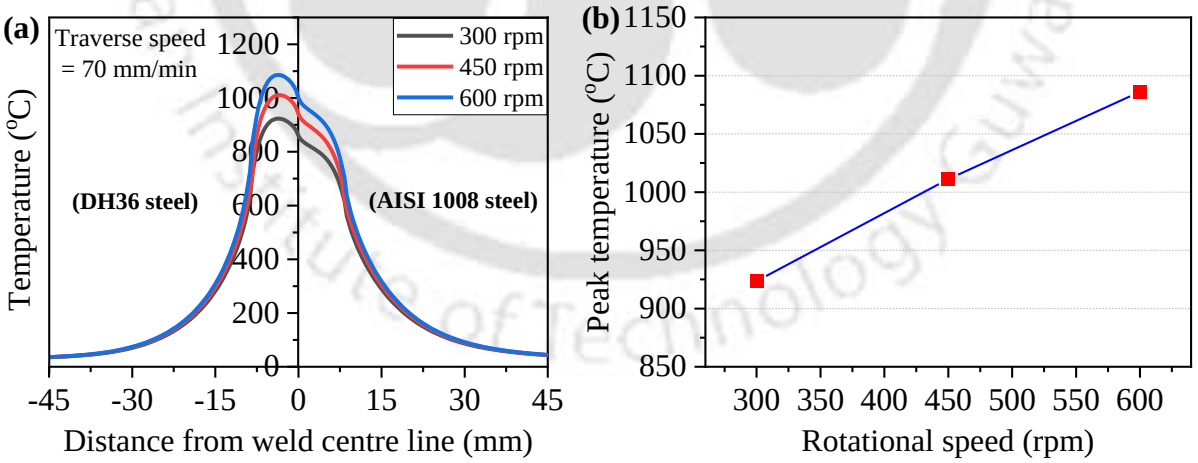

Fig. 5.6 *Influence of varying rotational speed on (a) peak temperature variation away from the weld centre line; and (b) peak temperature*

The high thermal conductivity of AISI 1008 steel promotes the additional heat loss to the backing plate, which resulted in a lower temperature in AISI 1008 steel, as shown in Fig. 5.6(a). In the AS, the maximum temperature values, i.e., 923.6 °C, 1011.2 °C, and 1086.1 °C are obtained at the rotational speed of 300 rpm, 450 rpm, and 600 rpm respectively, as shown in

Fig. 5.6(b). Therefore, the highest temperature increased by about 17.6% at the DH36 steel side by enhancing the rotational speed from 300 rpm to 600 rpm. This increase in the peak temperature is due to higher heat input resulting from the greater relative velocity at the tool/workpiece interface. At varying rotational speed, the peak temperature variation is similar to that reported for FSW of other materials, such as 304 austenitic stainless steel [131], dissimilar AISI 1008 and AISI 1078 steels [127], and 304 L stainless steel [128]. The maximum temperature in the DH36 steel is 149.5 °C and 129.7 °C higher than AISI 1008 steel at 300 rpm and 600 rpm, respectively. Fig. 5.7 shows the transient temperature distribution at varying rotational speed on the AS and RS.

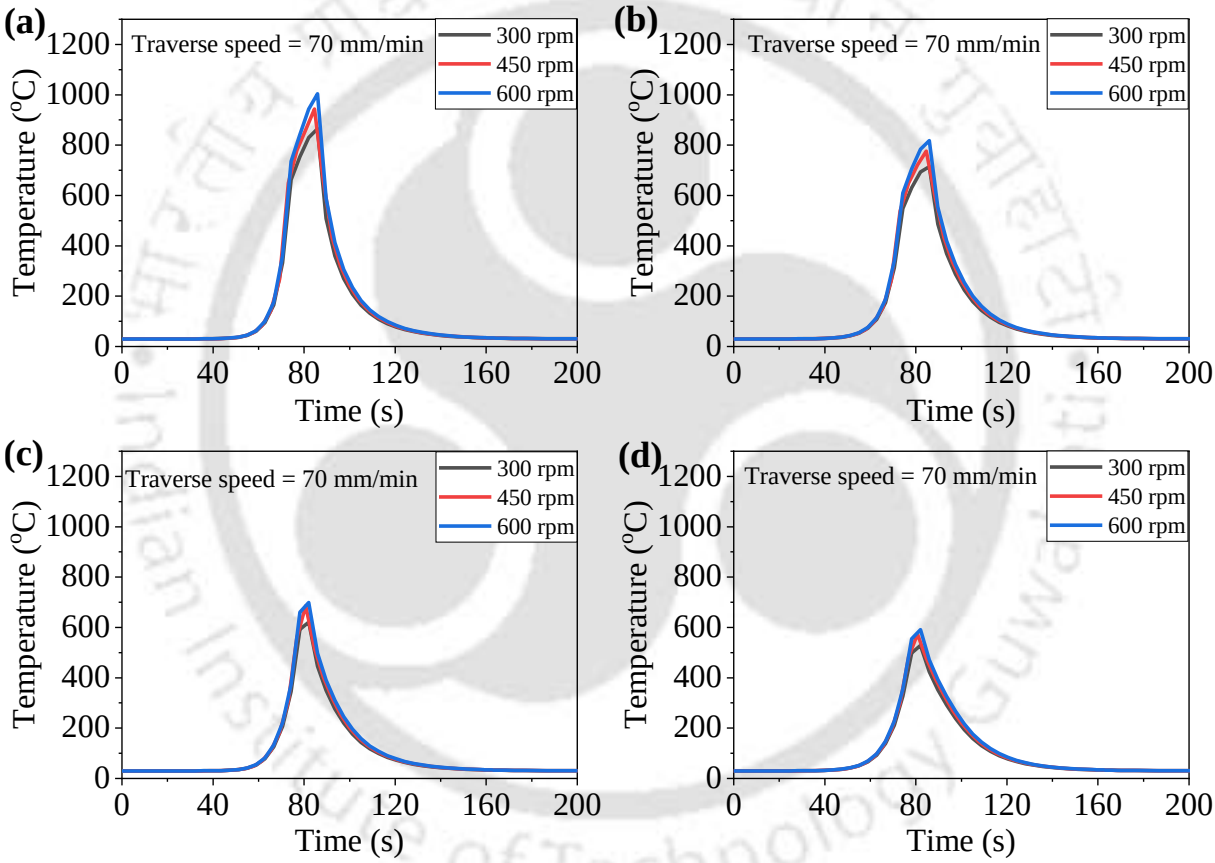

Fig. 5.7 *Transient temperature variation away from weld centre line at varying rotational speed at a distance of (a) 8 mm in DH36 steel; (b) 8 mm in AISI 1008 steel; (c) 12 mm in DH36 steel; and (d) 12 mm in AISI 1008 steel side*

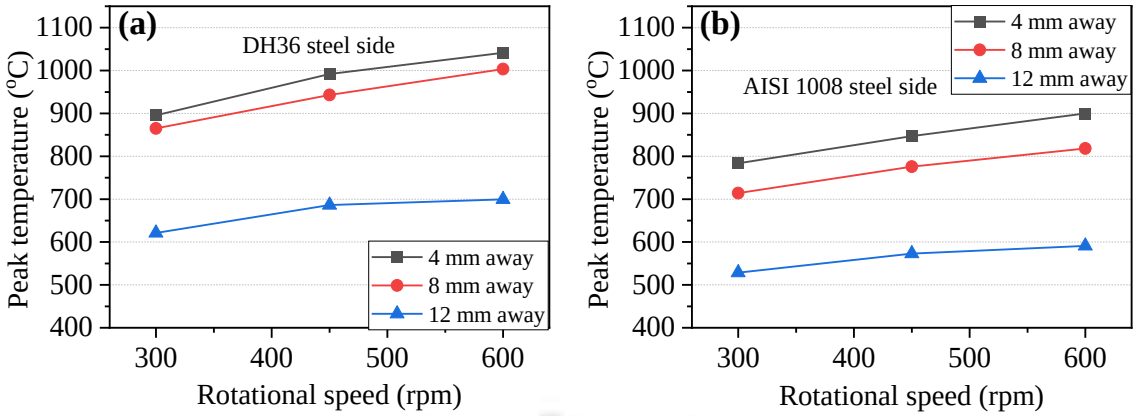

Fig. 5.8 *Influence of varying rotational speed on peak temperature in (a) DH36 steel; and (b) AISI 1008 steel side*

Increasing the rotational speed enhanced the peak temperature at 8 mm, and 12 mm distance from the weld centre line, as shown in Fig. 5.7. The rotational speed of 600 rpm produced the peak temperature, i.e., 141.5 °C, 185.1 °C and 108.6 °C higher than AISI 1008 steel side at 4 mm, 8 mm, and 12 mm respectively. In the DH36 steel side, the peak temperature is enhanced by 146 °C, 138.4 °C and 78.4 °C at 4 mm, 8 mm, and 12 mm by increasing the rotational speed from 300 rpm to 600 rpm, respectively, as shown in Fig. 5.8(a). However, it increased by 116.5 °C, 104.1 °C and 62.3 °C at 4 mm, 8 mm, and 12 mm in AISI 1008 steel with an increase of rotational speed from 300 rpm to 600 rpm, respectively, as shown in Fig. 5.8(b). Fig. 5.9 shows the temperature variation transverse to the weld direction at varying tool shoulder diameter.

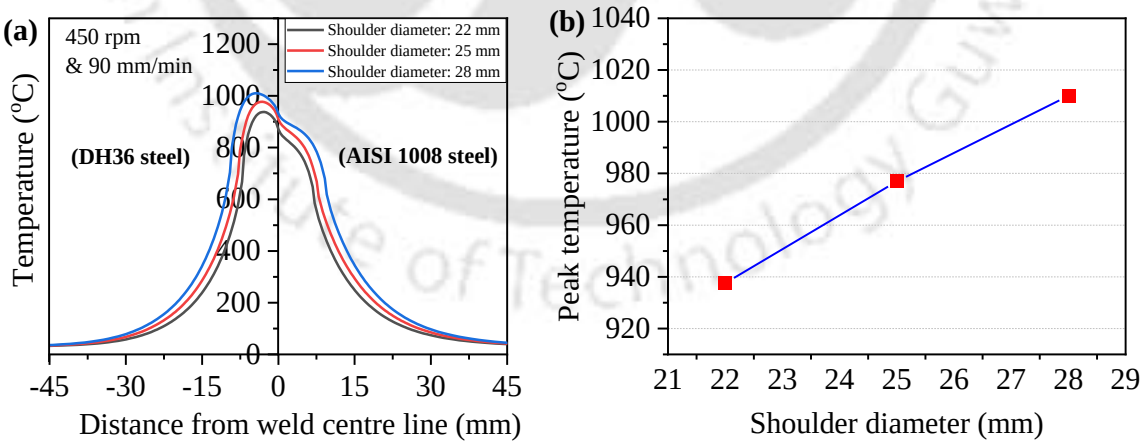

Fig. 5.9 *Influence of varying shoulder diameters on (a) peak temperature variation away from weld centre line; and (b) peak temperature*

The increase in the shoulder diameter increased the frictional contact area between the workpiece and shoulder, which led to an increase in peak temperature, as shown in Fig. 5.9. The peak temperature increased by around 7.7% when the shoulder diameter increased from

22 mm to 28 mm for the constant cylindrical pin diameter of 7 mm. The thermal history suggests the welding process parameters, i.e., rotational speed, traverse speed, and shoulder diameter need to be optimized for allowable temperature limits to improve the tool life and weld quality.

5.1.2 Validation of the Thermal Model

The transient temperature distribution was measured using K-type thermocouples connected with the data acquisition system at a rotational speed of 450 rpm with a traverse speed of 70 mm/min. The experimental transient thermal profiles in AISI 1008 steel side are compared with numerical results, as shown in Fig. 5.10.

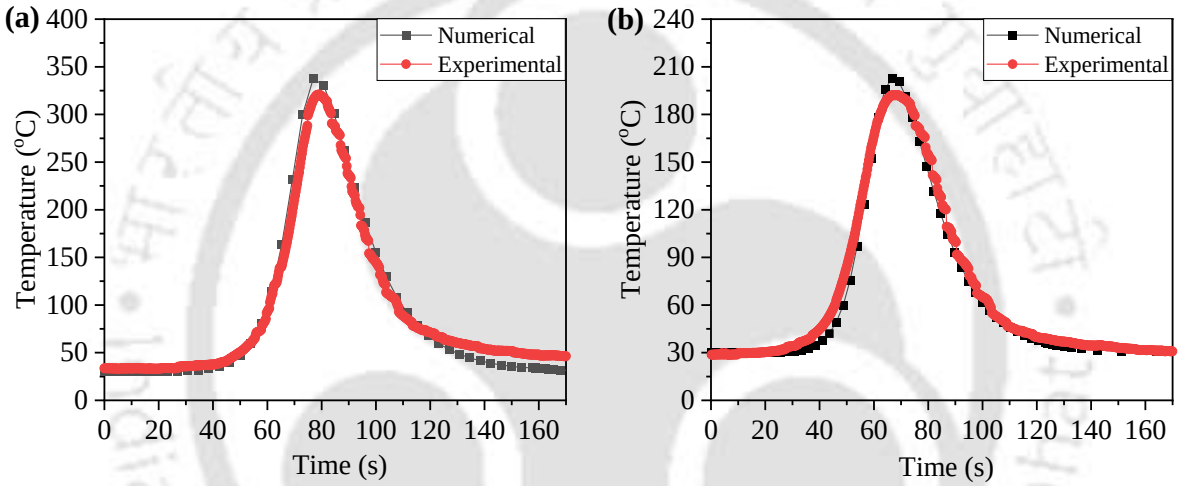

Fig. 5.10 *Comparison of FE and experimentally obtained thermal profiles at (a) 14 mm away; and (b) 16 mm away from the weld centre line*

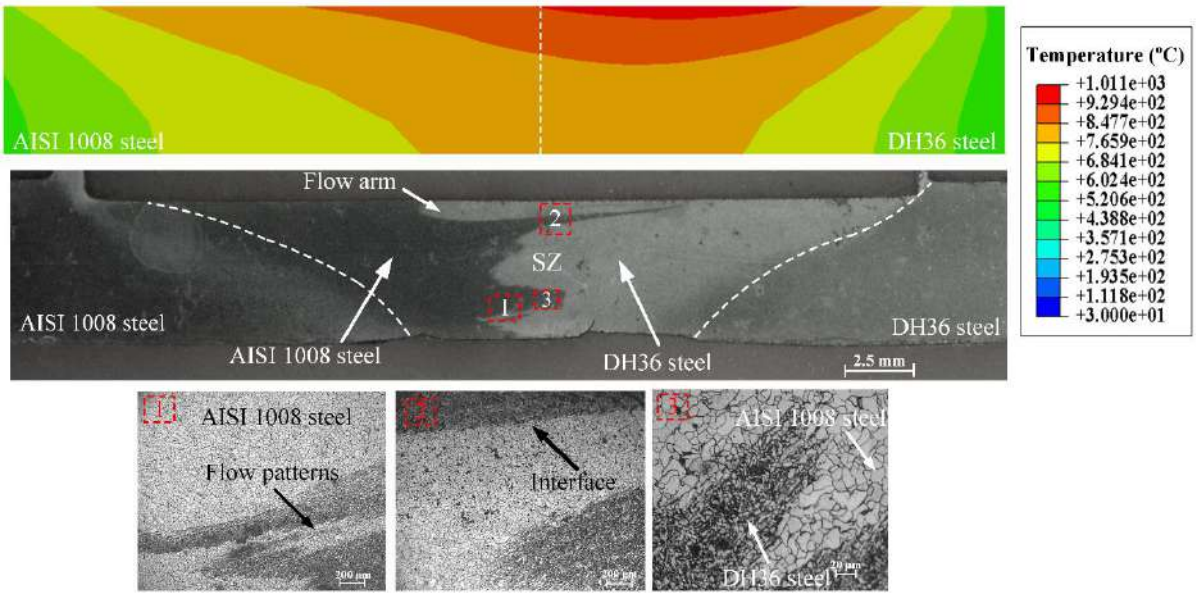

Fig. 5.11 *Numerical and experimentally obtained cross-sectional view of the welded sample at 450 rpm & 70 mm/min*

The transient thermal profiles obtained from FE analysis are matched reasonably well with the experiment for peak temperature with a maximum percentage error of 5.6%. There is also a good agreement between the calculated cross-sectional isotherm and experimentally measured micrographs of welded joints, as shown in Fig. 5.11. The temperature difference led to heterogeneity in macrostructure on the AS and RS of the welded sample. Furthermore, the flow arm region is formed at the top surface of the SZ since the higher heat generation at the top region facilitated the shoulder to drag the plasticized material from AS to the RS. The unmixed region contained the fine recrystallized grains in the SZ; however, the dissimilar steels are mechanically mixed and generated distinct flow patterns in the mixed zone.

5.2 COMPARATIVE STUDY OF THE FSW AND PAFSW

The 3D transient thermal phenomenological models for FSW and PAFSW were successfully established. The effect of traverse speed, rotational speed, preheating current, and plasma offset distance between the plasma source and the shoulder surface on the temperature distribution is investigated. The comparative study is performed based on the thermal history, vertical force, and mechanical and microstructural characterizations at different welding conditions. The process parameters for computing the thermal history in the numerical models of FSW and PAFSW are represented in Tables 5.2 and 5.3, respectively.

Table 5.2 *FSW process parameters*

Sr. no.	1	2	3	4	5	6	7
Rotational speed (rpm)	300	450	600	850		450	
Traverse speed (mm/min)			70		50	90	130

Table 5.3 *PAFSW process parameters*

Sr. no.	Rotational speed (rpm)	Traverse speed (mm/min)	Plasma offset (mm)	Preheating current (A)
1	300	70	8	20
2	450			
3	600			
4	850			
5	450	50		
6.		90		
7		130		
8	600	70	8	10
9				30
10	600	70	14	20
11			20	
12			30	

5.2.1 Thermal History

The temperature contour of plasma preheating of dissimilar steels at a current of 20 A and a traverse speed of 70 mm/min is shown in Fig. 5.12(a). Figs. 5.12(b) and 5.12(c) show the thermal contour of FSW & PAFSW at rotational speed, traverse speed, plasma offset, and current of 450 rpm, 70 mm/min, 8 mm, and 20 A, respectively. It is observed that preheating temperature of 685 ^{o}C enhanced the peak temperature of FSW from 1013 ^{o}C to 1079 ^{o}C. The thermal contour of plasma heating produced an oblong influence due to the continuous traverse movement with the FSW tool.

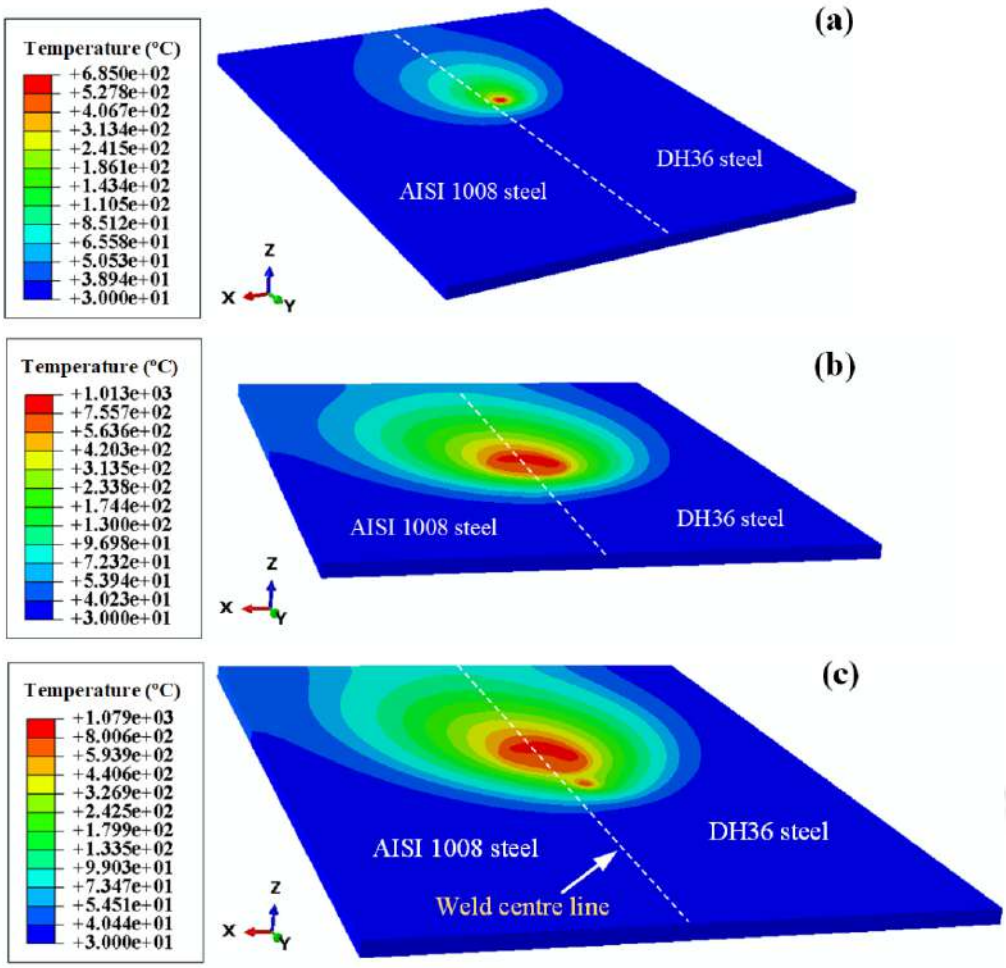

Fig. 5.12 *Temperature contour of (a) plasma preheating; (b) FSW; and (c) PAFSW*

The additional temperature zone generated near the FSW tool in the PAFSW process demonstrates that the plasma preheating at an offset distance of 8 mm can provide an opportunity for minimum welding defects. The welding phase is produced the maximum temperature lower than the melting temperature of AISI 1008 steel [184] and DH36 steel [183], which confirms the solid-state nature of the FSW and PAFSW process. The temperature decreased from the weld centre line in the transverse direction, which could be attributed to the heat loss through conduction to the backing plate, convection, and radiation.

5.2.1.1 Influence of Traverse Speed

Fig. 5.13 shows the calculated comparative peak temperature distribution between FSW & PAFSW in the transverse direction to the welding at varying traverse speed. The differential thermo-physical properties of both steels produced the temperature dissimilarity on the DH36 steel and AISI 1008 steel side, as shown in Fig. 5.13(a).

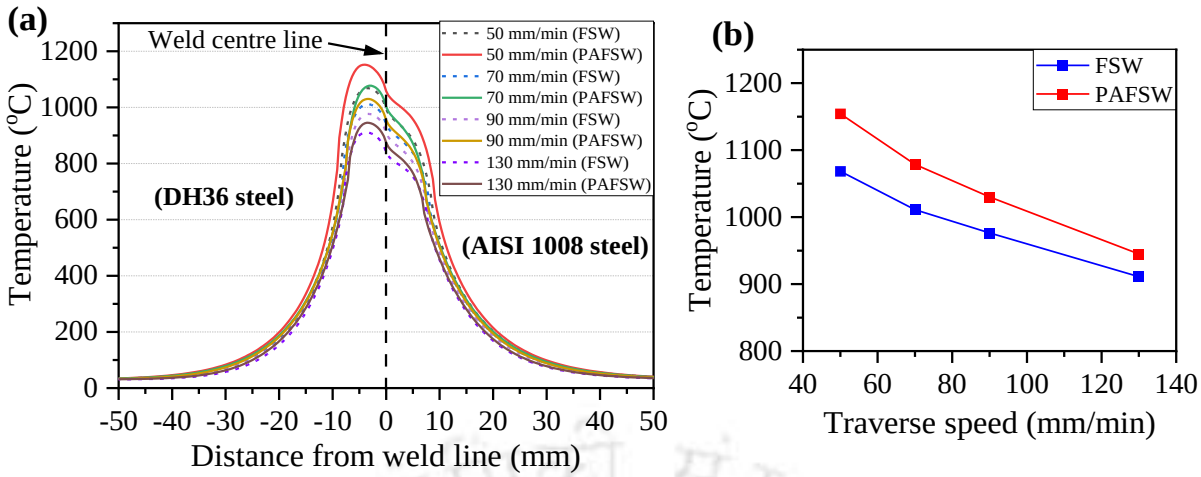

Fig. 5.13 *(a) Peak temperature distribution at varying traverse speed; and (b) peak temperature comparison between FSW & PAFSW*

The low thermal conductivity and the plasma assistance produced a higher temperature in the DH36 steel side than the AISI 1008 steel. Due to the higher heat input, the peak temperature trend in FSW & PAFSW increased with a decrease in traverse speed, as shown in Fig. 5.13(b). With the assistance of plasma arc, the DH36 steel experienced the maximum temperature of 133.7 °C and 171.5 °C greater than that of AISI 1008 steel at 130 mm/min and 50 mm/min, respectively. Compared to FSW, preheating assistance enlarged the peak temperature by 34.4 °C and 86 °C at 130 mm/min and 50 mm/min, respectively. This temperature increment on the harder material (DH36 steel) can provide the proper mixing of dissimilar steels by improving the material flow and heat generation. At the higher traverse speed, it is challenging for the tool to stir a harder material caused by the low temperature ahead of the tool, which results in a higher vertical force. Therefore, a preheating source is helpful in case of higher traverse speed conditions. The additional preheat source at higher traverse speeds can generate adequate heat input for sufficient dynamic recrystallization and fine-grained microstructure in the SZ [94]. Fig. 5.14 shows the temperature measuring points on the top weld surface. Figs. 5.15(a,b) and 5.15(c,d) show the temperature profiles at 5 mm and 10 mm distance transverse to welding direction in both steels, respectively.

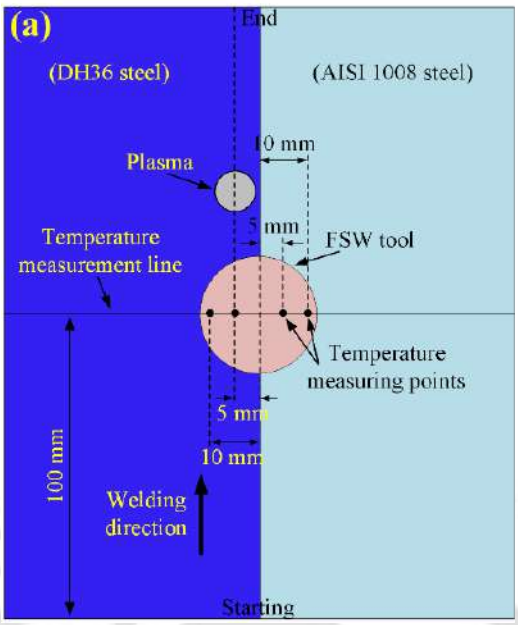

Fig. 5.14 *Temperature measuring positions on the top surface*

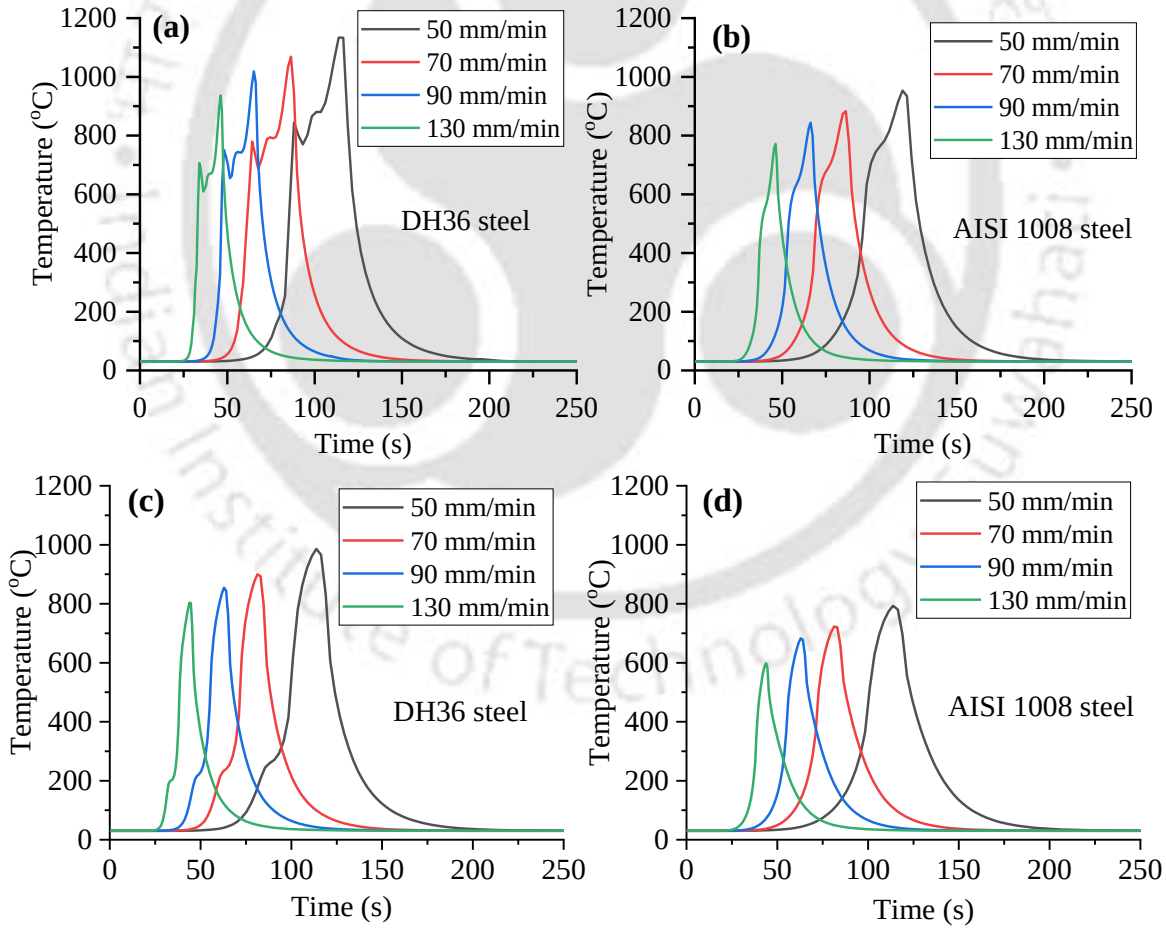

Fig. 5.15 *Transient thermal profiles in PAFSW at varying traverse speed at a distance of (a,b) 5 mm; and (c,d) 10 mm from weld centre line*

It is observed that the plasma preheating generated the higher transient temperature profiles on the DH36 steel side compared to the similar location at AISI 1008 steel, as shown in Fig. 5.15. The lower temperature in AISI 1008 steel is due to its high thermal conductivity, which promotes the additional heat loss to the backing plate. At 5 mm and 10 mm distances with a traverse speed of 50 mm/min, DH36 steel experienced a peak temperature of 180.4 ^{o}C and 192.8 ^{o}C greater than the AISI 1008 steel, respectively. This higher temperature in harder material (i.e., DH36 steel) can improve the tool life and weldability. Besides, transient thermal profiles show a sudden rise to the extreme temperature caused by the higher heat generation rate as the tool reached the measured points. Then the thermal profiles show the slow cooling rate as the tool moved away from the measured points. Fig. 5.16 shows the temperature distribution in the transverse direction at varying traverse speed with and without plasma preheating.

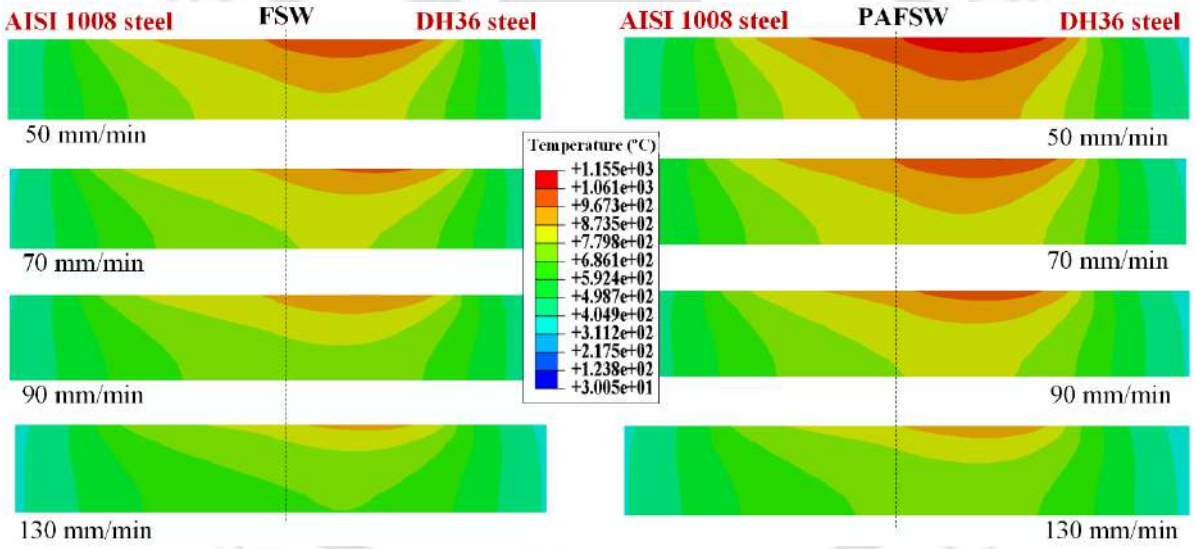

Fig. 5.16 *Transverse cross-sectional view at varying traverse speed*

The plasma preheating arc increased the temperature zone in the DH36 steel as compared to normal FSW, as shown in Fig. 5.16. The higher temperature in the SZ through the thickness direction generally improves the flow of plasticized material for the sound quality weld joint. The differential thermal properties of dissimilar steels are generated the asymmetric temperature distribution across the SZ. The maximum temperature is produced at the top surface compared to the bottom surface due to greater heat generation by friction at the workpiece/shoulder interface. However, the heat conduction through the backing plate in the thickness direction created a sharp temperature gradient. It is also observed that the isotherm size reduced by increasing the traverse speed from 50 mm/min to 130 mm/min due to low heat generation.

5.2.1.2 Influence of Rotational Speed

Fig. 5.17 shows the comparison between the peak temperature profiles of FSW & PAFSW at varying rotational speed. The addition of the plasma arc in front of the FSW tool produced the peak temperature of 141.2 ºC and 198 ºC greater in the DH36 steel compared to that of AISI 1008 steel at 300 rpm and 850 rpm, respectively.

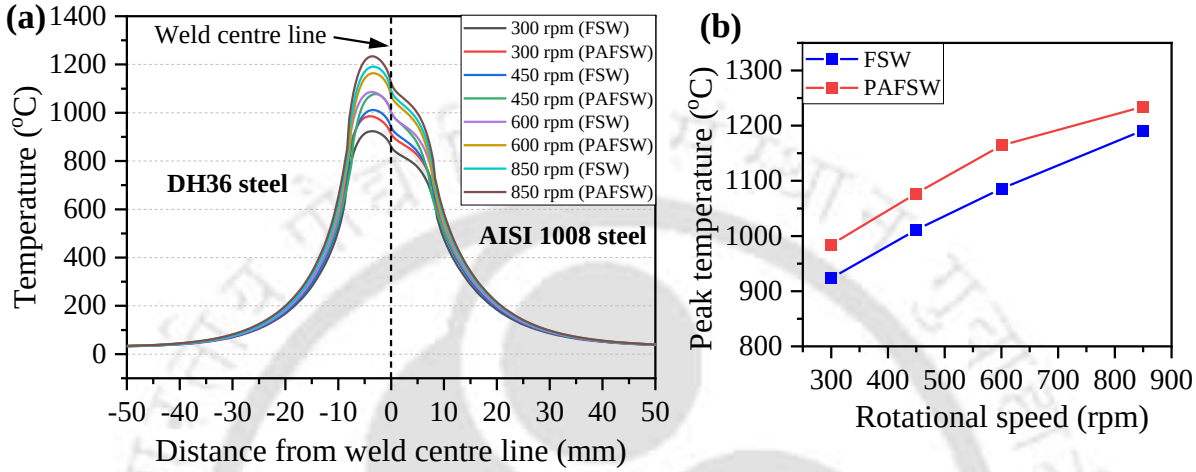

Fig. 5.17 *(a) Peak temperature variation from the weld centre line at varying rotational speed; and (b) peak temperature comparison between FSW and PAFSW*

The temperature increment due to the addition of preheating source increases the material plasticization and improves the mixing of dissimilar steels and weld quality [93]. With an increase in rotational speed from 300 rpm to 850 rpm, the temperature increased from 923.6 °C to 1191.2 °C without preheating, and 984.6 °C to 1234.4 °C with plasma preheating, as shown in Fig. 5.17(a). The maximum peak temperature difference (i.e., 78.25 ºC) between FSW & PAFSW is observed at a rotational speed of 600 rpm. In contrast, the peak temperature difference reduced at a rotational speed of 850 rpm, as shown in Fig. 5.17(b). Selvaraj et al. [129] also mentioned that peak temperature increased by enhancing the rotational speed up to a certain level. Further enhancing the rotational speed reduced the growth rate in peak temperature and then reached the steady state to constrain the maximum temperature limit within the liquidus temperature of the workpiece. The peak temperature distribution indicated that the traverse and rotational speed are more important parameters to control the temperature distribution in hybrid FSW of dissimilar steels.

Figs. 5.18(a,b) and 5.18(c,d) show the transient thermal profiles away from the weld centre line at 5 mm and 10 mm distance in both steels, respectively. The peak temperature enhanced with an increase in the rotational speed. At a distance of 5 mm and 10 mm, the DH36 steel exhibited the peak temperatures of 216.2 ºC and 203 ºC higher than the AISI 1008 steel,

respectively, as shown in Fig. 5.18. The difference in the welding temperature generally changes the plasticized flow behaviour and microstructural characterizations between the dissimilar steels. Fig. 5.19 shows the comparison of transverse cross-sections of weldments obtained by the FSW and PAFSW at varying rotational speed.

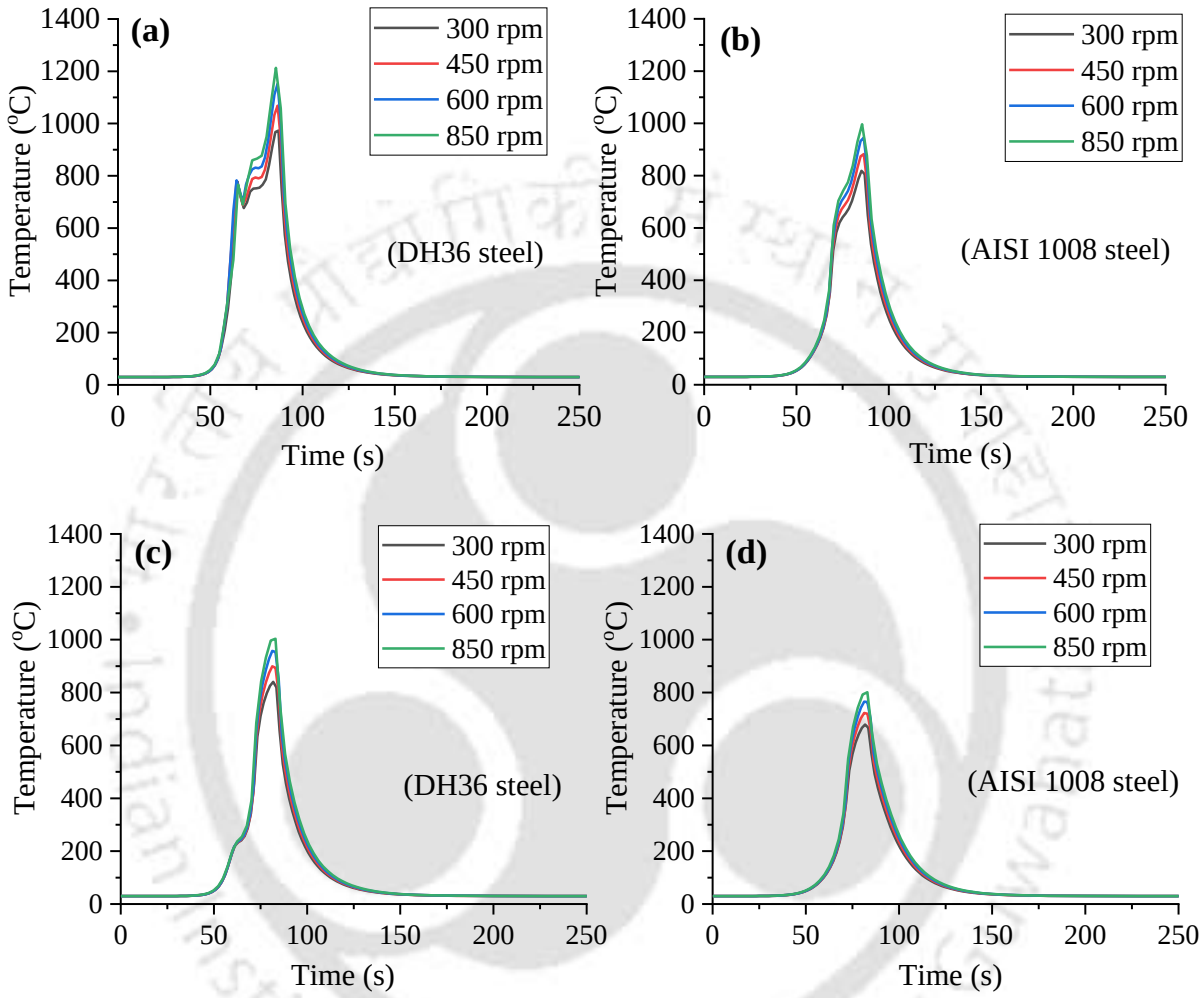

Fig. 5.18 *Transient temperature profiles in the PAFSW at varying rotational speed at a distance of (a,b) 5 mm; and (c,d) 10 mm from the weld centre line*

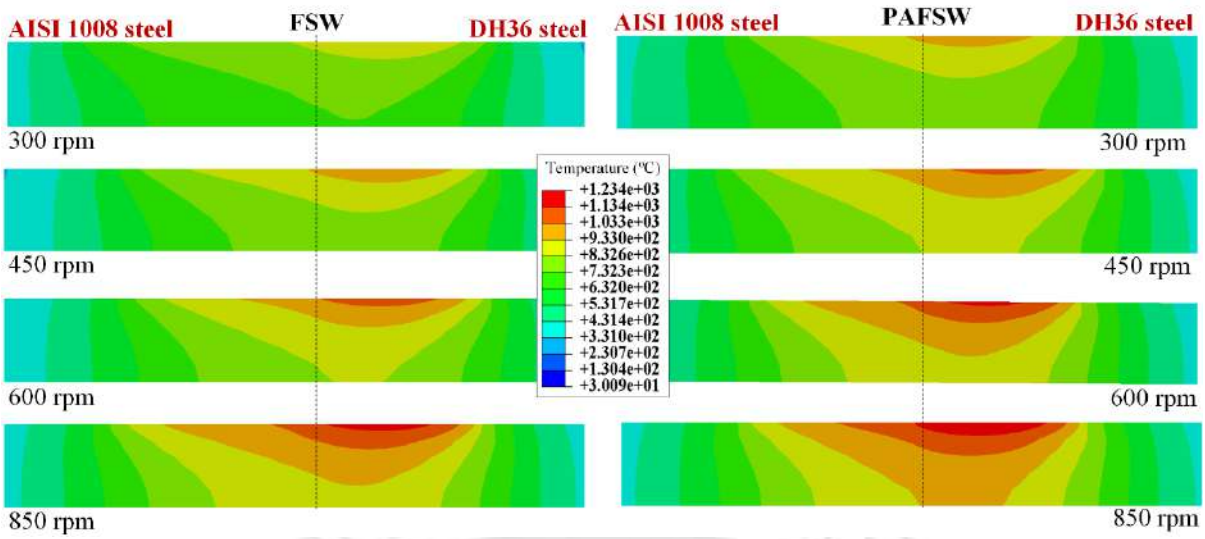

Fig. 5.19 *Transverse cross-sectional view at varying rotational speed*

Preheating assistance increased the temperature in the DH36 steel side (harder material), as shown in Fig. 5.19, which generally enhances the material flow from AS to RS and facilitates the appropriate mixing of the dissimilar steels. The size of the thermal isotherms increased due to higher heat generation with the application of plasma preheating. The wider temperature distribution is observed in AISI 1008 steel as a result of its high thermal conductivity, which leads to faster heat conduction on this side. With an increase in the rotational speed from 300 rpm to 850 rpm, the top surface (shoulder-affected region) is significantly enlarged caused by the higher frictional heat at the workpiece/shoulder interface.

5.2.1.3 Influence of Preheating Current

The effect of varying plasma preheating current on the peak temperature distribution during PAFSW is shown in Fig. 5.20. At 30 A, the maximum temperature difference between FSW and PAFSW on the DH36 steel is around 115 ^{o}C–125 ^{o}C, while it is lower, i.e., 90 ^{o}C–107 ^{o}C on the AISI 1008 steel side. The plasma arc with 30 A generated the peak temperature of 170 ^{o}C higher at the DH36 steel than the AISI 1008 steel. The peak temperature increased by 73.4 ^{o}C by increasing the current from 10 A to 30 A, as shown in Fig. 5.20(b). Increasing the preheating current can generate dynamically recrystallized refined grains in the SZ due to significant plastic deformation at higher heat generation [95].

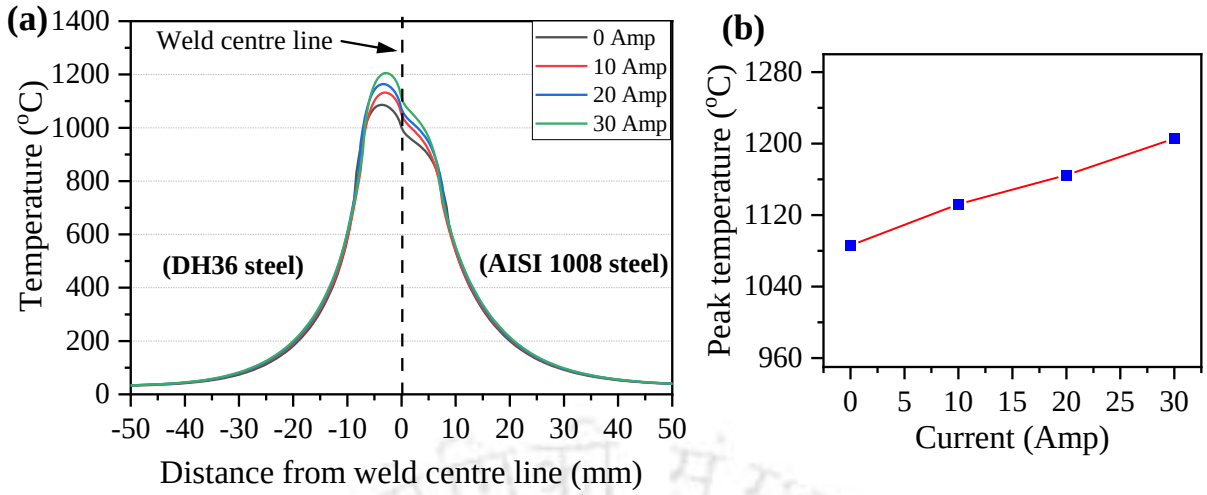

Fig. 5.20 *(a) Peak temperature variation at varying preheating current: and (b) peak temperature comparison between FSW and PAFSW*

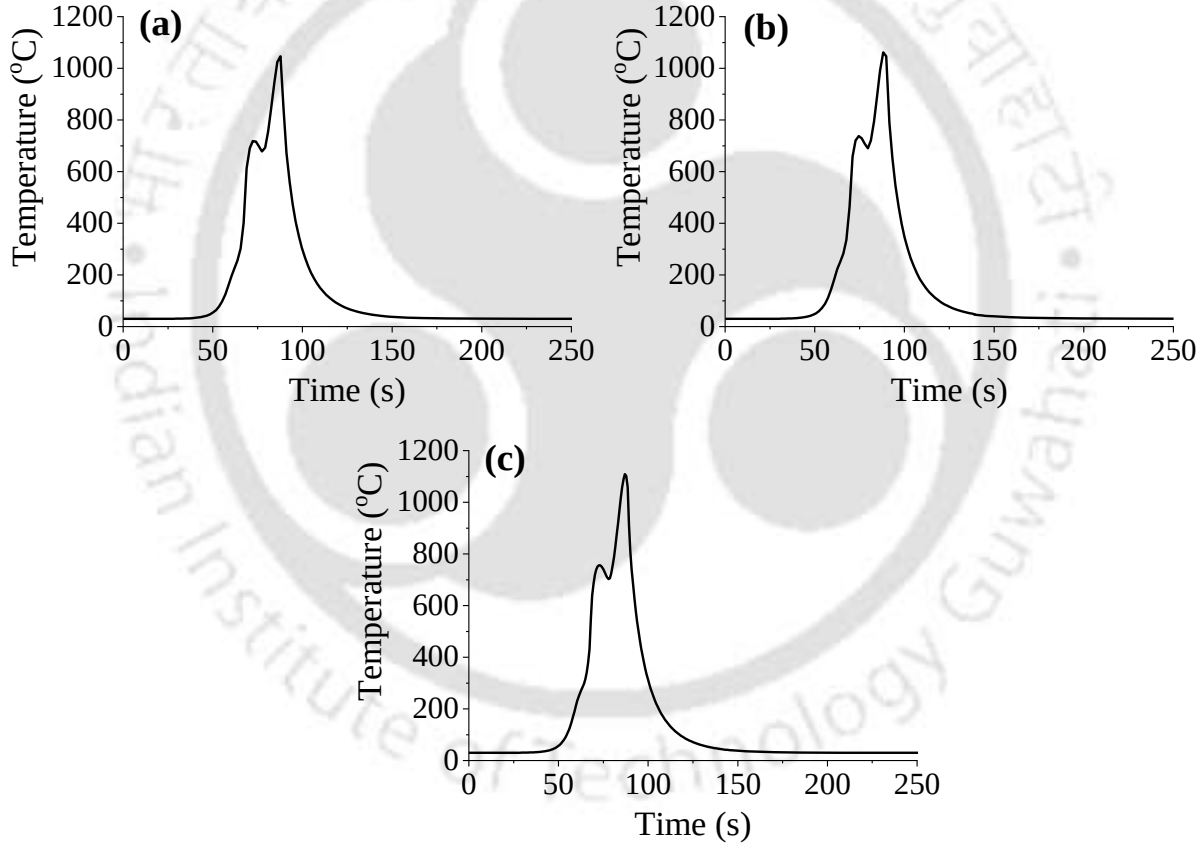

Fig. 5.21 *Transient temperature profiles at the weld centre line at varying preheating current: (a) 10 A; (b) 20 A; and (c) 30 A*

Increasing the preheating current from 10 A to 30 A enhanced the peak temperature from 1024.6 °C to 1108.7 °C at the weld centre during the PAFSW process, as shown in Fig. 5.21. It is observed that the influence of the preheating source is more significant on the harder material (DH36 steel), which is the requirement of FSW of high strength materials like steel to reduce the tool wear and improve the material flow behaviour. Yaduwanshi et al. [93] and Bang

et al. [79] reported that increasing the preheating current up to an optimum level reduced the formation of voids or tunnel defects in the SZ due to the uniform flow of plasticized material, further increasing the current reduced the weld quality.

5.2.1.4 Influence of Plasma Offset

The influence of varying the plasma offset distance in the PAFSW was investigated by keeping the other parameters constant, i.e., traverse speed, rotational speed, and current of 70 mm/min, 600 rpm, and 20 A, respectively. Varying the plasma offset from 8 mm to 20 mm showed not much difference in peak temperature, as shown in Fig. 5.22. The peak temperature is slightly reduced from 1164.8 ºC to 1147.3 ºC by changing the plasma offset from 8 mm to 20 mm. Further increasing the offset from 20 mm to 30 mm is significantly influenced the peak temperature, which decreased from 1147.3 ºC to 1116 ºC, as shown in Fig. 5.22(b). Ahmad et al. [99] investigated that the offset distance of 20 mm is suitable for laser preheating compared to other distances. They were observed reasonable temperature distribution and lower reaction force at a 20 mm offset distance during the hybrid FSW process. Fig. 5.23 shows the thermal contour of the PAFSW at varying plasma offset with constant rotational speed, traverse speed, and current of 600 rpm, 70 mm/min, 20 A, respectively.

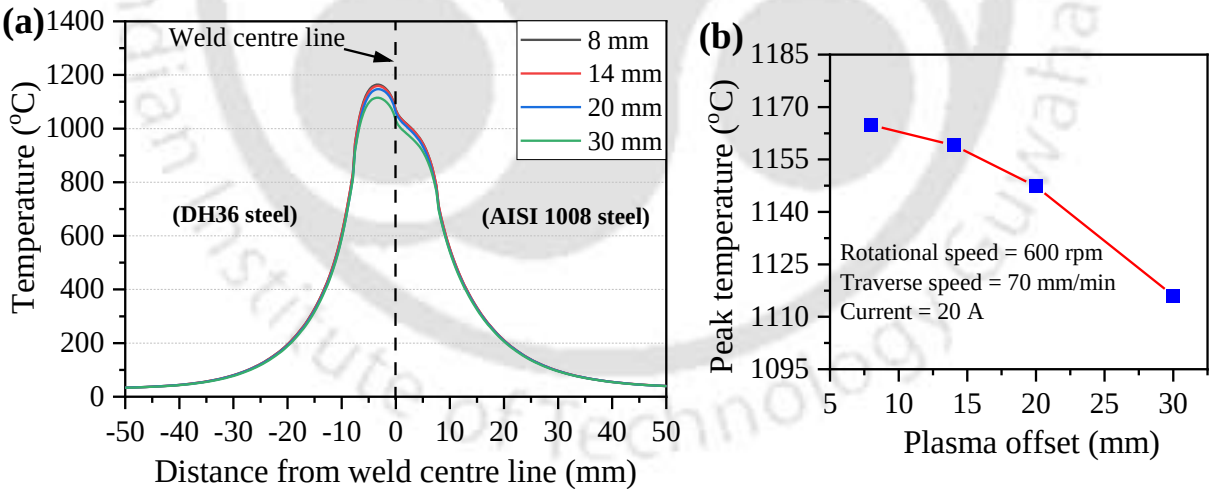

Fig. 5.22 *(a) Peak temperature variation from the weld centre line at different plasma offsets; (b) peak temperature comparison between FSW and PAFSW*

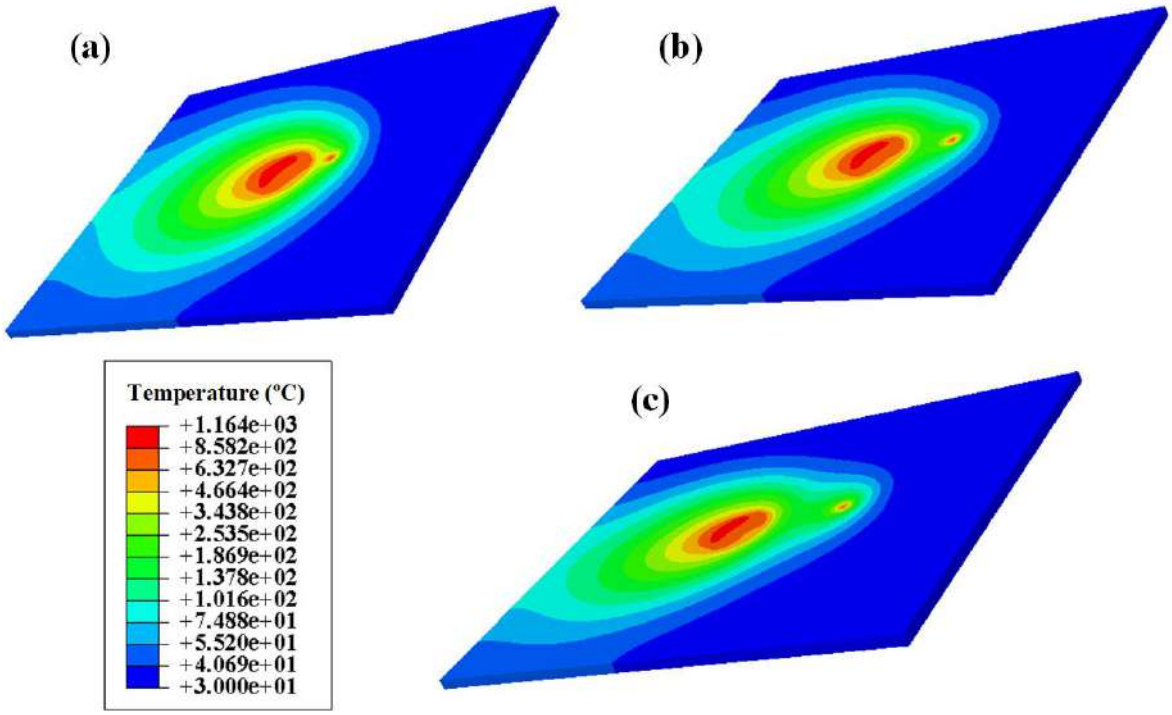

Fig. 5.23 *Thermal contour at varying plasma offset: (a) 8 mm; (b) 20 mm; and (c) 30 mm*

5.2.1.5 Validation of the Models

In this work, experiments of FSW & PAFSW were conducted to validate the developed FE models through thermal contour and thermal profiles at various positions transverse to the welding direction. Figs. 5.24(a) and 5.24(b) show the comparison of transient thermal profiles obtained from experimental and numerical results at a traverse speed, rotational speed, plasma offset, and current of 70 mm/min, 600 rpm, 8 mm, and 20 A for FSW and PAFSW, respectively.

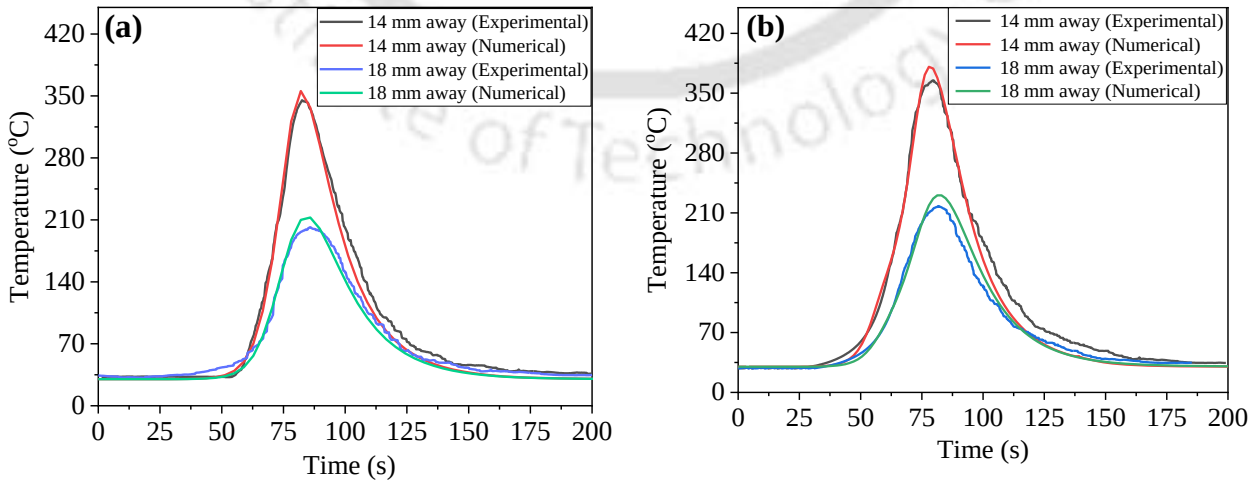

Fig. 5.24 *Comparison of experimentally and numerically measured transient thermal profiles of (a) FSW; and (b) PAFSW*

The developed numerical models were successfully verified with experimental results through transient thermal profiles with the maximum percentage error of 5.4% and 5.7% for peak temperature in the FSW and PAFSW, respectively. The excellent comparison reveals that the established 3D thermal model could be used to measure the transient temperature history during the FSW and PAFSW of dissimilar steels.

5.2.1 Axial Force, Microstructure and Mechanical Properties

The difference in welding temperature at different FSW & PAFSW parameters led to the change in axial force due to the variation in the yield/flow stress of the material. Fig. 5.25 shows the comparison of axial force variation between FSW and PAFSW at different welding parameters with a constant plasma offset of 8 mm.

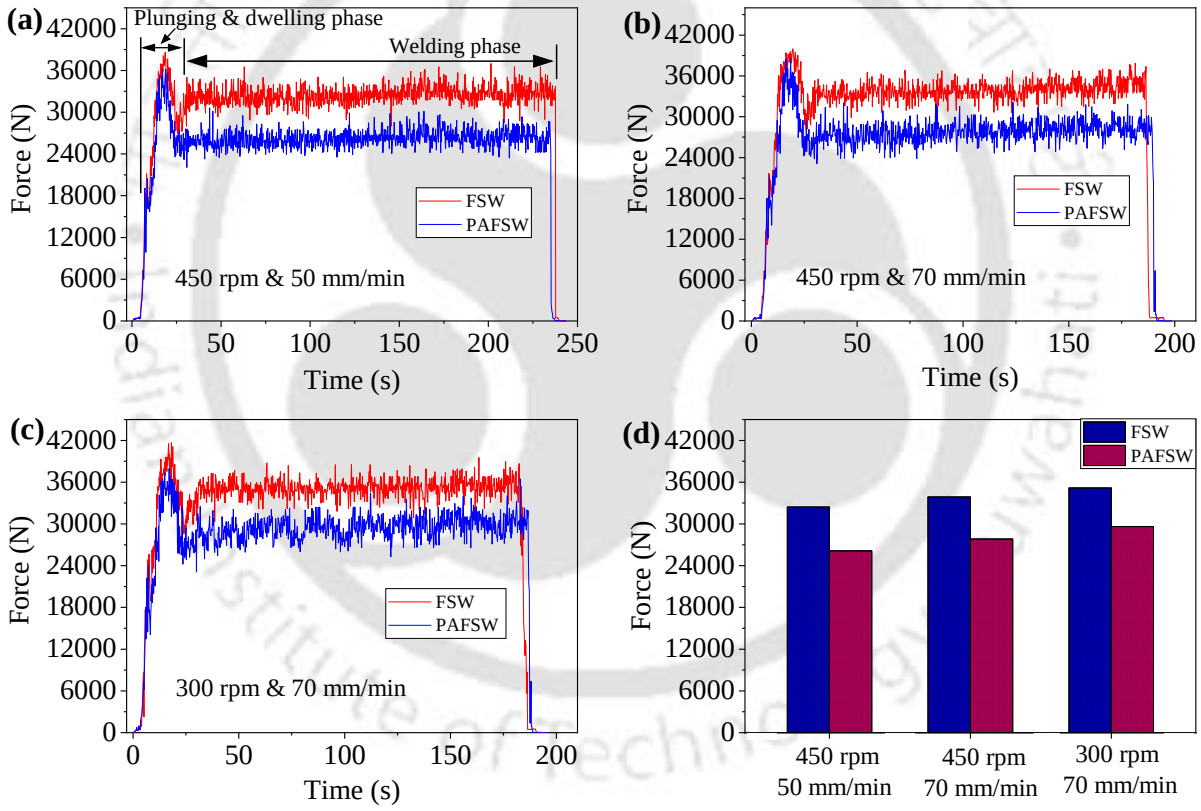

Fig. 5.25 *(a–c) Axial force variation in FSW and PAFSW at different parameters; and (d) comparison of average axial force between FSW and PAFSW*

As the tool shoulder comes into contact with the worksheets during the plunging phase, the axial force increases sharply. The plunging phase generated the maximum variation in the axial force caused by the absence of thermally softened material and the contact discrepancy between the tool and workpiece material. The higher frictional heat during the dwell phase reduced the axial force. The traverse phase then produced the axial force continuously in a

steady manner with minor fluctuations as the workpiece material adjacent to the tool sufficiently softened. The welding parameters, i.e., traverse and rotational speeds are significantly affected the axial force variation, as shown in Fig. 5.25. Furthermore, the plasma preheating reduced the average axial force by 15% to 20% during the welding phase, as shown in Fig. 5.25(d). The assistance of the preheating source made the material much warmer around the weld, which decreased the yield/flow stress of the dissimilar materials and reduced the axial force.

The macrographs of the FSW & PAFSW contained the three different regions, i.e., SZ, TMAZ, and HAZ on the AS and RS. The comparison of optical microstructure with an average grain diameter (AVG) in the SZ and TMAZ of FSW and PAFSW samples at a plasma offset of 8 mm is shown in Fig. 5.26.

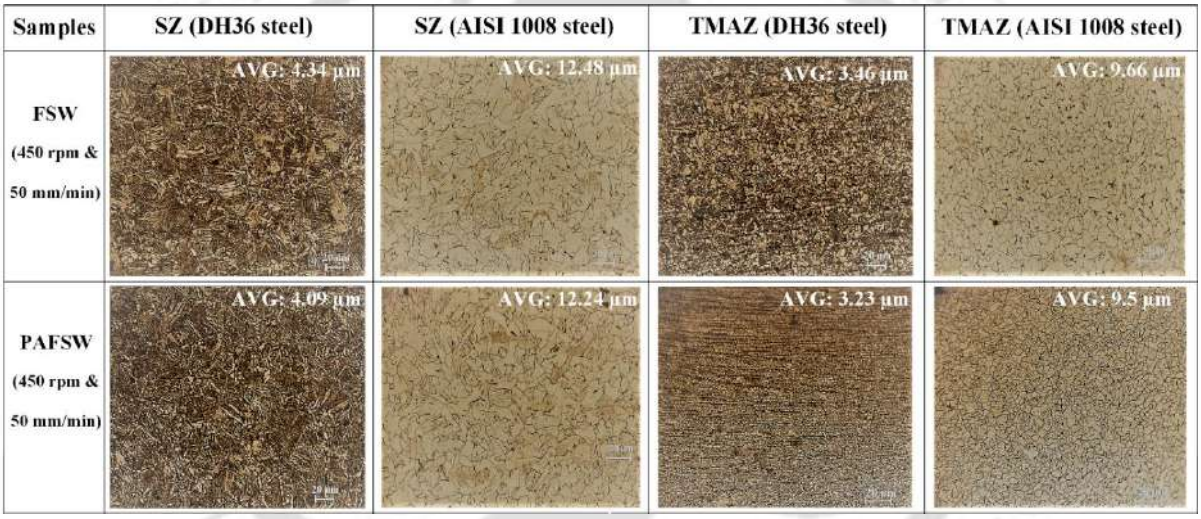

Fig. 5.26 *Comparison of the microstructure of SZ and TMAZ with AVG in the FSW and PAFSW*

It is observed that the PAFSW sample experienced a significant reduction in the AVG of SZ and TMAZ than the normal FSW, as shown in Fig. 5.26. In the PAFSW, the enhancement in plastic deformation induced the dynamic recrystallization and, subsequently, reduced the grain size. Sahu and Pal [185] also reported that higher plastic deformation and heat generation reduce the grain size by dynamic recrystallization in the FSW process. The grain size variation under the application of plasma preheating is significantly affected the mechanical properties, such as hardness and impact toughness of the welded samples.

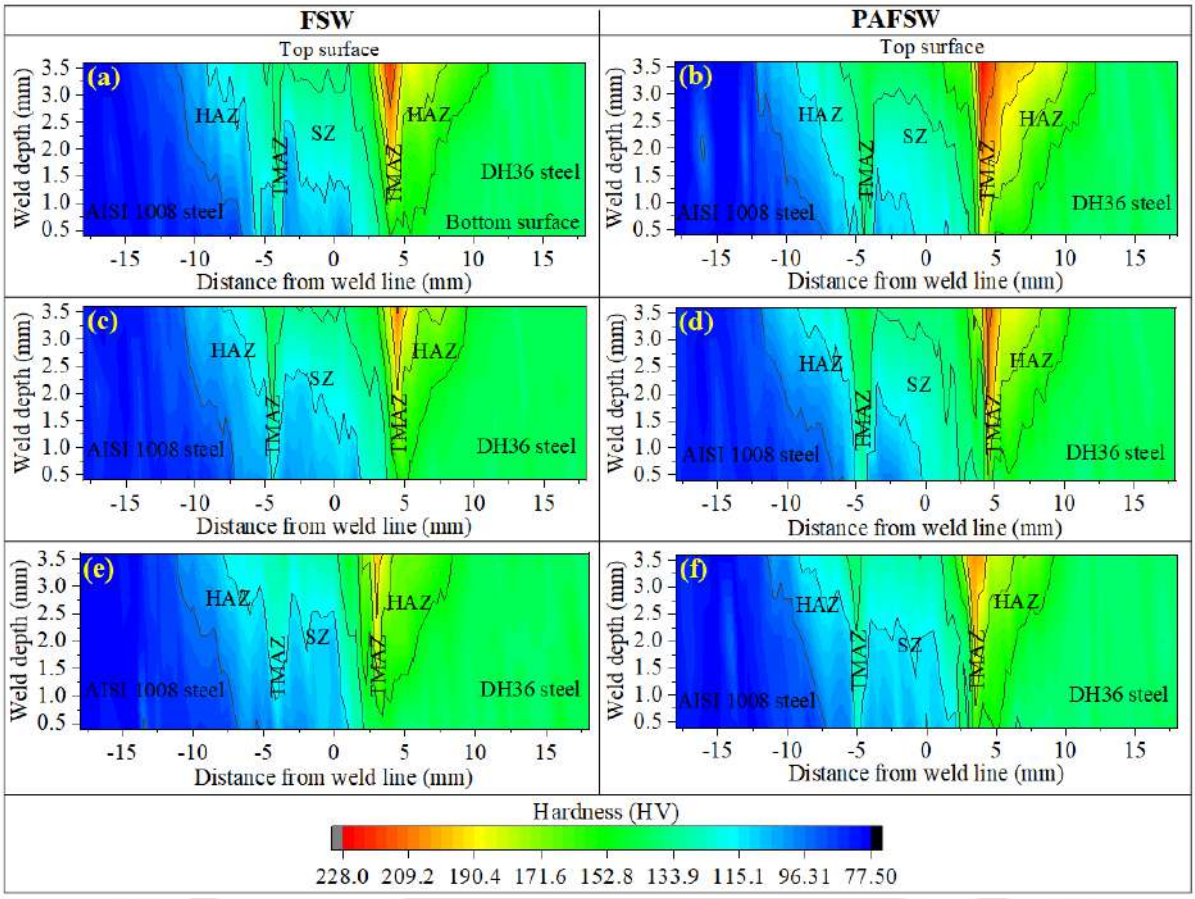

Fig. 5.27 *Microhardness contour in FSW and PAFSW samples at parameters: (a,b) 450 rpm & 50 mm/min; (c,d) 450 rpm & 70 mm/min; and (e,f) 300 rpm & 70 mm/min*

The plasma preheating assistance with FSW improved the hardness values as compared to that of normal FSW, as shown in Fig. 5.27, which is attributed to the refinement of the grains under temperature increment in PAFSW. The maximum hardness of 227.6 HV is experienced at 450 rpm & 50 mm/min in the TMAZ of the DH36 steel for PAFSW, whereas it is less, i.e., 221.4 HV for FSW. The hardness values are lower on the AISI 1008 steel side compared to the DH36 steel, as shown in Fig. 5.27. The higher hardness at the top surface is caused by the higher strain rate at the shoulder/workpiece interface due to greater frictional heat generation [49]. The fine-grained microstructure in the TMAZ produced the maximum hardness compared to that of SZ, which contained the coarse microstructure of acicular-shaped bainite ferrite and Widmanstatten ferrite in DH36 steel and AISI 1008 steel, respectively. The hardness heterogeneity is observed from the SZ to HAZ, which could be attributed to the formation of different flow patterns and microstructure variation. Figs. 5.28(a–c) shows the fractured tensile test samples, tensile strength, and impact toughness of the welded samples.

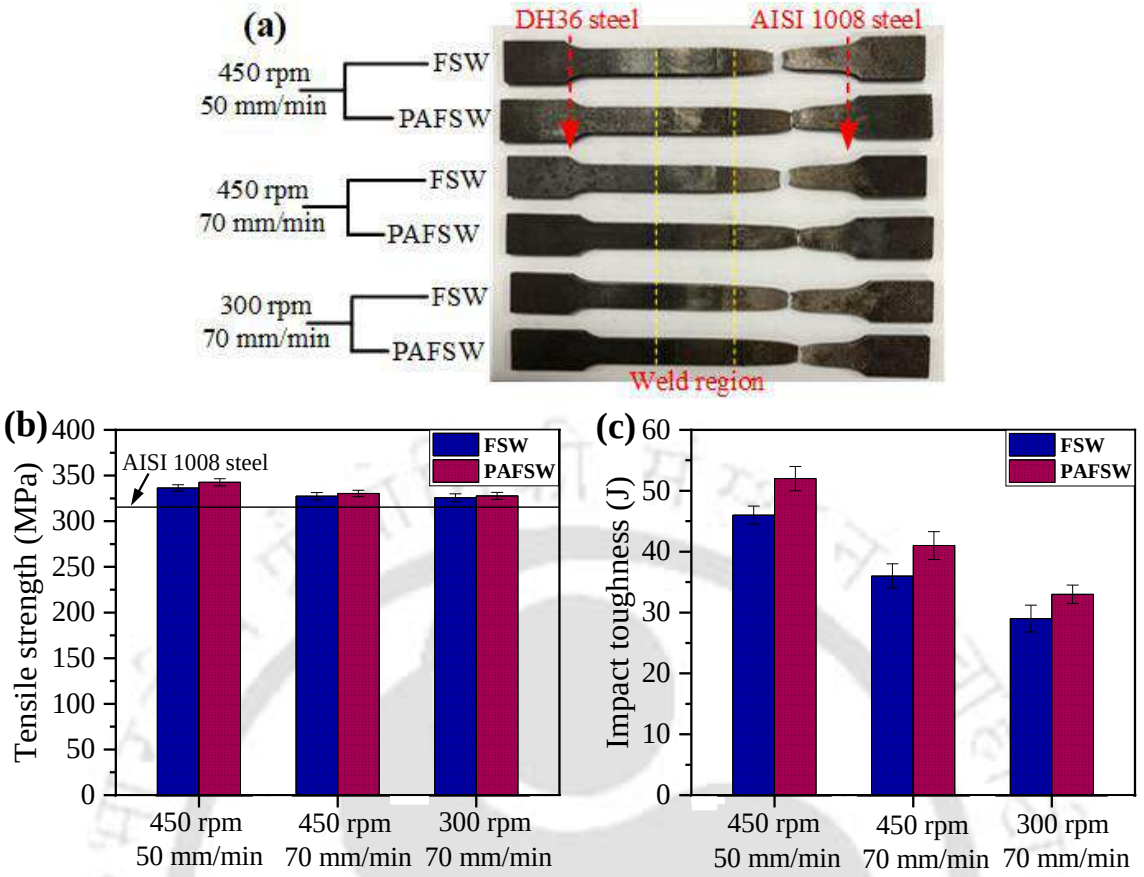

Fig. 5.28 *(a) Fractured tensile test samples; (b) tensile strength; and (c) impact toughness*

The FSW & PAFSW tensile samples are fractured by the side of the base material (AISI 1008 steel), as shown in Fig. 5.28(a). From the hardness contours, the base material (AISI 1008 steel) is found to be the softest part in the welded samples, which caused the tensile samples to be fractured in this region. The tensile strength of all samples is within the range of weaker base material (AISI 1008 steel) strength, as shown in Fig. 5.28(b). The PAFSW sample experienced the maximum tensile strength of 342.56 MPa at 450 rpm & 50 mm/min. The impact toughness values are increased with the application of plasma preheating, as shown in Fig. 5.28(c). Due to the higher grain refinement, the PAFSW produced the highest impact toughness of 53 J at 450 rpm & 50 mm/min, which is about 93% of the AISI 1008 steel and 13% higher than the FSW. The fractured surfaces of impact test samples are identified by using SEM to recognize the failure mode. Fig. 5.39 shows the comparison of the fractured surfaces in the FSW & PAFSW samples.

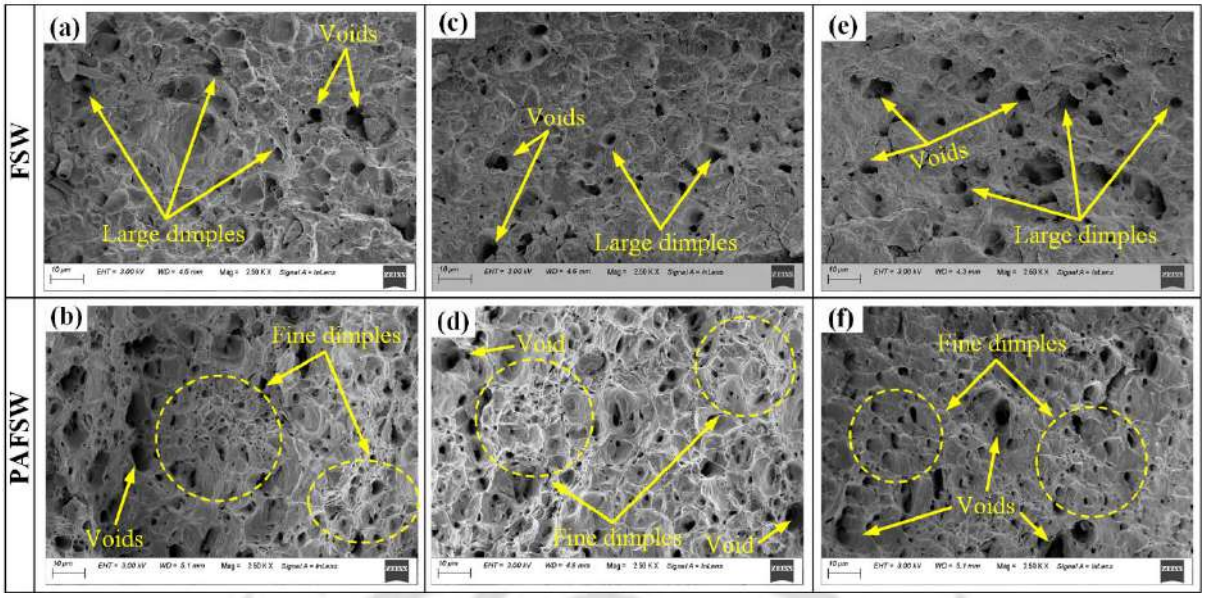

Fig. 5.29 *Comparison of impact fractured surfaces of FSW & PAFSW at parameters: (a,b) 450 rpm & 50 mm/min; (c,d) 450 rpm & 70 mm/min; and (e,f) 300 rpm & 70 mm/min*

The fracture surfaces of impact samples of FSW contained the deeper and lower population of dimples. On the other hand, a large amount of the smaller dimples/voids with different morphologies are found in the fractured surfaces of the PAFSW samples, as shown in Fig. 5.29. The fine dimples in PAFSW impact samples generally indicated comparatively higher impact toughness under sufficient plastic flow and heat generation. Yaduwanshi et al. [95] also found a large population of finer dimples in fractured surfaces of preheated FSW tensile samples, revealing relatively higher tensile strength than normal FSW. The random distribution of these voids/dimples in the fractured surfaces indicated the ductile fracture mechanism through the microscopic void coalescence.

5.3 SUMMARY

In this chapter, the comparison between FSW and PAFSW of dissimilar steels is discussed based on the thermal history obtained through the numerical analysis. The 3D transient thermal phenomenological models were established for FSW and PAFSW. The additional heat source, i.e., plasma arc heat source was modelled using the Gaussian distribution of heat flux. For the reliable comparative study, the effect of FSW parameters (i.e., traverse speed and rotational speed) and preheating parameters (i.e., plasma offset and preheating current) on thermal history was investigated. The calculated SZ isotherms and the transient thermal profiles in the FSW and PAFSW are matched fairly well with experimental results. Furthermore, the effect of the preheating temperature on the axial force, microstructure,

and mechanical properties (i.e., tensile strength, impact toughness, and hardness) was examined.

The isotherms and transient thermal profiles of developed 3D heat transfer models for both FSW and PAFSW are successfully validated with experimental results with a maximum percentage error of 5.4% and 5.7% for peak temperature in the transient thermal profiles, respectively. In the PAFSW process, increasing the preheating current & rotational speed and reducing the traverse speed enhanced the magnitude of peak temperatures, which is attributed to the higher heat generation. Increasing the plasma offset distance from the tool shoulder surface reduced the peak temperature. In the PAFSW, the additional preheating source is significantly reduced the average axial force by around 15% to 20% during the welding period. It is also observed that the assistance of the plasma preheating ahead of the FSW tool is significantly improved the hardness and impact toughness values compared to normal FSW, which could be attributed to the refinement of grains under higher heat generation. The tensile weld samples are fractured in the base material zone (i.e., AISI 1008 steel) and experienced tensile strength within the range of the AISI 1008 steel.

CHAPTER 6

EXPERIMENTAL STUDY ON THE JOINING OF DH36 STEEL AND ALUMINUM ALLOY

Chapters 4 and 5 presented the experimental and numerical investigation of FSW of dissimilar steel, i.e., DH36 steel and AISI 1008 steel. On the track of accomplishing the objectives, the study is progressed with the investigation of dissimilar FSW of steel and Al alloy. Accordingly, the current chapter includes the experimental analysis of the dissimilar FSW of DH36 steel and AA6061. In the dissimilar joining of steel and Al alloys, the tool offset is also crucial similar to tool rotational and traverse speeds. It significantly affects the IMCs formation and weld quality by controlling the heat generation and mixing of the dissimilar materials. In this work, the tool pin was shifted towards the soft material, i.e., AA6061 at various distances with constant rotational speed and traverse speed. The tool offset conditions were analyzed based on the macro/microstructure, IMCs formation in various regions, and mechanical properties of the welded joints. The weld characteristics were identified through SEM, optical microscope, EDS, and XRD analysis. A thorough analysis of fractured surfaces of tensile samples and Vickers microhardness are also presented in this chapter. Finally, the important outcomes of this experimental study are summarized at the end of this chapter.

6.1 PROCESS PARAMETERS

In this work, the DH36 steel and AA6061 sheets were joined using the FSW technique. Based on the trial and error procedure, the optimum rotational speed and traverse speed were chosen by conducting the preliminary experiments. Initially, trials were performed at a constant traverse speed to find the optimal rotational speed. Afterward the visual inspection and macro/micrographic analysis of the initial weldments, further trials proceeded to obtain the optimal traverse speed at a constant rotational speed. Finally, from the repetitive experiments, the rotational speed of 875 rpm with a traverse speed of 90 mm/min was chosen to perform the comprehensive research on the tool offset conditions. A constant tool tilt angle of 2^{o} was used for all the experiments. The selected working range of the tool pin offset values with a constant rotational speed of 875 rpm and traverse speed of 90 mm/min are shown in Fig. 6.1 and Table 6.1.

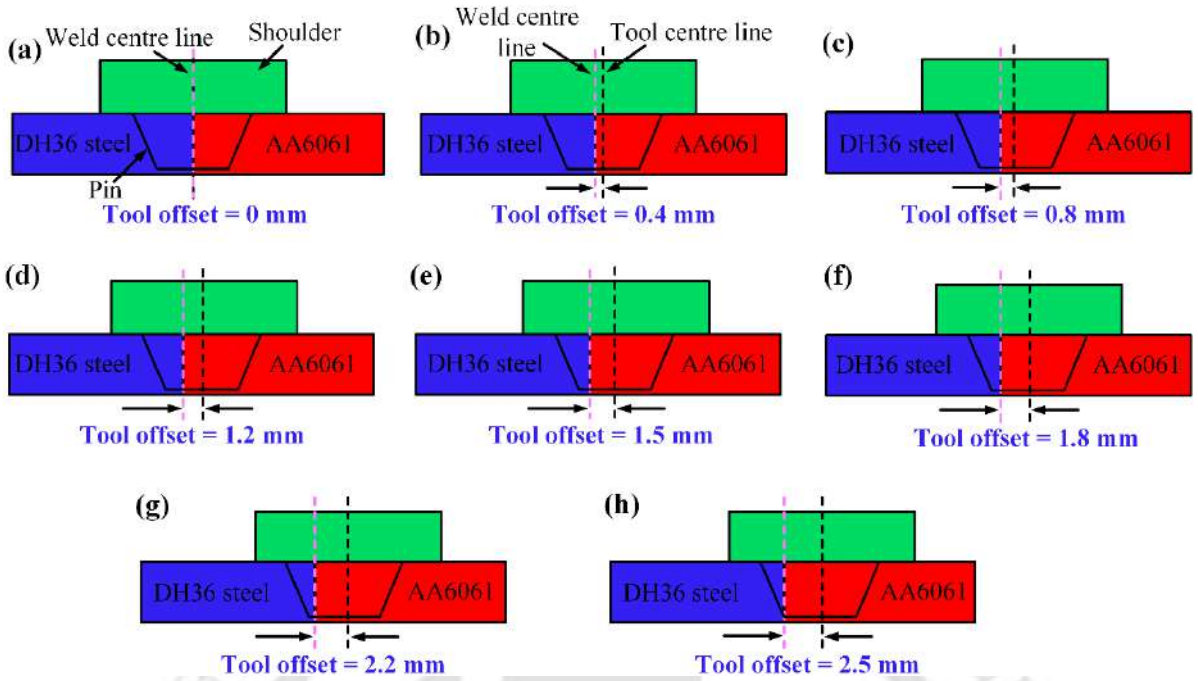

Fig. 6.1 *Schematic illustration of tool offset towards AA6061 by (a) 0 mm; (b) 0.4 mm; (c) 0.8 mm; (d) 1.2 mm; (e) 1.5 mm; (f) 1.8 mm; (g) 2.2 mm; and (h) 2.5 mm*

Table 6.1 *Tool offset values*

Sample no.	S_1	S_2	S_3	S_4	S_5	S_6	S_7
Tool offset (mm)	0.4	0.8	1.2	1.5	1.8	2.2	2.5

6.2 MACRO/MICROSTRUCTURE

A typical weld surface appearance and a cross-sectional view of the welded samples at different tool offset conditions are shown in Fig. 6.2. Fig. 6.3 shows SEM images at various regions in the weld cross-section at varying tool offset conditions. The smooth surface appearance of the welded samples is free from any defects at a tool offset of 0.8 mm, 1.2 mm, and 1.5 mm. The surface contained the uneven zig-zag lines at a tool offset of 1.8 mm. At a tool offset of 0.4 mm, 2.2 mm, and 2.5 mm, the defects like void and surface grooves are found on the surface due to the insufficient intermixing of the dissimilar materials. As shown in Fig. 6.2, the bright and black regions correspond to the AA6061 and DH36 steel in cross-sections, respectively. The discontinuous steel strip extruded from AS to the RS at a tool offset of 0.4 mm and 0.8 mm. However, the steel strip is continuous at a tool offset of 1.2 mm and 1.5 mm.

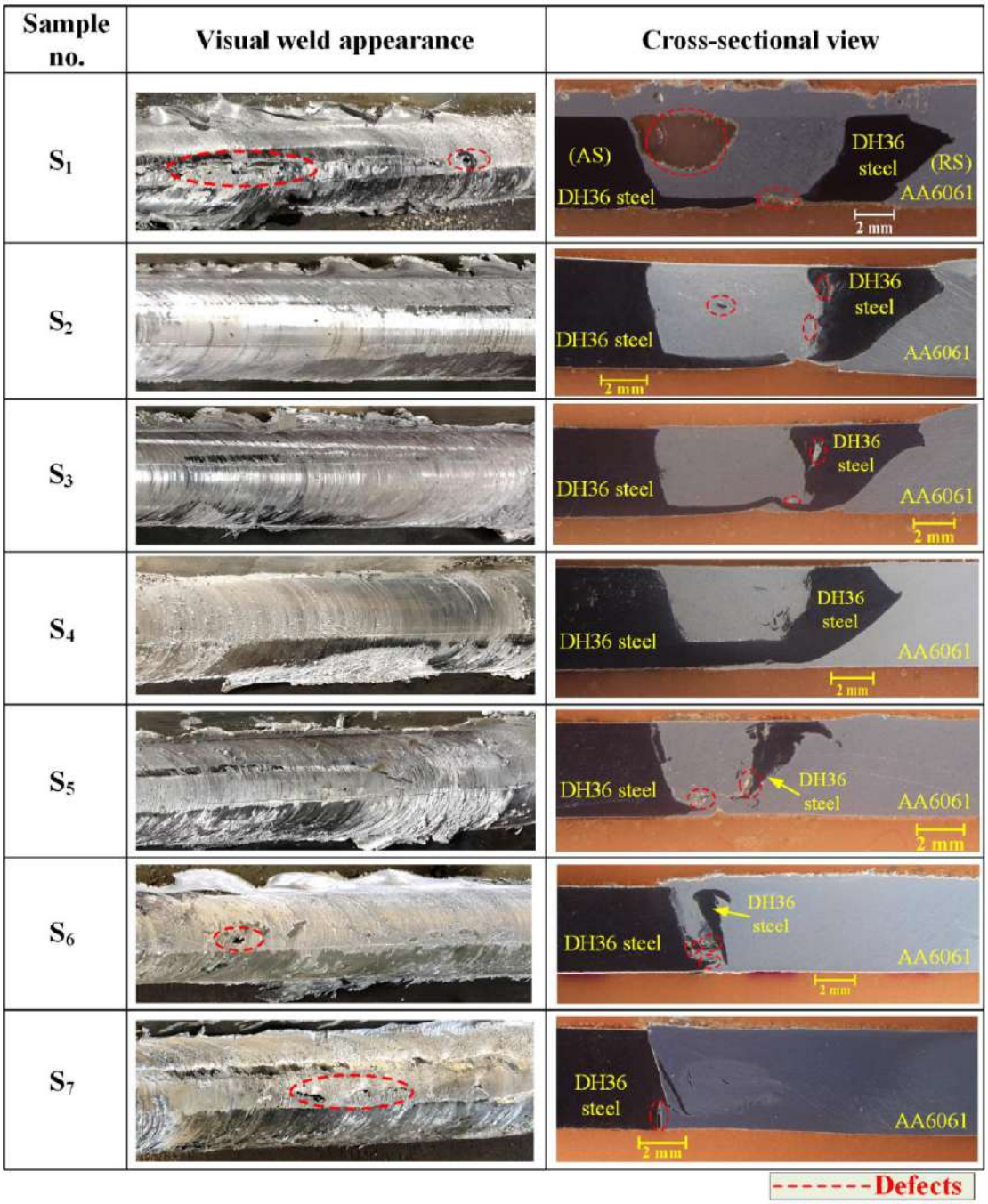

Fig. 6.2 *Weld surface appearances and a cross-sectional view of the welded samples*

During the traverse phase of the rotating tool, softening behaviour of the Al alloy made it easy for the harder steel to extrude towards RS. The different material flow patterns are formed as the strip extruded from the base of the DH36 steel and mechanically interlocked with the AA6061 matrix. The vertical force applied by the FSW tool pushed the steel and Al downward, and the backing plate restricted the downward movement at the bottom of SZ. Therefore, the pin length was kept lower than the thickness of the workpiece, so material from the bottom of the steel could be squeezed and transferred towards AA6061 through the narrow

passage designed by the pin bottom surface and backing plate. The extrusion of a higher amount of harder material increases the flow resistance and deteriorates the flow behaviour of dissimilar materials. Hence the larger voids are produced inside the SZ of sample S_1. The defects like voids and cracks are significantly reduced by increasing the tool offset from 0.4 mm to 1.2 mm. Compared to other welded samples, the defects are absent inside the SZ at a tool offset of 1.5 mm. Furthermore, the defects are generated by shifting the tool pin from 1.5 mm to 2.5 mm towards AA6061.

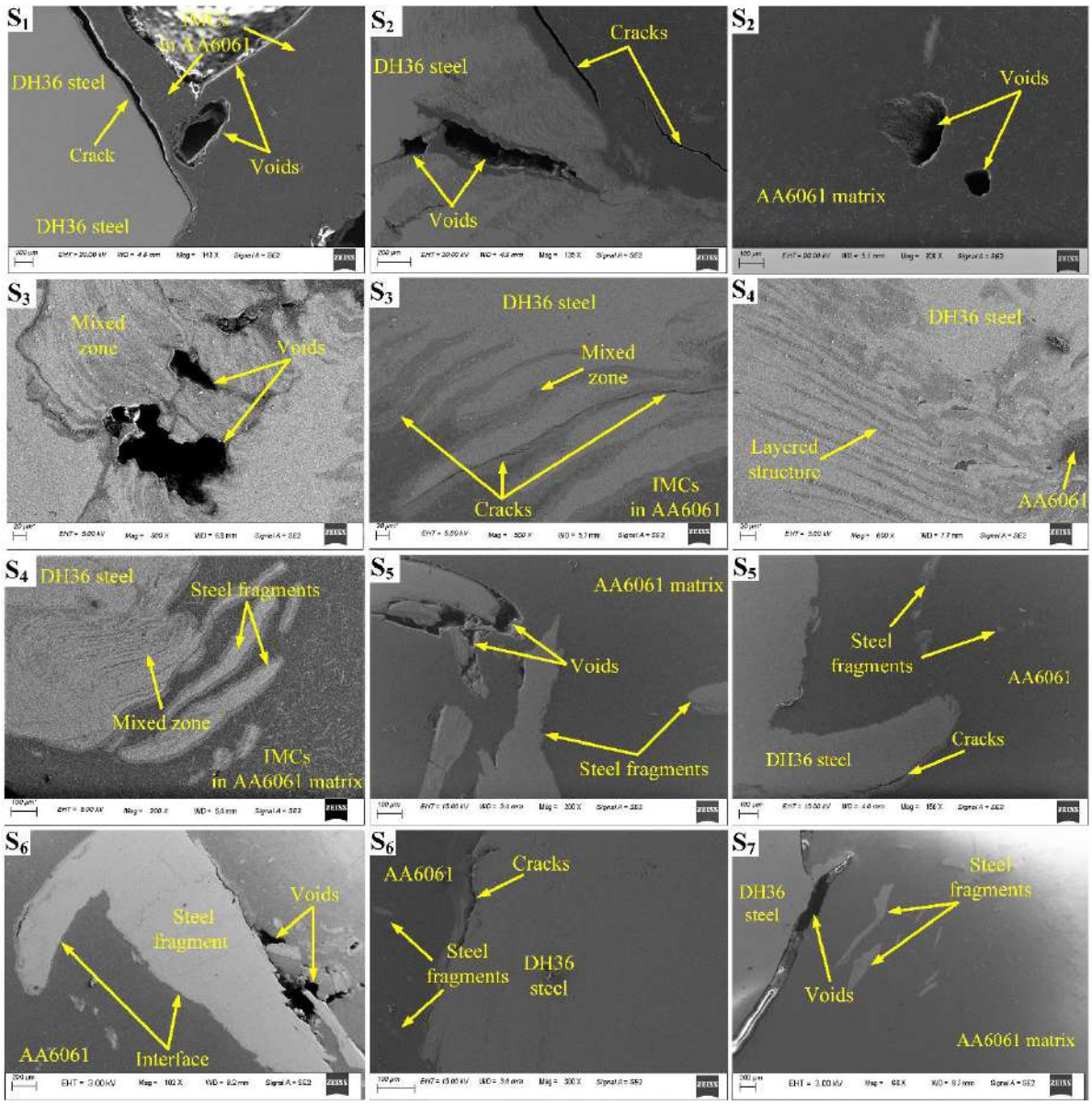

Fig. 6.3 *SEM images at the cross-section of welded samples*

At a tool offset of 1.8 mm–2.5 mm, the coarse steel fragments are detached from base steel and scattered inside the SZ due to the forge impact of the rotating tool pin. The coarse steel fragments produced the defects like cracks and voids inside SZ. Because the steel particles

are harder than the AA6061 matrix, it is challenging to flow and deform the steel fragments inside the AA6061 matrix. Hence the intermixing of steel fragments and AA6061 matrix is very difficult, which resulted in the cracks/voids formation at the Al/steel interface, as shown in Fig. 6.3. Sadeghian et al. [134] reported that the steel fragments commonly lead to a risk of macroscopic crack initiation and subsequently joint defects due to the different physical properties of the dissimilar materials. The tool pin slightly touched the edge of the steel sheet at a tool offset of 2.5 mm, which deteriorated the intermixing of the materials and produced cracks at the Al/steel interface, as shown in Fig. 6.3.

The cross-section of the weld joints consisted of different zones, such as SZ, mixed zone (MZ), steel extruded zone (SEZ), thermomechanically affected zone (TMAZ), heat-affected zone (HAZ), and base materials. The macrograph and various zones in welded samples S_2 and S_4 are shown in Figs. 6.4 and 6.5, respectively.

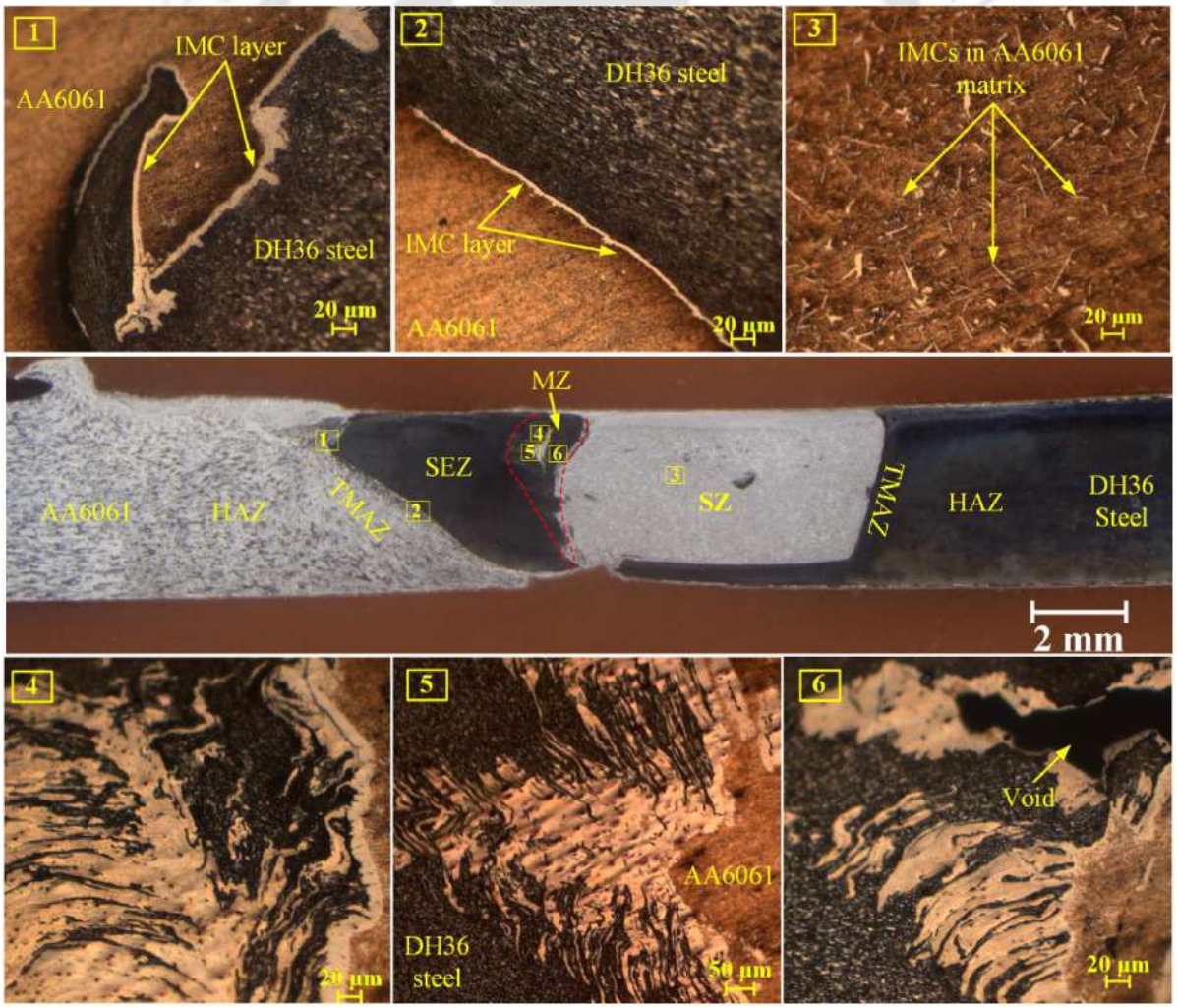

Fig. 6.4 *Macrostructure and various regions in sample S_2*

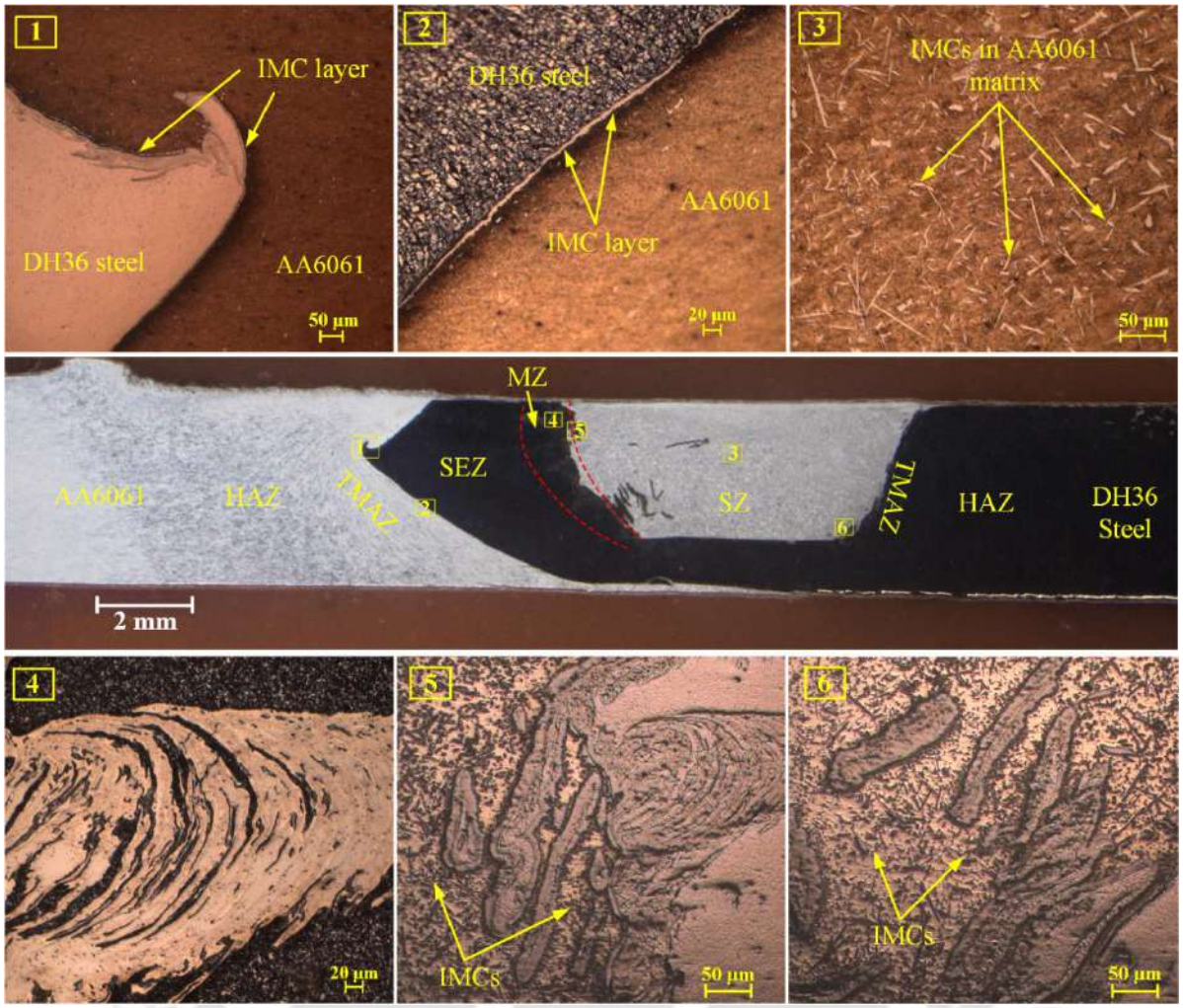

Fig. 6.5 *Macrostructure and various regions in sample S_4*

In the SEZ, the steel strip encompassed with an IMC layer at the outside boundary is visible in Figs. 6.4 and 6.5. The solid-state diffusion phenomena form the IMC layer due to the coinciding impact of axial forging, frictional heating, and material extrusion from AS to RS. The independent dispersion of IMCs along with the steel fragments is observed in the SZ, which is confirmed by EDS and XRD analysis in the next section. These IMCs are probably formed through the chemical reaction between the AA6061 matrix and sheared-off small steel fragments. The SZ could be considered an IMC enhanced AA6061 matrix due to the higher hardness of IMCs than base materials [65]. The varying tool offset is significantly affected the material flow and mixing between the AA6061 and DH36 steel.

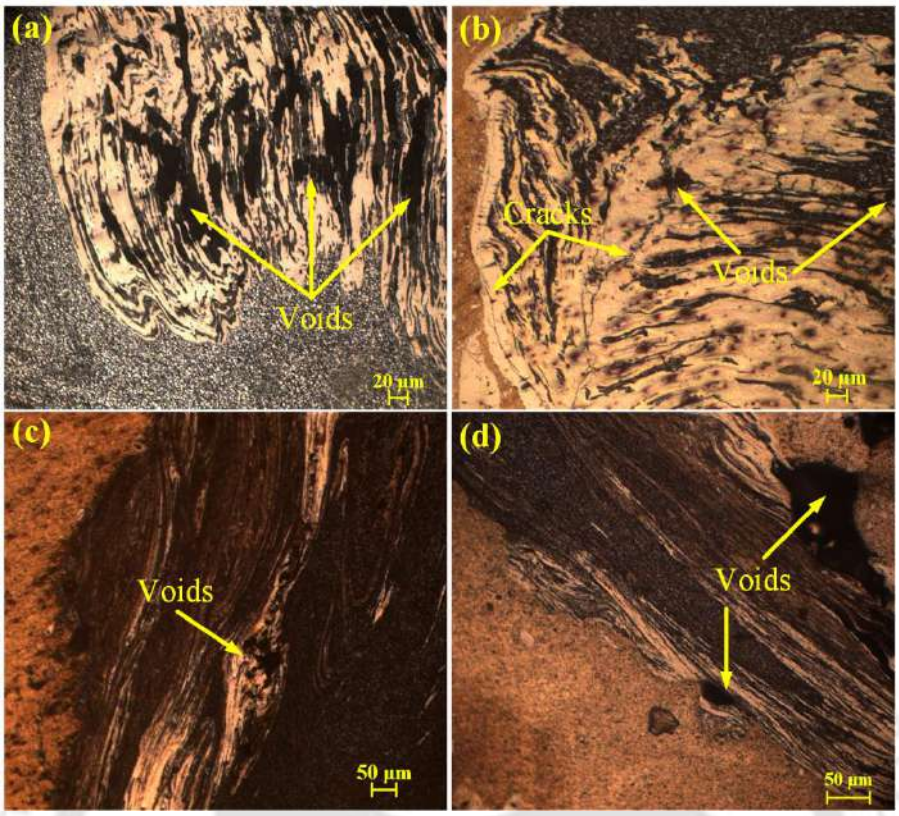

Fig. 6.6 *MZ in sample (a) S_1; (b) S_3; (c) S_5; and (d) S_6*

In the MZ, the intercalated layered structure is produced near the weld interface on the steel side, which resulted from severe stirring and mixing of the dissimilar materials under the heat generation by the rotating tool. A large amount of material from the DH36 steel interacted with the AA6061 at a lower tool offset, which resulted in higher flow resistance and improper diffusion due to the intense materials mixing by the extruded steel strip. Hence the defects are generated inside the MZ of samples S_1–S_3, as shown in Figs. 6.4 and 6.6. The defect-free material flow and mixing are observed at a tool offset of 1.5 mm, as shown in Fig. 6.5, which indicated good material stirring and mutual diffusion of AA6061 and steel inside the MZ. The flow separation reduces at an optimum tool offset, which leads to the filing of defected regions; therefore, a welded joint without defects could be expected. As shown in Figs. 6.6(c) and 6.6(d), with a further increase in the tool offset from 1.5 mm to 2.2 mm, the defects are also created inside the MZ due to improper material flow. The MZ was not generated inside the sample S_7 due to insufficient material flow because the tool slightly touched the edge of the steel sheet at a tool offset of 2.5 mm.

Figs. (6.7–6.10) show the higher–magnification microstructure at the different zones in DH36 steel and AA6061. A significant microstructural variation is observed in the SZ, TMAZ, and HAZ on each side of the weld joints. The base material, i.e., DH36 steel exhibited coarse-

grained ferrite surrounded by the pearlite bands, whereas coarse elongated grains are presented in AA6061 as shown in Figs. 6.7(a) and 6.7(b).

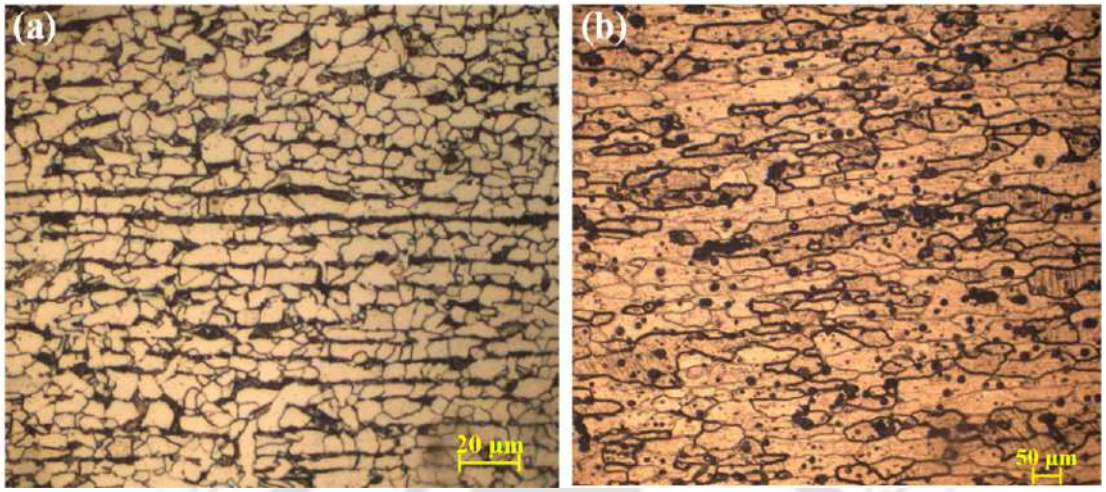

Fig. 6.7 *Microstructure of (a) DH36 steel; and (b) AA6061*

In the FSW, SZ is generated due to the direct interaction between the workpiece material and the rotating tool pin. However, the TMAZ is not affected by the tool pin, but the strain rate and temperature distribution adjacent to the SZ affect the TMAZ. A significant grain size reduction is observed in SZ from the 56.3 ± 2.1 µm and 15.9 ± 1.65 µm of AA6061 and DH36 steel base materials, respectively. The average grain size (AVG) in the SZ (DH36 steel) is significantly lower than SZ (AA6061). SZ (AA6061) exhibited the equiaxed refined-grained microstructure with AVG of 10.74 ± 1.12 µm, as shown in Fig. 6.8. The SEZ material extruded from the SZ under the combined effect of axial forging and frictional heating. As shown in Figs. 6.9(a–d), this zone exhibited the AVG of 2.84 ± 0.42 µm in samples S_1–S_4. As shown in Figs. 6.9(e–h), SZ (DH36 steel) experienced significant grain refinement with the AVG of 1.05 ± 0.24 µm in samples S_5–S_7.

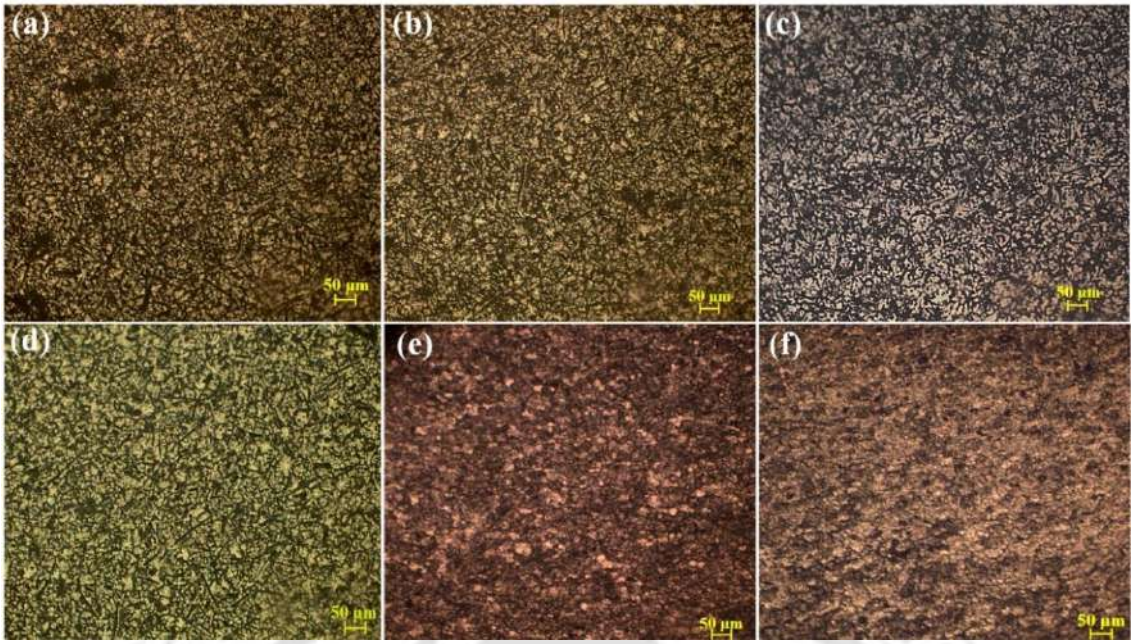

Fig. 6.8 *SZ (AA6061) in sample (a) S_1; (b) S_2; (c) S_3; (d) S_4; (e) S_5; and (f) S_6*

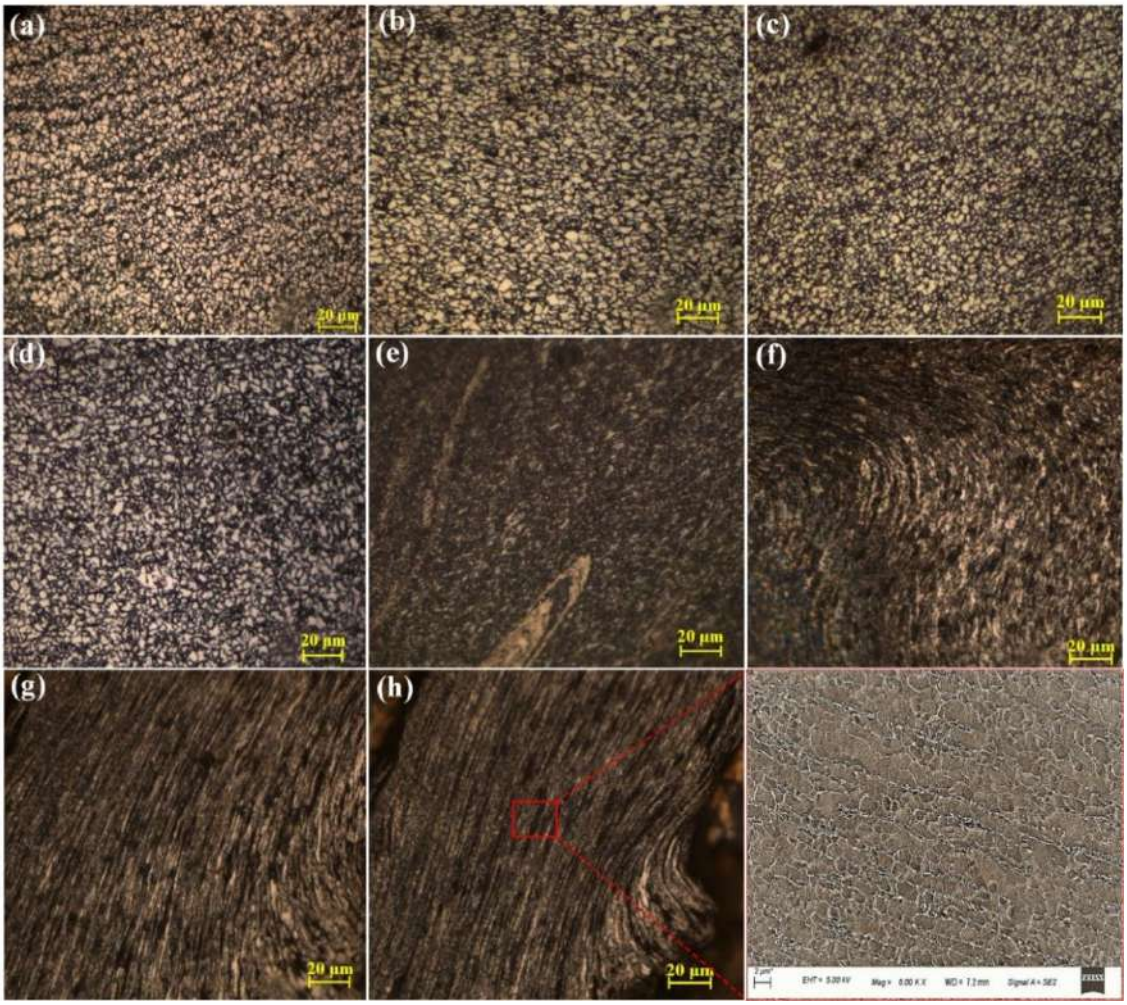

Fig. 6.9 *(a) SEZ in sample S_1; (b) SEZ in sample S_2; (c) SEZ in sample S_3; (d) SEZ in sample S_4; (e) SZ (DH36 steel) in sample S_5; (f) SZ (DH36 steel) in sample S_6; and (g,h) SZ (DH36 steel) in sample S_7*

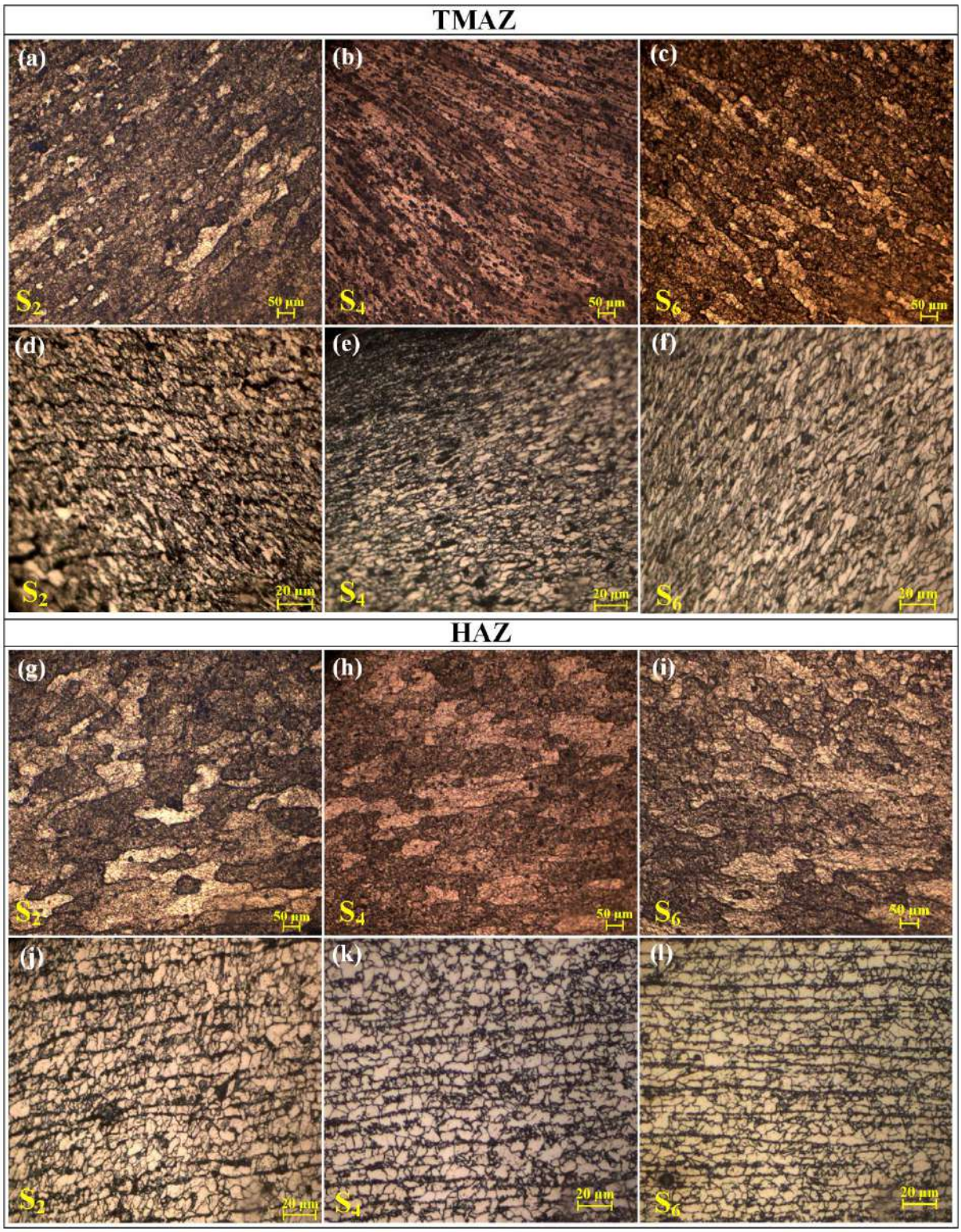

Fig. 6.10 *(a–c) TMAZ (AA6061); (d–f) TMAZ (DH36 steel); (g–i) HAZ (AA6061); and (j–l) HAZ (DH36 steel)*

The grain refinement in SZ is attributed to the dynamic recrystallization by severe plastic deformation and heat generation in the FSW process [16]. The fine-grained flow lines/patterns following the rotation of the tool are found in the SZ (DH36 steel), as shown in Figs. 6.9(e–h). These patterns in the FSW are formed by material deformation and material transference in the pin-influenced region. In TMAZ, the lack of dynamic recrystallization produced the elongated and deformed grains under insufficient heat and deformation, as shown in Figs. 6.10(a–f). Mao et al. [186] reported that the grains immediately changed by dynamic recovery and then elongated along the rotation direction of the pin due to the viscous shear force. The AVG in TMAZ (DH36 steel) and TMAZ (AA6061) is 4.7 ± 0.62 µm and 13.3 ± 1.23 µm, respectively. HAZ between the TMAZ and base materials is not affected by the plastic deformation, but experiences heat only during the welding process. As a result, this zone exhibited the grain coarsening compared to SZ of AA6061 and DH36 steel, as shown in Figs. 6.10(g–l).

6.3 CHARACTERIZATION OF IMC LAYER AND MZ

The critical issue during the joining of steel and Al is the formation of the IMC layer at the interface, which can significantly affect the mechanical performance of weldments. Numerous kinds of research were carried out regarding the formation and evolution of interlayer between Al and iron (Fe). As reported by Liu et al. [65], the atomic diffusion process initially forms a supersaturated solid solution of Al and Fe. Then, Al and Fe atoms transfer to specific regions and convert into IMCs when they extend to an appropriate level at equivalent pressure and temperature conditions. Finally, the IMC layer grows progressively by the diffusion of solute atoms. In the concern of tool offset in dissimilar FSW of steel and Al alloy, the tool interaction with the steel plate and tool shoulder controls solid-state diffusion through the heat generation and intermixing of the materials, which is primarily responsible for the generation of different IMCs [3]. The heat generation in the FSW is occurred due to friction and visco-plastic deformation of the workpiece material [83]. During the FSW of low-temperature alloys, the deformation component has a negligible effect, and the frictional component is nearly constant for a given set of welding parameters [108]. However, the deformation component plays a significant role in dissimilar FSW of steel and Al alloy since the steel has greater flow stress at one side of the weld joint. Ramachandran et al. [83] reported that more tool penetration inside the steel leads to severe stirring at the steel side due to the higher heat generation by the deformation component, which enhances diffusion and intermetallic reaction between Al and Fe. Liu et al. [65] also reported that the diffusion process

could be attributed to the extensive plastic deformation of the material and a higher strain rate adjacent to the tool pin. The activation energy required for the IMC reaction reduces with an increase in strain rate and pressure, which accelerates the intermetallic reaction for the formation of the IMCs [187].

In this work, SEM equipped with an EDS system was used to observe the metallurgical behaviour of the IMC layer at varying tool offset conditions. Figs. (6.11–6.14) show the EDS analysis and SEM Images at the Al/steel interface at varying tool offset. As shown in Fig. 6.11, the interface is distinguished by different colours with the mutual existence of Fe and Al from DH36 steel and AA6061 sides, which indicates the formation of the newly phased IMC layer at the interface.

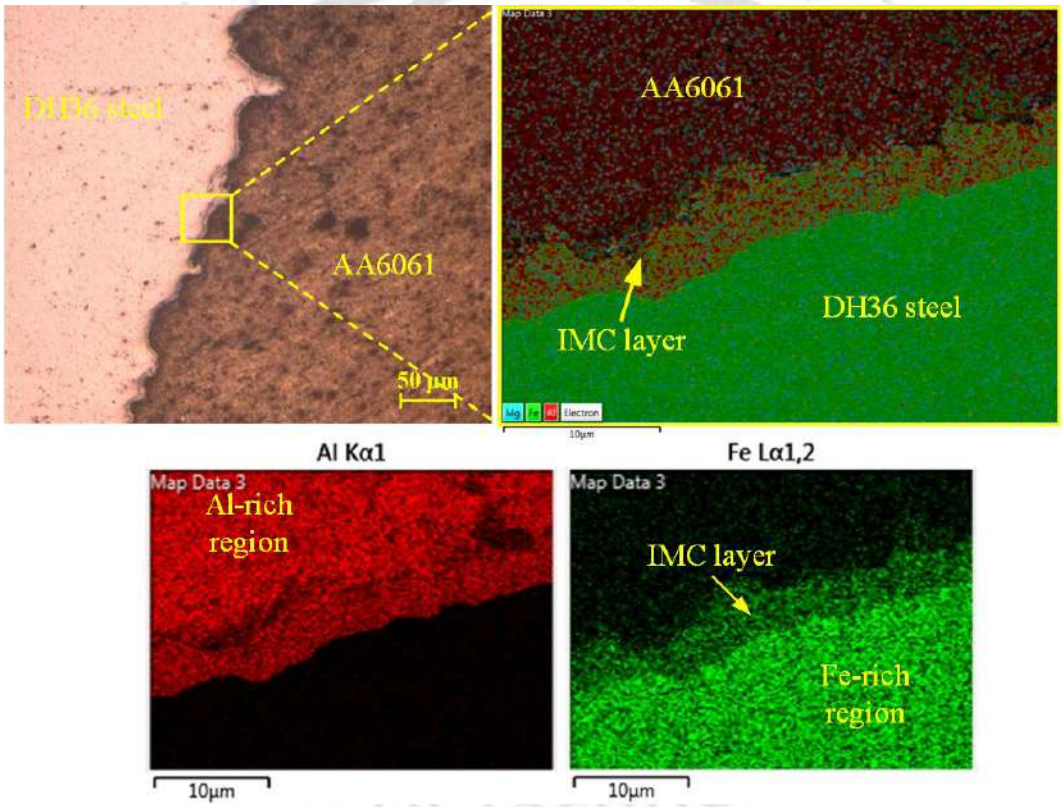

Fig. 6.11 *EDS elemental mapping at Al/steel interface in sample* S_5

In the EDS line scan at the interface region, the Al/Fe concentration fluctuations signified the IMC layer, which is marked by the dotted lines in Fig. 6.12. The intensity of Al and Fe increased towards the AA6061 and DH36 steel sides from the interface, respectively. The IMC layer indicated diffusion instead of purely mechanical mixing between base DH36 steel and AA6061 alloy. The excessively thick brittle IMC layer could result in cracks formation at the interface [83], which are visible at a lower tool offset of 0.4 mm and 0.8 mm in Figs. 6.13(a) and 6.13(b).

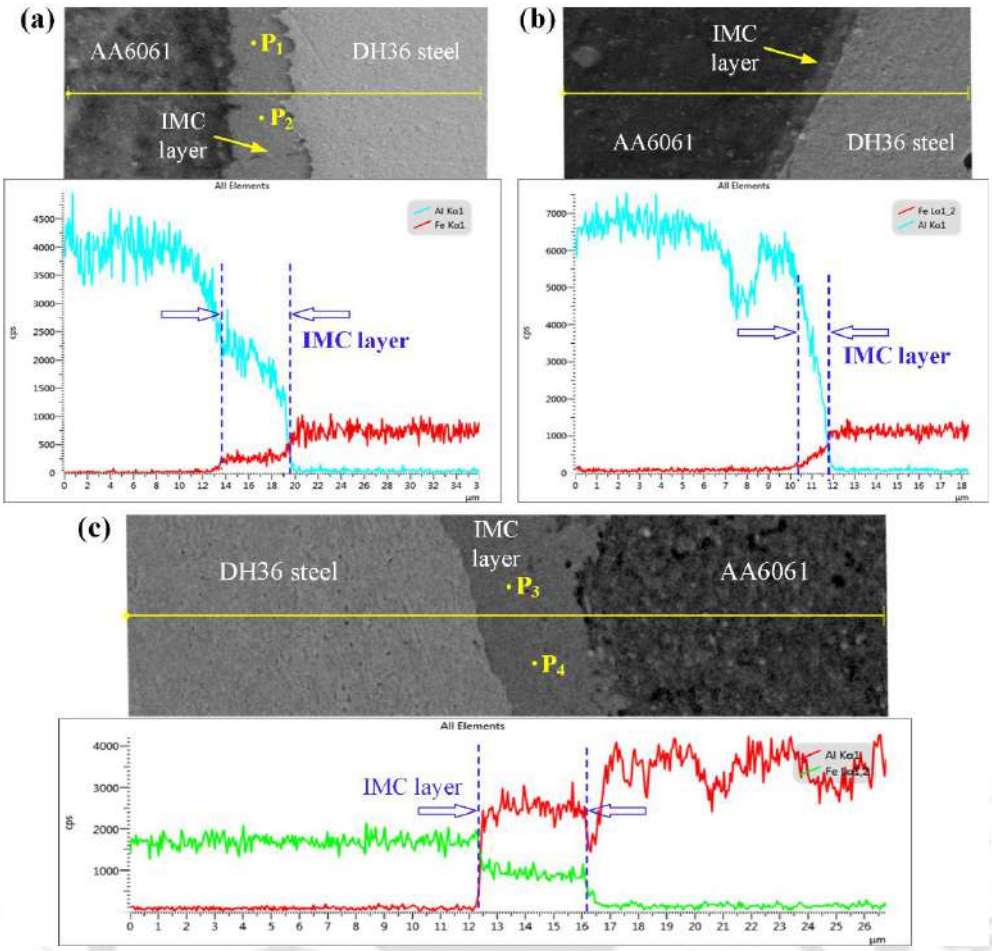

Fig. 6.12 *EDS line scan at Al/steel interface in sample (a) S_3; (b) S_7; and (c) S_5*

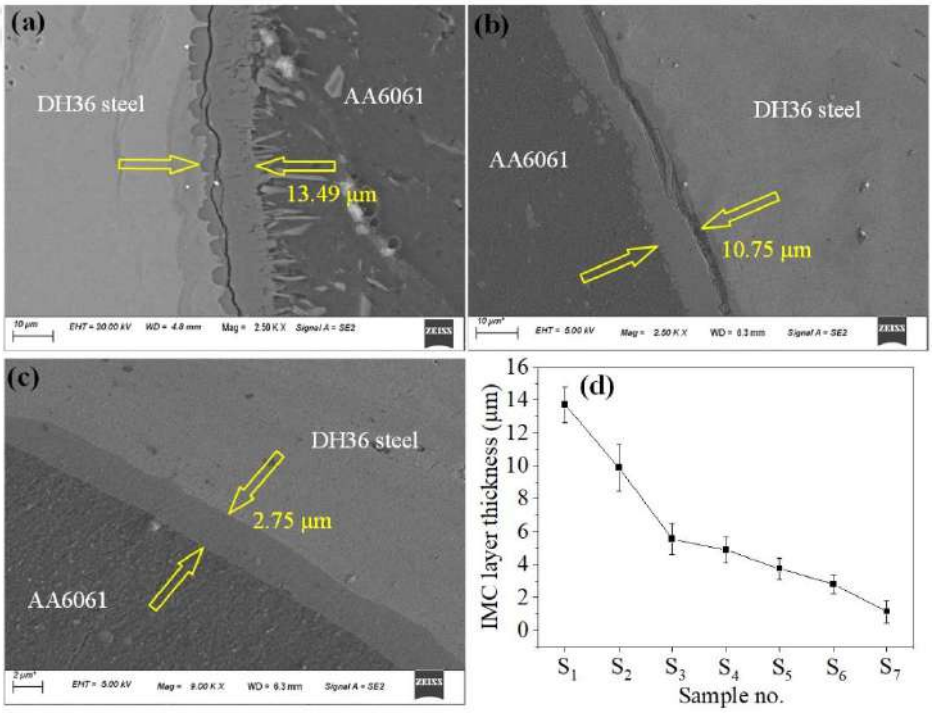

Fig. 6.13 *(a) Al/steel interface in sample S_1; (b) Al/steel interface in sample S_2; (c) Al/steel interface in sample S_6; and (d) average IMC layer thickness at varying tool offset*

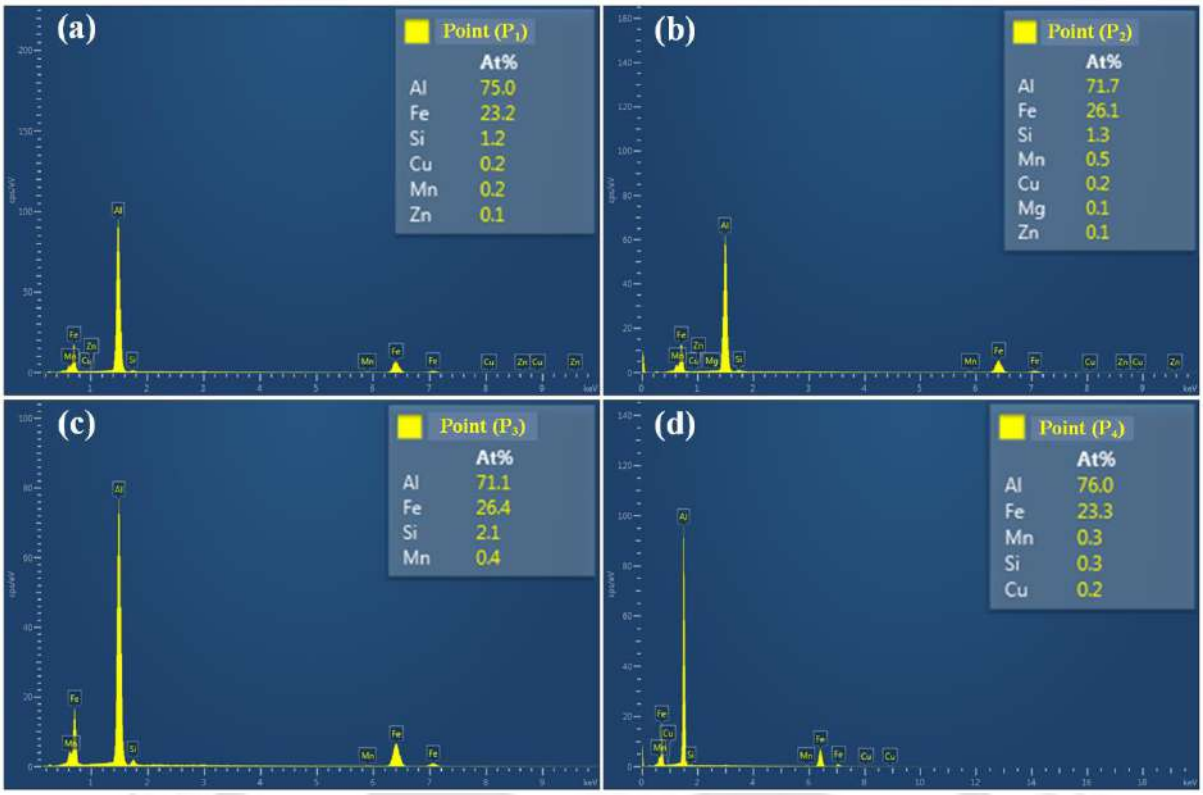

Fig. 6.14 *(a–f) EDS elemental spectrum analysis at various points marked in Fig. 6.12*

Table 6.2 *Feasible IMCs formation at varying tool offset*

Sample no.	S_1	S_2	S_3	S_4	S_5	S_6	S_7
IMCs at the MZ		$AlFe + AlFe_3$			$AlFe + Al_2Fe$		–
IMCs at interface				$Al_3Fe + Al_5Fe_2$			

The averaged IMC layer thickness at the interface at varying tool offset is shown in Fig. 6.13(d). The average IMC layer thickness continuously decreased with an increase in tool offset. A large amount of the steel experienced severe stirring action and heat generation at a smaller tool offset, which enhanced the diffusion and intermetallic reaction between Al and Fe. In contrast, the higher tool offsetting towards the Al side led to a lack of intermixing between steel and Al due to insufficient frictional heat for softening the steel part. The optimum thickness of the IMC layer is required, which can improve the weld quality by providing a better metallurgical bonding between the Al and Fe. The EDS point analysis was performed at various points to identify the chemical composition of the IMC layer, as shown in Fig. 6.14. The atomic percentage of Al and Fe at a point generally suggests the presence of corresponding Al–Fe IMCs. According to the Al/Fe phase (Fig. 1.7), the atomic percentage of major elements, i.e., 75.0% Al & 23.2% Fe at point (1) and 71.7% Al & 26.1% Fe at point (2) with a lesser amount of other elements propose the possible formation of Al-rich IMCs, namely Al_3Fe and

Al_5Fe_2 at the interface, respectively. Similarly, points P_3 and P_4 indicate the probable formation of Al_5Fe_2 and Al_3Fe IMCs at the interface, respectively. So, the EDS analysis confirmed that the metallurgical bonding occurred between AA6061 and DH36 steel through the significant diffusion of Fe and Al with other elements, such as Mg, Si, Mn, Zn, and Cu. As shown in Table 6.2, the IMCs, namely Al_3Fe and Al_5Fe_2 are formed at the interface at all tool offset conditions. The Al-rich IMCs, namely Al_3Fe and Al_5Fe_2 were reported as the most stable forms in FeAl system [188]. Pourali et al. [70] reported that the high thermal conductivity of the Al causes the formation of Al-rich IMCs at a relatively lower interface temperature than the SZ. According to the published literature [83], Al-rich IMCs, namely Al_3Fe and Al_5Fe_2 are possibly formed at a temperature range of 700 ^oC–900 ^oC. However, IMCs with lower Al composition, such as $AlFe_3$ and AlFe can be produced at a higher temperature of over 1000 ^oC. At atmospheric pressure, the Al–Fe phase diagram (Fig. 1.7) indicates that the $AlFe_3$ forms at about 552 ^oC followed by a first-order reaction temperature of around 1310 ^oC. Springer et al. [189] reported the formation of Al_5Fe_2 at a temperature range of 600 °C–800 °C in the FSW of low carbon steel and Al. Liu et al. [65] obtained the highest temperature of about 500 ^oC during the dissimilar FSW of 6061-T6 Al alloy and high-strength steel. In their study, the IMCs formation at this relatively lower temperature was justified by considering the effect of strain rate and pressure related to the mechanical welding force. With an increase in pressure and strain rate, the IMC layer can be formed at a relatively low welding temperature at constant diffusion time.

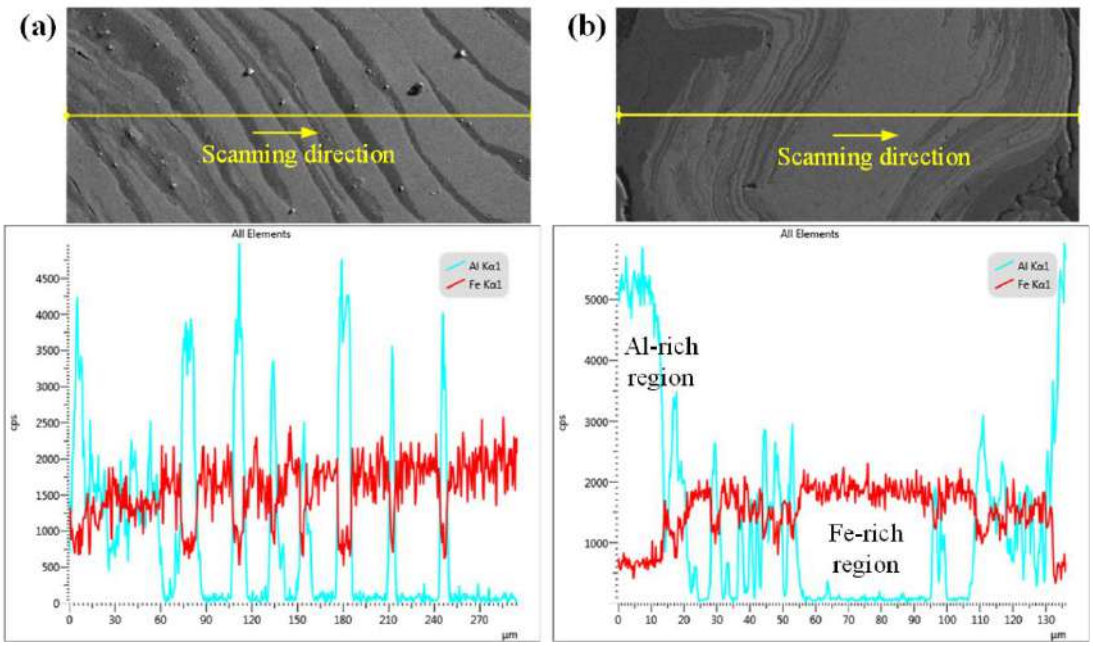

Fig. 6.15 *EDS line scan at the MZ in sample (a) S_4; and (b) S_5*

The MZ consisted of different flow features, which could be attributed to the plasticized fluid motion produced by the traverse and rotational movement of the tool. The tool offset plays a significant role in controlling the IMCs formation at the MZ. The EDS line scan contains the abrupt fluctuations of Al and Fe in the MZ, as shown in Fig. 6.15. These fluctuations signify the diffusion of the Al and Fe in the MZ and indicate the probability of IMCs formation. The composition of IMCs strongly depends on the reaction-diffusion between the Al and Fe, which is furthermore affected by the variation in tool offset. In this work, the EDS point analysis and elemental mapping were conducted to confirm the composition of IMCs at the MZ, as shown in Fig. 6.16. In EDS elemental mapping, the distribution of Al and Fe in the MZ is represented by cyan and red colors, respectively. White arrows point to the mutual existence of Al and Fe inside the intermixed region in Fig. 6.16, which suggests a reaction-diffusion between Al and Fe.

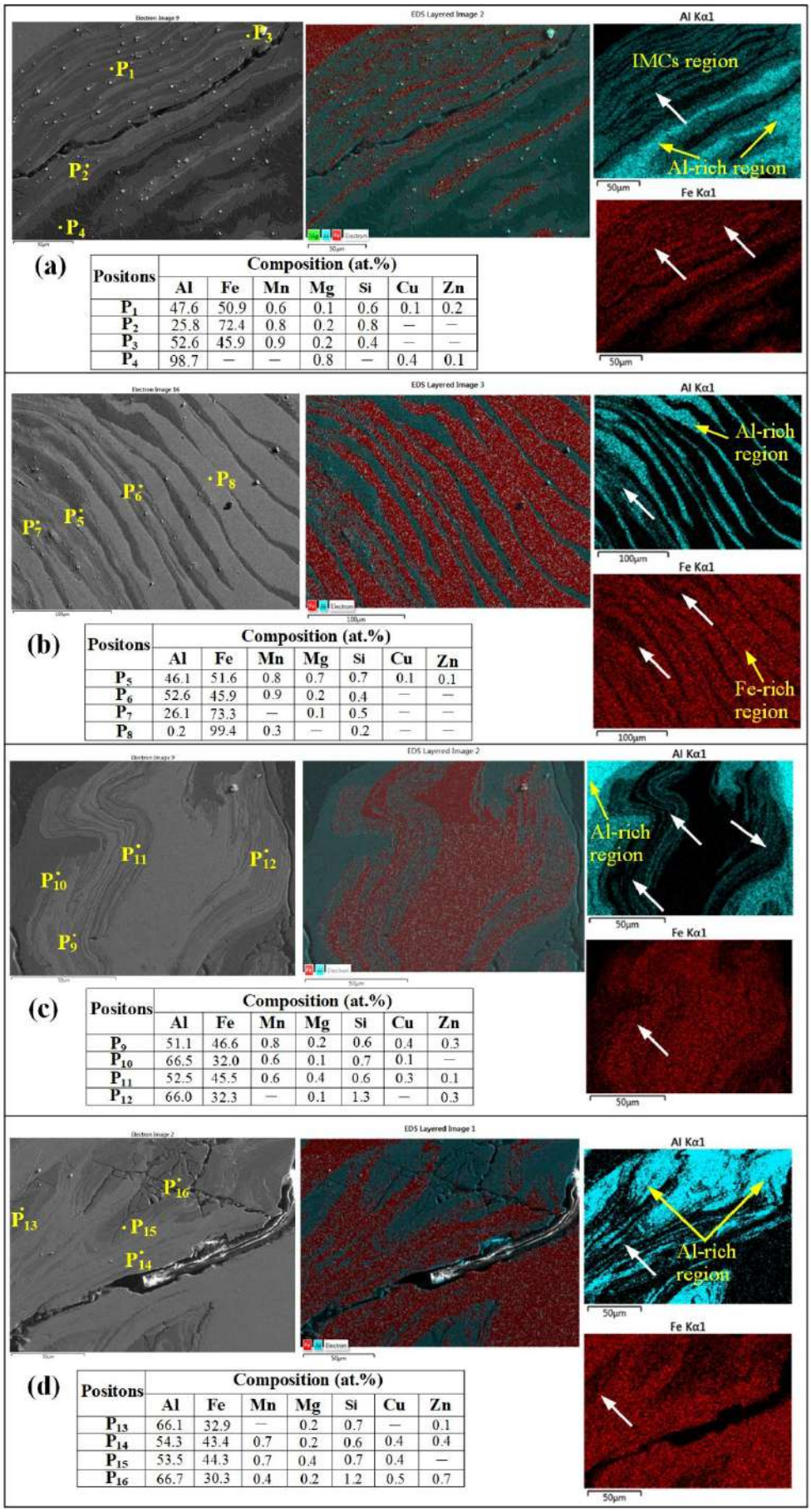

(a)

Positons	Composition (at.%)						
	Al	Fe	Mn	Mg	Si	Cu	Zn
P_1	47.6	50.9	0.6	0.1	0.6	0.1	0.2
P_2	25.8	72.4	0.8	0.2	0.8	—	—
P_3	52.6	45.9	0.9	0.2	0.4	—	—
P_4	98.7	—	—	0.8	—	0.4	0.1

(b)

Positons	Composition (at.%)						
	Al	Fe	Mn	Mg	Si	Cu	Zn
P_5	46.1	51.6	0.8	0.7	0.7	0.1	0.1
P_6	52.6	45.9	0.9	0.2	0.4	—	—
P_7	26.1	73.3	—	0.1	0.5	—	—
P_8	0.2	99.4	0.3	—	0.2	—	—

(c)

Positons	Composition (at.%)						
	Al	Fe	Mn	Mg	Si	Cu	Zn
P_9	51.1	46.6	0.8	0.2	0.6	0.4	0.3
P_{10}	66.5	32.0	0.6	0.1	0.7	0.1	—
P_{11}	52.5	45.5	0.6	0.4	0.6	0.3	0.1
P_{12}	66.0	32.3	—	0.1	1.3	—	0.3

(d)

Positons	Composition (at.%)						
	Al	Fe	Mn	Mg	Si	Cu	Zn
P_{13}	66.1	32.9	—	0.2	0.7	—	0.1
P_{14}	54.3	43.4	0.7	0.2	0.6	0.4	0.4
P_{15}	53.5	44.3	0.7	0.4	0.7	0.4	—
P_{16}	66.7	30.3	0.4	0.2	1.2	0.5	0.7

Fig. 6.16 *EDS analysis at the MZ in sample (a) S_2; (b) S_4; (c) S_5; and (d) S_6*

From Figs. 6.16(a) and 6.16(b), the atomic percentages at points P_1, P_3, P_5 and P_6 propose the possible large distribution of AlFe in samples S_2 and S_4. Furthermore, points P_2 and P_7 correspond to $AlFe_3$ in samples S_2 and S_4. In samples S_5 and S_6, the atomic percentages at points P_9–P_{16} propose the possible formation of AlFe and Al_2Fe, as shown in Figs. 6.16(c) and 6.16(d). Points P_4 and P_8 suggest the AA6061 and DH36 steel base materials inside the MZ, respectively. Table 6.2 summarises that MZ comprised different IMCs, namely AlFe and $AlFe_3$ in S_1–S_4 samples, whereas samples S_5 and S_6 contained Al_2Fe and AlFe. The tool offsets, such as 0.4 mm, 0.8 mm, 1.2 mm, and 1.5 mm promoted the diffusion of Fe atoms and produced the phases like AlFe and $AlFe_3$ inside the MZ. However, when the tool is further shifted towards the AA6061 side, the diffusion of Fe atoms is reduced due to lower string action and heat generation at the steel side. Hence, the diffusion of large Al atoms produced the phases like Al_2Fe with AlFe. For that reason, the composition and growth of IMCs could be controlled through the diffusion rate of Al atoms into Fe lattices by controlling the amount of interaction between the steel plate and tool. Inside the MZ, the IMCs at lamellar intercalated features are significantly affect the mechanical performance of welded joints [82]. Bilgin et al. [105] reported that the brittle IMCs, cracks, and voids in the MZ adversely affect the weld strength. However, the mechanical interlocking in the MZ contributes to improvement in joint strength [190]. Knibloe et al. [191] reported that the Fe–rich IMCs exhibit excellent corrosion resistance, which is essential for dissimilar Al and steel joints.

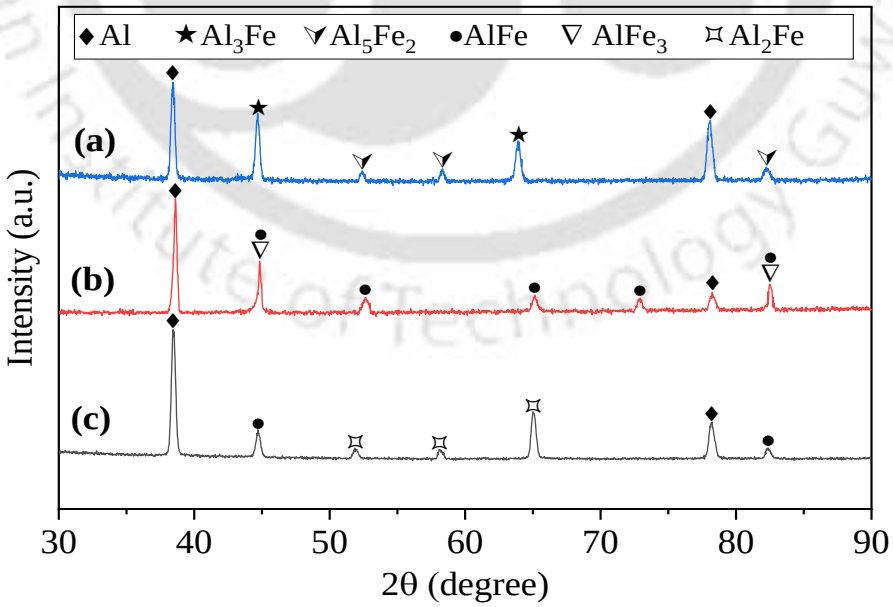

Fig. 6.17 *XRD analysis at (a) IMC layer in sample S_4; and (b) MZ in sample S_4; and (c) MZ in sample S_6*

In this study, XRD analysis was also executed at the weld cross-section to confirm the composition of IMCs at the interface and MZ. The MZ and the Al/steel interface were located at the centre of the area exposed by the XRD beam. As shown in Fig. 6.17, the peaks in XRD patterns confirmed the formation of Al_5Fe_2 + Al_3Fe IMCs at the interface, $AlFe_3$ + AlFe in MZ of sample S_4, and AlFe + Al_2Fe in MZ of sample S_6.

6.4 CHARACTERIZATION OF SZ

The irregular distribution of needle-like particles inside the SZ of samples S_1–S_6 is induced due to a greater strain rate by the severe stirring action of the rotating tool. Fig. 6.18(a) shows the optical microscopic image of the particles inside the SZ of sample S_1. As shown in Figs. 6.18(b–e), EDS elemental mapping signifies that the particles consisted of a large fraction of Al with a small Fe content. As shown in Figs. 6.18(f) and 6.18(g), the EDS point analysis suggests that these particles are bounded by Al_3Fe phases inside the AA6061 matrix.

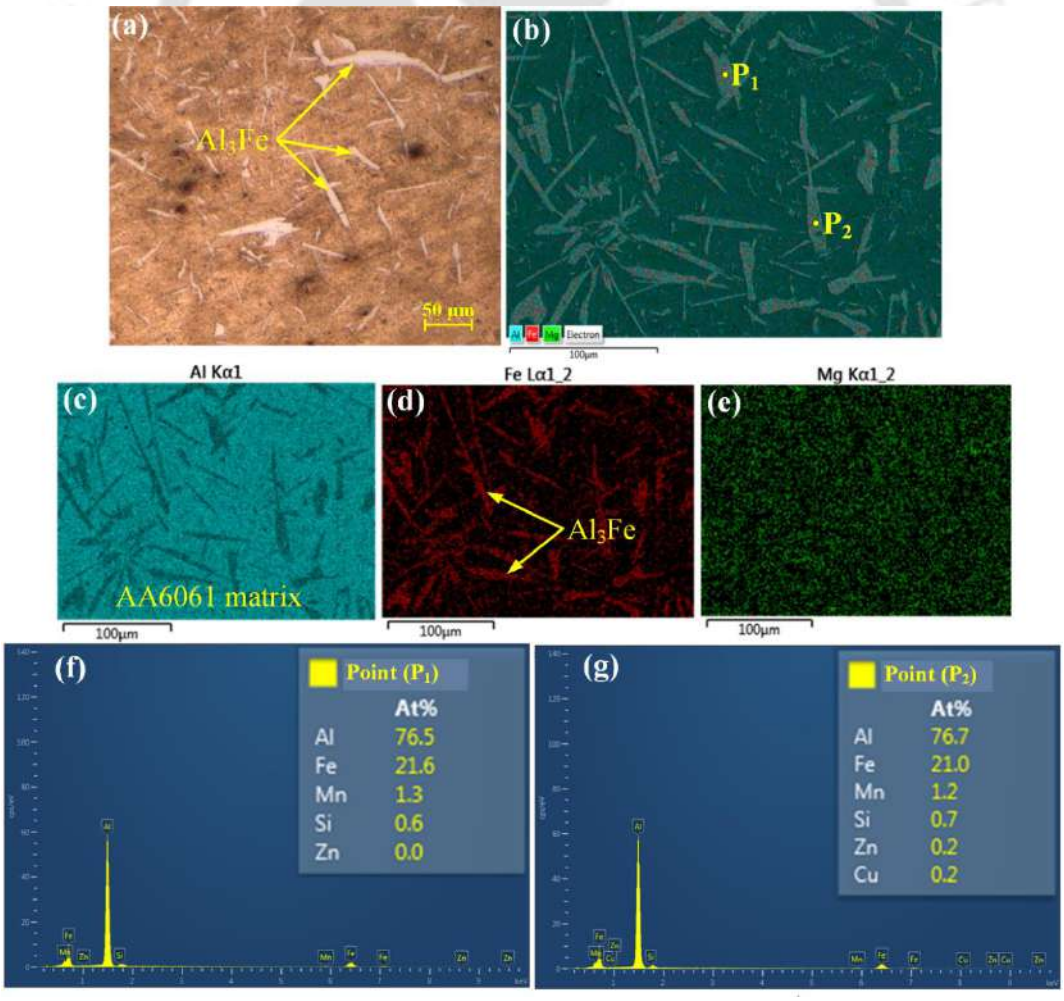

Fig. 6.18 *(a) Optical microscope image of SZ in S_1; (b–e) EDS elemental mapping; and (f–i) EDS point analysis of particles in SZ*

In this work, the Image analysis by the thresholding technique was performed at similar locations to quantify IMCs inside the SZ under the varying tool offset conditions. The quantification of IMCs in the SZ at different tool offsets is shown in Fig. 6.19.

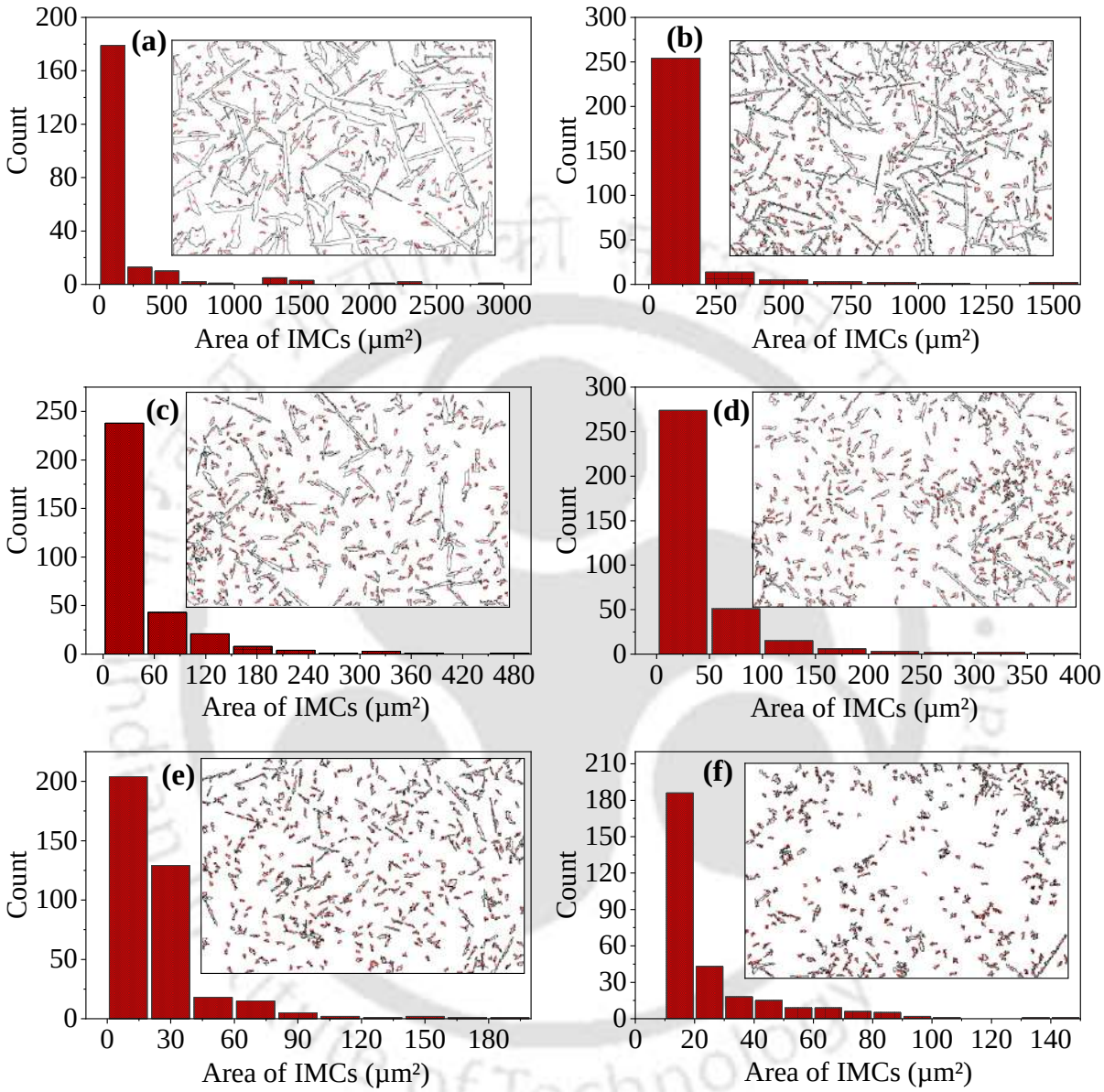

Fig. 6.19 *Quantification of IMCs inside SZ of sample (a) S_1; (b) S_2; (c) S_3; (d) S_4; (e) S_5; and (f) S_6*

The intensity of coarse IMCs reduced by increasing the tool offset from 0.4 mm to 2.2 mm, as shown in Fig. 6.19. The mean area of IMCs is 150.82 µm^2, 79.69 µm^2, 48.56 µm^2, 39.26 µm^2, 25.52 µm^2, and 21.88 µm^2 at a tool offset of 0.5 mm, 0.8 mm, 1.2 mm, 1.5 mm, 1.8 mm, and 2.2 mm, respectively. At a low tool offset (i.e., 0.4 mm), many IMCs in the AA6061 matrix are bulk in size, whereas the smaller IMCs are distributed at a higher tool offset of 2.2 mm. At a smaller tool offset, the large amount of the steel experienced the stirring action and

frictional heat, which facilitated the mutual diffusion and intermetallic reaction between Al and Fe. Hence, coarse IMCs detached from the Al/steel interface and scattered inside the SZ by stirring the action of the rotating tool pin. At a higher tool offset towards the AA6061 side, the low heat generation at the steel side retarded the intermixing and diffusion, which resulted in the scattering of smaller IMCs inside the SZ. Liu et al. [65] observed that some of the sheared-off steel fragments are entirely consumed and converted into IMCs by the reaction-diffusion between the steel fragments and the Al matrix. SZ could be considered an IMCs improved Al–matrix due to the higher hardness of IMCs compared to that of base Al and steel. On the other hand, the excessive formation of brittle IMCs can produce the defects like voids inside the SZ and adversely affect the mechanical performance of the dissimilar weldments. Therefore, it is essential to prevent the excessive IMCs formation in the FSW of dissimilar materials.

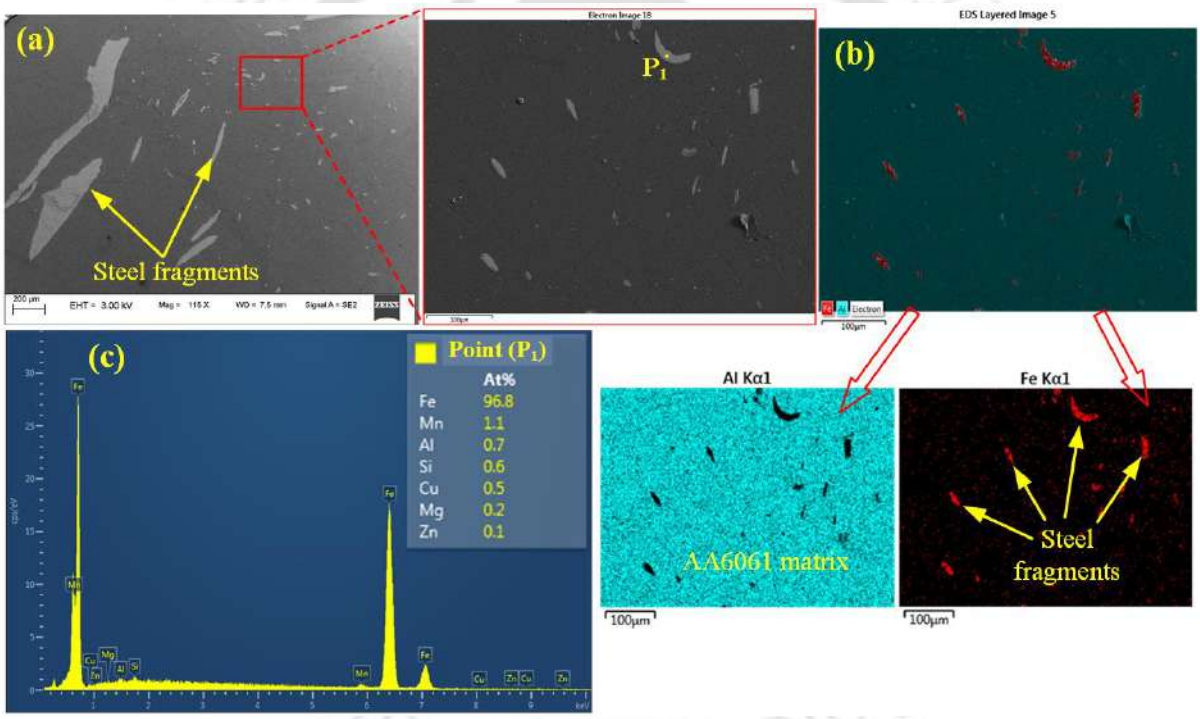

Fig. 6.20 *(a) SEM image of SZ in sample S_7; and (b–e) EDS elemental mapping and point analysis of particles inside SZ*

When the tool pin shifted entirely towards AA6061, IMCs are not generated inside the SZ of sample S_7 due to a lack of stirring action between steel and AA6061. However, only steel fragments with different sizes are identified inside the SZ at a tool offset of 2.5 mm. The EDS elemental mapping and point analysis confirm the existence of steel fragments in the AA6061 matrix because the point P_1 exhibits an atomic percentage of Fe atoms higher than 95%, as shown in Fig. 6.20. In the published literature [68,81], it was observed that the coarse steel

fragments produced the voids/cracks inside the SZ and provided an adverse effect on the joint strength.

6.5 MECHANICAL PROPERTIES

The microstructural heterogeneity, defects, and distribution of IMCs and steel fragments inside SZ are significantly influenced the mechanical performance of welded joints. Figs. 6.21(a–g) show that the pin offset variations are significantly affected the fracture path indicated by the dotted lines in the weld cross-section. The fractured tensile samples and tensile properties under varying tool offset conditions are shown in Figs. 6.21(h) and 6.21(i), respectively. The fractured surfaces of tensile specimens were characterized through fractographic SEM analysis to understand the failure mechanism, as shown in Fig. 6.22.

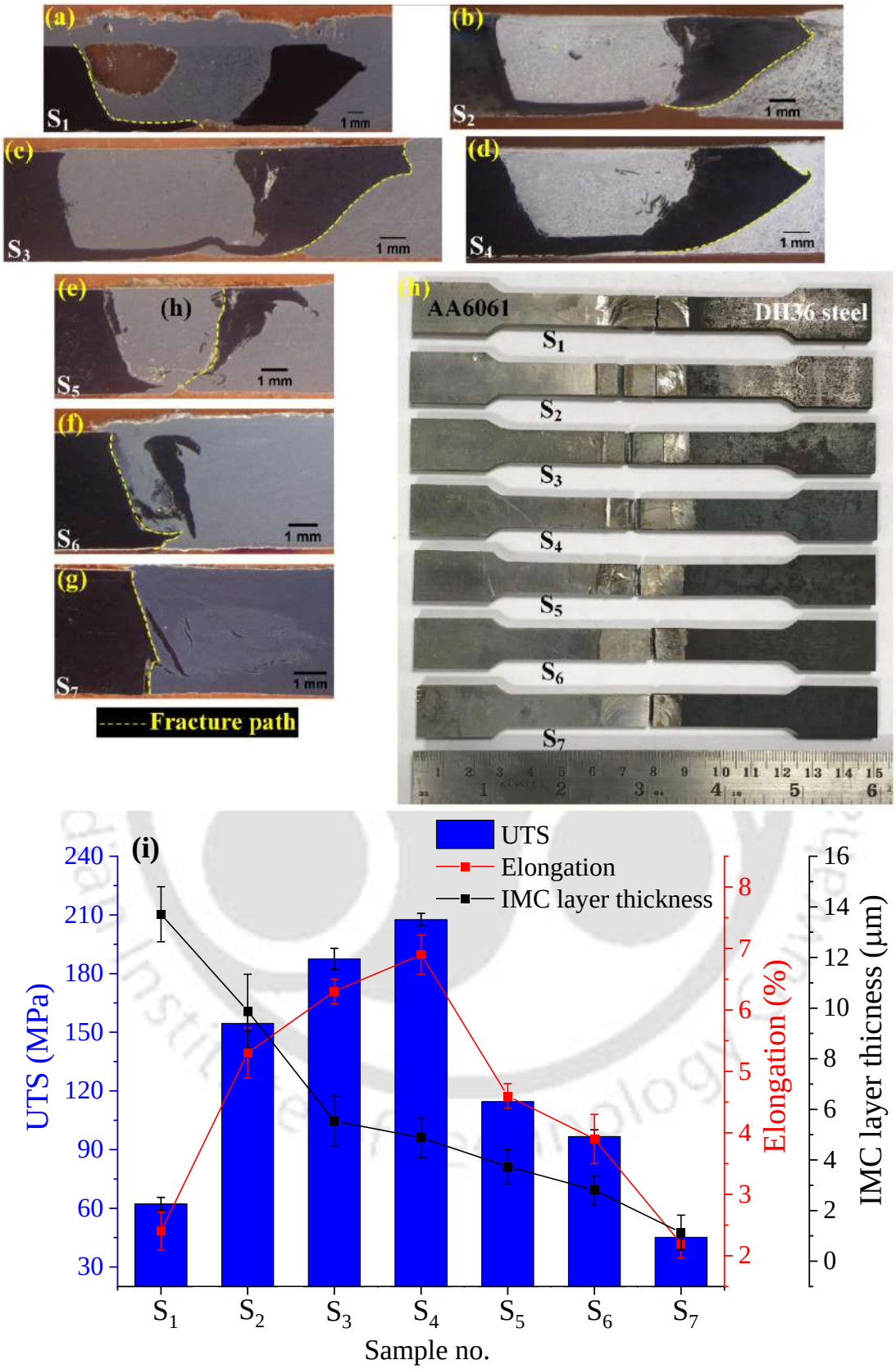

Fig. 6.21 *(a–g) Fracture path in the weld cross-section; (h) fractured tensile welded samples; and (i) effect of tool offset on tensile properties and IMC layer thickness*

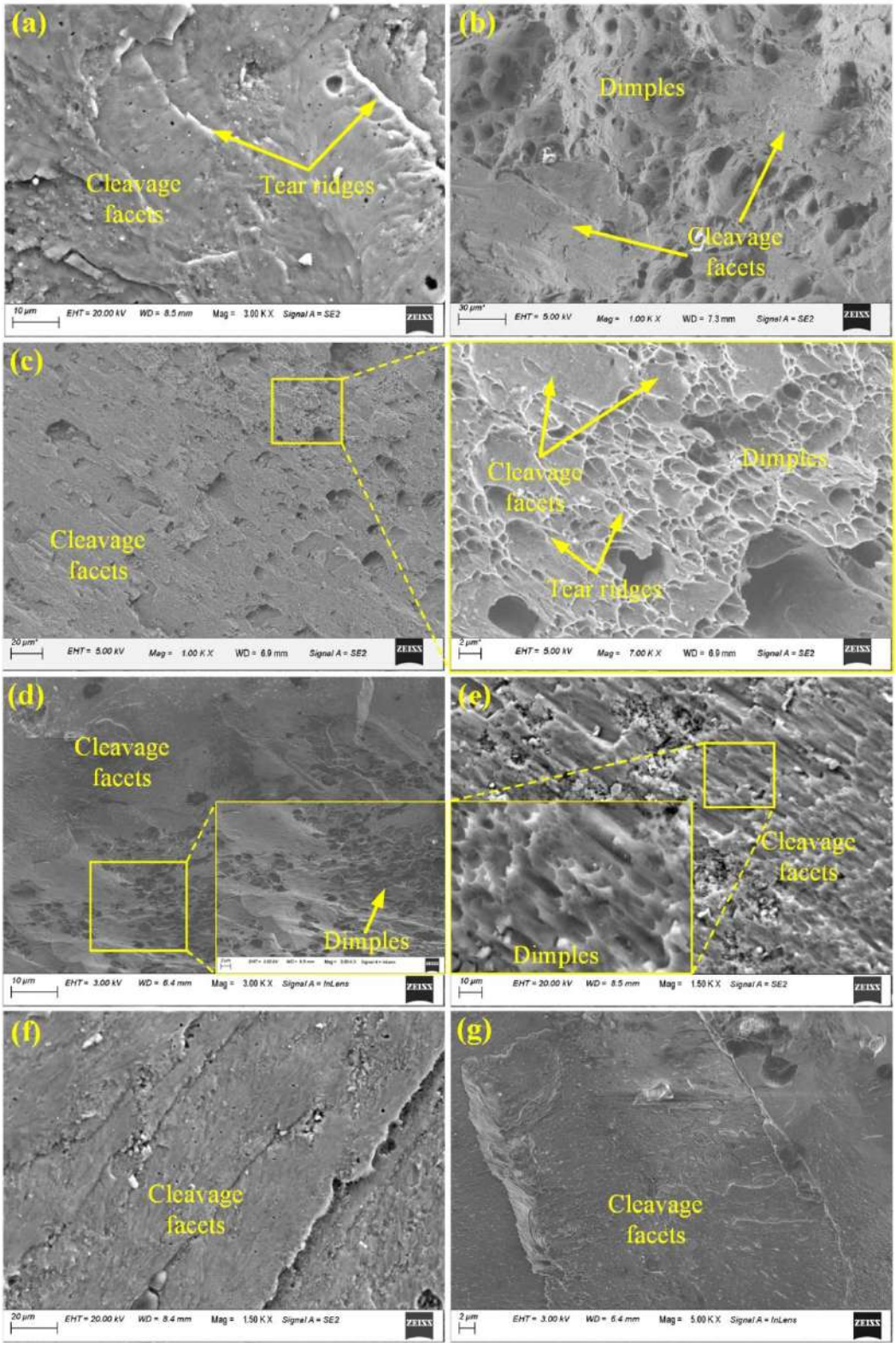

Fig. 6.22 *Fractography of fractured surface in tensile sample (a) S_1; (b) S_2; (c) S_3; (d) S_4; (e) S_5; (f) S_6; and (g) S_7*

It is observed that the UTS and elongation increased with an increase in tool offset up to 1.5 mm; however, these values are reduced by further enhancing the tool offset from 1.5 mm to 2.5 mm, as shown in Fig. 6.21(i). The reduction in UTS and elongation below tool offset of

1.5 mm is attributed to the generation of the voids inside the SZ due to the higher intensity of brittle Al_3Fe IMCs (Fig. 6.19) and thicker IMC layer of Al_3Fe and Al_5Fe_2. Hussein et al. [3] reported that the Al-rich IMCs, namely Al_3Fe, Al_2Fe, and Al_5Fe_2 are more detrimental to joint strength than Fe–rich IMCs like AlFe and $AlFe_3$. The Al-rich IMCs also reduced the ductility of the weld joints since these are more brittle than the Fe-rich IMCs [45]. In the thick IMC layer, the cracks could easily initiate and propagate through the hard IMC tangles, which Bozzi et al. [192] verified during the friction stir spot welding of Al6016 Al alloy and IF-steel. The change in phase volume of the excessively thick IMC layer caused stress concentration and deteriorated the bearing capacity of the weld joint. Apart from the IMC layer, the brittle IMCs inside the SZ lowered the joint strength because they constrained the material flow through their pinning action during the tensile testing. The tensile sample (S_1) fractured at the inner Al/steel interface, and the fractured surface revealed the brittle fracture mode through only cleavage facets, as shown in Fig. 6.22(a). Sample S_2 is fractured at the outside interface of the steel strip and experienced a tensile strength slightly larger than the sample S_1 due to relatively smaller voids, less intensity of IMCs in SZ, and smaller IMC layer thickness. Samples S_3 and S_4 fractured away from the SZ at the outside Al/steel interface of the continuous steel strip. The UTS of sample S_3 is lower than S_4, which is attributed to the relatively higher IMC layer thickness and defect generation like cracks and voids in SZ (Fig. 6.3). Sample S_4 exhibited the maximum UTS of 207.6 MPa, which is about 76.16% of the AA6061 base material. The fine-grained microstructure in the steel strip provided the inherent mechanical interlocking to the defect-free SZ, which improved the weld strength of sample S_4 compared to other tool offset conditions. The less brittle Fe–rich IMCs, such as AlFe and $AlFe_3$ (Fig. 6.16), and mechanical interlocking in the mixing region could also improve the weld strength [101]. Some brittle cleavage facets with irregularly shaped dimples are observed in the fractured surface of the tensile samples S_2, S_3, and S_4, as shown in Figs. 6.22(b–d), which indicated the combined ductile-brittle failure mode. It is observed that the samples S_5–S_7 experienced significant grain refinement in the SZ (Fig. 6.9) and a reducing trend of IMC layer thickness, as shown in Fig. 6.21(i), which are believed to be favourable for joint quality. However, the large cracks and voids at the interface of steel fragments and the AA6061 matrix (Fig. 6.3) dominated these strength-enhancing factors and reduced the UTS and elongation. A similar adverse effect of coarse steel fragments on the joint strength was observed by Ramachandran et al. [83]. The brittle IMCs, namely Al_2Fe with AlFe inside the MZ of samples S_5 and S_6 (Fig. 6.16) could also reduce the joint strength. Sample S_5 fractured at the interface between the coarse steel fragment and the AA6061 matrix. The fracture paths in samples S_6 and S_7 shifted from SZ to

the inner Al/steel interface. Sample S_7 experienced the lowest tensile strength compared to other tool offset conditions due to larger cracks at the inner Al/steel interface (Fig. 6.3). Yazdipour et al. [81] also obtained the lowest tensile strength due to cracks at the interface, which were produced by the insufficient stirring between materials when the pin surface just contacted the steel side or completely put in the Al side. Sample S_5 fractured under the combined ductile-brittle mode, as shown in Fig. 6.22(e); however, samples S_6 and S_7 fractured almost caused by the brittle fracture mechanism, as shown in Figs. 6.22(f) and 6.22(g). During the tensile test, the micro-cracks grow up, join together and generate the larger cracks under straining conditions [81], which resulted in a sudden fracture.

Figs. 6.23(a–d) show the Vickers micro-hardness profiles at the centre of weld cross-section for samples S_2, S_4, S_5, and S_6, respectively. The hardness profiles exhibited the oscillation behaviour caused by the different physical and mechanical properties of base materials, grain size variation, and spreading of the IMCs and steel fragments inside the AA6061 matrix.

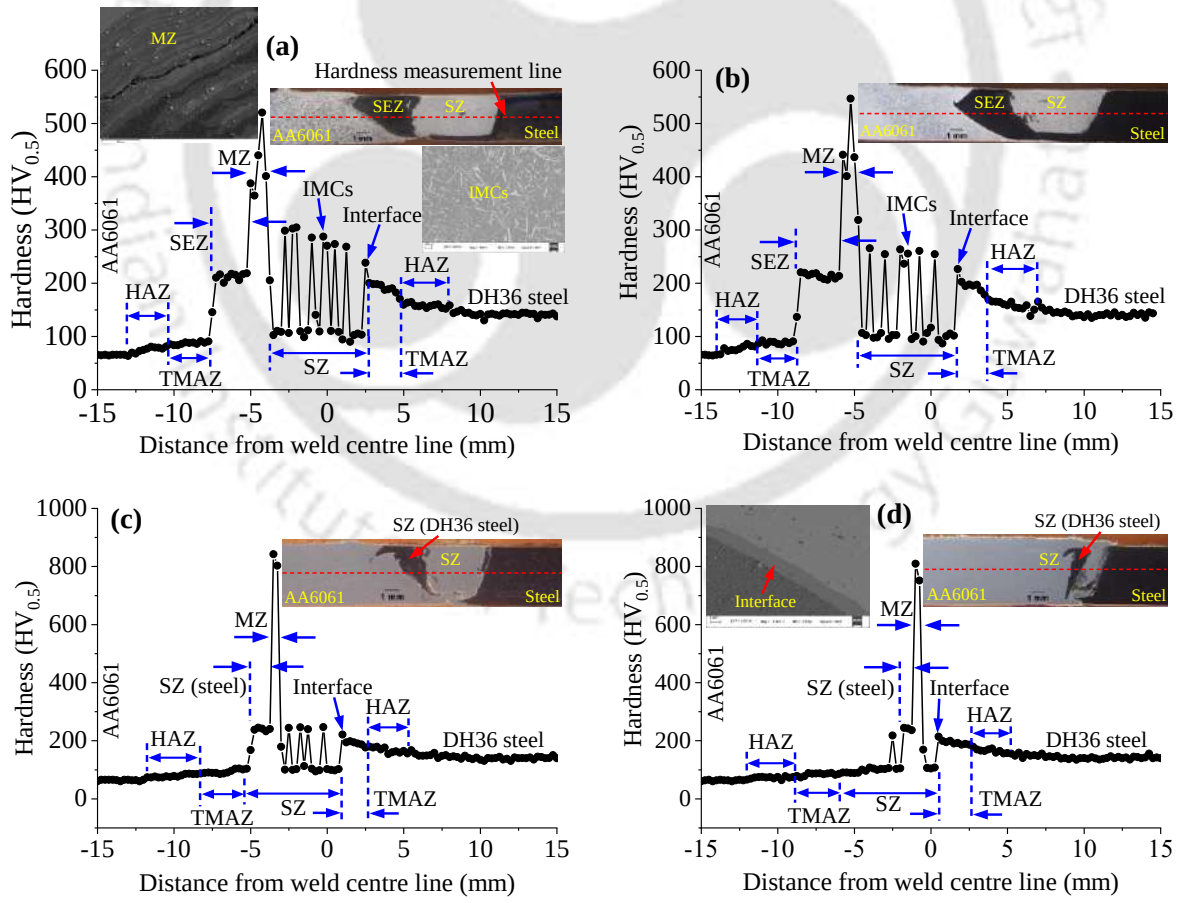

Fig. 6.23 *Hardness profiles at the centre of the weld cross-section in sample (a) S_2; (b) S_4; (c) S_5; and (d) S_6*

In samples S_2 and S_4, SEZ experienced the hardness higher than TMAZ and HAZ but lower than the SZ, as shown in Figs. 6.23(a) and 6.23(b), which could be related to microstructural variation (Fig. 6.9). The Hall-Petch strengthening suggests that the grain refinement improves the microhardness across the weld cross-section [16]. Thus, the significant grain refinement in SZ (DH36 steel) of samples S_5 and S_6 produced higher hardness as compared to that of SZ (AA6061), as shown in Figs. 6.23(c) and 6.23(d). The hardness values in TMAZ and HAZ are significantly higher than the base materials but lower than the SZ. The lower hardness in the HAZ signified that no significant metallurgical variation happened due to the low temperature at this zone. The low hardness at TMAZ (AA6061) compared to SZ could be attributed to the lower dislocation density due to the thermomechanical behaviour of this region. The hardness magnitudes reduced as approaching the base materials and turned into almost the hardness level of DH36 steel and AA6061 base materials. In the dissimilar FSW of steel and Al, apart from grain refinement, the other mechanisms like material flow, material inter-mixing, and distribution of IMCs and steel fragments are also responsible for hardness variation across the weld cross-section. The peak values in the hardness profiles mainly contributed to the IMCs and steel fragments in the SZ. The magnitudes of the hardness spikes reduced with an increase in tool offset are related to the IMCs area in SZ, which declined by shifting the tool towards the AA6061 (Fig. 6.19). The SZ acted as an Al matrix composite because the IMCs and steel fragments reinforced the SZ due to their relatively higher hardness than base materials [65]. The hardness magnitudes at the Al/steel interface (IMC layer) are higher than the AA6061 matrix inside SZ but lower than the individual IMCs distributed inside the SZ and MZ. Due to the limiting width of the hardness indenter, the microhardness impression covered some regions belonging to the AA6061 matrix during the measurement at the Al/steel interface. The soft Al matrix lowered the hardness magnitude at the interface relative to individual IMCs inside SZ and MZ. In current findings, the hardness spikes by intermetallic phases are within the range mentioned in the published literature [3,193]. The MZ experienced the highest hardness due to the extensive IMCs formation in this region (Fig. 6.16), which contributed to the brittle fracture mode. Anaman et al. [82] also reported the mixed layer as the hardest region due to Al–Fe solid solutions and IMCs. In samples S_1–S_4, the AlFe + $AlFe_3$ enriched MZ experienced the hardness magnitude in the range of 300 HV–515 HV, whereas the hardness magnitudes of 400 HV−951 HV are observed in the AlFe + $AlFe_3$ enriched MZ of samples S_5 and S_6. These hardness magnitudes are within the range reported by Hussein et al. [3]. Their study reported the hardness of different IMCs as AlFe: 400 HV–667 HV, $AlFe_3$: 330 HV–368 HV, and Al_2Fe: 1000 HV.

Consequently, from the experimental investigation, it is observed that the mechanical properties, especially tensile strength and hardness are significantly affected by microstructural variation, IMCs formation, and steel fragments inside the SZ. From Figs. 6.21 and 6.23, It is found that the IMC layer and scattered IMCs in SZ improved the hardness magnitudes. However, the thick IMC layer and extensive IMCs formation reduced the joint strength of samples S_1–S_3. Similarly, the grain refinement in steel fragments of samples S_5–S_7 enhanced the hardness magnitude in SZ, whereas the defects like cracks and voids created by steel fragments reduced the strength of the joints. From the present working conditions, sample S_4 achieved the successful weld quality at a tool offset of 1.5 mm with an average IMC layer thickness of 4.88 ± 0.79 µm. At this tool offset, the MZ is composed of less brittle IMCs, namely AlFe and $AlFe_3$. Additionally, the grain refinement in the steel strip provided the inherent mechanical interlocking to the SZ and improved the weld strength.

6.6 SUMMARY

In this chapter, the experimental findings on the joining of high-strength shipbuilding grade steel, i.e., DH36 steel with AA6061 are discussed. In this work, the macro/microstructure and IMCs formation in the various regions, such as Al/steel interface, SZ, and MZ was examined at different tool offset conditions. Furthermore, their subsequent effect on the mechanical properties of the welded joints was investigated.

It is observed that the tensile properties of the welded joints are substantially influenced by the formation of different IMCs. The ultimate tensile strength (UTS) increased with an increase in tool offset from 0.4 mm to 1.5 mm and then reduced with a further increase in tool offset from 1.5 mm to 2.5 mm. Sample S_4 (i.e., tool offset of 1.5 mm) exhibited the maximum UTS of 207.6 MPa, which is about 76.16% of the AA6061 base material. The reduction in UTS and elongation below tool offset of 1.5 mm is attributed to the generation of the voids inside the SZ due to the higher intensity of brittle Al_3Fe IMCs and thicker IMC layer of Al_3Fe and Al_5Fe_2. The brittle IMCs, namely Al_2Fe with AlFe inside the MZ at 1.8 mm and 2.2 mm tool offset further reduced the joint strength. The tool offset of 2.5 mm produced the lowest tensile strength compared to other tool offset conditions due to larger cracks at the inner Al/steel interface. The irregular distribution of hardness is attributed to the scattering of steel fragments and Al_3Fe IMCs inside the AA6061 matrix. The MZ acted as the hardest region due to the extensive IMCs formation in this zone.

CHAPTER 7

NUMERICAL STUDY ON THE JOINING OF DH36 STEEL AND ALUMINUM ALLOY

The previous chapter discussed the comprehensive experimental findings, including the metallographic and mechanical performance of the AA6061 and DH36 steel joints. Understanding of the temperature fields by triggering material flow associated with the tool–material interaction is also very substantial in eradicating defects from dissimilar weld joints, which is difficult through simple experiments. On the other hand, the numerical simulation of dissimilar FSW involves very complex multi-physical phenomena in heat generation, material movement, materials intermixing, and plastic deformation. The current chapter presents the numerical analysis of material flow behavior in AA6061 and steel joints. In this work, the volume of fluid (VOF) based multiphase CFD simulation was performed by incorporating a modified analytical model for dissimilar FSW of DH36 steel and AA6061. The impact of different rotational speeds on the temperature and plasticized material flow associated with the tool–material interaction was investigated. Based on the experimentally obtained feasible welding parameters, the calculated temperatures were validated with experimental results. Furthermore, the numerical results are also correlated/verified through their subsequent impact on the metallographic/mechanical behaviour of the joints. Finally, this chapter summarizes the crucial outcomes of the multiphase CFD modelling, correlated with experimentation.

7.1 PROCESS PARAMETERS

A three-dimensional multiphase CFD modelling based on the non-Newtonian viscoplastic, incompressible, and quasi-static steady-state behaviour was performed. The tool pin was shifted towards the AA6061 side by 1.5 mm from the weld line to avoid the tool wear and overheating of the Al alloy. The constant plunge depth of 0.1 mm was applied for all the experiments and simulations. Based on the preliminary experimental trials, the welding speed of 90 mm/min was selected to determine the impact of different rotational speeds on the weld characteristics and plasticized material flow behaviour. Table 7.1 shows the chosen values of the rotational speeds for detailed experimental and numerical investigation.

Table 7.1 *Rotational speeds for experimental and numerical investigation*

Sample no.	SN_1	SN_2	SN_3	SN_4
Rotational speed (rpm)	450	600	875	1200

The five planes are considered to understand the material flow characteristics in detail. At the mid-section of the workpiece, planes P1 and P2 are considered in transverse and along the weld direction, respectively, as shown in Fig. 7.1(a). As shown in Fig. 7.1(b), the horizontal XY planes P3, P4, and P5 are considered along the thickness direction at 0.2 mm, 2 mm, and 3.8 mm from the top surface, respectively.

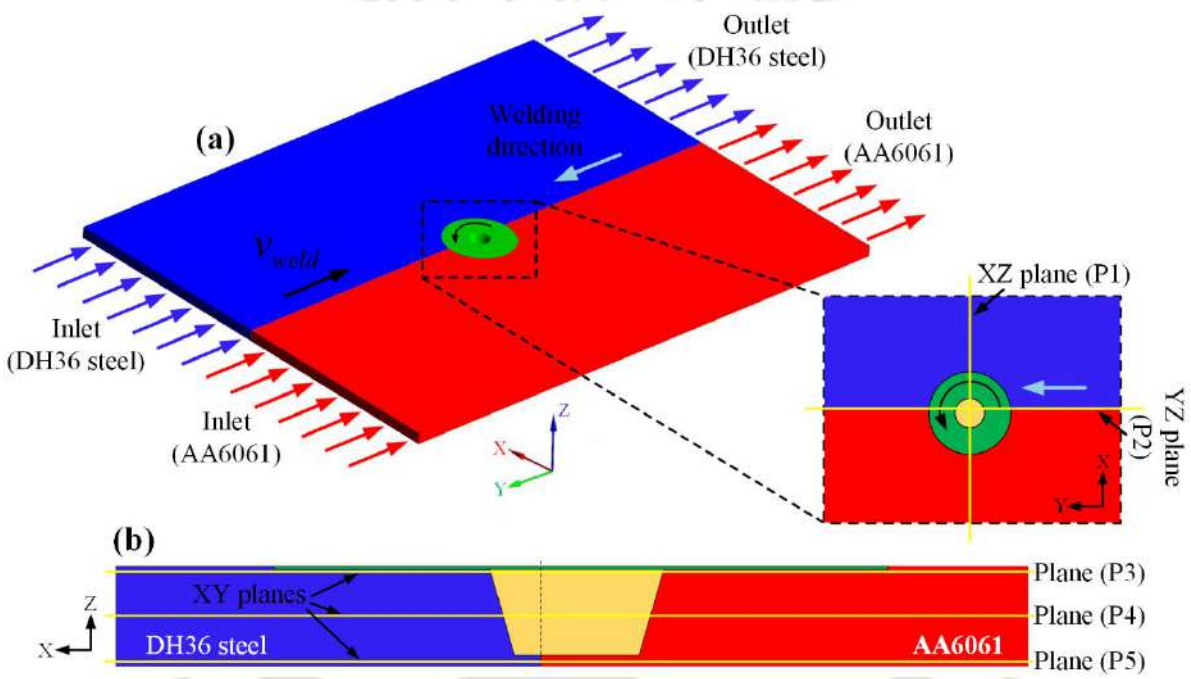

Fig. 7.1 *(a) CFD model for the dissimilar FSW; and (b) location of observation XY planes along the thickness direction*

7.2 VALIDATION OF THE CFD MODEL

The comparison of simulated results and experimentally measured temperature using an infrared thermometer and thermocouples are shown in Fig. 7.2. The transient temperature profiles recorded by K-type thermocouples at point T_1 positioned at 0.2 mm from the bottom surface. Due to the assumption of a steady-state welding stage, the thermal history at a specific point was captured by extracting the temperature curve across the line, which is parallel to the

weld line and passing through that point. Then, the transient temperature profile at a particular distance is calculated using the welding speed.

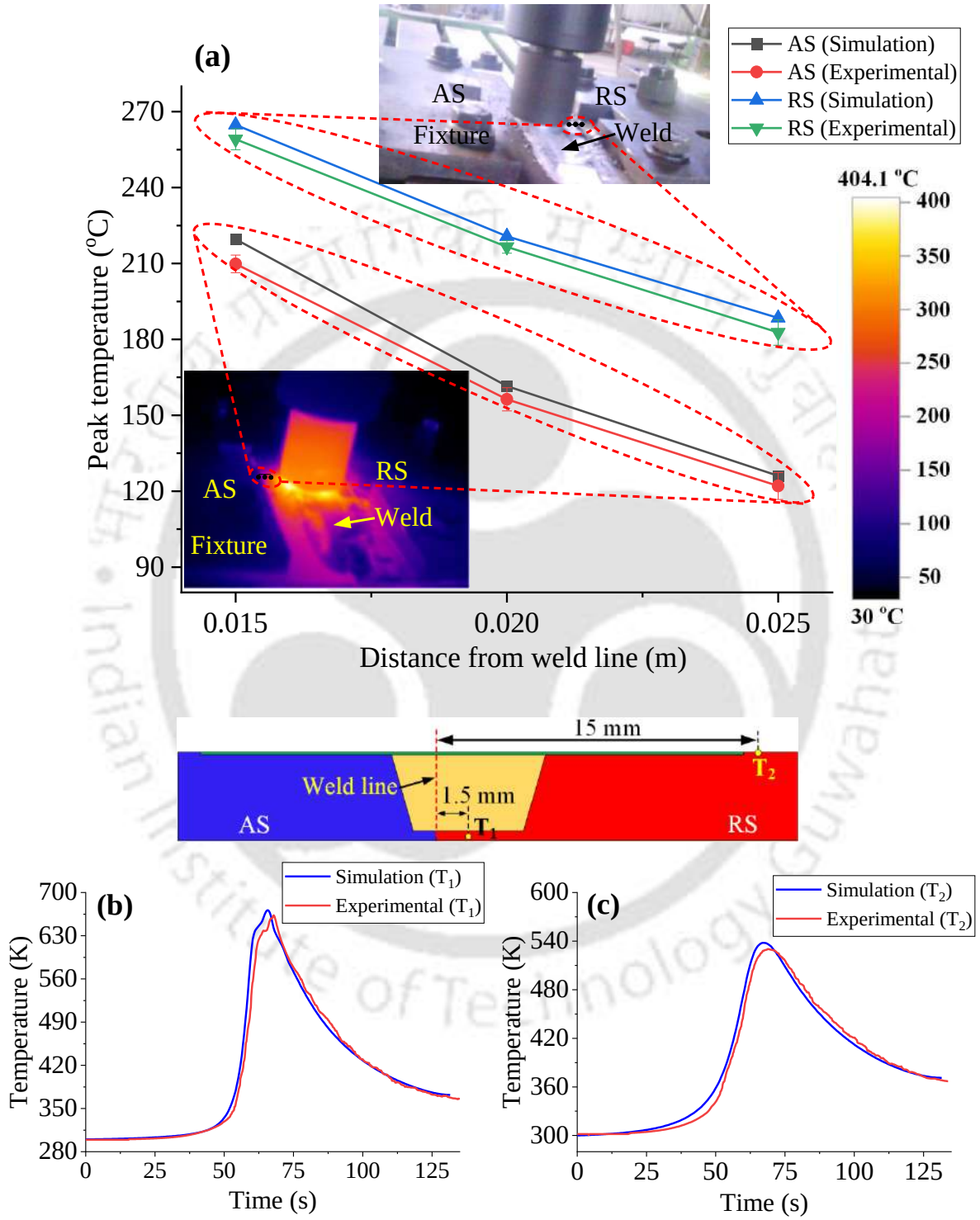

Fig. 7.2 *Comparison of simulated results and temperature recorded by (a) infrared thermometer; and (b,c) K-type thermocouples*

In sample SN_3, the calculated temperature magnitudes and profiles matched fairly well with the experimentally measured ones. The variance between the simulation and experimental results was less than 4%. The slight variance is due to the constant friction, convection, and radiation losses considered for the numerical model. Furthermore, minor errors could arise during the experimental measurement, influencing the reliability of the results.

7.4 MATERIAL FLOW AND METALLOGRAPHIC ANALYSIS

Fig. 7.3 shows the dynamic viscosity around the tool at varying rotational speed. It is observed that the viscosity around the shoulder and pin is lesser than the other locations caused by the higher heat generation, as shown in Figs. 7.3(a–d). An asymmetric viscosity field on both sides is observed due to a difference in the thermo-mechanical properties of base materials. The lowest viscosity is found at the outer shoulder edge on the AA6061 side, where the material flow velocity and strain rates were also maximum from the entire domain, discussed in the next section. In addition, the minimum viscosity of the material decreased with an increase in rotational speed due to higher heat input.

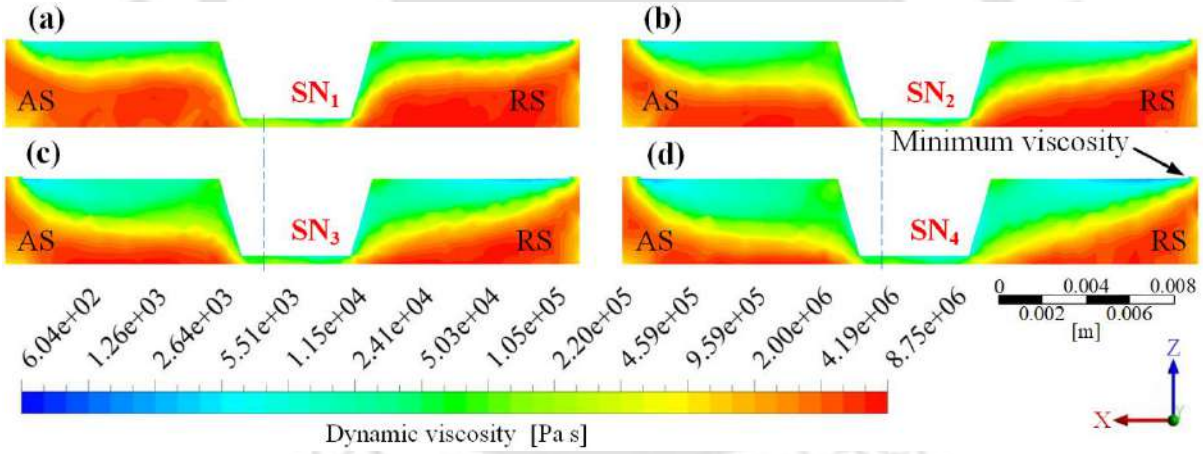

Fig. 7.3 *(a–d) Viscosity variation at varying rotational speed*

In this work, the axial force was measured at different welding conditions, and its variation is related to the temperature and dynamic viscosity of the material. Fig. 7.4(a) shows the axial force profiles at different rotational speeds. The axial force increased sharply when the tool shoulder contacted the material during the plunging phase. The peak values during the plunging phase are 8993.2 N, 8083.8 N, 7524.5 N, and 6857.7 N in samples SN_1–SN_4, respectively.

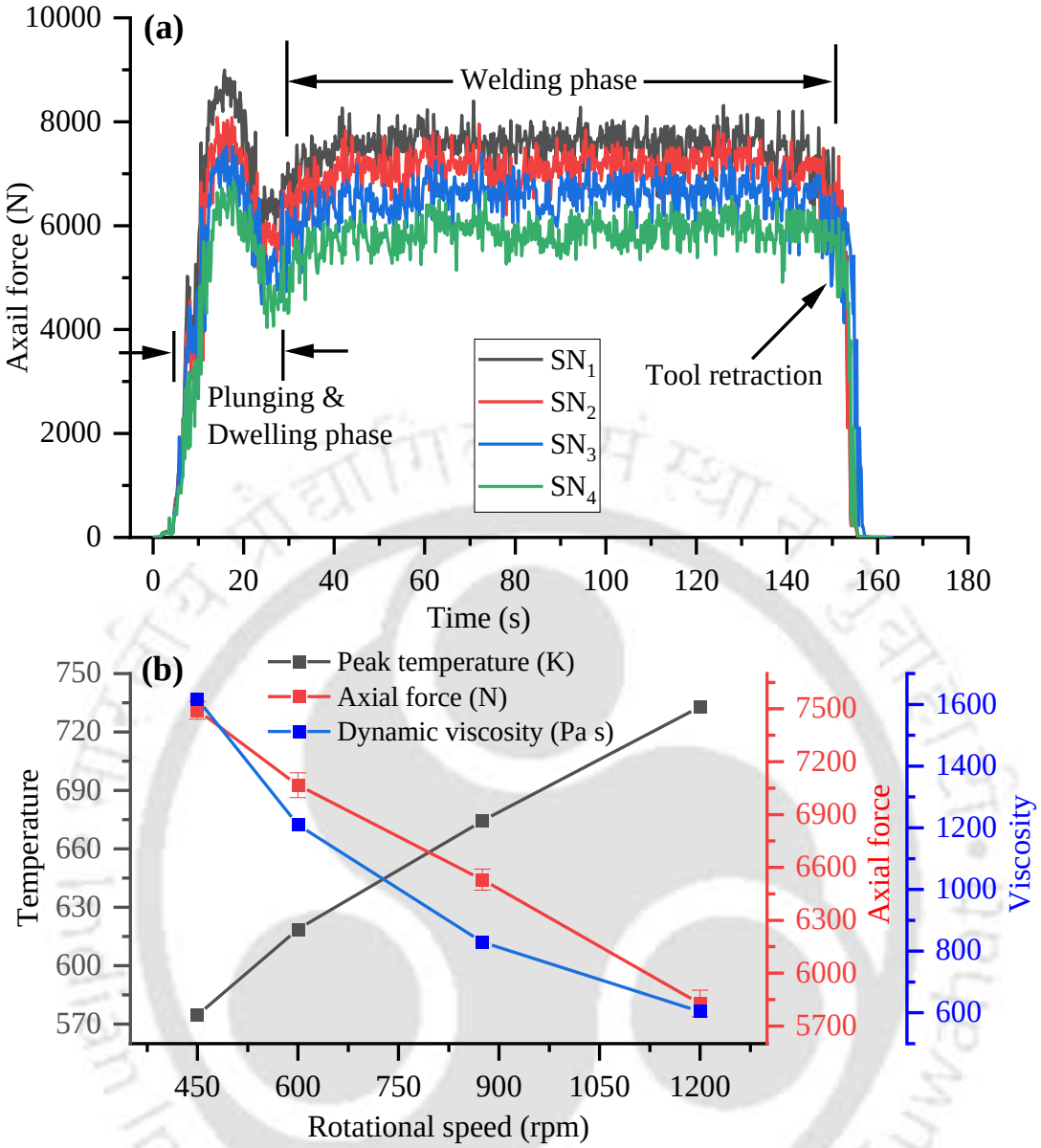

Fig. 7.4 *(a) Axial force variation; and (b) average axial force, peak temperature, and viscosity variation at varying rotational speed*

The lack of thermally softened material and contact inconsistency between the tool-workpiece material produced the most variance in axial force during the plunging phase. The axial force is lowered due to the greater frictional heat during the dwell phase. After that, the axial force is generated consistently with minor changes throughout the traverse phase since the workpiece material near the tool is adequately softened. As shown in Fig. 7.4(b), the average axial force during the welding phase was reduced from 7491.8 ± 50.2 N to 5828.1 ± 75.1 N by increasing the rotational speed from 450 rpm to 1200 rpm. The increase in peak temperature from 450 rpm to 1200 rpm reduced the dynamic viscosity of the dissimilar materials, which led to a decrease in the axial force.

In this study, the top section of the welded region is designated as the shoulder-affected zone (SAZ) because the shear and extrusion of the tool shoulder generate the primary driving force for the material flow in this zone. The middle and the lower sections are defined as the pin-affected zone (PAZ), where the driving force for the material flow originates mainly from the shear of the tool pin side. The 3D material flow velocity around the tool in sample SN_4 is shown in Fig. 7.5(a). Fig. 7.5(b) shows the materials flow vectors for intermixing of DH36 steel and AA6061, which can regulate the reaction-diffusion among the elements at the Al/steel interface. The material flow in transverse and horizontal cross-sections at the planes P3 (top), P4 (middle), and P5 (bottom) is shown in Fig. 7.5(c). The corresponding material velocity profiles with magnitudes along the transverse plane (P1) at different rotational speeds are shown in Figs. 7.6(a–d). The simulation results revealed that the velocity at the AA6061 side (RS) is higher than the DH36 steel side (AS). It is observed that the SAZ, i.e., plane (P3) exhibited a stronger plastic flow of material than that of the middle and bottom planes, as shown in Fig. 7.5(c). This is because the heat generation and radial distance are greater in this region, which resulted in higher linear velocity during the tool rotation. No plastic flow occurred in regions away from the tool, where the heat is transferred by conduction only. The horizontal planes P4 and P5 could be considered PAZ since the tool pin in these planes almost affected the material flow. From transverse velocity profiles shown in Figs. 7.6(a–d), it is also observed that the influence of the shoulder and viscous momentum transfer at the top surface is greater, causing maximum velocity fields in the SAZ. The highest material velocity is observed at the outer edge of the tool shoulder on the AA6061 side due to the viscosity, heat transfer coefficients, and density effects in the momentum and energy equations. The higher momentum at the outside edge (outer region) of the shoulder apparently caused the maximum velocity in this region. The momentum decreases away from the shoulder in a negative z-direction, which results in the lowest velocity at the bottom region.

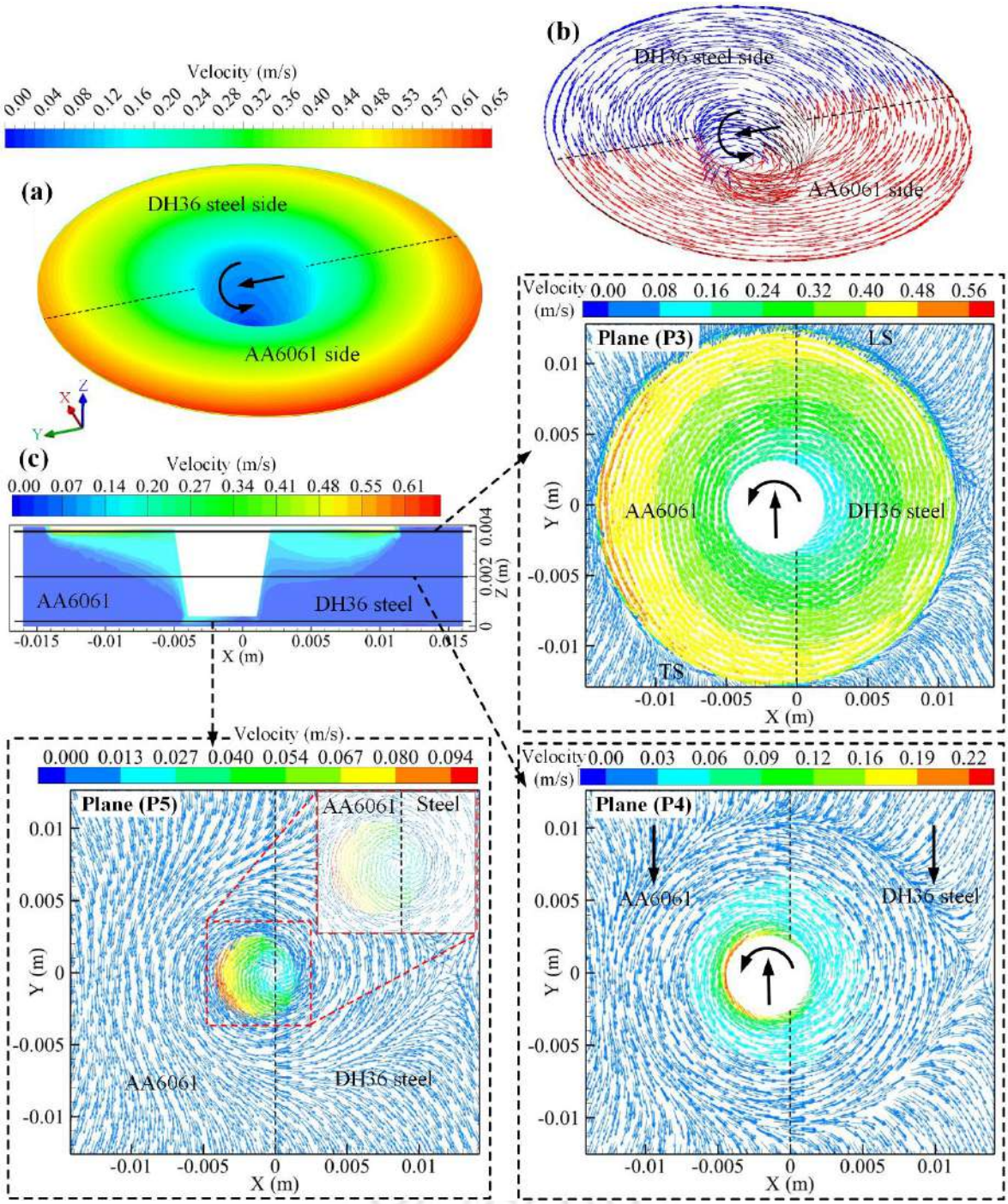

Fig. 7.5 *(a) Material velocity around the tool; (b) material flow vectors; and (c) transverse velocity profile and velocity vectors at different horizontal planes in sample* SN_4

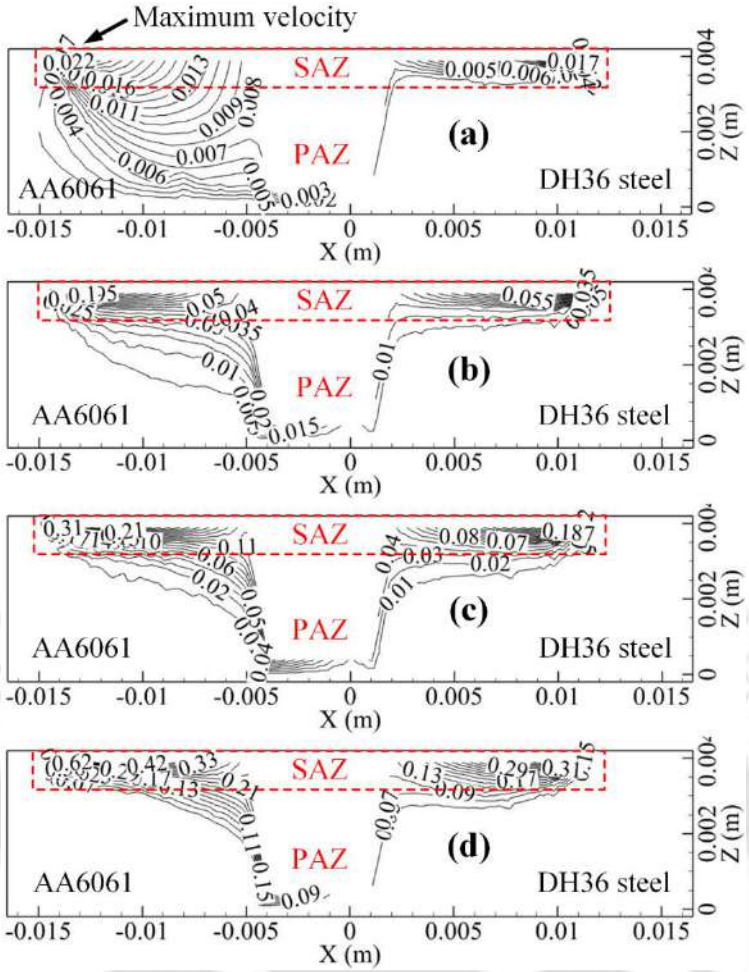

Fig. 7.6 *Material flow velocity profiles in sample (a) SN_1; (b) SN_2; (c) SN_3; and (d) SN_4*

The material velocity reduced as the distance between the edge of the tool shoulder and the centre of the SZ decreased. During the dissimilar FSW, two factors influence the velocity of material flow: primarily the thermal-mechanical properties of the two different materials, which substantially affect the degree of plastic deformation. In this investigation, material prone to plastic deformation (i.e., AA6061) had a greater flow velocity during the welding process. Secondary, the material flow velocity showed a gradient dispersion throughout the weld cross-section due to the asymmetric temperature distribution. The temperature is significantly affected the material viscosity, as shown in Fig. 7.3. The viscosity of the material decreased as the temperature increased; hence, the material flow velocity is enhanced. Furthermore, the maximum velocity is obtained as 0.024 m/s, 0.115 m/s, 0.326 m/s, and 0.66 m/s in samples SN_1–SN_4, respectively. The maximum velocity at the outer edge of the shoulder on the AA6061 side could also be related to the lowest viscosity in that region, as shown in Fig. 7.3. The viscosity is very low at the PAZ, and it increased as moved away from this region. As a result, material deformation is observed greater around the PAZ and less far away from

this region. On the front side of the tool, the deformed material flowed from AS to RS, and the shoulder rebounded the soft material back into the TS.

The weld characteristics depend on the flow of the plasticized material, which is further significantly affected by the temperature history. The degree of plastic deformation through velocity vectors at the plane (P4) at different rotational speeds is shown in Fig. 7.7.

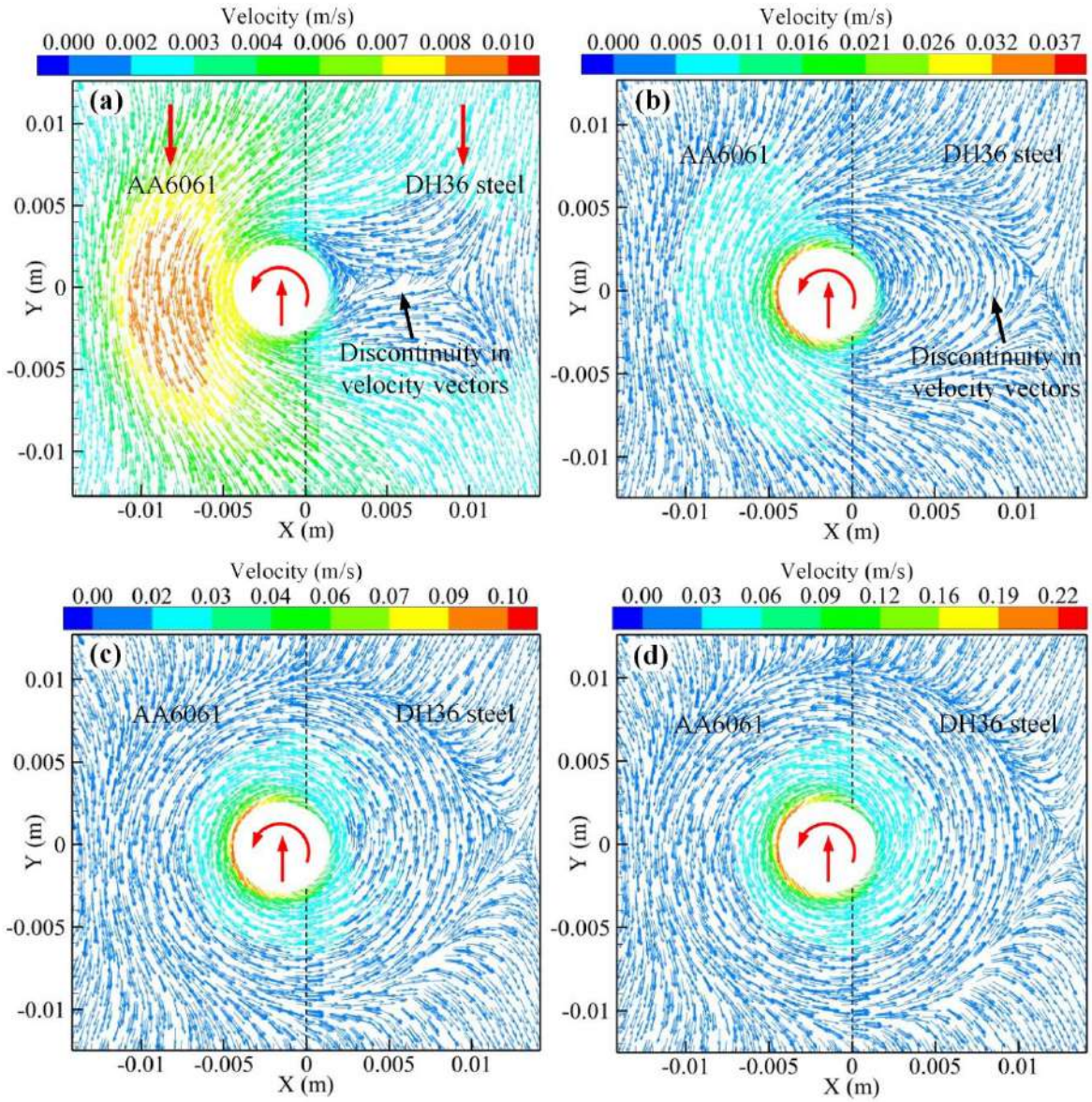

Fig. 7.7 *Velocity vector at the XY plane (P4) of sample (a) SN_1; (b) SN_2; (c) SN_3; and (d) SN_4*

Fig. 7.8 shows the velocity vectors at the plane (P5) and weld surface materials flow at different rotational speeds. In PAZ, velocity vectors at AS crossed the tool pin from RS to the trailing side of the tool. According to the velocity vectors, it can be concluded that the material squeezed at AS and sheared at RS. The velocity vectors also revealed that the plastic deformation at the AA6061 side is much higher than that of the DH36 steel side.

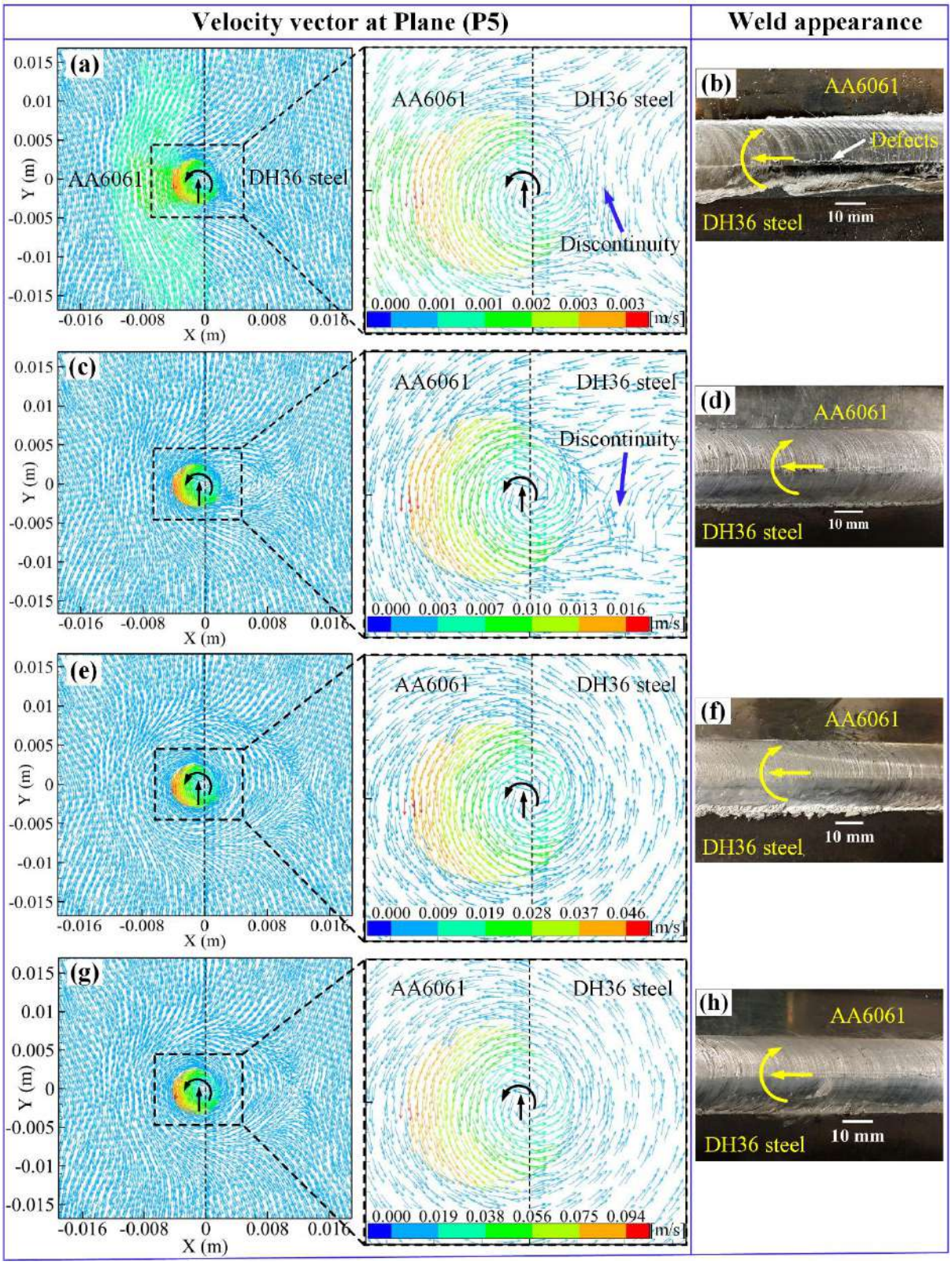

Fig. 7.8 *Velocity vector at the XY plane (P5) and weld appearance of sample (a,b) SN_1; (c,d) SN_2; (e,f) SN_3; and (g,h) SN_4*

In samples SN_1 and SN_2, the low rotational speed produced the discontinuous material flow in the PAZ at planes P4 and P5 due to relatively lower velocity at the steel side, as shown

in Figs. 7.7(a,b) and 7.8(a,c). The velocity vectors at PAZ in SN_1 and SN_2 indicated that the harder material, i.e., DH36 steel is not able to extrude easily from the AS at a low heat input, and subsequently created the discontinuity in the plastic flow of dissimilar materials. This discontinuity generated the surface defects, such as cracks on the weld surface, as shown in Fig. 7.8(b). However, the smooth surface appearance without any surface defects is observed in samples SN_2–SN_4.

Figs. 7.9 and 7.10 show the macrographs of welded samples at different welding conditions in various regions. The three primary zones in the dissimilar friction stir welded cross-section are the SZ, TMAZ, and HAZ with parent materials. In addition, a continuous steel strip extruded towards the AA6061 away from the SZ, named as steel extruded zone (SEZ) in SN_3 and SN_4, as shown in Figs. 7.10(a) and 7.10(b), respectively. From the cross-sectional point of view, the discontinuity in material flow produced the defects like cracks at the Al/steel interface of samples SN_1 and SN_2, as shown in Figs. 7.9(a) and 7.9(b), respectively. In samples SN_3 and SN_4, the higher heat generation softened the hard material and made it easier for DH36 steel to flow from AS to RS at sufficient velocity. Hence, the flow of plastic material is significantly improved and becomes more uniform in PAZ, as shown in Figs. 7.7(c,d) and 7.8(e,g). More plasticized material around the pin flowed from AS to RS due to the severe stirring action created by the rotating tool. Whereas, despite the uniform flow, the intense material mixing at higher welding temperatures and lower dynamic viscosity also produced the defects like cracks/voids in sample SN_4, as shown in Fig. 7.10(b). Steel fragments of irregular shapes separated from bulk DH36 steel and scattered throughout the SZ of all samples. Compared to the other tool rotational speed conditions, the extensive dispersion of steel fragments was identified inside the sample SN_1, as shown in Fig. 7.9(a). The bulk DH36 steel is not properly plasticized and could not flow to the top of the weld in lower heat input conditions. Moreover, irregularly shaped steel fragments from the bulk DH36 steel are detached and scattered at the bottom of SZ. The deformation and intermixing of the coarse steel fragments in the AA6061 matrix are challenging due to their comparatively higher density and hardness. The higher hardness and density of steel fragments limited the streamline flow of viscous aluminum. As a result, the viscous aluminum could not fill the small gaps between the steel fragments, resulting in defects, such as tunnels and cracks around the stirring periphery. Crack initiation is occurred mainly by these fragments, which increases the chance of macroscopic cracks with subsequent joint defects.

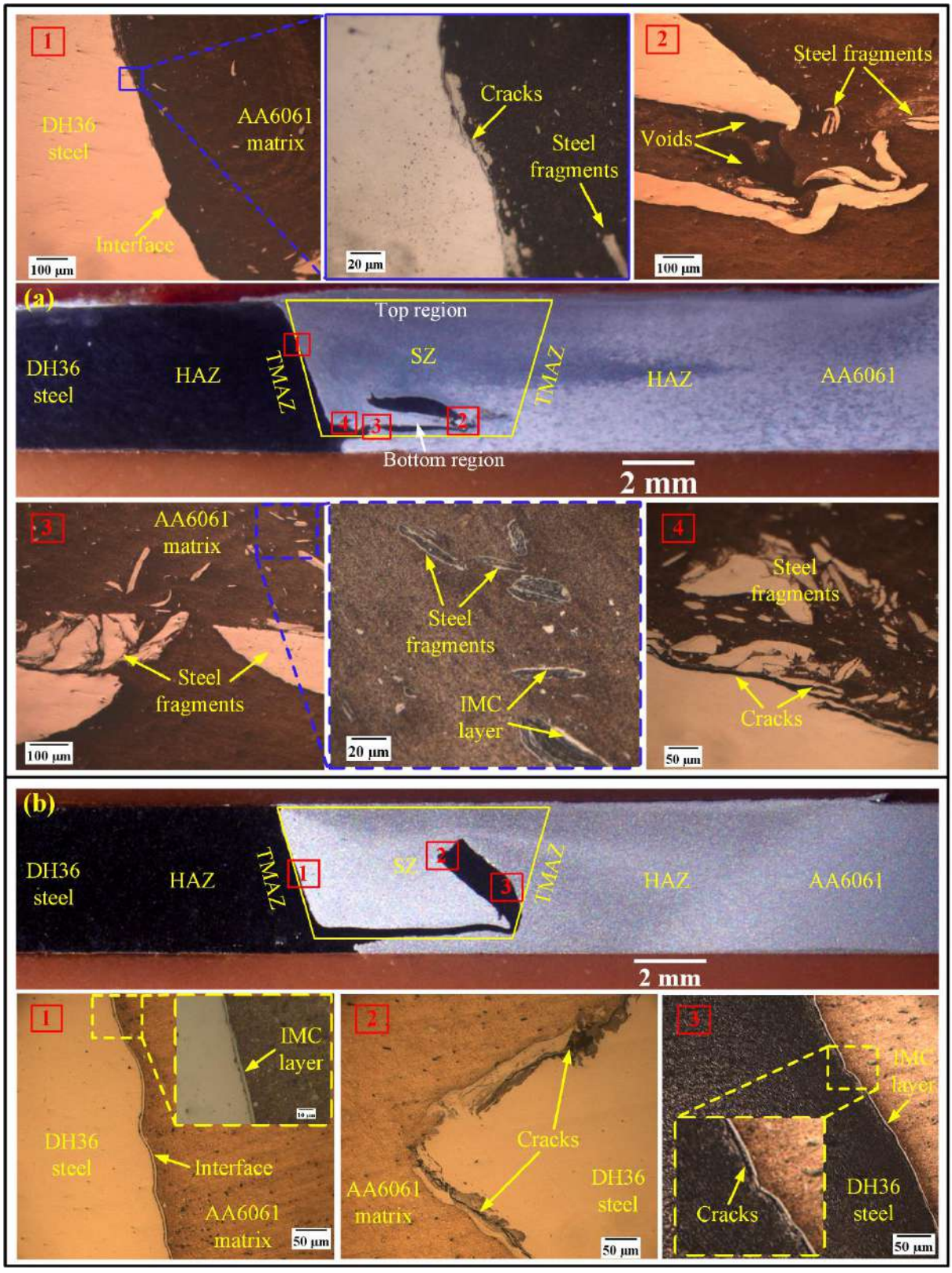

Fig. 7.9 *Various regions in macrograph of sample (a) SN_1; and (b) SN_2*

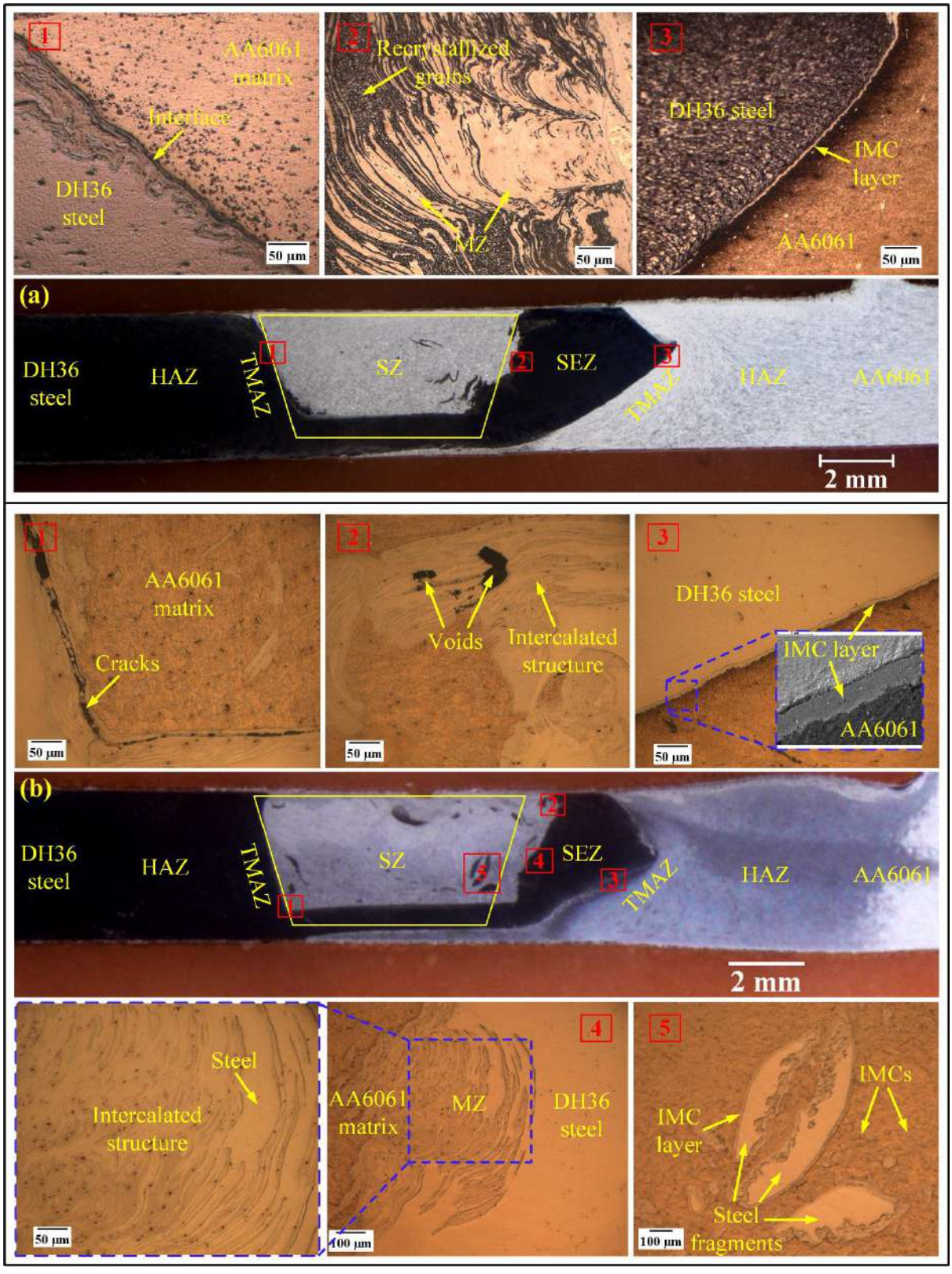

Fig. 7.10 *Various regions in macrograph of sample (a) SN_3; and (b) SN_4*

The material velocity at the bottom of SZ is lowest, as shown in Fig. 7.6(a); hence, it is easy to produce the defect here at low heat input, as shown in Fig. 7.9(a). Tang and Shen [153] agreed with this view. As shown in Fig. 7.10, a continuous strip from the base of the DH36

steel extruded from the SZ and transferred towards AA6061 in samples SN_2 and SN_3 due to increased material velocity at higher heat input. The lower heat generation and material velocity delayed the material revolution, causing the steel fragments to spread throughout the SZ. The axial force pushed the Al and steel downward, while the extrusion force of the backing plate (Fig. 1.10) restrained the downward movement at the bottom. The material at the bottom of the steel is compressed and transferred to AA6061 through the shallow route between the pin bottom surface and the backing plate. As shown in Fig. 7.10(a), no macro or micro defects are detected in the cross-section of sample SN_3 caused by the uniform material flow under sufficient heat generation. Furthermore, two different zones separated the Al/steel interface region: the IMC layer and mixed zone (MZ) at the Al/steel boundary. The solid-state diffusion process is generally responsible for the generation of the IMC layer, which is caused by the simultaneous effect of axial forging, frictional heating, and material extrusion from AS to RS. Besides the IMC layer, the individual IMCs separated from the interface and distributed inside the AA6061 matrix due to the stirring action of the rotating tool. Some of the steel fragments inside the SZ encompassed the IMC layer. These IMCs generated through the chemical reaction despite the only mechanical mixing between the sheared-off steel fragments and the AA6061 matrix. In the MZ, an intercalated layered structure with dark and light brown sections is detected, as shown in Fig. 7.10. These intercalated layered structures are produced adjacent to the weld interface at the steel side at different rotational speeds. Due to severe frictional heat generated by the rotational tool, the mixing and stirring of different materials usually formed these structures.

The temperature and strain rate history are significantly affected the microstructure evolution, material recrystallization, and, finally, mechanical characterization of the weld joints. Fig. 7.11 shows the calculated strain rate at different transverse planes around the tool, the microstructure of SZ (AA6061), and SZ (DH36 steel) at varying rotational speed.

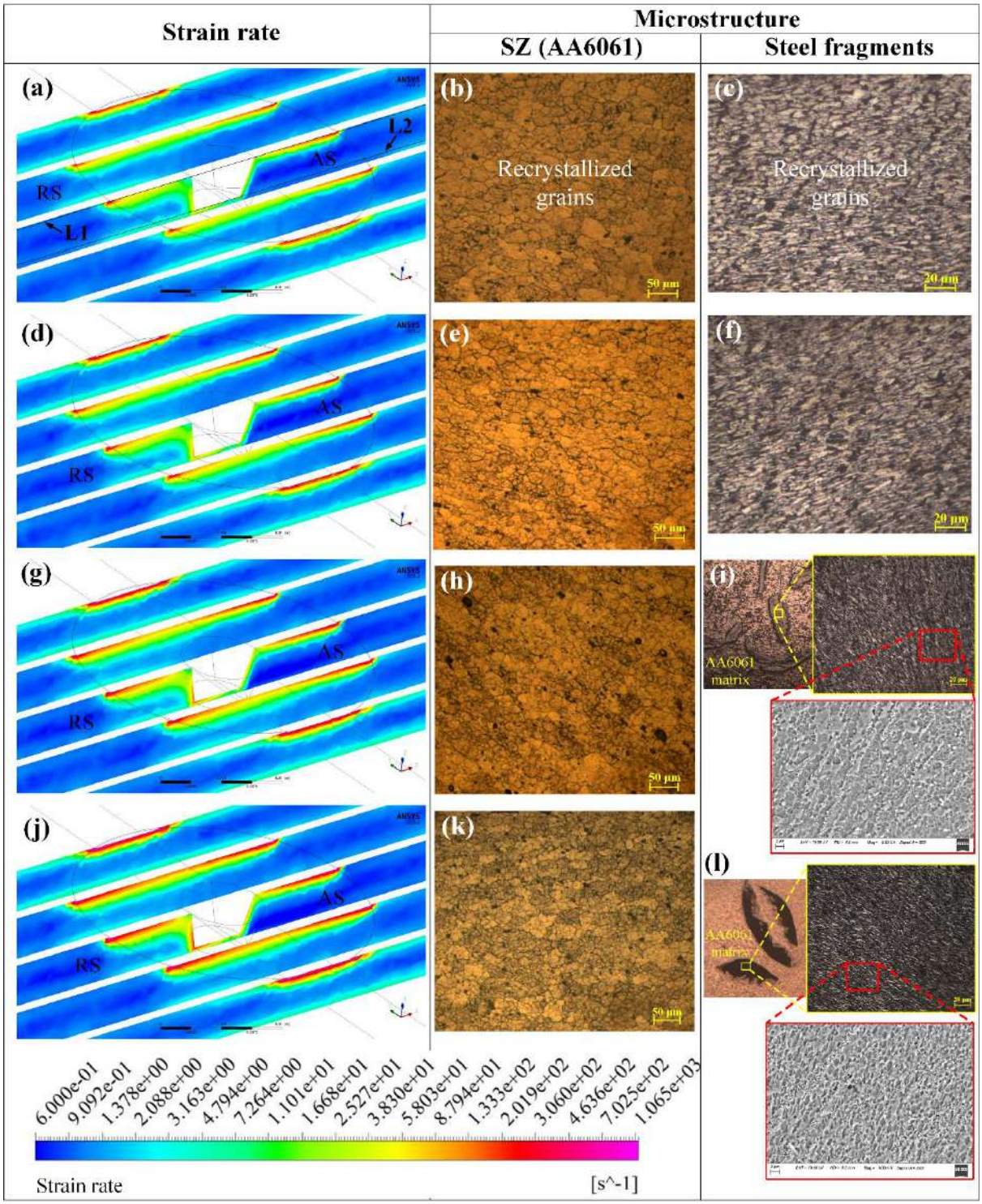

Fig. 7.11 *Strain rate, SZ (AA6061) microstructure, and SZ (DH36 steel) microstructure of sample (a–c) SN_1; (d–f) SN_2; (g–i) SN_3; and (j–l) SN_4*

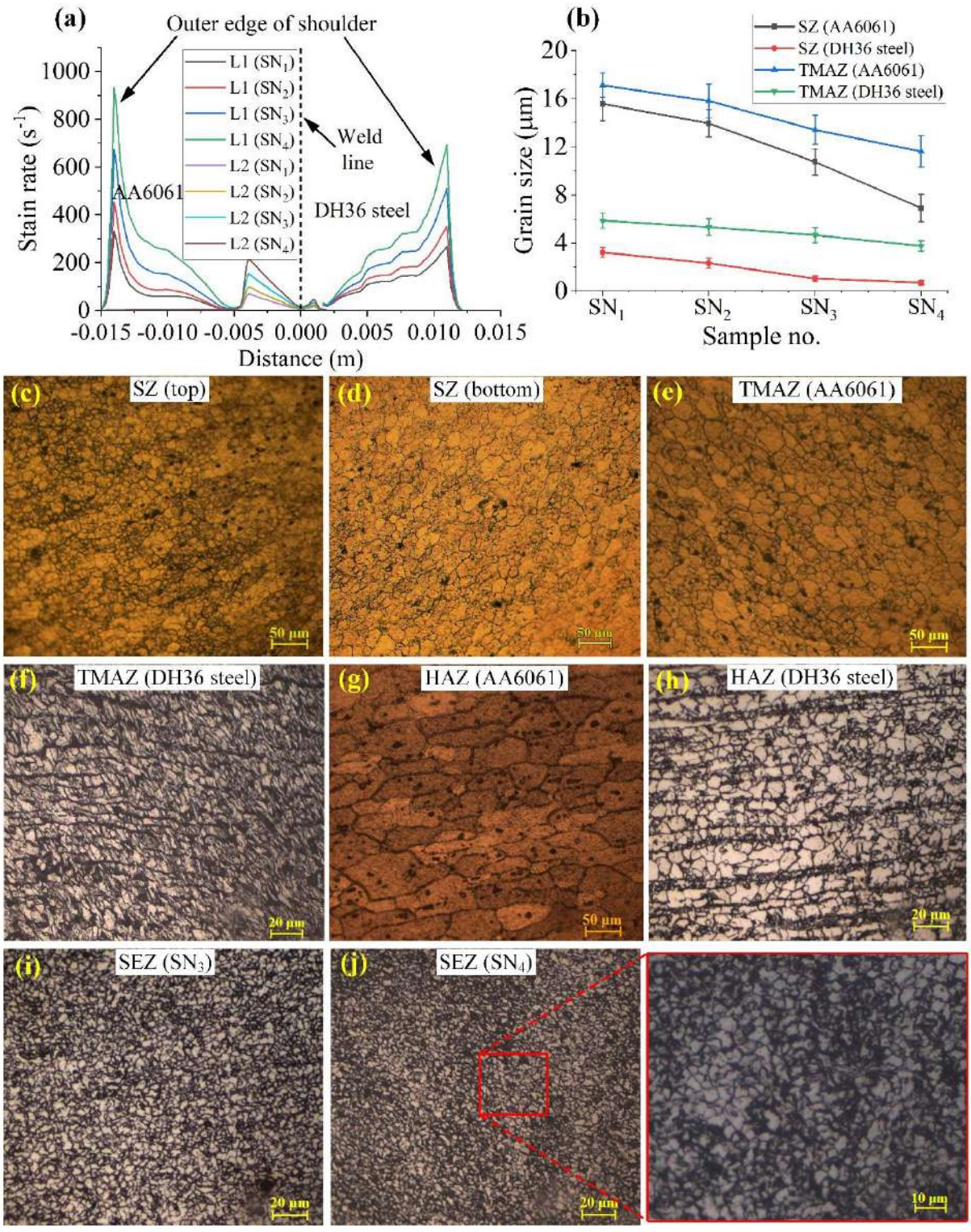

Fig. 7.12 *(a) Strain rate at top and bottom line at varying rotational speed; (b) grain size variation; microstructure of (c) SZ at top region; (d) SZ at bottom region; (e,f) TMAZ; (g,h) HAZ; and (i,j) SEZ*

The variation in temperature, deformation, and viscosity of plasticized material is significantly affected the strain rates. The maximum strain rate is observed at the SAZ and decreases towards the bottom area of the SZ. Furthermore, the strain rate is greater in the

bottom region due to the higher welding temperature nearby the pin tip. As shown in Figs. 7.11(a,d,g,j), with an increase in rotational speed from 450 rpm to 1200 rpm, the strain rate significantly increased from 414.04 s^{-1} to 1105.57 s^{-1} due to higher temperature. The strain rate profiles are plotted at top line L1 and bottom line L2 (marked in Fig. 7.11(a)) at 0.1 mm and 3.6 from the top surface, respectively. As shown in Fig. 7.12(a), the AA6061 side experienced a higher strain rate than the DH36 steel due to the greater welding temperature. The top line is subjected to more strain than the bottom due to greater frictional heat between the tool shoulder and workpiece. The strain rate is found to be maximum on the outer shoulder edge at the AA6061 side, where the flow velocity is also the highest.

In the FSW, grain refinement is interrelated to the stirring action of the rotating tool, which causes dynamic recrystallization due to the simultaneous effects of plastic deformation and frictional heating. The size of recrystallized grains is calculated as follows [194]:

$$d^{-1} = a + b\,ln(Z) \tag{7.1}$$

where d is the grain diameter, a and b signify the constitutive constants, and Z is the Zener-Hollomon parameter expressed in Equation (3.2). According to the above equation, when the Z-parameter is larger, the grain size is smaller due to the dynamic recrystallization (DRX). From Equation (7.1), the Z parameter increases with an increase in strain rate and a decrease in temperature. Figs. 7.11(b,e,h,k) and 7.11(c,f,i,l) show that the significant grain refinement occurred in SZ (AA6061) and SZ (DH36 steel) by increasing the rotational speed, respectively. Although the heat input is increased with an increase in rotational speed. However, the grain size variation is more sensitive to strain rate than the temperature for the employed materials. Sahu and Pal [195] reported that the greater strain rate under severe plastic deformation elongates the grains and divides them into smaller grains by the geometric DRX mechanism. The grain size in SZ considerably decreased from the 56.3 ± 2.1 µm and 15.9 ± 2.65 µm of AA6061 and DH36 steel base materials, respectively. As shown in Fig. 7.12(b), the average grain size in SZ lowered from 3.22 ± 0.4 µm to 0.7 ± 0.18 µm in DH36 steel and 15.56 ± 1.43 µm to 6.9 ± 1.14 µm in AA6061, when the rotating speed increased from 450 rpm to 1200 rpm. Whereas TMAZ exhibited the grain size reduction from 5.86 ± 0.64 µm to 3.75 ± 0.43 µm in DH36 steel and 17.1 ± 1.1 µm to 11.6 ± 1.3 µm in AA6061. In the published literature, the grain size reduction in SZ and TMAZ was also obtained by enhancing the rotational speed in the dissimilar FSW of steel and Al alloy [1]. The higher strain rate under severe plastic deformation at SAZ resulted in a finer-grained microstructure in SZ (top) than the SZ (bottom), as shown in Figs. 7.12(c) and 7.12(d). As shown in Figs. 7.12(e) and 7.12(f),

TMAZ experienced the elongated grains in AA6061 and DH36 steel, which is caused by an absence of DRX under inadequate heat and deformation. The SZ in the FSW is generated under the direct interaction of the workpiece with the rotating tool pin. However, the tool pin does not affect the TMAZ, but it is affected by the temperature history and plastic strain near the SZ. The grains rapidly changed by dynamic recovery and subsequently stretched by the viscous shear force along the revolving pin direction. The heat-affected zone (HAZ) is exposed to a temperature field but not mechanically deformed. As a result, grain size variation in this zone is smaller than SZ and TMAZ, as shown in Figs. 7.12(g) and 7.12(h). The material of SEZ is extruded from the SZ and deposited in AA6061 due to frictional heating and axial forging. As shown in Figs. 7.12(i) and 7.12(j), this zone contained a grain size of 2.84 ± 0.42 μm in samples SN_3 and SN_4, respectively.

7.5 COMPOSITION AND PHASE ANALYSIS

The formation of the IMC layer at the interface during the welding of steel and Al is a major issue that can significantly impact the mechanical characterization of joints. It is well established that the formation and growth of the IMC layer at the Al/steel interface depend on the heat input and degree of plastic deformation. In this work, the metallurgical behaviour of the IMC layer was studied using TEM and SEM equipped with an EDS system. The detailed magnified morphology of the Al/steel interface through SEM images and EDS analysis at different rotational speeds are shown in Figs. 7.13(a–d). The interface is coloured differently because of the mutual existence of Al and Fe, as shown in Fig. 7.13(a). At the interface area, the Al/Fe concentration variances in the EDS line scan indicate the IMC layer, which is highlighted by the green colour in Figs. 7.13(a) and 7.13(c). The Al and Fe concentrations increased from the interface zone towards the AA6061 and DH36 steel sides. The IMC layer between the base DH36 steel and the AA6061 alloy suggested the reaction-diffusion rather than pure mechanical mixing. From Fig. 7.13(a), it can be understood that the IMC Layer in sample SN_4 is non-uniform, whereas it is continuous and uniform in sample SN_1.

A thin, continuous, and uniform IMC layer is required for adequate metallurgical bonding at the interface. However, the irregular discontinuities in the IMC layer can induce stress concentration, which results in the cracking of this layer. Fig. 7.13(e) shows the averaged IMC layer thickness variation with peak temperature and strain rate as a function of tool rotational speed.

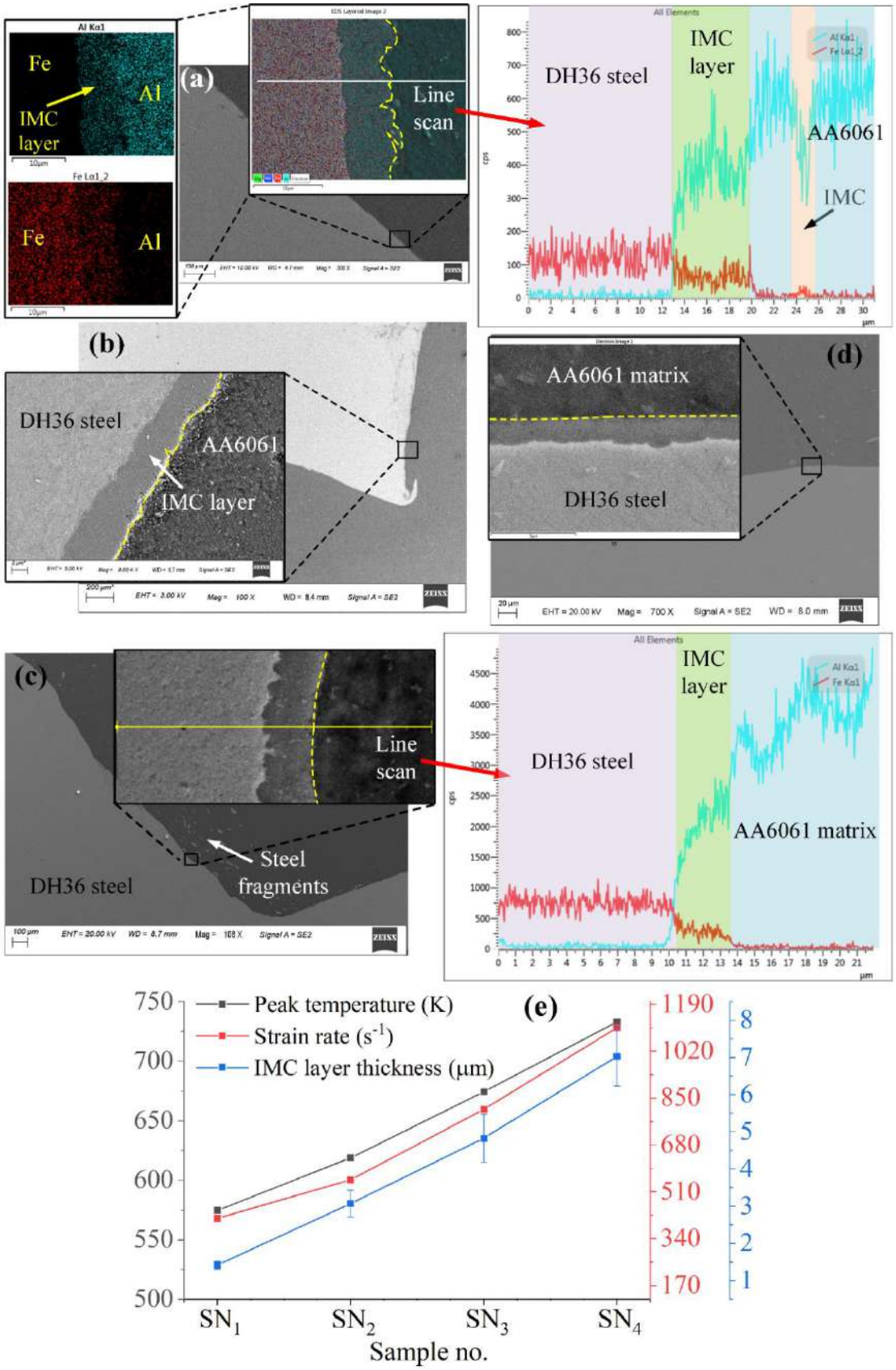

Fig. 7.13 *SEM and EDS analysis of the interface in sample (a) SN_4; (b) SN_3; (c) SN_2; (d) SN_1; and (e) temperature, strain rate, and IMC layer thickness variation at varying rotational speed*

The IMC layer thickness increased with peak temperature and strain rate. With an increase in rotational speed from 450 rpm to 1200 rpm, the IMC layer thickness increased from 1.42 ± 0.1 µm to 7.03 ± 0.79 µm. At the Al-Fe interface, the IMC layer generation and growth kinetics is a diffusion-controlled phenomenon that can be explained using the parabolic and Arrhenius laws shown below [152]:

$$x_t^{\,2} = \dot{k}_r t_e = \dot{k}_o t_e \, exp\left(\frac{-\dot{Q}_a}{\dot{R}T}\right) \tag{7.2}$$

where x_t is the IMC layer thickness, t_e is the exposure time, $\dot{k}_r$ is the rate constant, $\dot{k}_o$ is the pre-exponential factor, $\dot{R}$ is the universal gas constant, $\dot{Q}_a$ is the effective activation energy, and T is the processing temperature. According to this equation, the process parameters or variables that impact the activation energy and peak temperature for element diffusion can change the thickness or shape of the IMC layer at the interface. It is observed that the peak temperature during the welding process is enhanced by increasing the rotational speed, as shown in Fig. 7.4(b). According to Equation (7.2), the increase in processing temperature (T) at the constant time (t) accelerates the inter-diffusion phenomena for various elements, which results in the thicker IMC layer formation. Additionally, the plastic deformation caused by the stirring function of the rotating tool may control the IMC layer formation during the FSW process. Fig. 7.11 revealed that the strain rate increased with an increase in rotational speed, which reduces the activation energy needed for the IMC reaction [187] and speeds up the growth of IMCs. Liu et al. [65] also mentioned that the extensive plastic deformation and a greater strain rate facilitate the diffusion process. In this work, TEM analysis was also conducted to clarify the formation and composition of the IMC layer in sample SN_3. Figs. 7.14(a) and 7.14(b) show typical TEM images under lower and higher magnification, respectively. The IMC layer contained dual sub-layers designated as Phase (A) (adjacent to the Al) and Phase (B) (adjacent to the Fe). The different morphology and contrast of Phase (A) and Phase (B) indicate that the chemical composition of phase (A) could be different from Phase (B). Furthermore, the selected area electron diffraction (SAED) shows diffraction ring patterns in Figs. 7.14(c) and 7.14(d). The crystalline nature of Phase (A) indexed with (434), (443), (040), and (511) planes, and phase (B) indexed with (330), (022), and (441) crystalline planes, which are matched with XRD results based on the d-spacing value. From Figs. 7.14(e) and 7.14(f), the EDS analysis shows that the atom ratio of Al to Fe for Phase (A) and Phase (B) is 3.2 and 3.1 with the presence of other minor elements like Si, Mg, Cu, Zn, and Mn. According to the atomic ratio with reference to the Fe–Al phase diagram (Fig. 1.7), and the SAED patterns,

phase (A) and phase (B) are identified as IMCs, namely $FeAl_3$ and Fe_2Al_5 at the Al/steel interface, respectively.

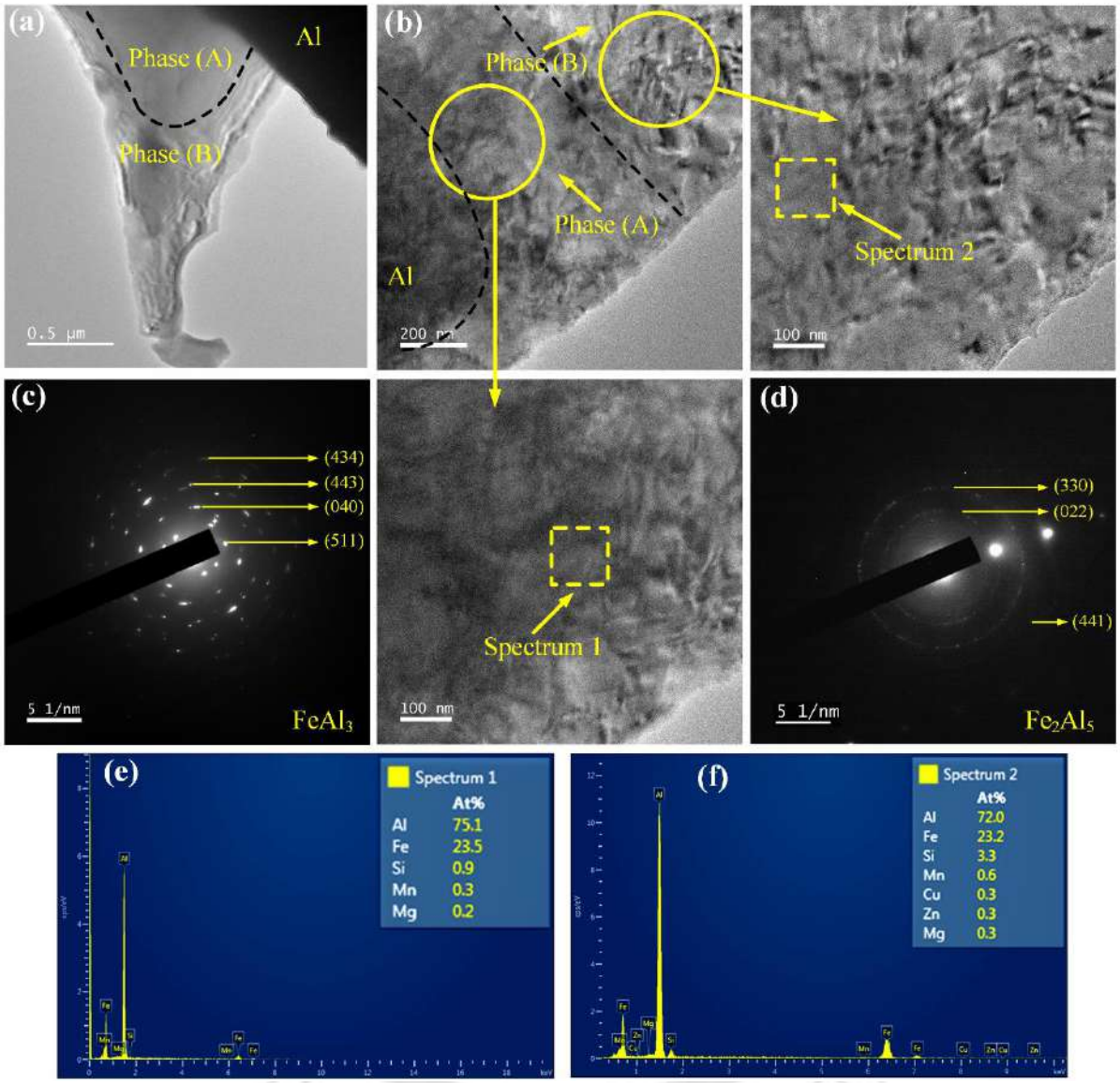

Fig. 7.14 *(a,b) TEM image at the joint interface; (c) SAED pattern of phase (A); (d) SAED pattern of phase (B); and (e,f) EDS elemental spectrums of both phases*

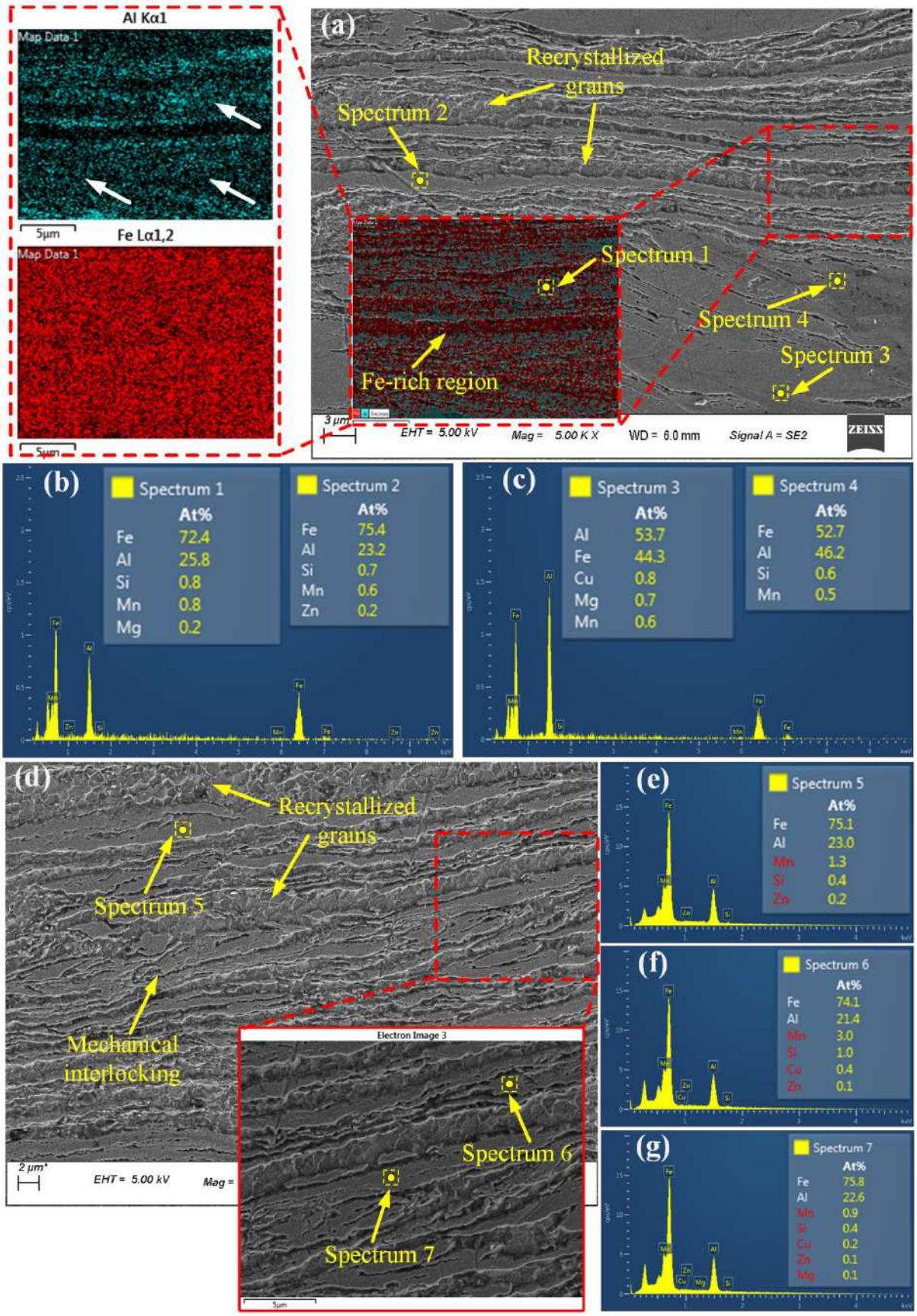

Fig. 7.15 *(a) Intercalated layered structure in sample SN_3; (b,c) EDS elemental spectrums for SN_3; (d) Intercalated structure in sample SN_2; and (e–g) EDS elemental spectrums for sample SN_2*

The plasticized fluid motion is created by the traverse and rotating action of the tool, which resulted in a generation of an intercalated layered structure in the recrystallized grained steel, as shown in Fig. 7.15. The rotational speed significantly impacts the IMCs formation by reaction-diffusion between the Al and Fe at the MZ. The composition of IMCs at the MZ is confirmed by EDS elemental mapping and point analysis, as shown in Figs. 7.15(a–g). The distribution of Fe and Al in the MZ is marked by red and cyan shades in EDS elemental mapping, respectively. White arrows in Fig. 7.15(a) indicate the mutual presence of Al and Fe inside the mixing region, which indicate a reaction-diffusion between Fe and Al. From Figs. 7.15(b) and 7.15(c), the atomic composition in spectrum 1 and spectrum 2 at MZ propose the probable large distribution of Fe_3Al, and spectrum 3 and spectrum 4 correspond to FeAl. According to Pourali et al. [70], the FeAl is generated at a temperature higher than that of Fe_3Al. In this study, the temperature in samples SN_3 and SN_4 is higher than SN_1 and SN_2, as shown in Fig. 7.4(b). Consequently, IMCs, namely Fe_3Al and FeAl are observed in samples SN_3 and SN_4. However, as shown in Figs. 7.15(e–g), spectrums 5–7 revealed the formation of single Fe-rich IMC, namely Fe_3Al. The single Fe_3Al IMC is observed in the MZ of the samples SN_1 and SN_2. The extensive IMCs/defects enriched lamellar intercalated features can adversely impact the mechanical characterization of welded joints. Conversely, the mechanical interlocking provided by intercalated features can improve the joint strength.

The uneven distribution of needle-like particles is found inside the SZ, which is caused by a higher strain rate due to the intense stirring action of the rotating tool. Figs. 7.16(a) and 7.16(b) show the optical microscopic image and EDS elemental mapping of these particles inside the SZ of sample SN_3. The EDS elemental mapping and line scan reveal that a large percentage of Al bounded the particles with a small amount of Fe, marked by orange colour in an aqua-coloured AA6061 matrix in Fig. 7.16(c). As shown in Fig. 7.16(d), the atomic percentage, such as 75.4% Al and 22.4% Fe with other minor elements (i.e., Mn, Si, Cu, Mg, and Zn), suggest that these particles encompassed with $FeAl_3$ phase. In the FeAl structure, $FeAl_3$ is said to be the simplest phase to produce in terms of kinetic considerations [152]. As shown in Fig. 7.16(e), the SAED patterns are indexed to (443), (040), and (511) planes of polycrystalline natured $FeAl_3$ in agreement with the XRD analysis as well. Instead of pure mechanical mixing between the Al matrix and steel fragments, the reaction-diffusion consumed some sheared-off steel particles and transformed them into IMCs.

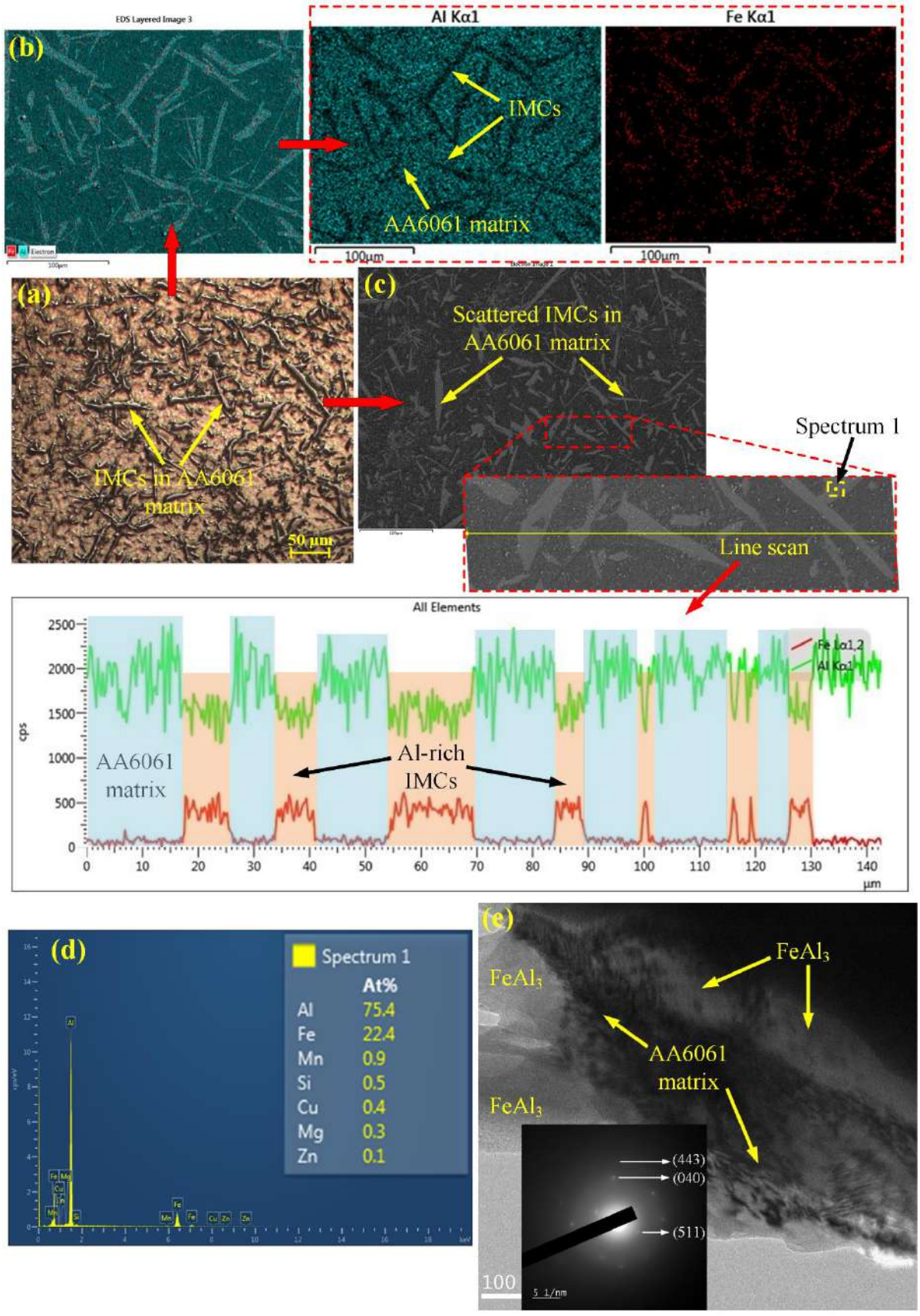

Fig. 7.16 *(a) Optical microscopic image of SZ; (b,c) EDS analysis of particles in SZ; (d) EDS elemental spectrum; and (e) TEM image and the corresponding SAED pattern of particles*

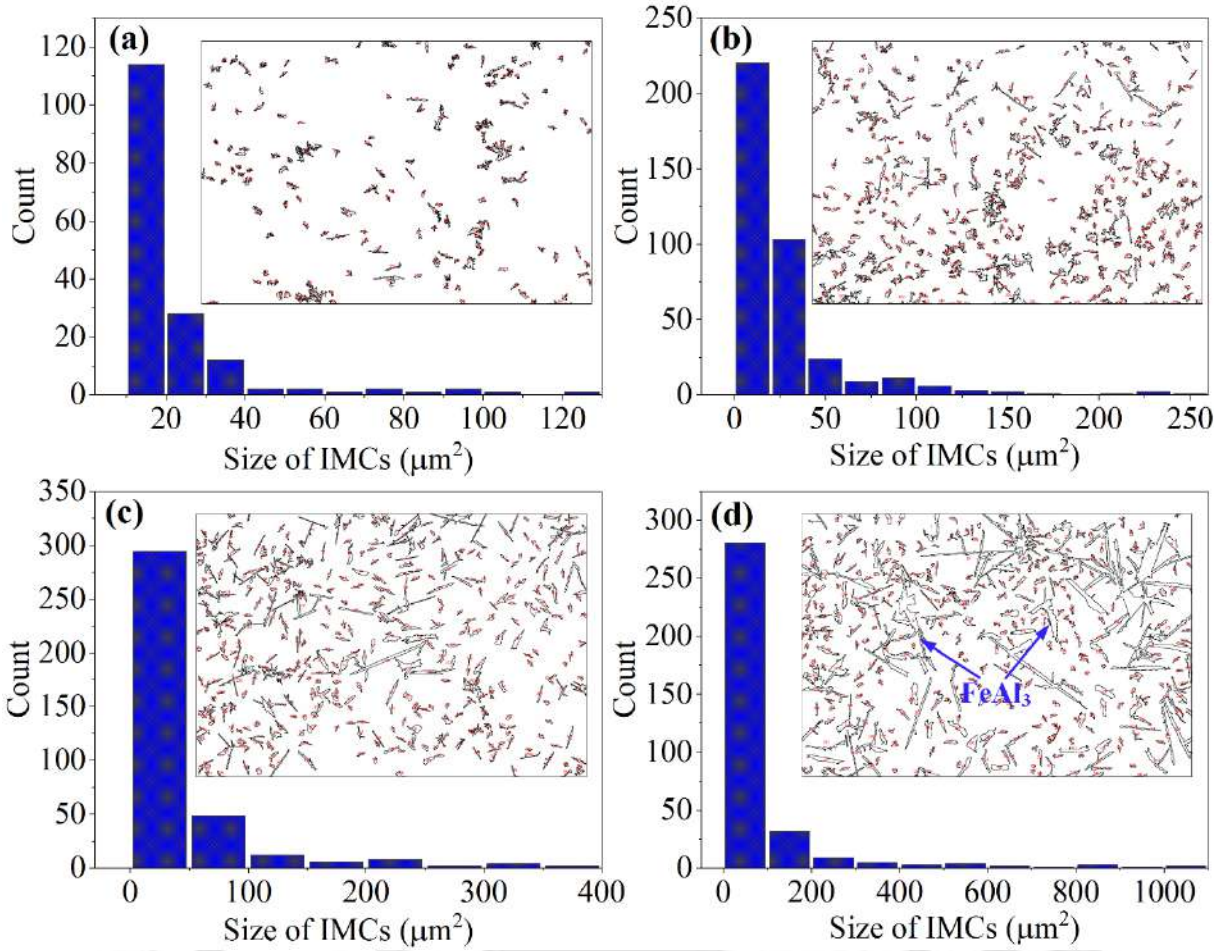

Fig. 7.17 *Quantification of IMCs in SZ of sample (a) SN_1; (b) SN_2; (c) SN_3; and (d) SN_4*

Image analysis for quantification of IMCs at comparable places in the SZ at different rotational speeds is shown in Fig. 7.17. The intensity of bulky IMCs enhanced with an increase in rotational speed from 450 rpm to 1200 rpm. The mean area of IMCs is 21.13 μm^2, 29.26 μm^2, 43.57 μm^2, and 79.6 μm^2 at a rotational speed of 450 rpm, 600 rpm, 875 rpm, and 1200 rpm, respectively. The intense material flow and strain rate under higher heat generation facilitated the intermetallic reaction and mutual diffusion between Fe and Al, which resulted in the generation of bulky IMCs in the AA6061 matrix. SZ could be considered an IMCs reinforced Al matrix since the hardness of IMCs is greater than the parent steel and Al, as discussed in the next section. On the other hand, excessive brittle IMCs may result in defects, such as voids inside the SZ, which adversely influence the mechanical characteristics of welded joints. Consequently, an excessive IMC generation in the FSW of dissimilar materials should be minimized.

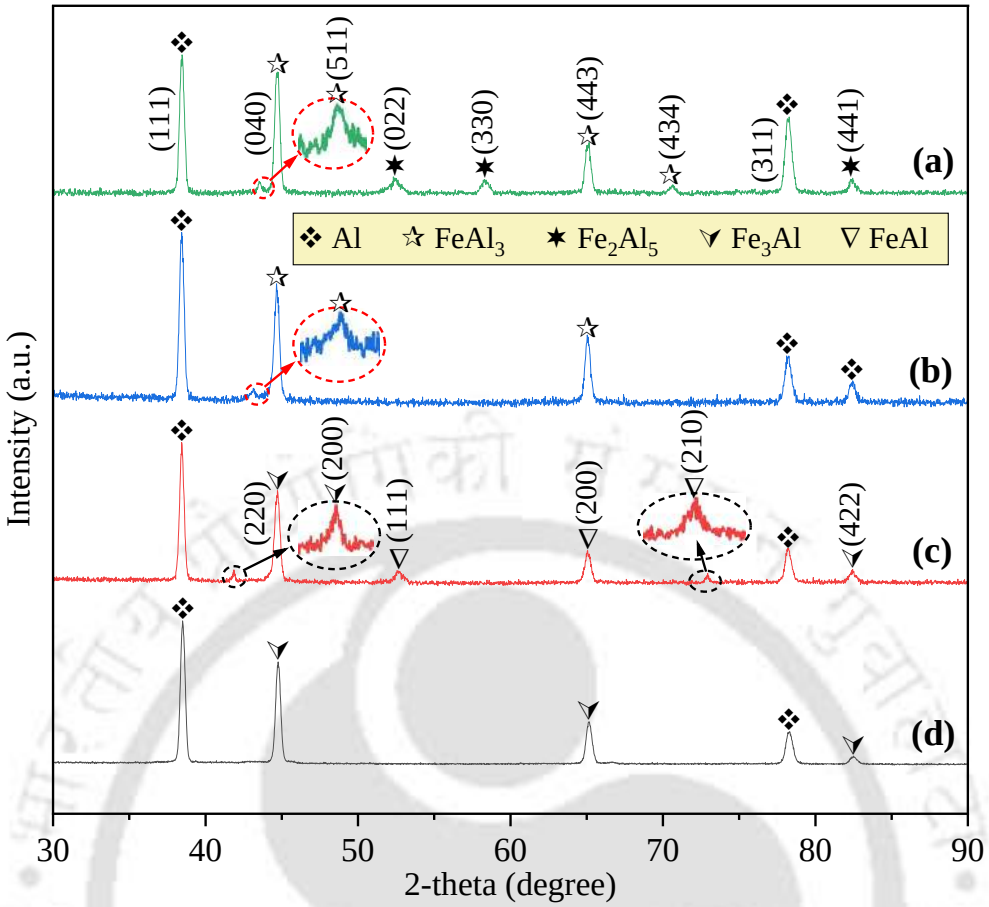

Fig. 7.18 *XRD analysis of (a) IMC layer in sample SN_3; (b) SZ in sample SN_3; (c) MZ in sample SN_3; and (d) MZ in sample SN_2*

In addition, peaks in diffraction patterns of XRD graphs confirmed the trigonal $FeAl_3$ and monoclinic Fe_2Al_5 in the interface with corresponding planes, as shown in Fig. 7.18(a). Fig. 7.18 (b) confirmed the scattering of $FeAl_3$ IMCs inside the SZ. According to TEM and XRD analysis, the intercalated structure exhibited Fe_3Al and FeAl with a cubic crystal system in sample SN_3, as shown in Fig. 7.18(c). Furthermore, diffraction peaks in Fig. 7.18(d) confirmed the occurrence of only Fe_3Al IMC in the MZ of sample SN_2.

7.6 MECHANICAL CHARACTERIZATION

The mechanical characterization (i.e., hardness and tensile properties) of welded joints is significantly influenced by the material flow, microstructural heterogeneity, and spreading of IMCs and steel fragments inside the SZ. Figs. 7.19(a–d) show the Vickers micro-hardness maps plotted by measuring the hardness values at five lines across the weld cross-section under different rotational speeds. The fluctuation behaviour of the hardness profiles is induced by differences in physical/mechanical characteristics of base materials, grain size variation, and dispersion of IMCs and steel fragments inside the AA6061 matrix.

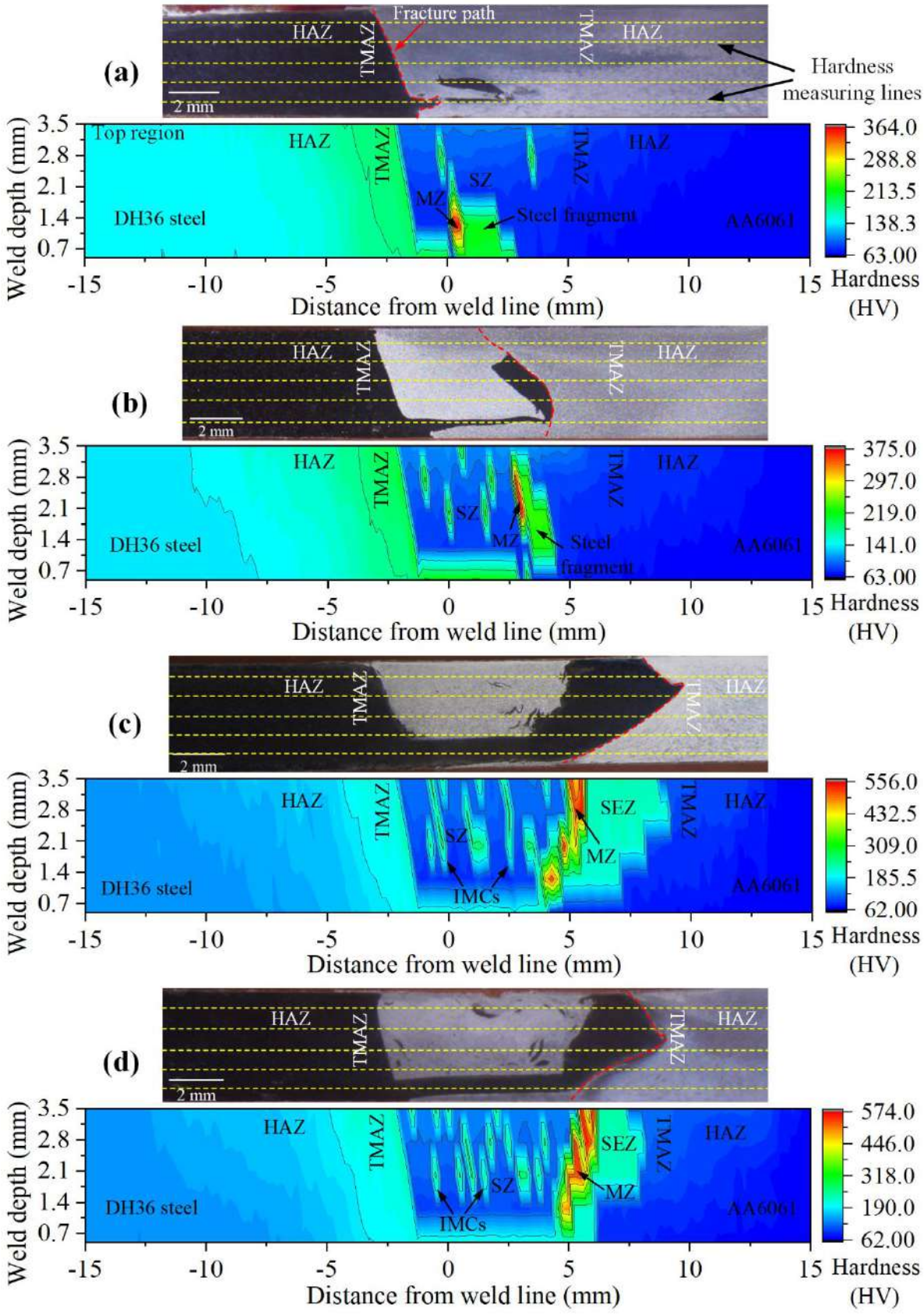

Fig. 7.19 *Transverse hardness map in sample (a) SN_1; (b) SN_2; (c) SN_3; and (d) SN_4*

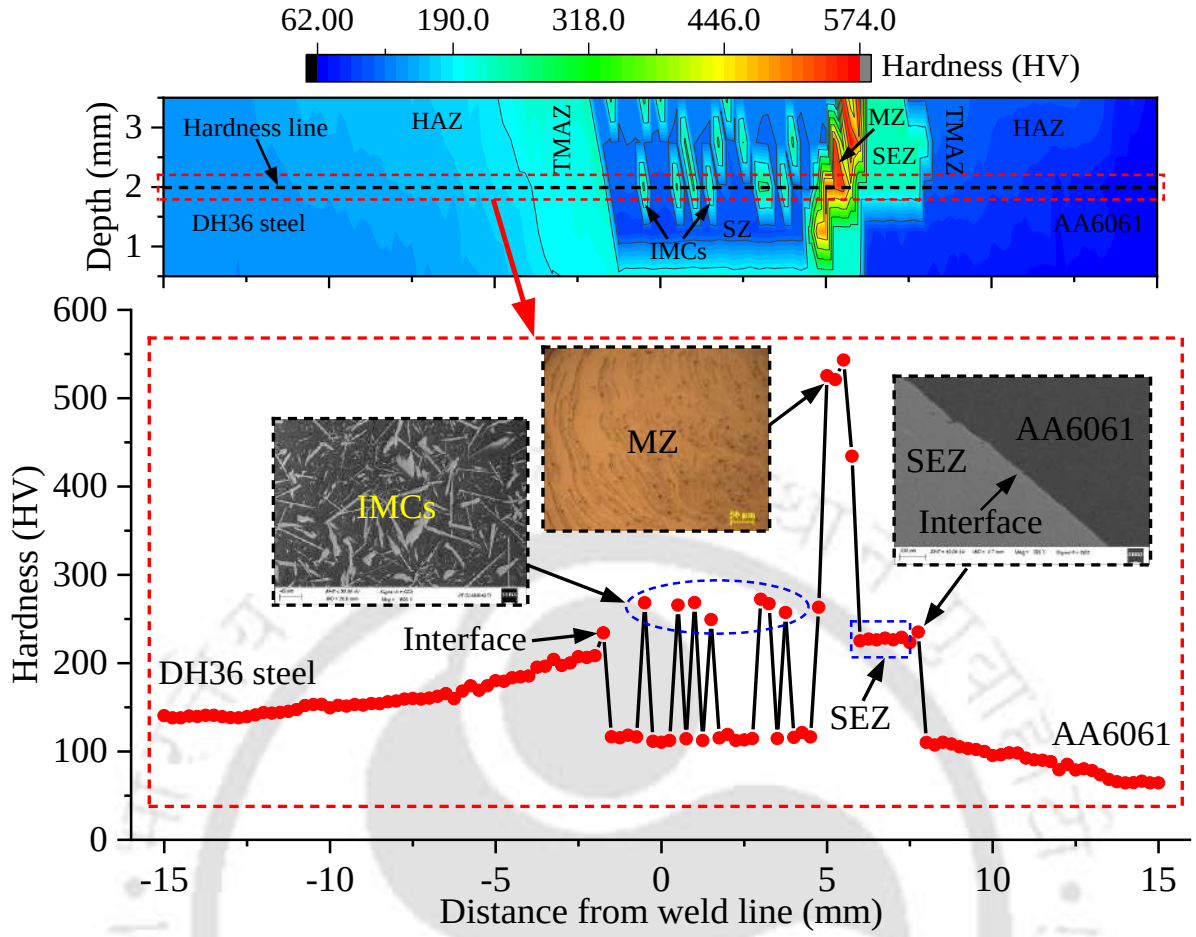

Fig. 7.20 *Hardness profile at the middle line of the map in sample SN_4*

According to the Hall–Petch strengthening [10], the significant grain refinement in the SZ (AA6061) produced higher hardness as compared to TMAZ and HAZ but lower than the SZ (DH36), as shown in Fig. 7.19. The average hardness of the SZ (DH36 steel) is 208.3 HV, 224.4 HV, 240.3 HV, and 257.4 HV in samples SN_1–SN_4, respectively. Besides this, the average hardness of the AA6061 matrix inside the SZ is 87.8 HV, 94.2 HV, 107.2 HV, and 118.5 HV in samples SN_1–SN_4, respectively. This increasing trend of hardness values with an increase in rotational speed is attributed to the grain refinement at a higher strain rate (Fig. 7.12(b)). SEZ in samples SN_3 and SN_4 experienced an average hardness of 217.6 HV and 227.4 HV, which is significantly higher than the TMAZ and HAZ. As the hardness measuring points approached the base materials, their magnitudes decreased and became almost as base DH36 steel and AA6061. The lower hardness of TMAZ compared to SZ is related to the low dislocation density caused by the thermomechanical behaviour of this zone. The lower temperature provided little effect on the hardness of HAZ, which indicated that no significant metallurgical changes occurred in this zone. Furthermore, the top region experienced greater hardness magnitudes than that of the bottom and middle, which is caused by the comparatively

fine-grained microstructure at a higher strain rate at SAZ. In addition to grain refinement, other factors that contribute to hardness variation across the weld cross-section include material inter-mixing, material flow, spreading of IMCs, and steel fragments in the dissimilar FSW of steel and Al. As shown in Fig. 7.19, the steel fragments and IMCs in the SZ mainly produced the peak hardness levels. Their magnitudes increased in samples SN_1 to SN_4, which could be related to the enhanced IMCs area by increasing the rotational speed (Fig. 7.17). The SZ could be considered an Al matrix composite because the steel fragments and IMCs have a comparably higher hardness than the base materials. The IMC layer at the interface exhibited greater hardness magnitudes than the AA6061 matrix but lesser than the individual IMCs scattered across SZ and MZ, as shown in Fig. 7.20. During the Al/steel boundary assessment, the microhardness imprint covered some areas of the AA6061 matrix caused by the limited breadth of hardness indenter. In comparison to IMCs distributed at the MZ and SZ, the softened AA6061 matrix dropped the hardness at the Al/steel boundary. The MZ exhibited the maximum hardness because of the substantial formation of IMCs in this zone (Fig. 7.15), which can contribute to the brittle fracture mechanism. The hardness magnitude of 356.2 HV–374.5 HV is observed in the Fe_3Al enriched MZ of samples SN_1 and SN_2, whereas the samples SN_4 and SN_5 exhibited the hardness of 343.2 HV–573.2 HV in the FeAl + Fe_3Al enriched MZ. The magnitudes of hardness were inside the limits reported by Hussein and Hadzley [3]. According to their findings, the different IMCs exhibit hardness, such as FeAl: 400 HV–667 HV, and Fe_3Al: 330 HV–368 HV. The fracture path is significantly affected by different rotational speeds, which are marked by the red dotted lines in Fig. 7.19. Fig. 7.21(a) shows fractured tensile samples and tensile characteristics at different rotational speeds. As shown in Figs. 7.21(b–e), fractographic SEM analysis was used to examine the fracture surfaces of tensile samples for determining the failure mode.

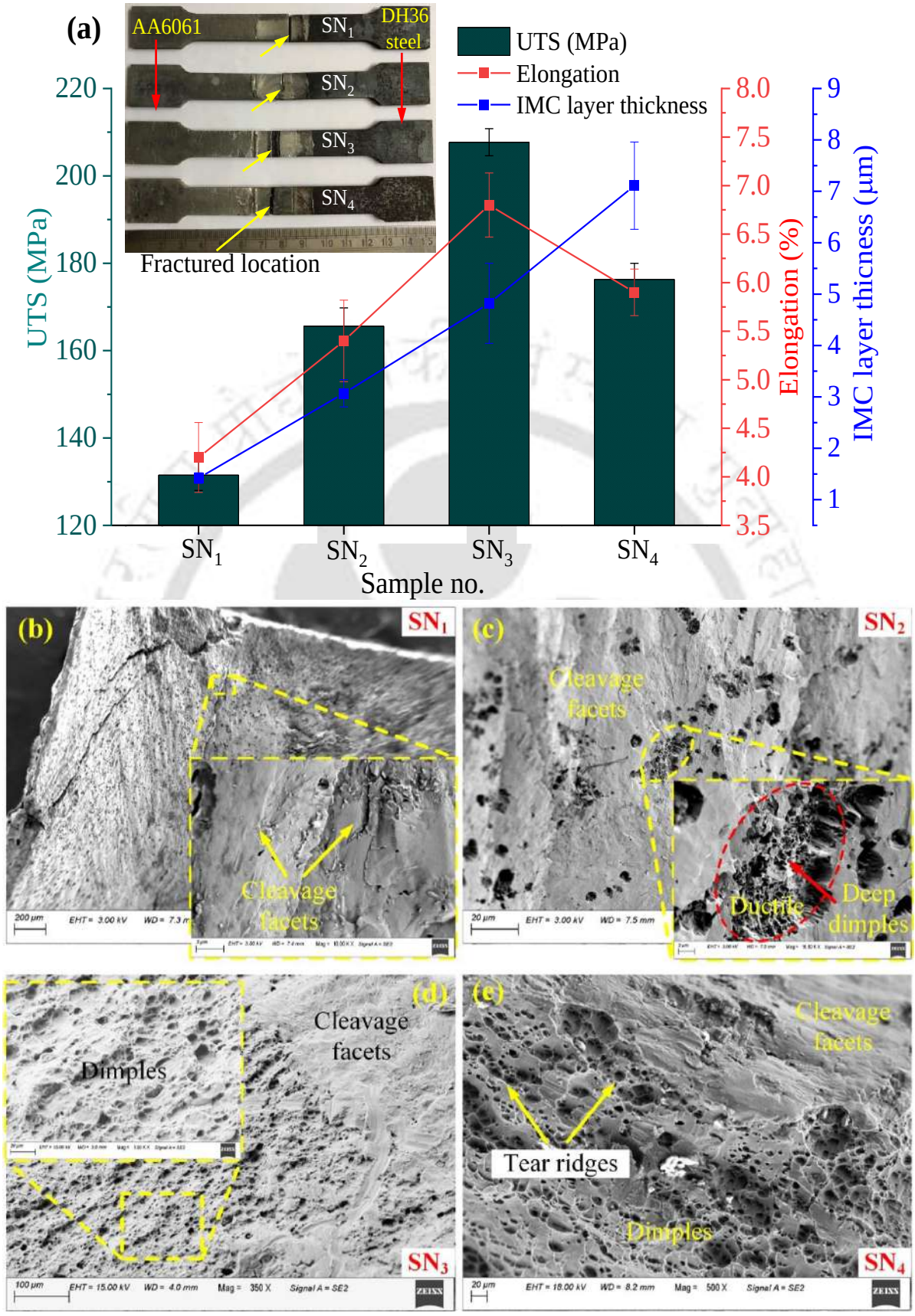

Fig. 7.21 *(a) Tensile properties and IMC layer thickness variation at varying rotational speed; and (b–e) fracture morphology of tensile samples*

It is observed that the increase in rotational speed up to 875 rpm improved the UTS and elongation; however, these values are lowered by further increasing the rotational speed from 875 rpm to 1200 rpm, as shown in Fig. 7.21(a). Samples SN_1 and SN_2 exhibited significant grain refinement in the SZ (Fig. 7.11) and a relatively smaller IMC layer thickness, as shown in Fig. 7.21(a), both of which are deemed to be favourable for joint strength. However, at low heat input, the voids/cracks (Fig. 7.9) due to steel fragments and discontinuous material flow (Figs. 7.8(a) and 7.8(c)) in the SZ dominated these strength-improving aspects and decreased the tensile properties. Sample SN_1 experienced the lowest tensile properties and fractured inside the SZ at the inner interface, as shown in Fig. 7.19(a). Whereas the tensile sample SN_2 fractured from the outer interface of the AA6061 matrix and steel fragment, as shown in Fig. 7.19(b). As shown in Fig. 7.21(b), the fractured surface indicated the brittle fracture mechanism through only cleavage facets in sample SN_1. The fractured surface of the tensile samples SN_2–SN_4 revealed some irregularly shaped dimples with cleavage facets, as shown in Figs. 7.21(c–e), which specified the mixed ductile-brittle failure mechanism. Samples SN_3 and SN_4 fractured from the outer Al/steel boundary of the continuous steel strip at the outside of the SZ, as shown in Figs. 7.19(c) and 7.19(d). The reduction in UTS and elongation above 875 rpm (i.e., at 1200 rpm) is attributed to the formation of voids as a result of intensive mixing, higher intensity of brittle IMCs, i.e., $FeAl_3$ (Fig. 7.17), and thick dual phased IMC layer of $FeAl_3$ and Fe_2Al_5. Cracks can easily form and spread over the hard IMC tangles in the thick IMC layer, which was confirmed by Bozzi et al. [192] in the friction stir spot welding of IF-steel and Al6016 Al alloy. Furthermore, the stress concentration by variation in phase volume of the thick IMC layer deteriorated the weld strength. In addition to the thick IMC layer, the IMCs inside the SZ could reduce the joint strength by restricting material flow through pinning action during the tensile test. The Al-rich IMCs, namely $FeAl_3$, $FeAl_2$, and Fe_2Al_5 are more detrimental to joint strength and ductility since their brittleness is much higher than Fe-rich IMCs, namely FeAl and Fe_3Al [45,152]. Sample SN_3 revealed the highest UTS of 207.4 MPa, which is around 76% of the AA6061 base material. The weld strength of sample SN_3 is improved compared to other samples due to the uniform material flow (Fig. 7.8(e)) and inherent mechanical interlocking provided by the fine-grained steel strip to the defect-free SZ. The relatively lesser brittle Fe–rich IMCs, namely FeAl + Fe_3Al (Fig. 7.15), and mechanical interlocking by the intercalated lamellar structure in the mixing zone are also favourable to the weld strength. Consequently, Figs. (7.19–7.21) revealed that the IMC layer and scattered IMCs/steel fragments in the SZ enhanced the hardness values. On the other hand, the coarse steel fragments, extensive IMCs

formation, and thick IMC layer lowered the weld strength because they are responsible for the defects like voids and cracks inside the SZ.

7.7 SUMMARY

This chapter addressed the VOF-based multiphase computational fluid dynamics simulation by incorporating a modified analytical model for dissimilar FSW of DH36 steel and AA6061. In the simulation, the impact of different rotational speeds on the temperature and plasticized material flow properties (i.e., viscosity, velocity, and strain rate) associated with the tool–material interaction was investigated. The simulation results revealed that the variation in rotational speed is significantly affected the temperature and material flow around the FSW tool. Table 7.2 summarize the material flow behaviour and weld quality varying rotational speed.

Table 7. 2 *Material flow behavior and weld quality at varying rotational speed*

Rotational speed (rpm)	Maximum flow velocity (m/s)	Velocity vectors	Material features	Joint quality
450	0.024	Discontinuous	Steel fragments	Defective
600	0.115	Discontinuous	Extruded steel strip in SZ	Defective
875	0.326	Uniform	Extruded steel strip in AA6061	Good
1200	0.66	Uniform	Extruded steel strip in AA6061	Defective

The maximum velocity and strain rate are obtained at the outer edge of the shoulder due to the lowest dynamic viscosity on the AA6061 side. The velocity vectors revealed the discontinuity in the advancing side at 450 rpm and 600 rpm, whereas these are improved and become uniform at 875 rpm and 1200 rpm. Transmission electron microscopy analysis revealed the formation of a dual-phased IMC layer of $FeAl_3$ and Fe_2Al_5 at the interface. Its thickness increased with an increase in rotational speed due to the enhanced intermetallic reaction at a higher temperature and strain rate. The rotational speed of 875 rpm produced good weld quality with the maximum joint strength~207.4 MPa at the IMC layer thickness of 4.83 ± 0.65 μm. The intercalated structures acted as the hardest zone because of extensive IMCs formation, namely Fe_3Al at 450 rpm and 600 rpm, and Fe_3Al + FeAl at 875 rpm and 1200 rpm.

CHAPTER 8

EXPERIMENTAL STUDY ON THE JOINING OF STAINLESS STEEL AND ALUMINUM ALLOY

Chapters 6 and 7 included the experimental and numerical investigation of the dissimilar FSW of DH36 steel and AA6061. As discussed in Chapter 1, the joining of 304 stainless steel with Al alloys has also attracted many industries for efficient and lightweight constructions. This chapter presents the detailed experimental analysis of dissimilar friction stir welded 304 SS and AA6061 joints. In this work, FSW technique was employed to find the optimal tool traverse speed. For this purpose, five different traverse speeds at a constant rotational speed of 875 rpm were considered. The welded joints were characterized based on the mechanical properties, micro/macrographs, and quantification of steel fragments and IMCs inside the SZ. A detailed analysis was performed to predict the effect of different traverse speeds on grain size at various zones, intercalated structure, IMC layer thickness, and the fraction of IMCs/steel fragments. Furthermore, their coinciding effect on mechanical properties, i.e., tensile properties and hardness of welded joints was examined. A thorough analysis of fractured surfaces of tensile samples is also presented in this chapter. Finally, the chapter is ended by summarizing key findings from this experimental study.

8.1 PROCESS PARAMETERS

In this experimental work, 6061-T6 Al alloy (AA6061) and 304 stainless steel (304 SS) sheets were used as base materials. A constant tool tilt angle of 2º was used for all the experiments. Before conducting the experiments, each sheet was polished using different graded emery papers to confiscate the oxide and then fixed on the fixture to produce butt joints. Based on the repetitive experiments using a trial and error technique, the rotational speed of 875 rpm and tool offset of 1.5 mm were selected to comprehensively investigate the impact of tool traverse speed on weld characterization. Table 8.1 shows the different traverse speeds chosen for the current work.

Table 8.1 *Working range of tool traverse speeds*

Sample no. (S. no.)	SN_1	SN_2	SN_3	SN_4	SN_5
Traverse speed (mm/min)	30	50	70	90	120

8.2 MACRO/MICROSTRUCTURE

A typical weld surface appearance and macrographs at varying traverse speed are shown in Fig. 8.1. The surface defects appeared at a traverse speed of 30 mm/min and 50 mm/min, as shown in Figs. 8.1(a) and 8.1(c). The extensive heat generation and deformation softened the Al side at a lower traverse speed. Then the softened material is expelled from the bottom of the shoulder towards the outward direction in the form of flash, which results in defects generation like grooves. The sound quality surface appearance is observed at a traverse speed of 70 mm/min and 90 mm/min, as shown in Figs. 8.1(e) and 8.1(g). The surface defects are also observed by enhancing the traverse speed from 90 mm/min to 120 mm/min, as shown in Fig. 8.1(i). The higher traverse speed produced less heat generation, which led to the insufficient intermixing of dissimilar materials and surface defects formation. The surface defects at inappropriate traverse speeds adversely affect the weld joint strength.

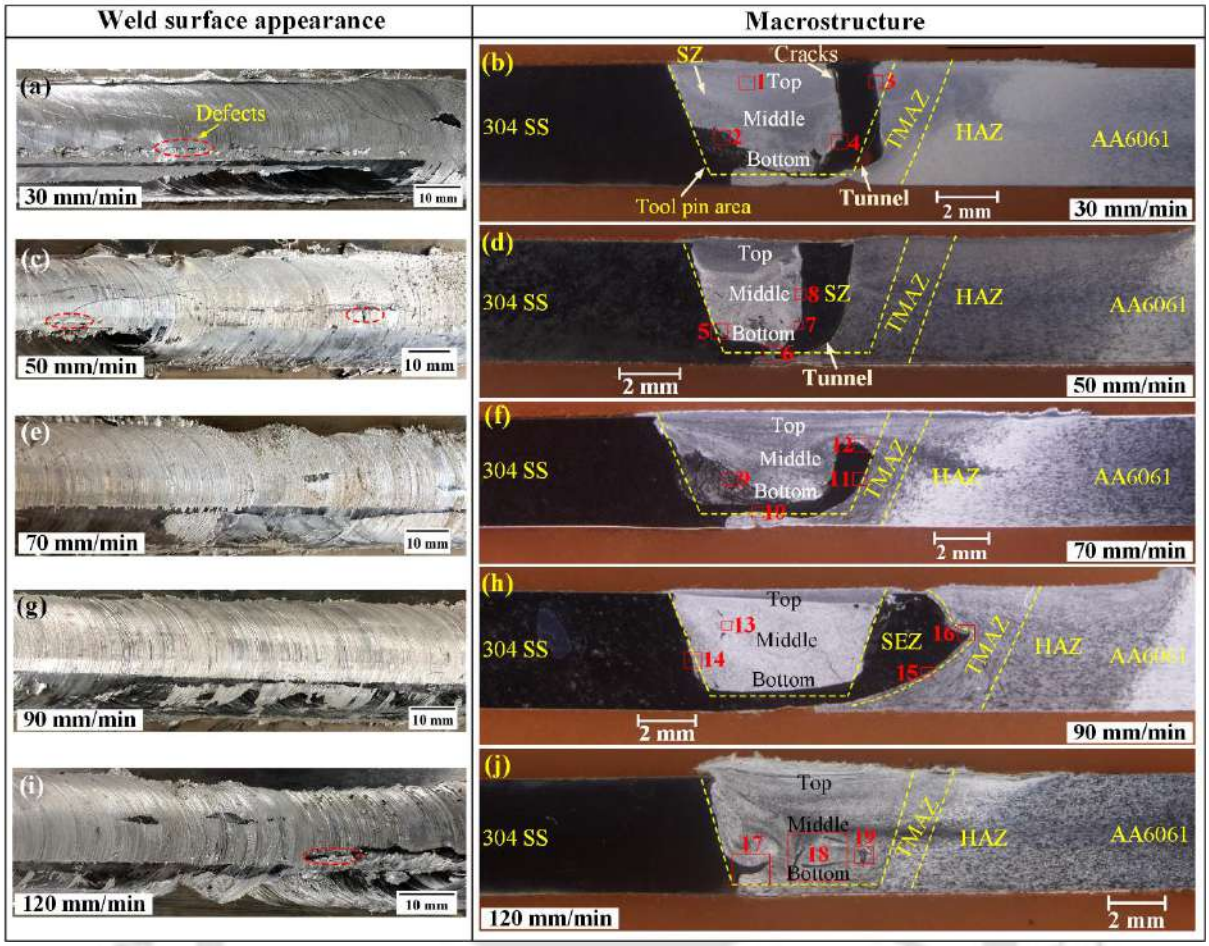

Fig. 8.1 *Weld surface appearance and macrographs of welded sample (a,b) SN_1; (c,d) SN_2; (e,f) SN_3; (g,h) SN_4; and (i,j) SN_5*

The micrographs at the various regions (marked in Fig. 8.1) of dissimilar welded samples are shown in Fig. 8.2. The bright and black regions in the macrographs correspond to AA6061 and 304 SS, respectively. The three primary zones in the dissimilar friction stir (FS) welded cross-section is the SZ, TMAZ, and HAZ with base materials. Besides these zones, a continuous steel strip extruded towards the AA6061, named as steel extruded zone (SEZ), as shown in Fig. 8.1(h). The more rigid material, i.e., stainless steel, extruded from the AS and distributed in the direction of the AA6061. At a traverse speed of 90 mm/min (i.e., SN_4), the continuous strip extruded towards the AA6061 without any generation of defects inside the SZ, as shown in Figs. 8.1(h) and 8.2. This continuous extruded steel strip is favourable to the weld joint strength since it acts as a mechanical interlocking to the SZ. As a result, the 90 mm/min traverse speed produced sufficient heat input during dissimilar welding, which resulted in adequate material flow and intermixing of 304 SS and AA6061 alloys. The interface is clearly evident with different colours of 304 SS and AA6061. Besides, the irregularly shaped steel fragments are detached from bulk 304 SS and distributed inside the SZ of all samples. The

shear force induced by the rotating tool results in the detachment of the steel (Fe-rich) fragments from the base steel sheet. It is also observed that cross-sectional defects generation capacity increased from the traverse speed 90 mm/min to 30 mm/min. The defects like tunnels, voids, and cracks are evident inside the SZ in samples SN_1–SN_3, which is attributed to the scattering of IMCs and steel fragments inside the SZ.

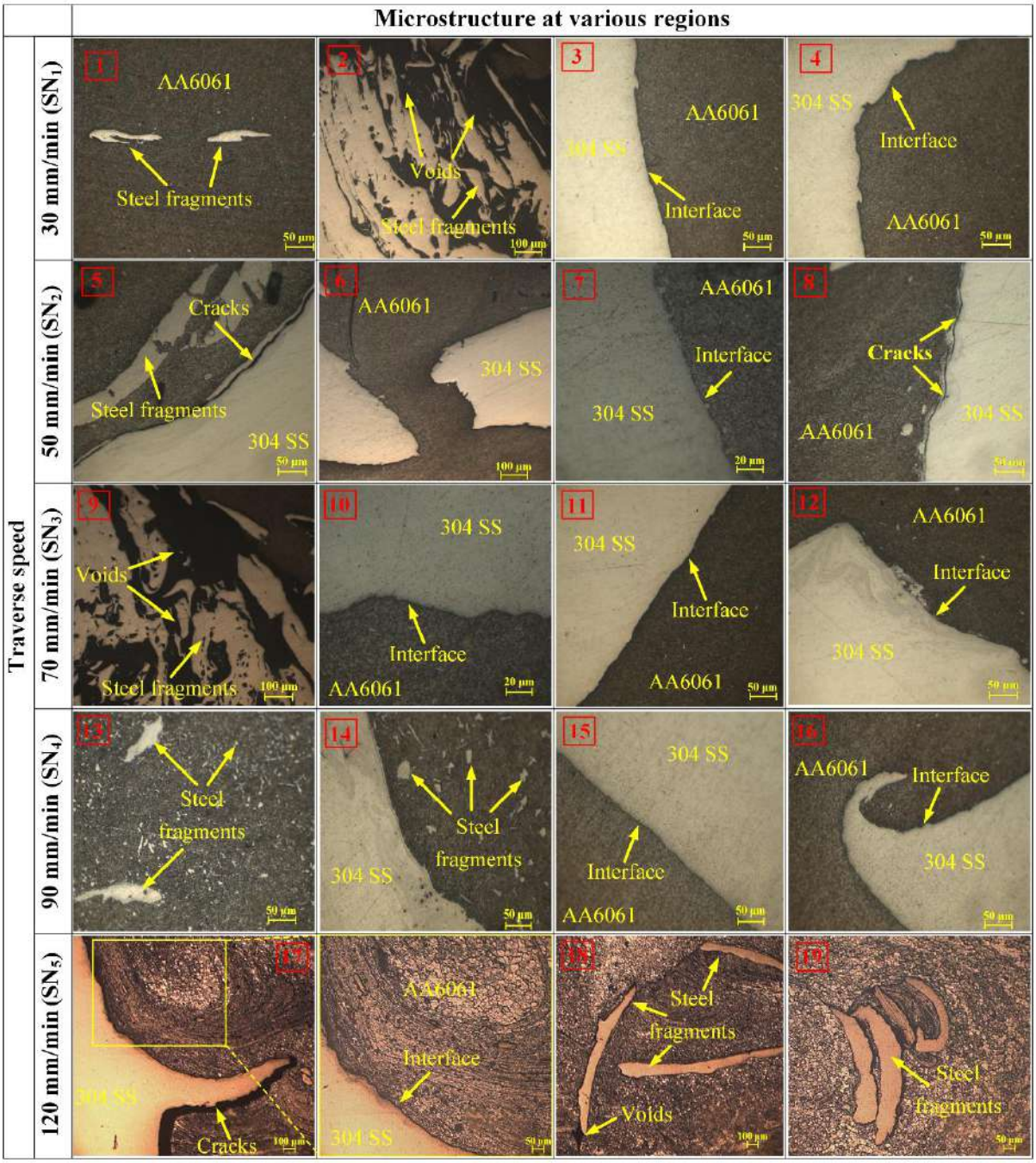

Fig. 8.2 *Micrographs of the various regions marked in Fig. 8.1*

The quantification of steel fragments inside the SZ through image analysis at varying traverse speed is shown in Fig. 8.3. The needle-like uneven dispersion of particles is also

witnessed inside the SZ, as shown in Figs. 8.4(a) and 8.4(b), which could be induced at a higher strain rate by the stirring phenomenon of the rotational tool. The EDS point analysis is performed to confirm their composition, and the results are shown in Figs. 8.4(c) and 8.4(d). From the Al/Fe phase diagram (Fig. 1.7), the atomic percentages at points P1 and P2 suggest these particles as Al-rich IMCs, namely Al_3Fe.

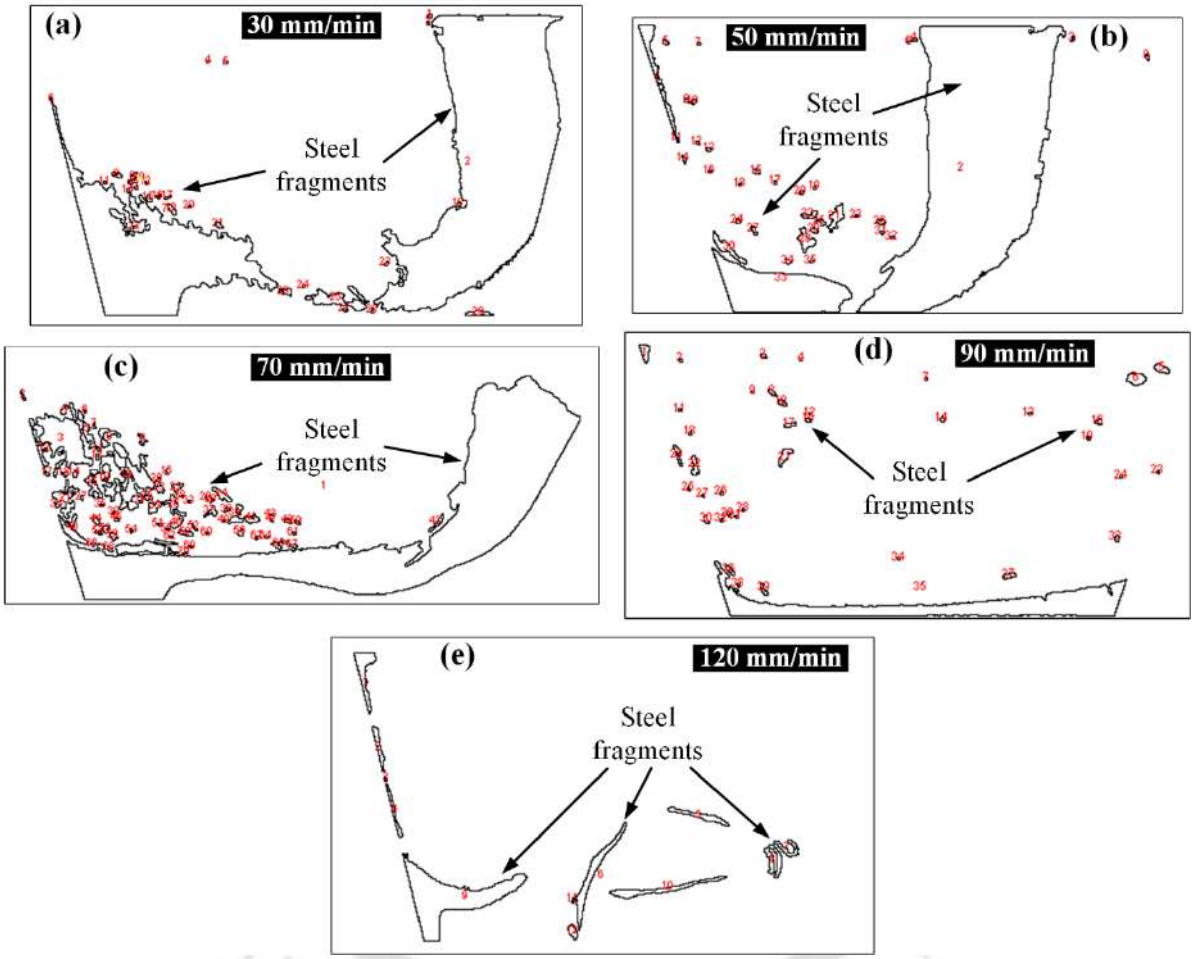

Fig. 8.3 *Quantification of steel fragments inside the SZ of sample (a) SN_1; (b) SN_2; (c) SN_3; (d) SN_4; and (e) SN_5*

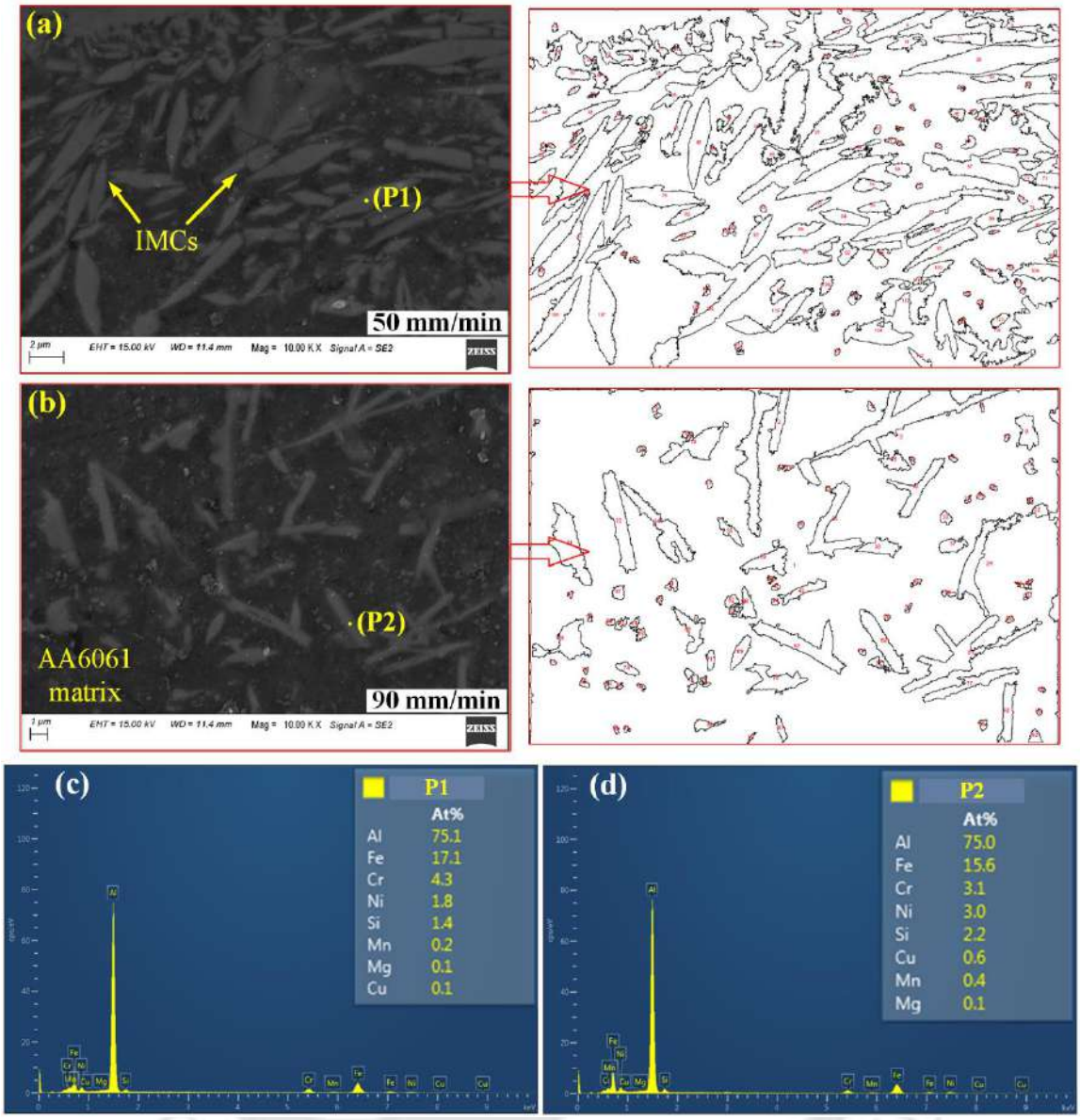

Fig. 8.4 *(a) IMCs in sample SN_2; (b) IMCs in sample SN_4; and (c–d) EDS elemental point analysis*

The Image analysis was performed at similar locations inside the SZ to compare the size of IMCs at varying traverse speed, and the results are shown in Figs. 8.5(a–e). The intensity of the coarse IMCs inside the SZ increased with a decrease in traverse speed, as shown in Figs. 8.5(a–e). It is also observed that the 30 mm/min traverse speed created a more area fraction of IMCs and steel fragments in the SZ of sample SN_1, as shown in Fig. 8.5(f). The steel fragments and IMCs occupied 35.01% and 0.084% of the total area of SZ, respectively. The area fraction of the steel fragments and IMCs reduced with an increase in traverse speed. The mean area of the IMCs is 1.75 μm^2, 1.54 μm^2, 1.2 μm^2, 0.74 μm^2, and 0.28 μm^2 in samples SN_1–SN_5, respectively. The larger area fraction of IMCs and steel fragments inside the AA6061 matrix

of the SZ is attributed to the intense material flow and intermixing under higher heat generation at a lower traverse speed.

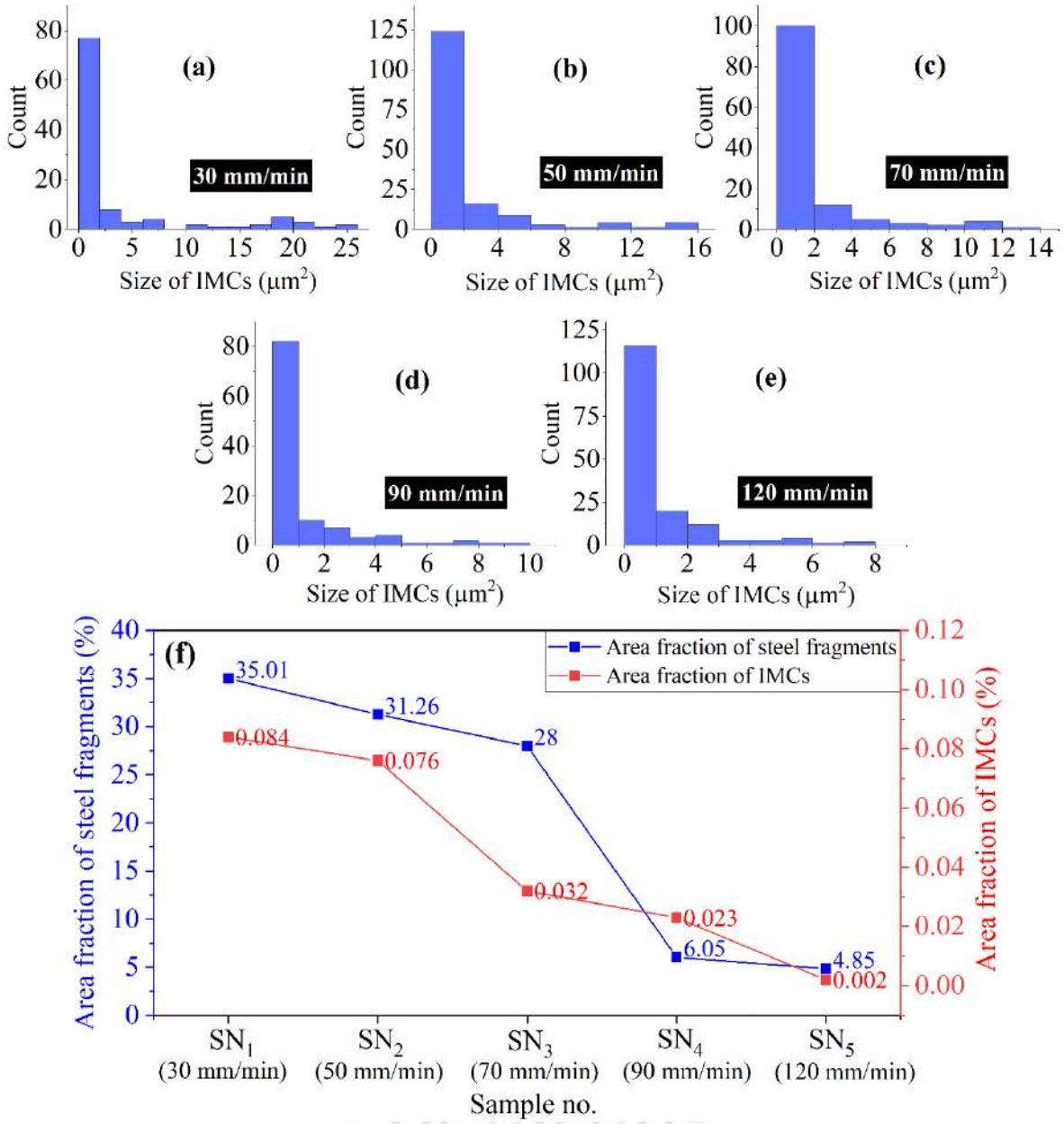

Fig. 8.5 *Quantification of IMCs in sample (a) SN_1; (b) SN_2; (c) SN_3; (d) SN_4; (e) SN_5; and (f) area fraction of steel fragments and IMCs at varying traverse speed*

The higher heat generation softened the hard material (i.e., 304 SS) and made it easy for steel fragments to be scattered inside the AA6061 matrix. Furthermore, it is difficult to deform and intermix the coarse steel fragments in the AA6061 matrix due to the different physical/mechanical properties of the base materials. The large steel fragments provided the restriction in the material flow and generated the defects like tunnels or cracks in the SZ, which are shown in samples SN_1–SN_3. Accordingly, the intensity of cracks and voids is dependent on

the fraction of steel fragments inside the SZ. The relatively higher proportion of steel fragments in sample SN_1 generated wider defects inside the AA6061 matrix of SZ. The higher area fraction of IMCs could also produce defects like voids inside the SZ due to their inherent brittle nature. The steel fragments generally cause the possibility of macroscopic crack initiation and, subsequently, defect generation. The higher traverse speed is not provided enough time for the tool pin to detach and intermix the steel fragments inside the AA6061 matrix, which resulted in the low area fraction of steel fragments and IMCs inside the SZ. Furthermore, the inadequate stirring of dissimilar materials at lower heat input produced the defects like cracks on the interface in sample SN_5, as shown in Fig. 8.2. The sharp corners at the cracks are detrimental to the weld quality since they act as stress risers.

The as-received base material microstructures of AA6061 and 304 SS are illustrated in Figs. 8.6(a) and 8.6(b), respectively. The microstructure of AA6061 exhibited coarse elongated grains, whereas the 304 SS base material is composed of equiaxed austenite grains with some annealing twin boundaries.

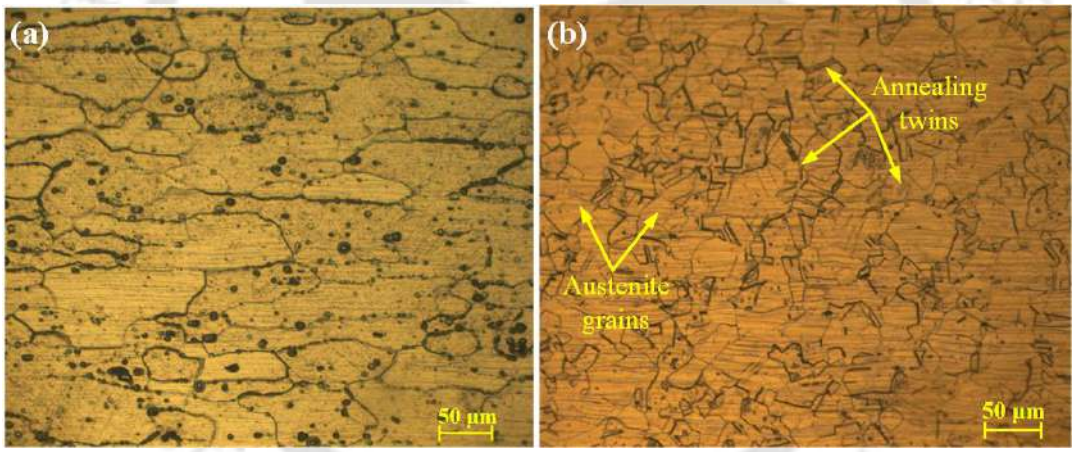

Fig. 8.6 *Microstructure of (a) AA6061; and (b) 304 SS*

The microstructural study under higher magnification was conducted to analyze the different zones in 304 SS and AA6061. As shown in Fig. 8.7, the equiaxed refined grains are observed in the SZ (AA6061). In contrast, the steel fragments, i.e., SZ (304 SS) exhibited the refined grains, which are elongated in the shear direction, as shown in Fig. 8.8(a). The grain refinement in the SZ is attributed to the dynamic recrystallization under the thermo-mechanical action during the FSW process. The material in SEZ is extruded from the SZ by the rotating action of the tool. As a result, this region also exhibited grain refinement through dynamic recrystallization (DRX), as shown in Fig. 8.8(b).

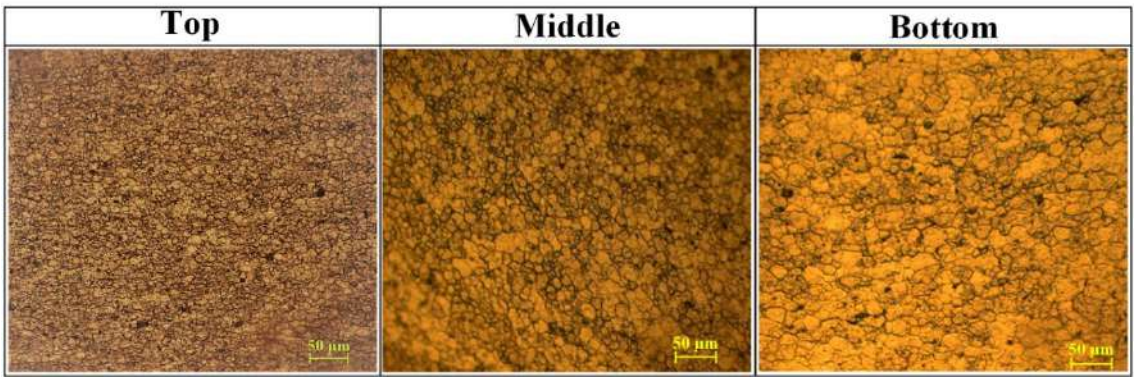

Fig. 8.7 *Microstructure at the top, middle, and bottom of the SZ (AA6061) in sample SN_2*

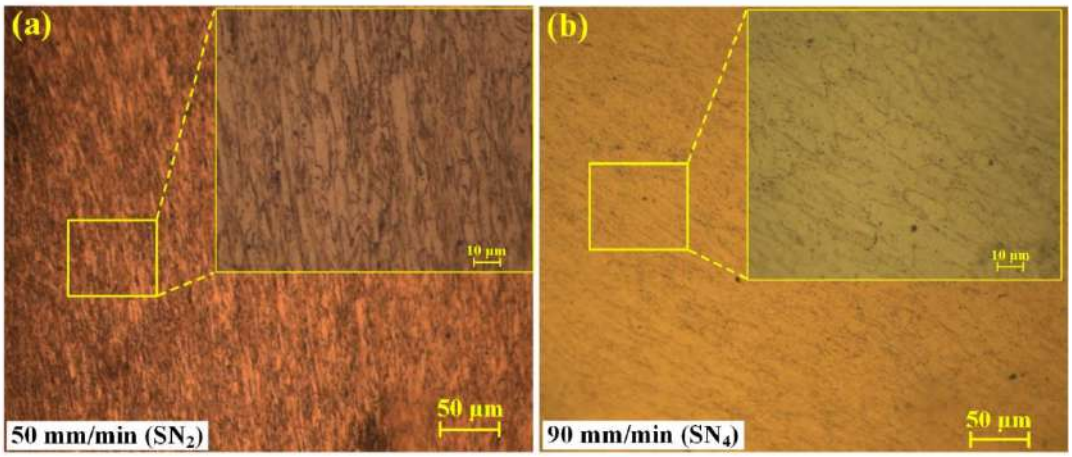

Fig. 8.8 *Microstructure (304 SS) of (a) SZ in sample SN_2; and (d) SEZ in sample SN_4*

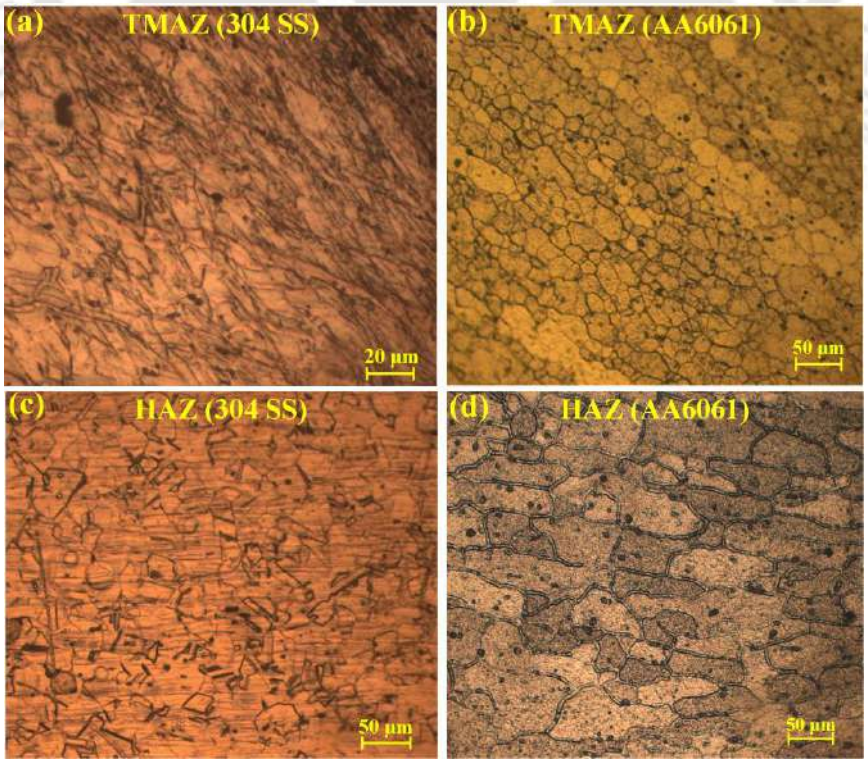

Fig. 8.9 *Microstructure of (a,b) TMAZ; and (c,d) HAZ in sample SN_2*

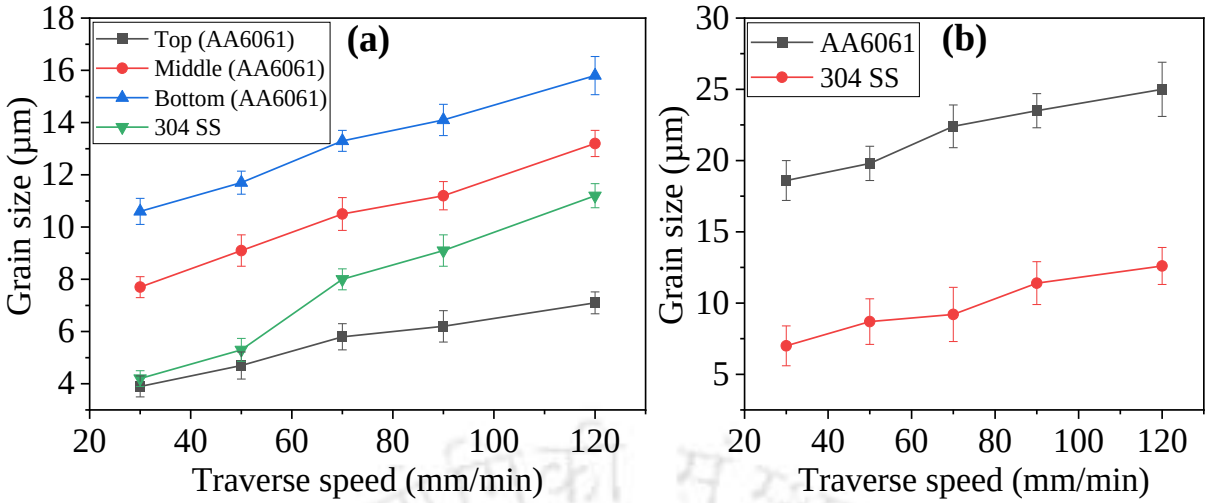

Fig. 8.10 *Grain size variation at varying traverse speed in (a) SZ; and (b) TMAZ*

A comparatively more fine-grained microstructure is observed at the top of SZ than bottom and middle, as shown in Fig. 8.7. At the top region, the interaction of the shoulder surface with the workpiece produced additional frictional heat and a greater strain rate [196], which resulted in more grain refinement through the dynamic recrystallization process. Compared to the SZ, TMAZ (AA6061) and TMAZ (304 SS) experienced the coarse elongated grained microstructure in the shear direction, as shown in Fig. 8.9. TMAZ produced the elongated equiaxed grains in AA6061 and austenite grains in 304 SS caused by an absence of dynamic recrystallization under insufficient heat and deformation. The SZ in the FSW is generated under the direct interaction of the rotating tool pin to the workpiece. The TMAZ is not directly influenced by the tool pin but by the thermal history and plastic deformation adjacent to the SZ. The grains instantly transformed through dynamic recovery and then elongated alongside the rotating pin direction by the viscous shear force. HAZ between the base materials and TMAZ is not influenced by the plastic deformation, which resulted in grain coarsening, as shown in Fig. 8.9. The interaction of the rotating tool with dissimilar materials causes a large variation in the plastic flow and thermal history, which results in microstructural variation across the weld cross-section. Fig. 8.10(a) shows the impact of traverse speed on the average grain size at the top, bottom, and middle of SZ (AA6061) and middle of the SZ (304 SS). Fig. 8.10(b) shows the grain size variation with different traverse speeds in TMAZ of AA6061 and 304 SS. The grain size in the SZ is significantly decreased from the 24.2 ± 2.65 µm and 56.3 ± 2.1 µm of 304 SS and AA6061 base materials, respectively. TMAZ of the 304 SS experienced a grain size smaller than the TMAZ (AA6061).

Moreover, both materials exhibited an average grain size in the TMAZ higher than the SZ. It is observed that the grain size is significantly changed by varying the traverse speed, and it is found to be reduced with a reduction in traverse speed. By decreasing the traverse speed from 120 mm/min to 30 mm/min, the grain size is reduced by 52.6% and 31% in the SZ (SS 304) and SZ (AA6061), respectively. However, it is reduced by 44.4% and 25.6% in TMAZ of SS 304 and AA6061, respectively. In this study, dynamic recrystallization under extreme plastic deformation is considered as the determinative phenomenon for the grain size variation. The lower traverse speed causes more contact time between the rotating tool and the workpiece, which enhances the plastic deformation by the stirring action of the tool. Hence, the DRX phenomenon reduced the grain size by decreasing the traverse speed. Eyvazian et al. [1] also reported that the more refined grains at the lower traverse speed could be attributed to the formation of nucleates under extensive shear deformation.

8.3 COMPOSITION ANALYSIS

The critical issue in dissimilar FSW of Al/steel is the distribution of IMCs and steel fragments. The scattering of steel fragments and IMCs from the interface into the Al matrix creates a composite-like structure in the SZ. In this study, EDS composition analysis of the defective region is executed for sample SN_3. The SEM image with an optical microscopic image (OM) of the defective region is shown in Fig. 8.11(a). The irregular-shaped steel fragments and the extensive dispersion of IMCs are evident due to the intense stirring action created by the rotating tool pin. EDS elemental mapping and fluctuation in the line scan confirm the steel fragments inside the defective region, as shown in Fig. 8.11(b). The atomic proportion of Fe and Al at a point commonly proposes corresponding Al–Fe IMCs. According to the Al/Fe phase diagram (Fig. 1.7), the atomic percentages at points P1–P4 in Figs. 8.11(c–f) suggest the dispersion of Al-rich IMCs, namely Al_3Fe inside the defective region. The inherent brittle nature of excessive IMCs could also be responsible for defects (i.e., voids) formation inside the SZ. The steel fragments inside the SZ are found to be encompassed with IMCs, as shown in Figs. 8.12(a–c). These IMCs are possibly generated through the chemical reaction despite the only mechanical mixing between the sheared-off steel fragments and the AA6061 matrix. From Fig. 8.12(d), the atomic percentage at point P1 proposes that the steel fragments are encompassed with possible IMCs, namely Al_3Fe.

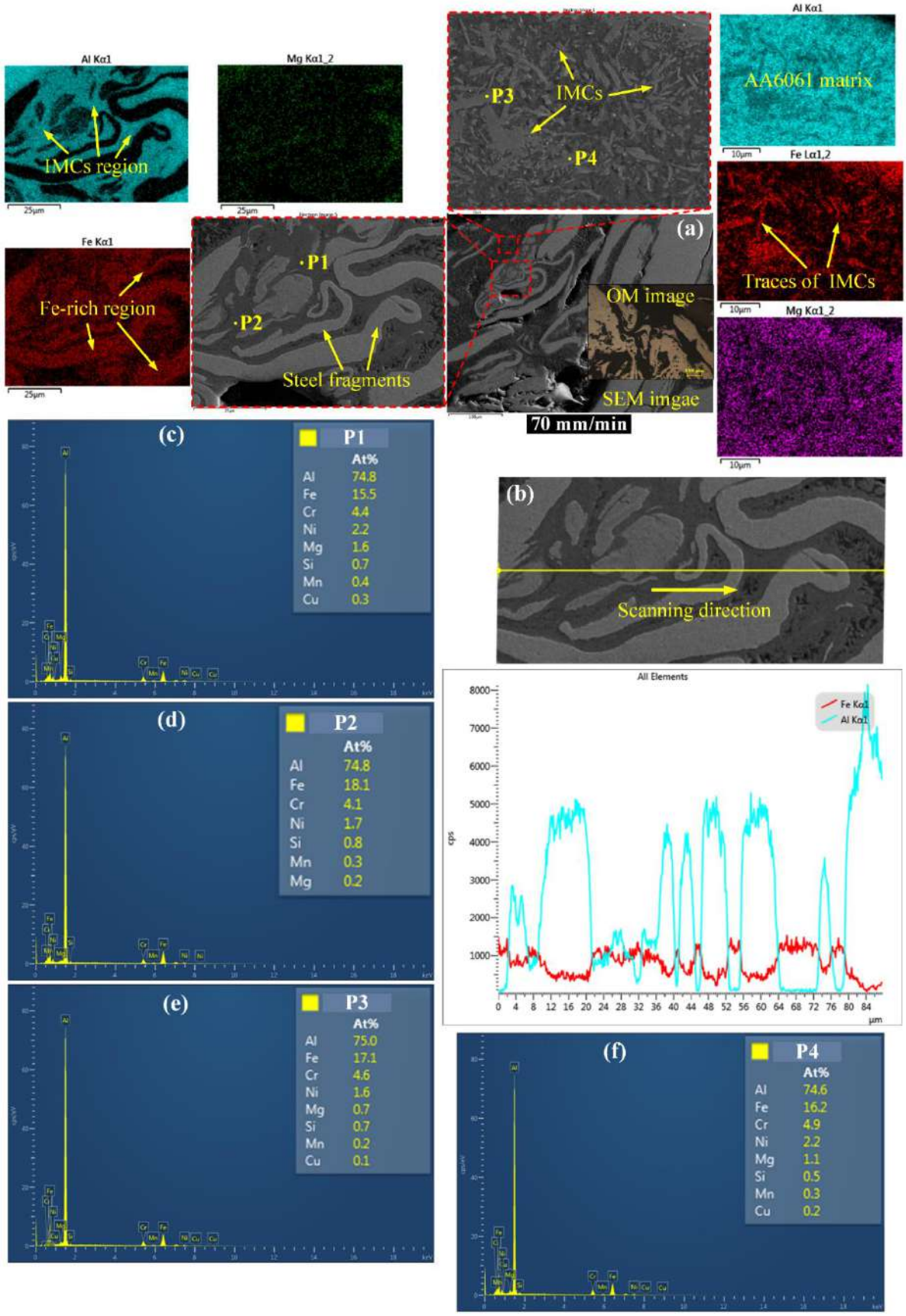

Fig. 8.11 *(a) Defective region in sample SN_3; (b) EDS line scan; and (c–f) EDS elemental analysis*

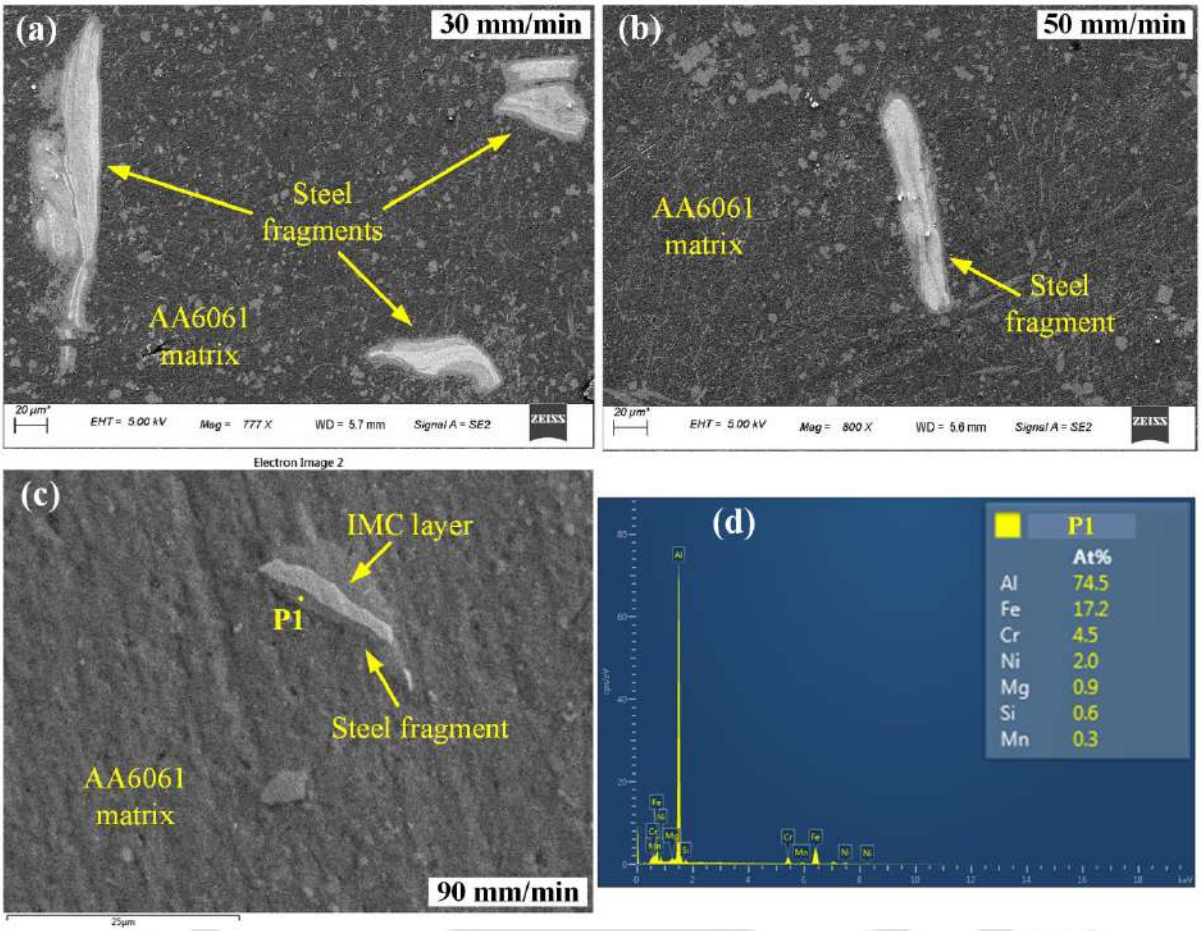

Fig. 8.12 *(a) SEM image of SZ in sample SN_1; (b) SZ in sample SN_2; (c) SZ in sample SN_4; and (d,e) EDS elemental analysis*

The IMC layer generation at the Al/steel interface is critical for the mechanical performance of the weldments. The coinciding consequence of frictional heating, axial forging, and material extrusion from AS (304 SS) towards the RS (AA6061) generated the IMC layer at the interface due to the solid-state diffusion phenomena. Liu et al. [65] mentioned that a supersaturated solid solution of Fe and Al is initially formed by the atomic diffusion process, which is induced by the extensive plastic deformation at a greater strain rate near the tool pin. Then, Fe and Al atoms are transferred to specific regions and converted into the IMCs when they extend to a suitable level at the equivalent pressure and temperature. Lastly, the IMC layer is enhanced gradually through the diffusion of solute atoms. The irregularities in the IMC layer on the steel side could be attributed to the crystallization and growth of the IMCs. The valleys indicated the primarily formed nuclei of IMCs in the steel side, which tend to absorb the diffused Fe and Al elements. Then they grow in depth and transverse directions under suitable pressure and temperature conditions. The region without undergoing the transverse growth of IMC nuclei remained as wave peaks at the interface. In this work, SEM equipped with an EDS system was used to observe the properties of the Al/steel interface layer at a higher

magnification. The EDS elemental chemical mapping at the interface is shown in Fig. 8.13. The different colours are distinguished the interface with the communal existence of Fe from 304 SS and Al from the AA6061 side, which indicates the generation of the new phased IMC layer. During dissimilar FSW, the dispersion of main alloying elements, i.e., Cr, Ni, and Mg, along with Al and Fe at the interface of all samples is observed.

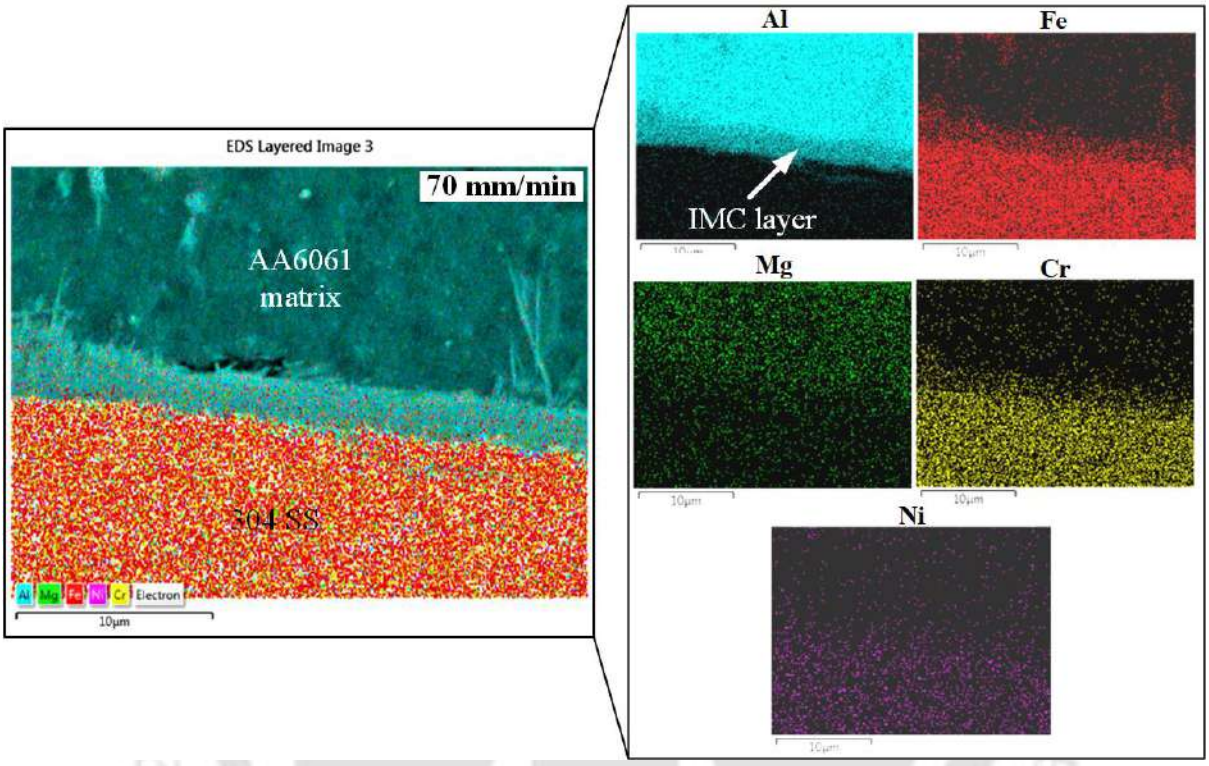

Fig. 8.13 *EDS elemental mapping at the AA6061/304 SS interface in sample* SN_3

Figs. 8.14(a–e) show the SEM images and line scan of the Al/steel interface at different traverse speeds. The unceasing Al/Fe concentration fluctuations in the line scan indicate the IMC layer at the interface region, which is illustrated by means of dotted outlines in Fig. 8.14. The intensity of Fe and Al enhanced as moving from the interface towards the base 304 SS and AA6061 side, respectively. It is observed that the average (AVG) IMC layer thickness enlarged by reducing the traverse speed. During the FSW process, the traverse speed controls the time spent during the linear movement of the tool per rotation. Heat input and plastic deformation increase at a lower traverse speed since the friction at the tool/workpiece interface persists longer in a particular area.

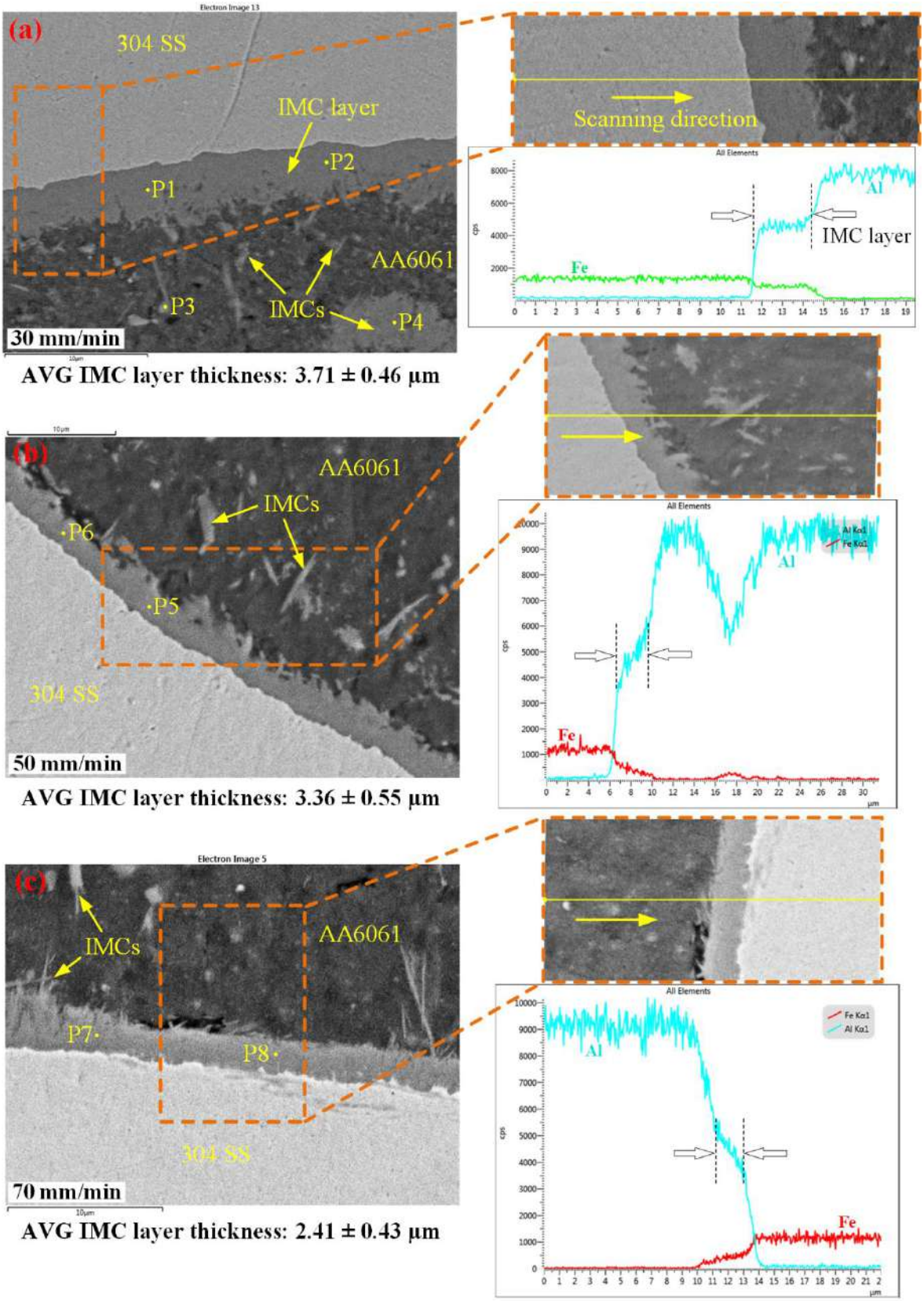

Fig. 8.14 *SEM image and EDS line scan in sample (a) SN_1; (b) SN_2; (c) SN_3; (d) SN_4; and (e) SN_5*

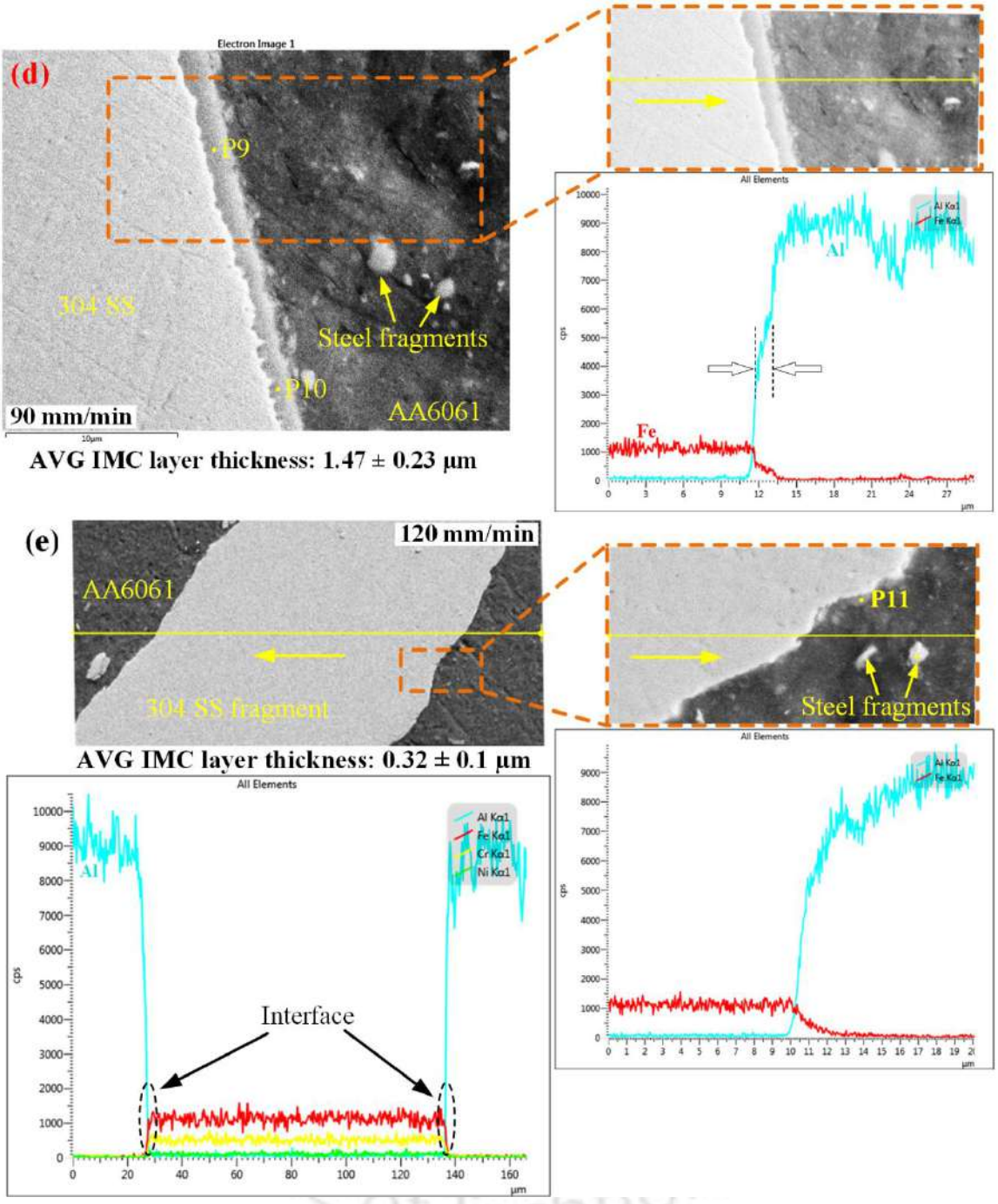

Fig. 8.14 *Continued*

In this perspective, at a lower traverse speed, the excessive stirring under higher heat generation eased the intermetallic reaction and atomic diffusion between Al and Fe, which resulted in a growth in IMC layer thickness. The hard IMC tangles in a highly thick IMC layer can act as a stress riser, whereas a thin IMC layer suggests insufficient metallurgical bonding between dissimilar materials. Therefore, it is essential to find an IMC layer thickness to improve the joint strength by providing a better metallurgical bonding at the Al/steel interface. In this work, the EDS point examination was carried out at different points to identify the

composition of the IMC layer in samples SN_1–SN_5, and the results are expressed in Table 8.2. Based on the EDS elemental composition, the Al-rich IMCs, namely Al_3Fe are probably formed at the Al/steel interface. Pourali et al. [70] mentioned that the higher thermal conductivity of aluminum leads to the generation of Al-rich IMCs at a comparatively lower interface temperature than the SZ.

Table 8.2 *EDS analysis corresponding to the points marked in Fig. 8.14*

Source	Analysis position	Composition (at.%)								Possible constituents
		Al	Fe	Cr	Ni	Si	Mg	Mn	Cu	
Fig. 8.14(a)	P1	75	16.2	3.4	2.8	1.9	0.2	0.2	0.3	Al_3Fe
	P2	74.9	16.2	3.6	1.9	2.5	0.2	0.4	0.3	
	P3	75.2	17.1	3.6	1.4	2.2	–	0.4	0.3	
	P4	74.5	17.7	4.4	1.4	1.4	–	0.3	0.3	
Fig. 8.14(b)	P5	75.6	14	6.3	2.4	0.4	0.9	–	0.3	
	P6	74.8	15.9	4.2	2.4	1.8	0.3	0.3	0.5	
Fig. 8.14(c)	P7	74.7	17.1	4.2	1.6	1.9	–	0.3	0.3	
	P8	75.3	16.3	4.5	1.5	1.4	–	0.3	–	
Fig. 8.14(d)	P9	74.6	15.6	4.4	1.1	3.1	0.6	0.2	0.4	
	P10	74.9	14.1	6.8	2.4	0.4	1	–	0.3	
Fig. 8.14(e)	P11	75.7	16.7	4.5	1.5	1.1	0.1	0.3	–	

An in-depth analysis of the Al/steel interface and SZ was performed by the AFM technique. Figs. 8.15(a–d) show the two-dimensional and three-dimensional AFM topographic images at the interface region and SZ in sample SN_4. It is observed that the surface irregularity increased as moving towards the SZ from the base 304 SS, as shown in Fig. 8.15(a), which indicates that the SZ is much rougher than the base material (304 SS). The peaks in surface roughness are attributed to the distribution of the steel fragments and IMCs in the AA6061 matrix. On the other hand, a drop in the surface roughness indicated the occurrence of grain refinement in the SZ [197].

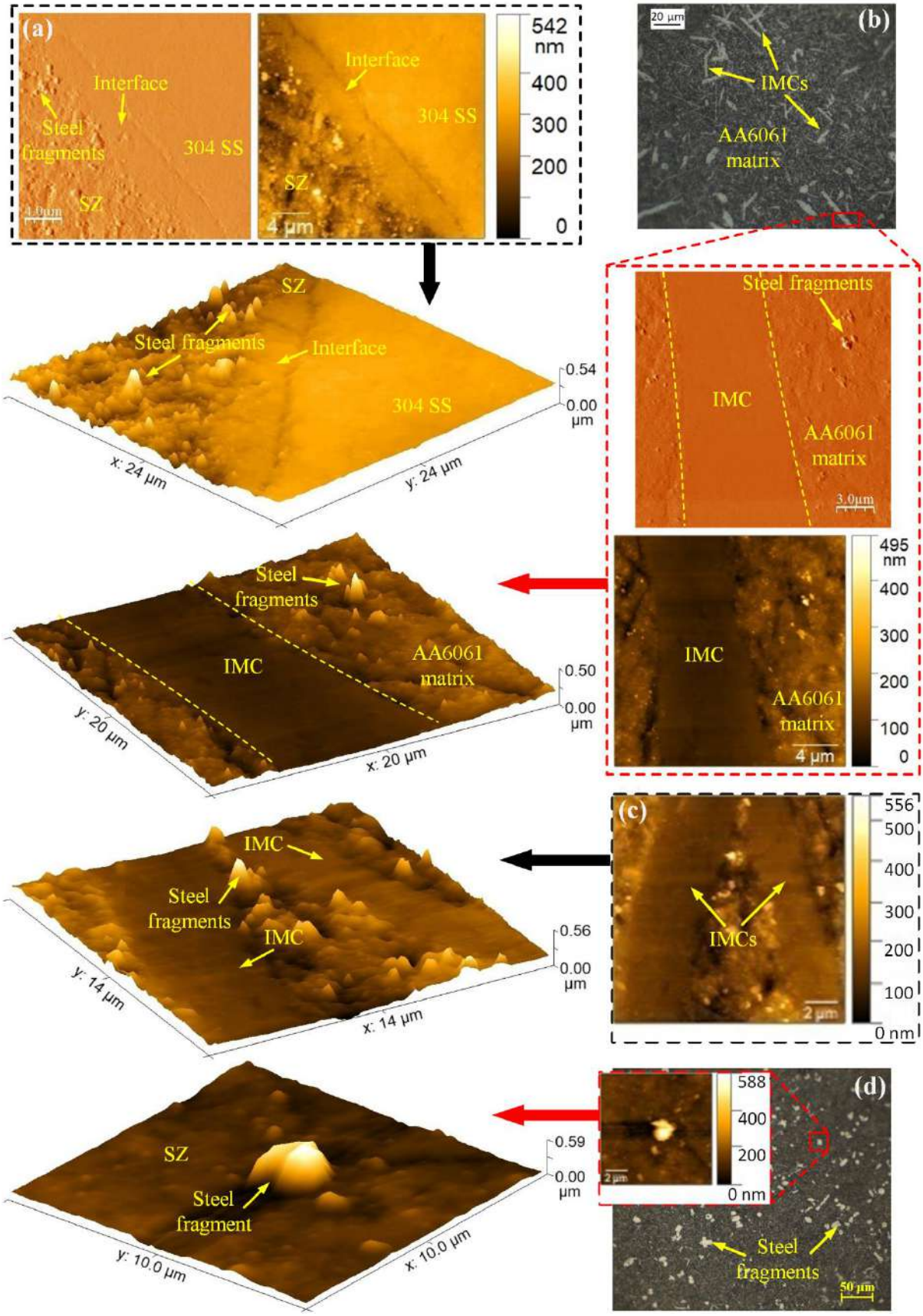

Fig. 8.15 *AFM analysis of the (a) interface region; and (b–d) SZ*

From Figs. 8.15(b–d), it is observed that the steel fragments inside the SZ created peak heights significantly greater than the IMCs. In the dissimilar FSW of steel and Al, the cracks are generated initially on the base steel side due to shear stress induced by the rotating tool. Further deformation causes the generation of steel fragments by the growth of these cracks and then mechanically encompassed inside the SZ through the rotating action of the tool. Conspicuously, a similar mechanism produces the smaller steel fragments from the larger ones. Besides this, some of them transformed into IMCs through the reaction-diffusion process instead of pure mechanical mixing between the Al matrix and steel fragments. Hereafter, the IMCs are consumed inside the AA6061 matrix and produce lower peak heights than the steel fragments. Consequently, SZ could be considered a steel fragments/IMCs improved Al–matrix caused by the greater hardness of steel fragments/IMCs than the base AA6061 and 304 SS, which is discussed in the next section. Bahrami et al. [198] also employed a similar technique (AFM) to confirm the spreading of the SiC nano-particles in the Al matrix of the FS welded 7075 aluminum alloy.

The Al (black) and Fe (white) interface is separated by two distinct regions: IMC and mixed layers. An intercalated layered structure with dark and light grey parts is detected in the mixed layer, as shown in Figs. 8.16 and 8.17. The intercalated layered structures are generated adjacent to the weld interface at the steel side. The mixing and stirring of the dissimilar materials produced these structures due to severe frictional heat generation.

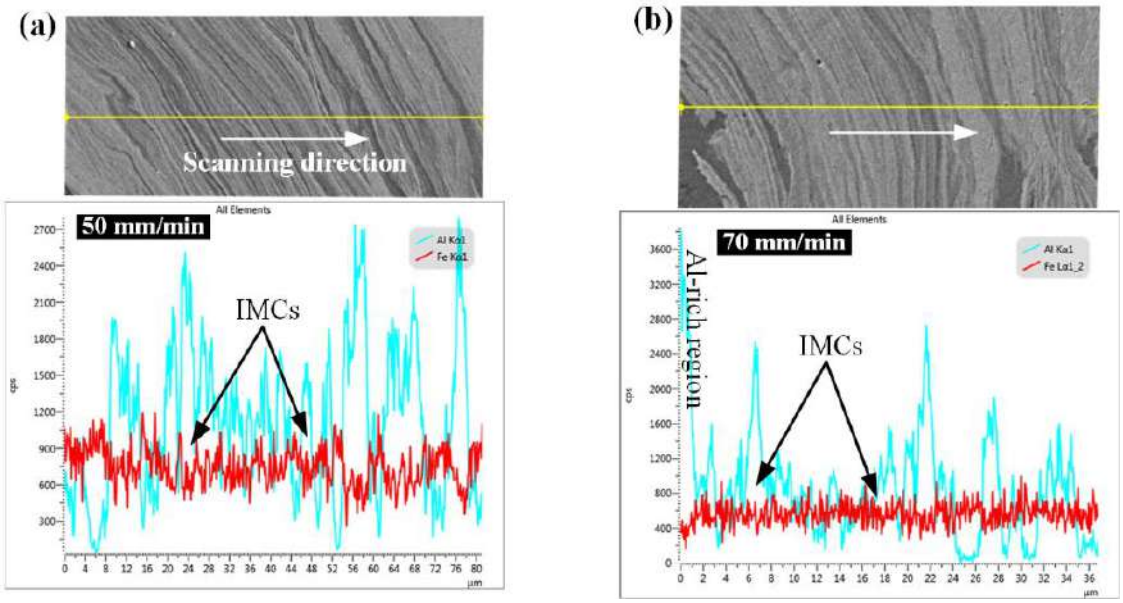

Fig. 8.16 *EDS line scan at the intercalated structure in sample (a) SN_2; and (b) SN_3*

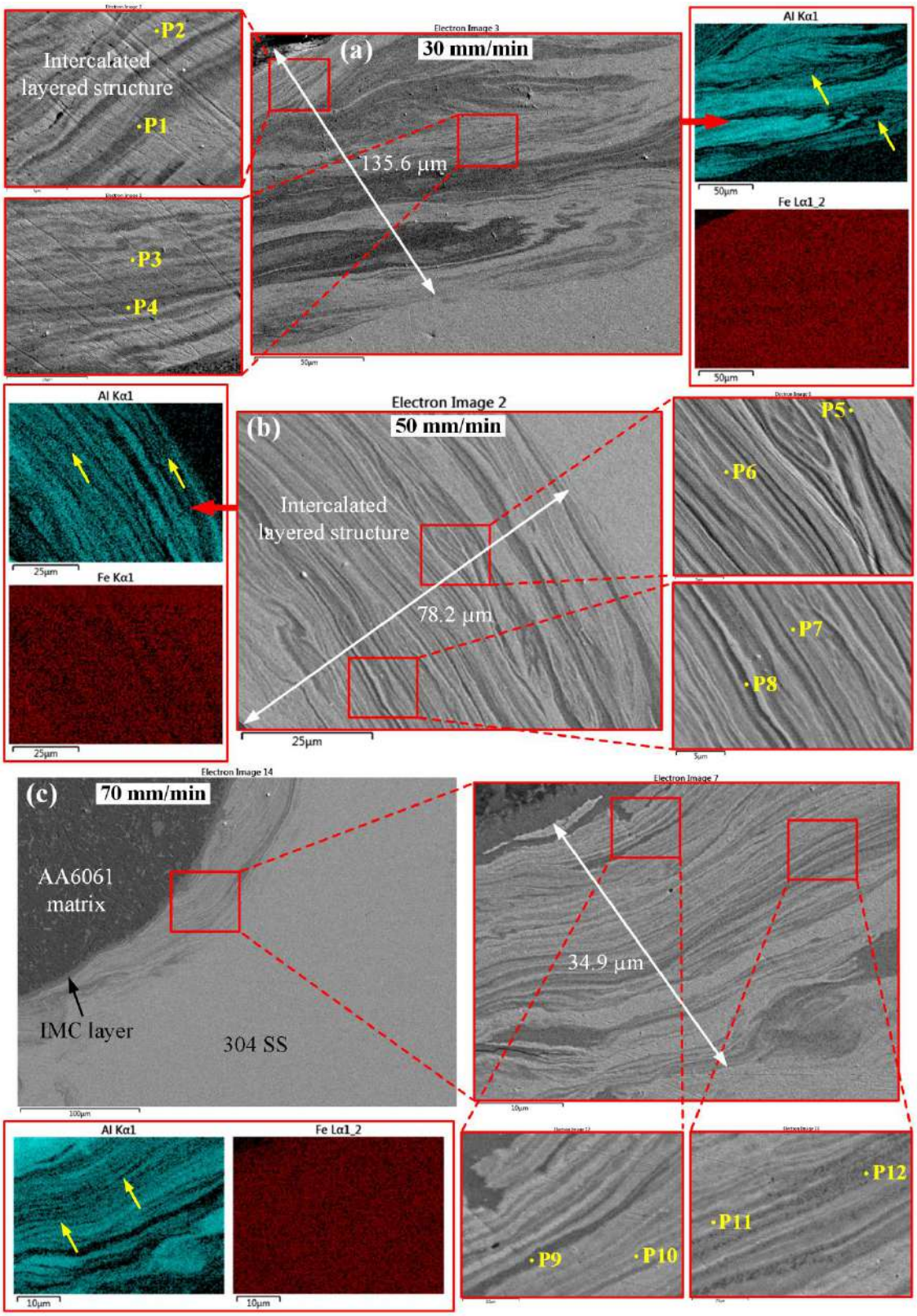

Fig. 8.17 *SEM image and EDS elemental mapping at the intercalated structure in sample (a) SN_1; (b) SN_2; (c) SN_3; (d) SN_4; and (e) SN_5*

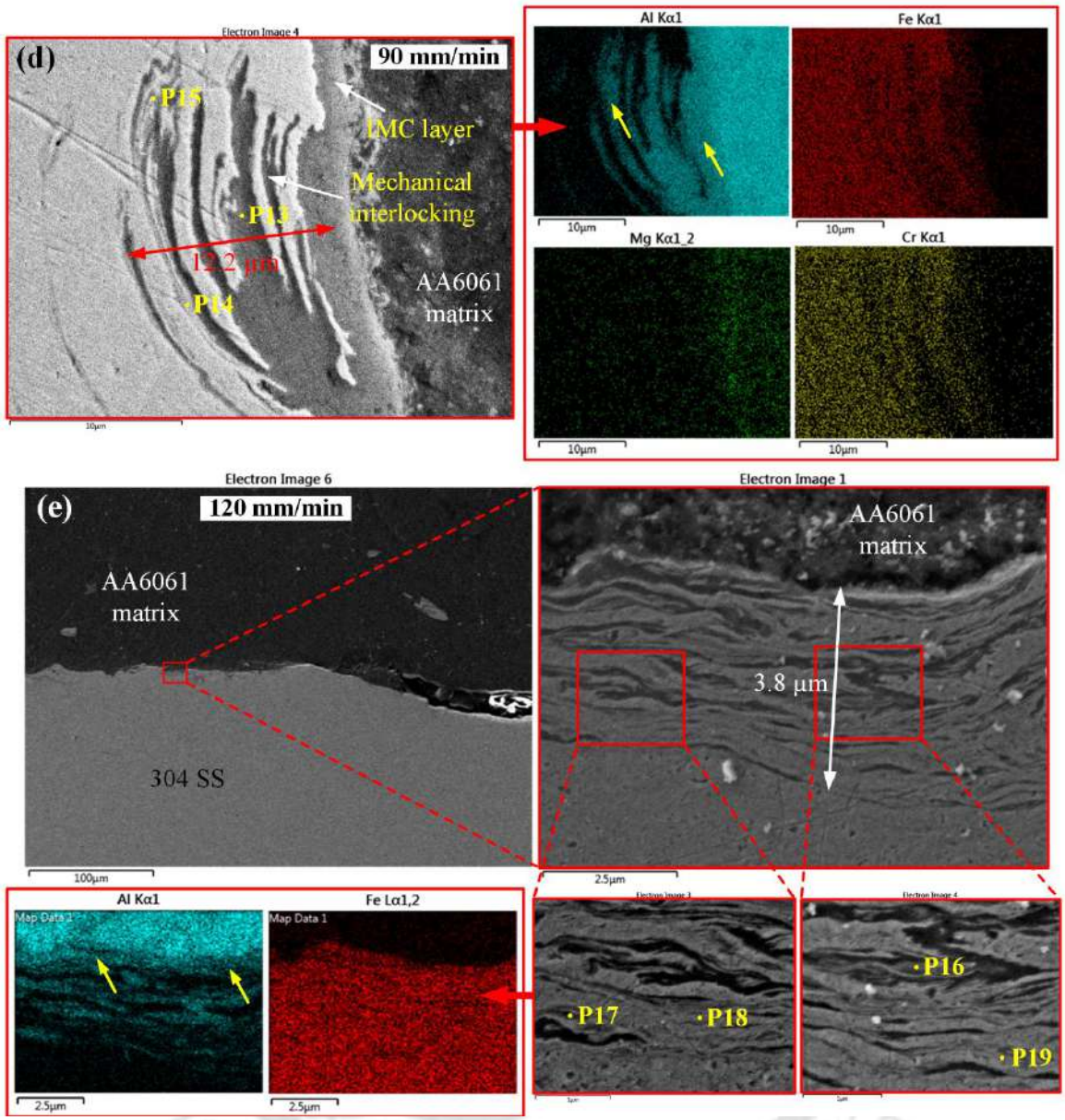

Fig. 8.17 *Continued*

Table 8.3 *EDS analysis corresponding to the points marked in Fig. 8.17*

Source	Analysis position	Composition (at.%)									Possible constituents
		Al	Fe	Cr	Ni	Si	Mg	Mn	Cu	Zn	
Fig. 8.17(a)	P1	75.9	16.6	4.3	1.7	1.5	–	–	–	–	Al_3Fe
	P2	50.3	35.2	8.9	4.1	0.6	0.3	0.6	–	–	AlFe
	P3	49.4	36.4	9.3	3.7	0.3	–	0.4	–	0.5	
	P4	75.4	16.4	3.7	2.7	1.3	0.2	0.3	–	–	Al_3Fe
	P5	75.2	18	4	1.7	0.8	0.1	0.2	–	–	
Fig. 8.17(b)	P6	51.1	34.3	8.7	3.9	0.6	–	–	1.2	0.2	AlFe
	P7	49.4	32.4	10.1	3.6	0.7	–	0.6	2.4	0.7	
	P8	75	18.2	4.4	1.3	0.8	–	0.3	–	–	Al_3Fe
	P9	75.4	18.5	3.9	1.1	0.9	–	0.2	–	–	
Fig. 8.17(c)	P10	52.3	33.3	9.5	3.5	0.7	0.1	0.5	–	0.2	AlFe
	P11	48.5	36.8	10.7	3.2	0.5	–	0.3	–	–	
Fig. 8.17(d)	P12	76.1	18.6	3.5	1	0.7	0.1	–	–	–	Al_3Fe
	P13	75.9	18.4	3.2	1.2	0.7	–	0.4	0.1	–	
	P14	26	52.1	14.6	5.7	0.7	0.1	0.7	0.1	0.1	$AlFe_3$
	P15	48.7	36.6	9.3	4.1	1.2	0.1	–	–	–	AlFe
	P16	48.7	36	10.1	3.3	0.9	0.1	1	–	–	
Fig. 8.17(e)	P17	75.1	17.1	4.3	1.6	1.5	0.2	0.1	–	–	Al_3Fe
	P18	27	52.2	13.7	5.4	0.5	–	1.2	–	–	$AlFe_3$
	P19	27.6	50.1	13.8	6.8	0.5	–	1.2	–	–	

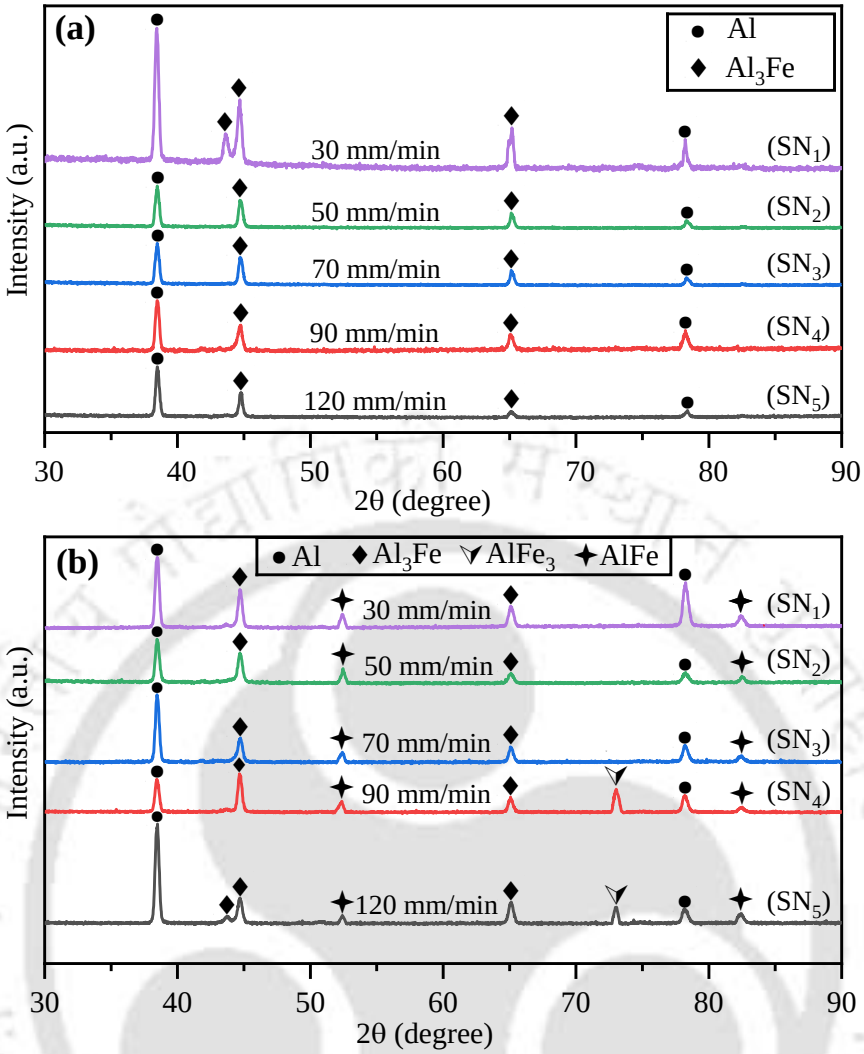

Fig. 8.18 *XRD analysis of (a) interface; and (b) intercalated structure at varying traverse speed*

EDS elemental mapping indicated that the darker region is primarily composed of Al with a small amount of Fe. However, the lighter region is identified as the flowed/deformed 304 SS portion, which contained diffused Al from the AA6061 base material. In intercalated structures, the diffusion of major elements, namely Fe and Al are signified by red and cyan colours, respectively. The mutual diffusion of Fe and Al inside the intermixed region is pointed through yellow arrows. In the EDS line scan, the abrupt Al and Fe concentration fluctuations signify the probability of IMCs formation in the intercalated structure, as shown in Fig. 8.16. In this regard, the EDS point analysis and elemental mapping were executed to identify the composition of IMCs in these structures, as shown in Fig. 8.17. From Table 8.3, the atomic percentages at various points suggest the probable large distribution of Al-rich Al_3Fe (dark grey) + Fe-rich AlFe (light grey) IMCs inside the intercalated structure of samples SN_1–SN_3. However, points P14, P18, and P19 suggest the formation of additional IMCs, namely $AlFe_3$

with AlFe and Al_3Fe in samples SN_4 and SN_5. Besides the EDS analysis, peaks in diffraction patterns of XRD graphs also confirmed the Al_3Fe IMCs at the interface, Al_3Fe + AlFe at the intercalated structure in SN_1–SN_3, and Al_3Fe + AlFe + $AlFe_3$ in SN_4 and SN_5, as shown in Fig. 8.18. According to the Al-Fe phase diagram (Fig. 1.7), the Fe_3Al is usually formed at a temperature lower than that of FeAl. Hence, the portion of FeAl converted into Fe_3Al at the higher traverse speed under lower heat generation. Wan and Huang [4] reported that the Fe-rich IMCs, namely AlFe and $AlFe_3$ exhibit better ductility and toughness than the Al-rich IMCs like Al_3Fe and Al_5Fe_2. The IMCs inside the intercalated structure indicated in situ solid-state chemical reactions between AA6061 and 304 SS base alloys instead of simple mixing and mechanical interlocking of dissimilar materials.

8.4 MECHANICAL CHARACTERIZATION

As discussed in previous sections, micro cracks, voids, IMCs, steel fragments, and microstructural heterogeneity are significantly influenced the mechanical characterizations of welded joints. The fracture path across the cross-section of the joints at varying traverse speed is shown in Fig. 8.19(a). The fractured tensile samples and stress-strain curves at different traverse speeds are shown in Fig. 8.19(b). Fig. 8.20 shows the UTS trend with IMC layer thickness and area fraction of steel fragments at varying traverse speed. The SEM analysis was conducted to characterize the fractured surfaces of tensile samples, as shown in Fig. 8.21.

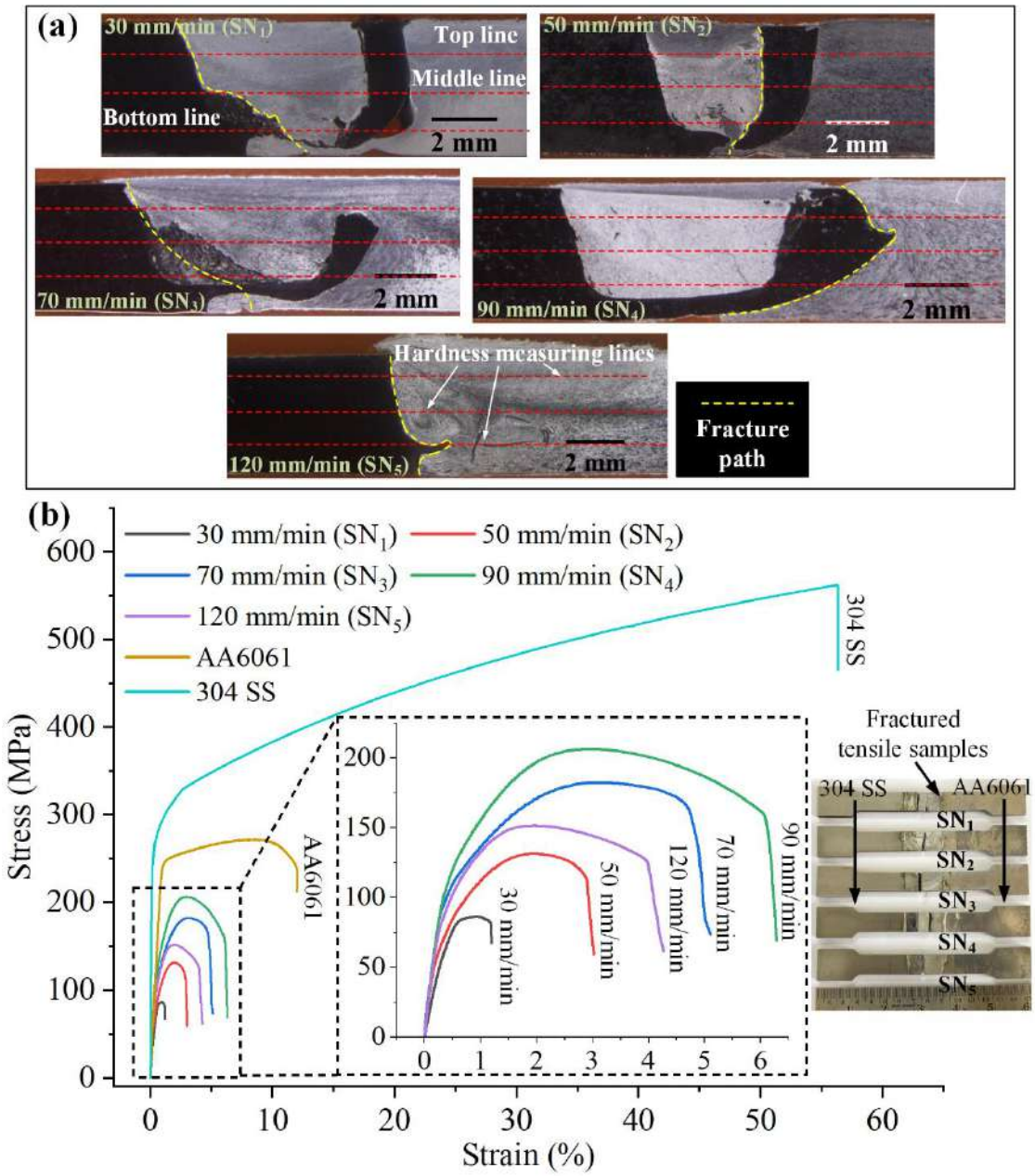

Fig. 8.19 *(a) Fracture path and hardness measuring lines across the weld cross-section; and (b) stress-strain curves at varying traverse speed*

It is observed that sample SN_4 fractured away from the SZ at the outer 304 SS/AA6061 interface, as shown in Fig. 8.19(a). As shown in Fig. 8.19(b), it experienced the highest elongation (strain) of 6.2% and weld strength of 206.2 MPa, which are around 51.6% and 75.6% of the AA6061 base material, respectively. The tensile properties of sample SN_4 are improved compared to other samples due to the inherent mechanical interlocking provided by the fine-grained steel strip (Fig. 8.1) to the defect-free SZ. The mechanical interlocking provided by the intercalated lamellar structure, and ductile Fe–rich IMCs, namely $AlFe + AlFe_3$ (Fig. 8.17) inside the mixing zone are favourable for the elongation and weld strength.

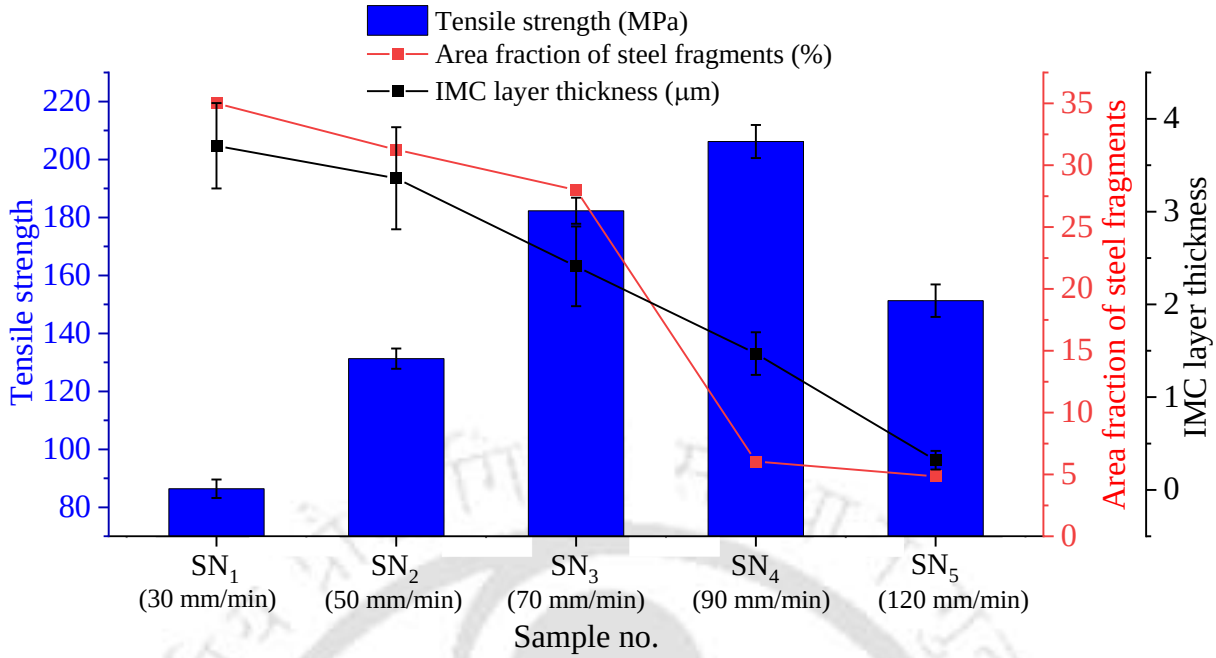

Fig. 8.20 *Tensile strength variation with IMC layer thickness and area fraction of steel fragments at varying traverse speed*

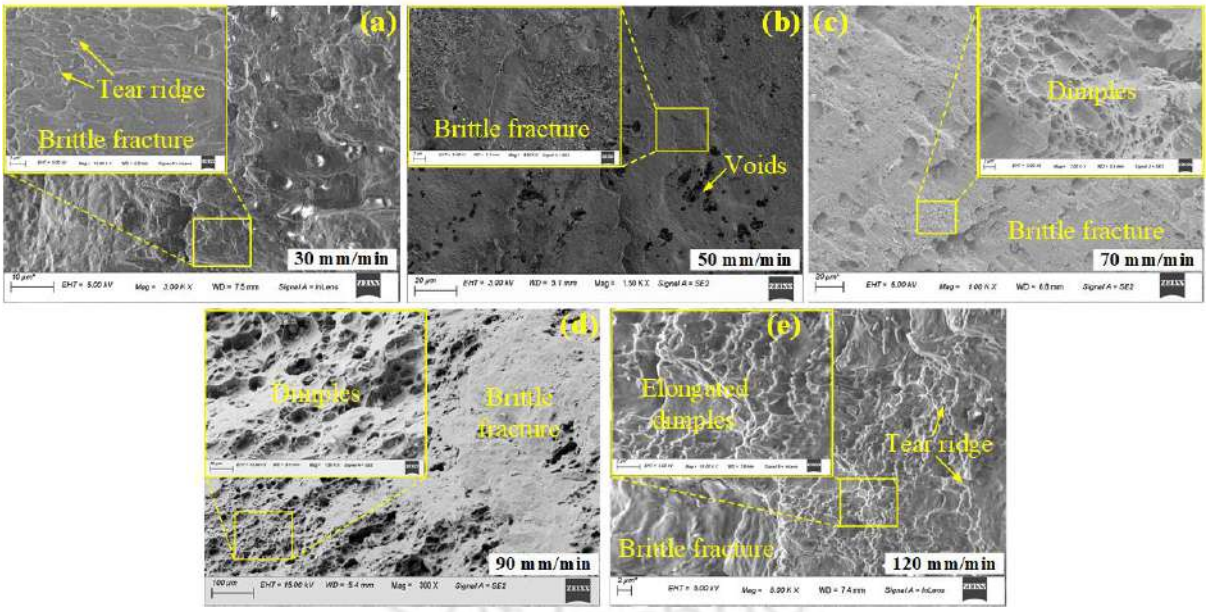

Fig. 8.21 *Fracture morphology in tensile sample (a) SN_1; (b) SN_2; (c) SN_3; (d) SN_4; and (e) SN_5*

The UTS and elongation are reduced with a decrease in traverse speed from 90 mm/min to 30 mm/min, as shown in Fig. 8.19(b). This is attributed to the formation of the voids in the SZ caused by a higher area fraction of steel fragments/brittle Al_3Fe IMCs (Fig. 8.5) and a thick IMC layer of Al_3Fe. Hussein et al. [3] also reported that the Al-rich IMCs, namely Al_2Fe, Al_3Fe, and Al_5Fe_2 are more detrimental to weld strength than Fe-rich IMCs like $AlFe_3$ and AlFe. At the Al/steel interface, the phase volume usually changes at a thicker IMC layer, which could

produce stress concentration and deteriorate the tensile properties. The individual IMCs inside the SZ enhance the brittleness by constraining material movement through pinning action during the tensile test. As shown in Fig. 8.20, sample SN_1 exhibited the minimum tensile strength compared to other traverse speed conditions due to the defects created by the relatively thick IMC layer and more scattering of steel fragments/IMCs. In sample SN_1, the higher area fraction of brittle IMCs (i.e., Al_3Fe) inside the SZ also adversely affected the joint strength. Furthermore, the UTS and elongation reduced with an increase in traverse speed from 90 mm/min to 120 mm/min, as shown in Fig. 8.19(b). In sample SN_5, IMCs layer thickness and area fraction of IMCs/steel fragments inside the SZ are lesser than the other samples. Accordingly, these strength-improving factors would produce a higher weld strength. However, the defects like bigger cracks at the Al/steel interface (Fig. 8.2) are generated due to insufficient stirring under low heat input at higher traverse speed. These defects dominated over the strength-improving factors and reduced the joint strength and elongation. As shown in Figs. 8.21(c–d), the fracture morphology revealed that the tensile samples SN_3–SN_5 contained brittle flat surfaces with some irregularly shaped ductile dimples, which signifies that the failure occurred under the combined ductile-brittle mode. Besides this, samples SN_1 and SN_2 revealed the brittle failure mode due to flat surfaces only in fractured surfaces, as shown in Figs. 8.21(a) and 8.21(b). The micro-cracks generally propagate, join together and produce bigger cracks at straining conditions during the tensile test, which generally causes a sudden fracture mode.

The Vickers micro-hardness is measured across the cross-section along the top, middle, and bottom line from the upper weld surface, respectively, as shown in Fig. 8.19(a). The hardness profiles at varying traverse speed are plotted in Figs. 8.22(a–e). The hardness of 304 SS and AA6061 base material is 168.5 HV and 64.2 HV, respectively. The microstructural heterogeneity across the weld cross-section and different thermomechanical properties of base materials are responsible for the oscillation behaviour in the hardness profiles.

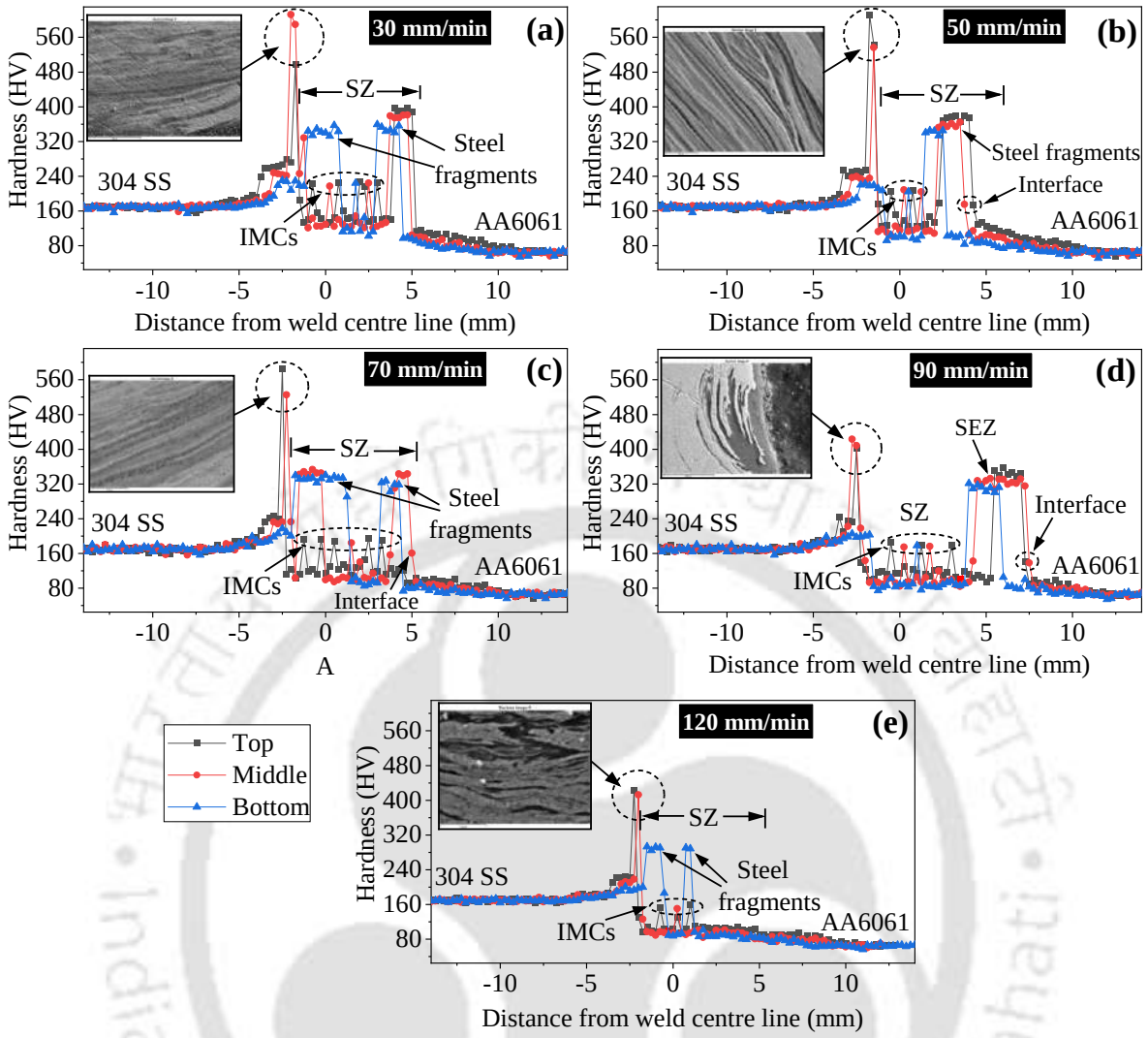

Fig. 8.22 *Hardness distribution in sample (a) SN_1; (b) SN_2; (c) SN_3; (d) SN_4; and (e) SN_5*

It is observed that the steel fragments significantly enhanced the hardness values within the AA6061 matrix in the SZ. On the other hand, the large steel fragments reduced the joint strength, as shown in Fig. 8.20. It is difficult to deform and intermix the large steel fragments in the AA6061 matrix because their hardness and density are higher than the AA6061. The softened Al easily deformed during the welding, whereas the harder steel fragments restricted the flow of the viscous Al and produced the improper material flow at the surface region of steel fragments. Consequently, the viscous Al could not fill the surface gaps between the steel fragments and the Al matrix. The unfilled gaps generated the defects like tunnels or cracks inside the AA6061 matrix (Fig. 8.2), which are detrimental to the weld joint strength.

At a lower traverse speed of 30 mm/min, the maximum hardness in the SZ (304 SS) and SZ (AA6061) is 396.5 HV and 144.4 HV, respectively. At a higher traverse speed of 120 mm/min, it is 293.3 HV and 110.4 HV in the SZ (304 SS) and SZ (AA6061), respectively. The grain refinement with a decrease in traverse speed is responsible for the increase in hardness

magnitudes. The comparatively fine-grained microstructure (Fig. 8.7) produced greater hardness magnitudes at the top line than that of the bottom and middle line, as shown in Fig. 8.22. The hardness values decreased as moving toward base materials and almost turned to the level of 304 SS and AA6061. TMAZ and HAZ on both sides experienced significantly greater hardness values than the base materials while lower than the SZ. Furthermore, TMAZ and HAZ in the 304 SS side exhibited hardness magnitudes higher than the AA6061. According to Hall–Petch strengthening [16], the fine-grained microstructure across the weld cross-section improved the hardness values. The low hardness at TMAZ than the SZ could be attributed to the low dislocation density by the thermomechanical behaviour of this zone [81]. In the dissimilar FSW of Al and steel alloy, the additional mechanisms except for grain refinements, i.e., IMCs formation, material flow, and material inter-mixing can dominate and monitor the hardness variation. Apart from the steel fragments, the hardness spikes are caused by the spreading of the IMCs, which could be considered as reinforcing elements in the Al matrix due to their relatively greater hardness than the base materials. The magnitude of the hardness spikes reduced from samples SN_1 to SN_5 because the area fraction of IMCs within the SZ decreased by enhancing the traverse speed (Fig. 8.5). The hardness of the IMC layer at the interface is larger than the AA6061 matrix, but less than the individual IMCs distributed in the SZ and mixed region. During the Al/steel interface measurement, the microhardness imprint covered certain portions of the AA6061 matrix due to the limited breadth of hardness indenter. The softer AA6061 matrix lowered the hardness value at the interface compared to the hardness induced by individual IMCs. As shown in Fig. 8.22(d), SEZ in the sample SN_4 experienced a hardness higher than the individual IMCs as well as the TMAZ (304 SS) because it exhibited the comparatively fine-grained microstructure. The hardness was also measured at the intercalated features inside the mixed region. This region experienced the highest hardness due to the formation of extensive IMCs, namely Al_3Fe + AlFe in samples SN_1–SN_3 and Al_3Fe + AlFe + $AlFe_3$ in samples SN_4 and SN_5. In this region, the hardness magnitude varied in the range of 382 HV–614 HV in samples SN_1–SN_3 and 350 HV–484 HV in samples SN_4 and SN_5. Anaman et al. [82] also observed the mixing region as the hardest region caused by Al-Fe solid solutions and IMCs.

8.5 SUMMARY

In this chapter, a comprehensive experimental investigation on the joining the 304 SS with AA6061 is discussed. In this study, a detailed analysis was performed to predict the effect of different traverse speeds on grain size at various zones, IMC layer thickness, and the fraction of IMCs/steel fragments inside the SZ. Furthermore, their coinciding effect on mechanical properties, i.e., tensile properties and hardness of welded joints was investigated. A thorough analysis of fractured surfaces of tensile samples is also discussed in this chapter.

From the experimental investigation, it is observed that microstructural variation, steel fragments, and IMCs formation in the SZ are significantly influenced the mechanical properties, particularly weld strength, ductility, and hardness. It is understood that the grain refinement and dispersed IMCs in SZ enhanced the hardness values. However, the thicker IMC layer and larger area fraction of steel fragments and IMCs reduced the joint strength and ductility of samples SN_1–SN_3. Similarly, the defects like larger cracks at the interface decreased the strength and ductility of the sample SN_5 due to insufficient stirring. From the chosen traverse speed conditions, sample SN_4 experienced the sound weld quality at a 90 mm/min traverse speed with an average IMC layer thickness of 1.47 ± 0.23 µm. At this traverse speed, the mixed region consisted of IMCs, namely Al_3Fe + AlFe + $AlFe_3$, and the area fraction of IMCs and steel fragments is about 0.023% and 6.05% of the SZ area, respectively. Furthermore, the fine-grained microstructure in the 304 SS strip delivered the essential mechanical interlocking to the SZ and enhanced the weld strength. The intercalated features in the mixed region acted as the hardest zone caused by the intense IMCs generation in this zone, namely Al_3Fe + AlFe in samples SN_1–SN_3, and Al_3Fe + AlFe + $AlFe_3$ in samples SN_4 and SN_5.

CHAPTER 9

NUMERICAL STUDY ON THE JOINING OF STAINLESS STEEL AND ALUMINUM ALLOY

The experimental investigation on the dissimilar joining of 304 SS and AA6061 are covered in the previous chapter. This chapter expands the research on this joining with the assistance of CFD-based three-dimensional coupled thermal-fluid flow analysis. In this work, a steady-state multi-species transport model (STM) coupled with a mixture model was established for the first time, where the CFD solver transported species mass fractions of the materials. The strain rates & temperature-dependent viscosity, and heat generation, including tool-workpiece contact conditions were employed in the model through user-defined functions. The developed model can capture the transversal/horizontal material features and embedded steel fragments/strips in the weld joints. The impact of the tool rotational speed on the axial force, torque, temperature, velocity, strain rate, viscosity, and material intermixing was understood by triggering material flow associated with the tool-workpiece interaction. In addition, experimental findings, such as temperature measurement and macrographs of the weld cross-section were used to validate the simulation results. Furthermore, the consequence of flow properties on the IMC layer and joint efficiency was also investigated in detail. The summery of the numerical investigation is presented at the end of the chapter.

9.1 PROCESS PARAMETERS

A novel multi-species transport model based on CFD phenomena was developed for the dissimilar FSW of 304 SS and AA6061. Based on the experimental trials, the tool geometry and welding/machine parameters, i.e., tool traverse speed of 90 mm/min, tool offset of 1.5 mm towards AA6061 from weld line, and plunge depth of 0.1 mm were chosen. Table 9.1 shows the rotational speeds chosen for evaluating the material flow and intermixing phenomena. As illustrated in Fig. 9.1, five planes (marked by red lines) were chosen to understand the material flow properties. The vertical planes V1 (XZ) and V2 (YZ) were taken at the mid-section of the weld plate, while horizontal XY planes H1, H2, and H3 were at 0.2 mm, 2 mm, and 3.8 mm from the top surface, respectively.

Table 9.1 *Selected rotational speeds*

Rotational speed	R_{sp1}	R_{sp2}	R_{sp3}	R_{sp4}
(rpm)	300	600	875	1200

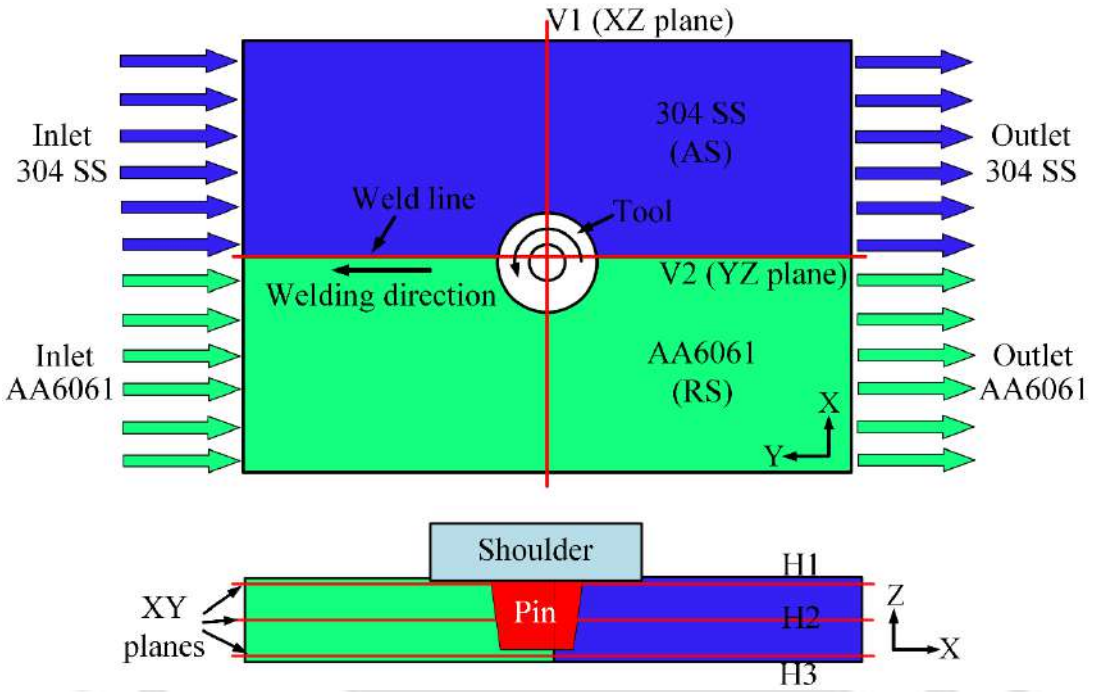

Fig. 9.1 *Location of the observation planes*

9.2 VALIDATION OF THE STM MODEL

The validation of STM results with experimentally measured temperatures is shown in Fig. 9.2. Fig. 9.2(a) shows the comparison between the calculated temperature and the temperature measured by an IR camera. The temperature measurements were performed at 15 mm, 20 mm, 25 mm, and 30 mm from the shoulder surface on the RS. The calculated peak welding temperature at measuring points fairly matched with the experimental values. Furthermore, the STM results are also compared with the transient temperature profiles recorded by K-type thermocouples at points P_1 and P_2, which are positioned at 0.2 mm from the bottom surface, as shown in Figs. 9.2(b) and 9.2(c). Due to the assumption of a steady-state welding stage, the thermal history at a specific point is captured by extracting the temperature curve across the line, which is parallel to the weld line and passing through that point. Then, the transient temperature profile at a particular distance is calculated using the welding speed.

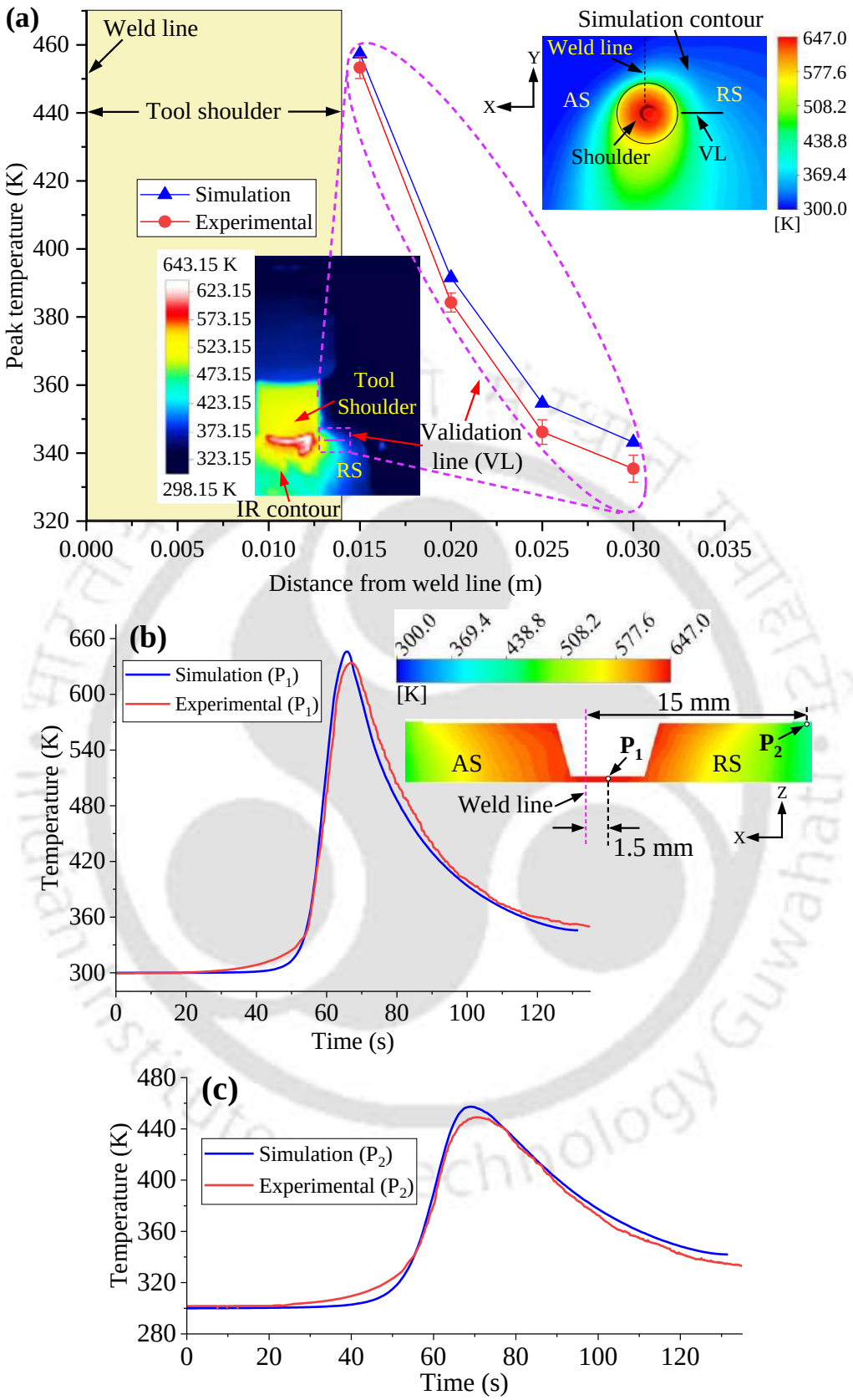

Fig. 9.2 *Validation of STM results with temperature measured by (a) infrared thermometer; and (b,c) thermocouples at* R_{sp3}

It is observed that the calculated temperature profiles also matched with those obtained by experimental measurement. The transient temperature profile showed a sharp increase to the highest temperature followed by a gradual decrease. When the tool reached adjacent to the measuring points, the heat is generated quickly, and then cooling took place slowly as the tool moved away from those points. The inconsistency between the experimental and simulation results is less than 4%. The possible causes of the minor variation include constant consideration of radiation, convection, and friction losses in the STM. Additionally, minor errors could affect the accuracy of the findings during the experimental measurement.

9.3 MATERIAL FLOW BEHAVIOUR

The asymmetrical temperature distribution is observed on AS and RS caused by differences in the thermo-mechanical characteristics of the base materials, as shown in Fig. 9.3(a). The greater heat transfer characteristics of AA6061 enabled the heat to be conducted more quickly in the RS, which resulted in more heat dispersion on the AA6061 side compared to the 304 SS. The top observation line (L1) exhibited a wider peak temperature profile than that of the middle (L2) and bottom (L3), as shown in Fig. 9.3(a). The higher heat generation by the shoulder produced a temperature region broader on the top portion (shoulder/workpiece interface). In agreement with Kadian et al. [109], the less heat transfer to the backing plate produced the maximum temperature at the L3 line, i.e., close to the pin tip. It is observed that the peak temperature increased by enhancing the rotational speed from 300 rpm to 1200 rpm, as shown in Fig. 9.3(b).

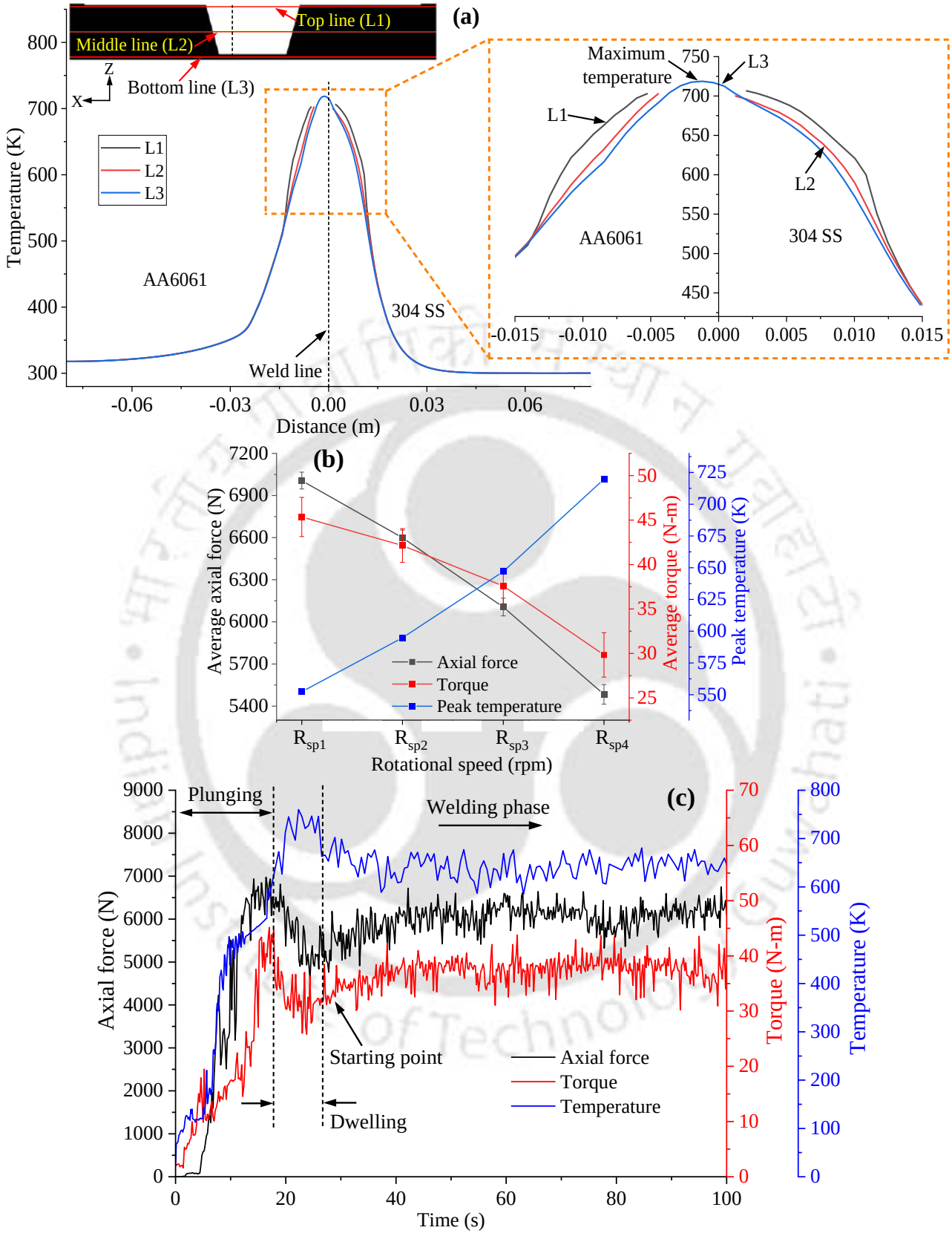

Fig. 9.3 *(a) Peak temperature variation along thickness at R_{sp4}; (b) peak temperature profiles at vaying rotational speed; (c) average axial force, average torque, and peak temperature at varing rotational speed; and (d) axial force, torque, and temperature curves with time at R_{sp3}*

The temperature distribution generally provides a significant impact on the axial force and torque during the welding process. The axial force is essential to maintain the contact between the tool and the workpiece surface [199]. Consequently, the variation of axial force and torque deviation is correlated to the time-temperature findings. The average axial force during the welding phase reduced from 7006.4 ± 60 N to 5483.1 ± 70 N and torque from 45.35 ± 2.2 N-m to 29.84 ± 2.5 N-m with an increase in rotational speed from R_{sp1} to R_{sp4}, as shown in Fig. 9.3(b). The reduction in force/torque could be attributed to the dynamic viscosity of the material, which is subsequently reduced with an increase in temperature, as discussed in the next section. Fig. 9.3(c) shows the correlation between the axial force, torque, and time-temperature profiles. During the plunging phase, the force and torque increased sharply when the tool shoulder made contact with the material. The highest values of the force/torque are obtained during the plunging phase. The peaks in force/torque during the plunging phase are caused by a lack of thermally softened material. After that, the force/torque values decreased due to the higher temperature in the dwelling phase. Then, because the workpiece material close to the tool is already sufficiently softened, the force/torque with temperature is constantly produced with a slight variation throughout the welding phase.

The upper portion of the weld region is denoted as the shoulder-affected zone (SAZ) since the prime driving forces for material flow in this region are produced by shear and extrusion of the shoulder. The central and bottom regions are designated as the pin-affected zone (PAZ), where the material movement is primarily caused by shear on the tool pin side. The velocity and strain rate adjacent to the tool are significantly impacted by the temperature variations. It is observed that the velocity and strain rate around the tool periphery is higher than the other positions due to the greater heat generation, as shown in Figs. 9.4(a) and 9.4(b). The highest strain rate and flow velocity fields are obtained in the SAZ since the effect of viscous momentum transfer by the shoulder is greater at the top portion. In the AA6061 and 304 SS sides, the higher strain rate led to more grain refinement at the SAZ than the PAZ, as shown in Fig. 9.4(b). The geometric dynamic recrystallization due to the greater strain rate and plastic deformation elongates the grains and splits them into smaller grains [195,200]. Moreover, the coinciding impact of heat generation and axial force expelled the plasticized material from beneath the shoulder and generated the flash on the AA6061 side.

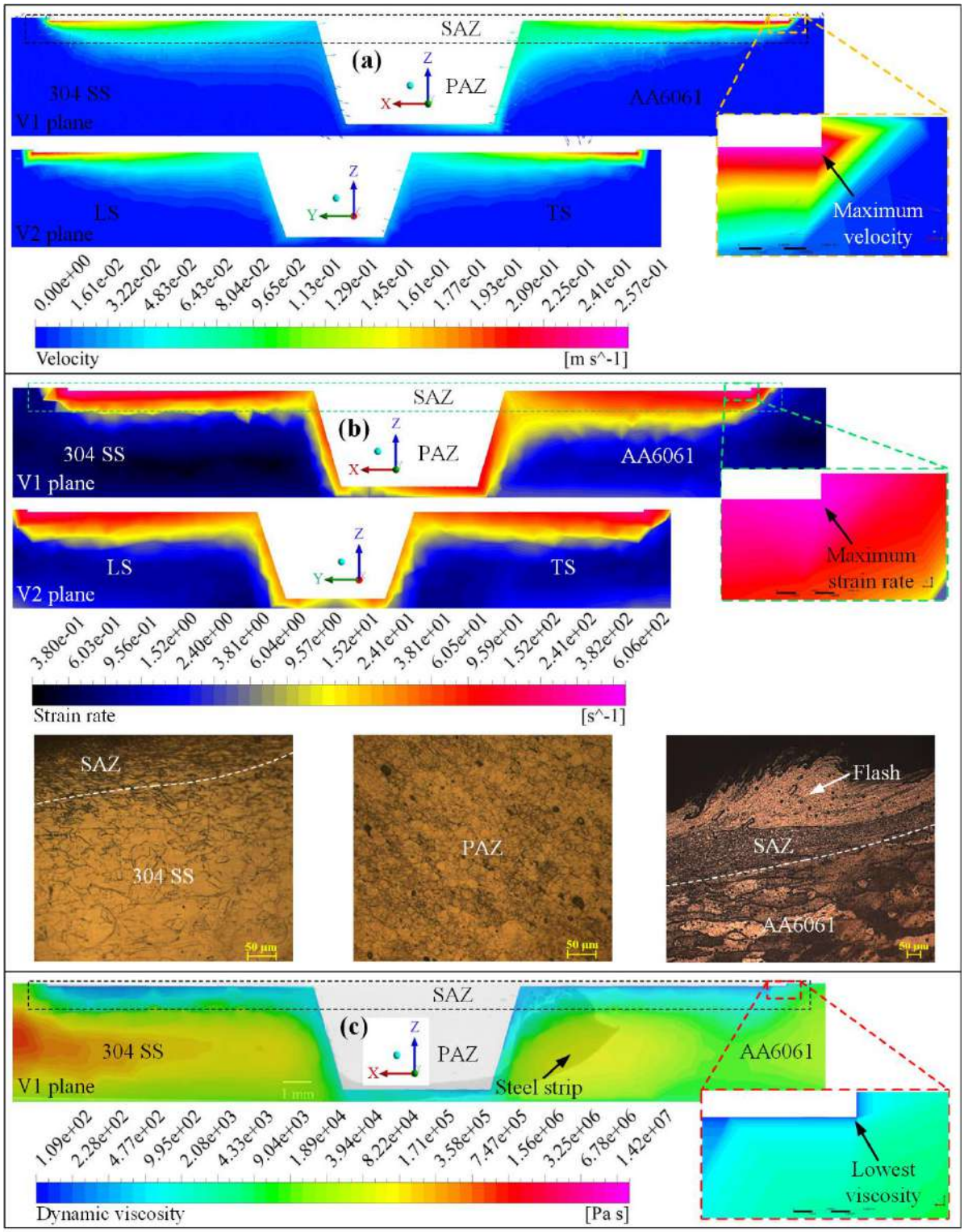

Fig. 9.4 *(a) Cross-sectional contour plot of flow velocity; (b) calculated strain rate and experimental micrographs revealing the SAZ & PAZ; and (c) mapping of experimental macrograph and calculated dynamic viscosity at* R_{sp3}

The maximum material strain rate and flow velocity are obtained on the outside shoulder edge on the AA6061 side, where the dynamic viscosity is also lowest from the whole domain, as shown in Fig. 9.4(c). According to the earlier section, the strain rate and temperature

variables are used to compute the viscosity in the model. A higher viscosity region is observed on the AS. Furthermore, the steel strip movement produced a greater viscosity on the AA6061 side, as shown in Fig. 9.4(c). The higher temperature fields reduced the dynamic viscosity around the tool periphery than in the other regions.

The velocity magnitude contours along the V1 and V2 planes at R_{sp1}–R_{sp4} are shown in Fig. 9.5. In the V2 plane, the TS exhibited material flow velocity values higher than the leading side (LS). This could be attributed to the more significant temperature at the trailing side (TS), which adequately softened the material behind the rotating tool and made it easier to flow at the TS. Additionally, the density, heat transfer coefficients, and viscosity variations in the momentum & energy equations are responsible for the maximum flow velocity on the outside edge of the shoulder in the RS (V1 plane).

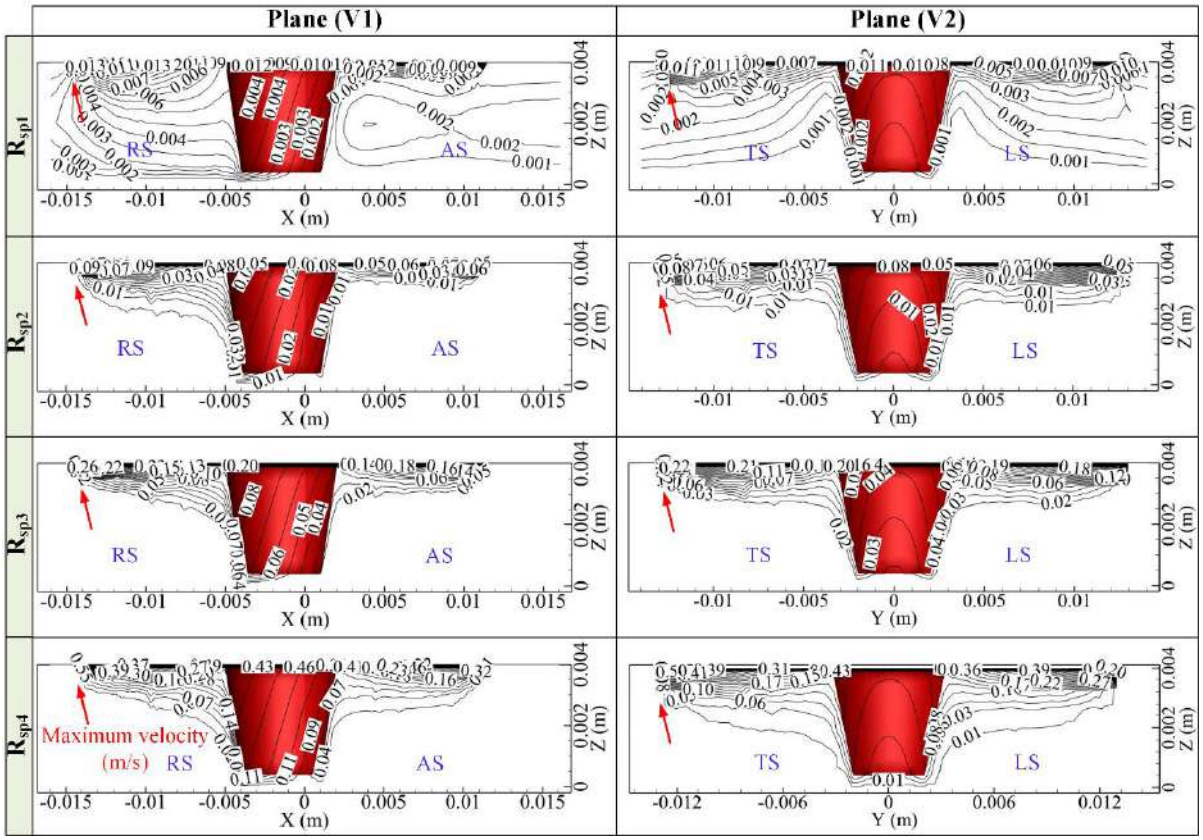

Fig. 9.5 *Flow velocity profiles with magnitude at varying rotational speed*

Fig. 9.6 shows the calculated strain rate around the tool at various transverse planes. The strain rate values are significantly enhanced by increasing the rotational speed. The strain rate dropped rapidly outside the stirring zone of the assisted shoulder. Furthermore, the strain rate magnitudes are higher at the bottom region because of the greater welding temperature close to the pin tip. The strain rate and velocity outlines are plotted at lines L1, L2, and L3 (marked

in Fig. 9.3(a). Due to the greater temperature on the AA6061 side, there is a larger material flow velocity and strain rate than the 304 SS side, as shown in Fig. 9.7(a). The higher frictional heat at the workpiece/shoulder contact produced a greater velocity and strain rate in the top line than the bottom line. The flow velocity is maximum at the outer edge on the AA6061 side, where the strain rate is also the maximum. The minimum viscosity reduced from R_{sp1} to R_{sp4}, which subsequently increased the strain rate from 345.13 s^{-1} to 1013.4 s^{-1}, and flow velocity from 0.014 m/s to 0.573 m/s, as shown in Fig. 9.7(b).

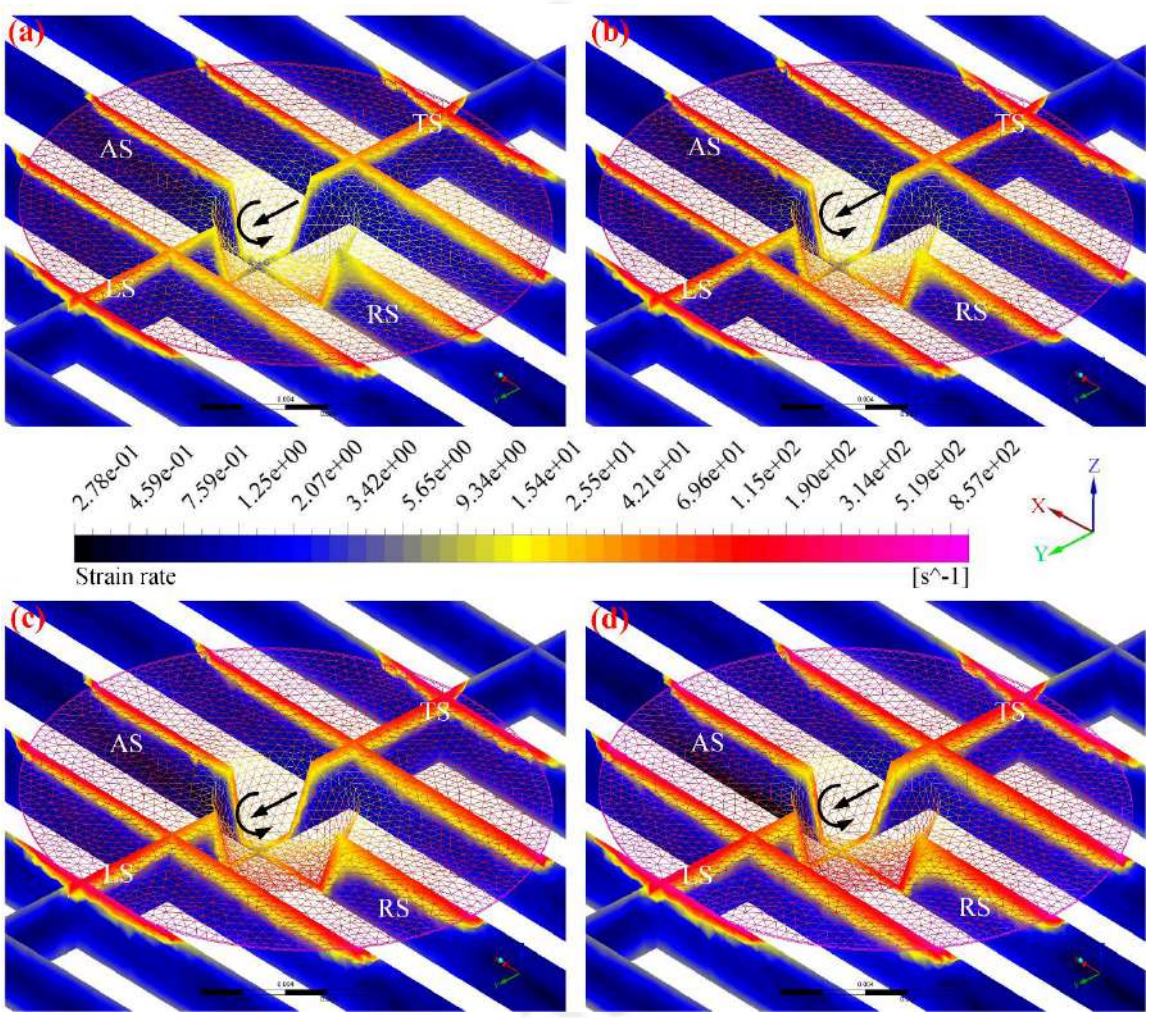

Fig. 9.6 *Strain rate contour plots around the tool at different planes for (a) R_{sp1}; (b) R_{sp2}; (c) R_{sp3}; and (d) R_{sp4}*

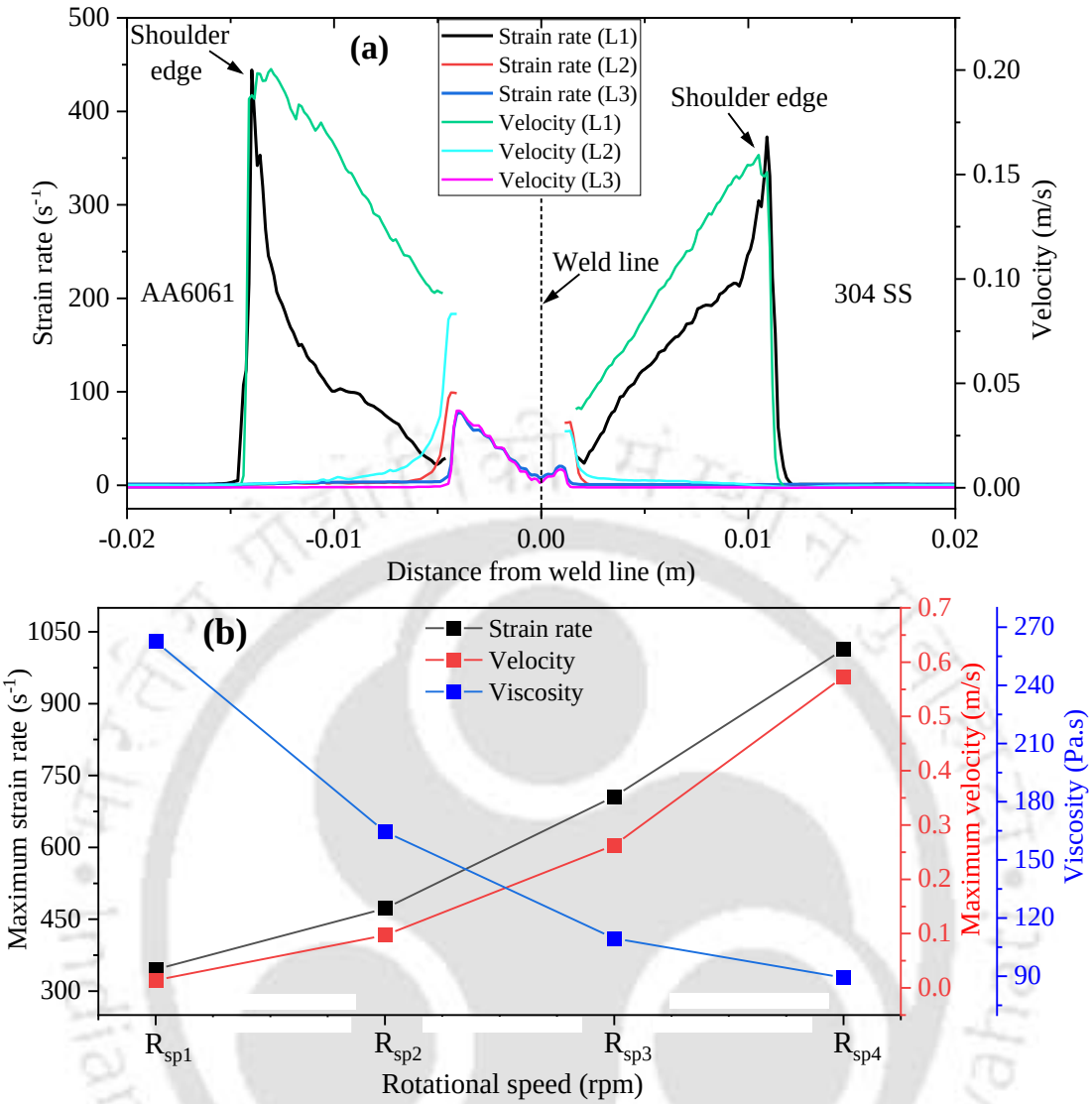

Fig. 9.7 *(a) Strain rate and flow velocity variation with distance from the weld line at R_{sp3}; and (b) maximum strain rate, maximum flow velocity, and lowest dynamic viscosity at varying rotational speed*

The three-dimensional material flow velocity across the tool at R_{sp3} is shown in Fig. 9.8(a). Fig. 9.8(b) shows the mapping of experimentally and simulated streamlines across the tool. The intermixing of the material flow vectors of 304 SS and AA6061 is shown in Fig. 9.8(c), which could control the reaction-diffusion between the constituents at the IMC layer. The pressure measurement through CFD simulation could offer valuable information about the plasticized material forging around the tool and the creation of the defect in the joint. The pressure distribution at the tool/workpiece interface, i.e., around the tool at R_{sp3} is shown in Fig. 9.8(d). The pressure magnitude is significantly greater in front of the tool (LS) as compared to the backside of the tool (TS).

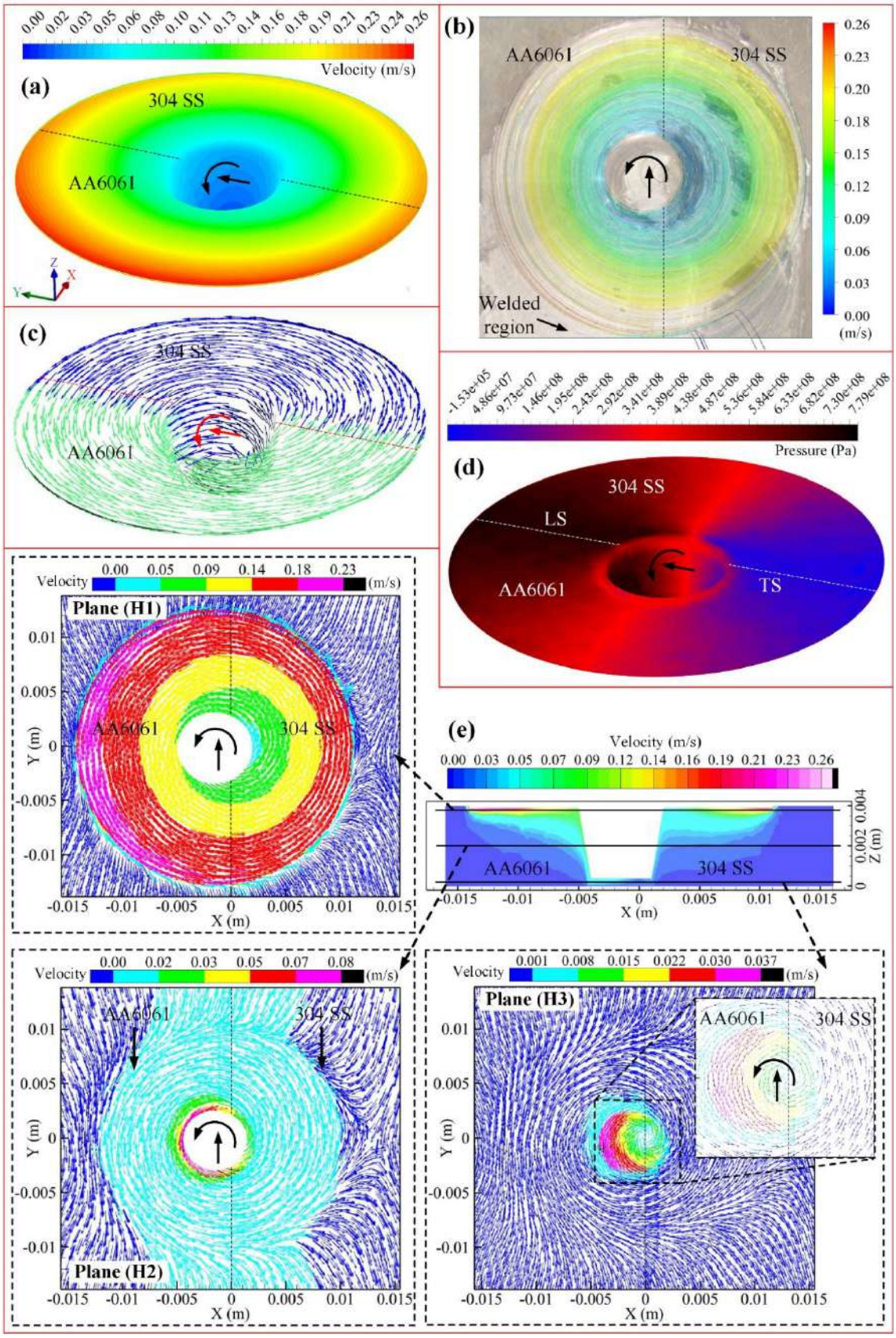

Fig. 9.8 *(a) Flow velocity around the tool; (b) velocity streamlines; (c) material flow vectors; (d) pressure distribution; and (e) velocity vectors in different planes at* R_{sp3}

This behaviour is explained by material forging, which draws the plastic material from ahead of the tool to the SZ. The different physical characteristics of the base materials cause uneven pressure distribution around the tool axis. The results show that the R_{sp3} generated the maximum pressure of 7.79e + 08 Pa at the LS and -1.53e + 05 Pa at the TS. Al-moussawi et al. [165] also reported the highest pressure at the front of the tool shoulder rather than the backside due to the tool traversing action. The material flow velocity vectors in the transverse plane (V1) and horizontal planes H1, H2, and H3 are shown in Fig. 9.8(e). The simulation results showed that the AA6061 side (RS) velocity is greater compared to the 304 SS side (AS). A more intense movement of plasticized material is found in the SAZ or plane (H1) than the central and bottom planes, as represented in Fig. 9.8(e). This is attributed to the tool rotation at a faster linear velocity because the radial distance and heat generation are higher in SAZ. No material movement happened in areas far from the shoulder and pin, where the heat is transmitted through the conduction only. The tool pin in planes H2 and H3 almost interfered with the material flow; thus, these planes can be regarded as PAZ. The varying driving forces and frictional heat cause the different flow vectors at the top, central, and bottom areas.

The velocity fields through the streamlines of circumferential flow around the tool at R_{sp3} is shown in Fig. 9.9(a). A smaller gap between streamlines is observed in the RS since the AA6061 has a higher flow ability than the 304 SS. However, the poor flow capability of material results in a significant gap between the streamlines, where welding defects can easily occur. Almost circular, closed streamlines indicate that the material flows around the tool pin repeatedly. The closed streamlines occupy a wider area at the top region due to higher momentum transportation from the rotating shoulder. The broader rotational zone at the SAZ than the PAZ is attributed to lower viscosity (Fig. 9.4(c)) and higher temperature generated by extreme stirring action of the tool shoulder. The material flow in the Z-direction creates a closed loop circulated flow around the tool pin. Transversely, the material initially entered the tool periphery; then, it is pushed to the top region, where it flowed towards the SZ in the direction of the weld centre, as shown in Fig. 9.9(b). Then, the rotating tool pin caused the materials (304 SS and AA6061) to move downward, as shown in Figs. 9.9(c) and 9.9(d). When the material is swirled to the underside of the tool pin, it is squeezed upwards once again. Finally, once the material left the stirring zone, it flowed horizontally, which is generally characterized by the deposition phenomena. A certain amount of material circulates around the pin repeatedly before leaving the pin and moving on to the deposition phase.

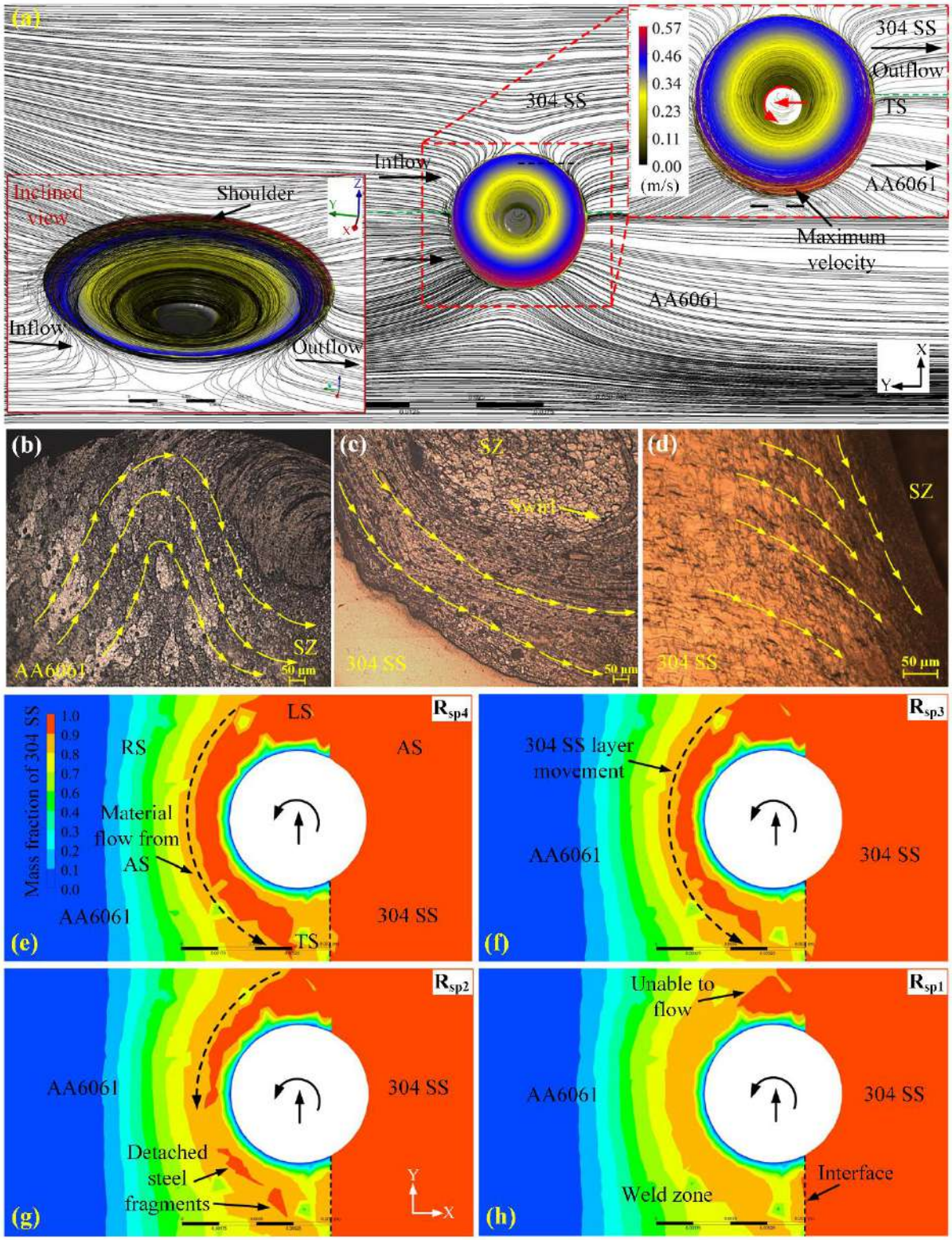

Fig. 9.9 *(a) Material flow velocity streamlines; (b–d) micrographs revealing the material movement around the SZ; and (e–h) horizontal material movement around the tool at different rotational speeds*

In this regard, Figs. 9.9(e–h) show the calculated material flow in terms of mass fraction around the tool in the horizontal XY plane at 1 mm from the top surface. The plasticized

material stuck to the tool surface is initially sheared in the advancing/leading quadrant, after which it is moved and collected over the retreating/leading quadrant, as illustrated in Fig. 1.10. Finally, the collected material is transported to the TS, layer by layer at R_{sp4} and R_{sp3}, as shown in Fig. 9.9(e) and 9.9(f). The higher pressure (Fig. 9.7(d)) under the forging effect at the LS made it easier for 304 SS to move from AS to RS ahead of the tool and then deposited in the TS. The relatively higher heat generation and materials flow velocity enhanced the flow capability of 304 SS; hence it is deposited in the AA6061 side after bypassing the tool. With a decrease in rotational speed from R_{sp3} to R_{sp2}, the steel fragments separated from the 304 SS layer and dispersed in the TS, as shown in Fig. 9.9(g). However, Fig. 9.9(h) revealed that the lowest rotational speed (R_{sp1}) could not be able to extrude the steel from base 304 SS due to inadequate flow velocity. In view of that, the insufficient flow velocity reduced the mixing and stirring of the materials with a decrease in rotational speed.

A typical surface appearance of weld joints at different rotational speeds is shown in Fig. 9.10. The surface defects like cracks/grooves are observed at rotational speeds R_{sp1} and R_{sp2}, as shown in Figs. 9.10(a) and 9.10(b). This is attributed to the improper material flow of AA6061 and 304 SS due to insufficient material flow velocity, as discussed in the next section. The uniform material flow at rotational speeds R_{sp3} and R_{sp4} produced smooth surface appearances without any internal defects, as shown in Figs. 9.10(c) and 9.10(d).

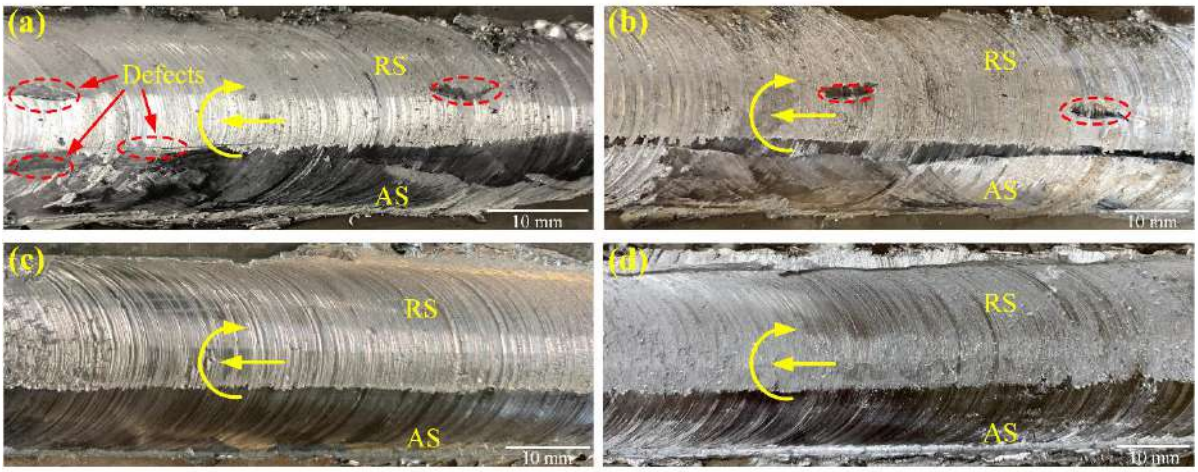

Fig. 9.10 *Weld surface appearance at (a) R_{sp1}; (b) R_{sp2}; (c) R_{sp3}; and (d) R_{sp4}*

The movement of the plasticized material affects the weld characteristics, which are subsequently influenced by the heat generation and flow parameters. The material movement through mapping of the calculated velocity vectors on experimental weld joints at the plane (H2) is shown in Figs. 9.11(a) and 9.11(b). Figs. 9.11(c) and 9.11(d) show the velocity vectors in the V1 plane at R_{sp1} and R_{sp2}, respectively.

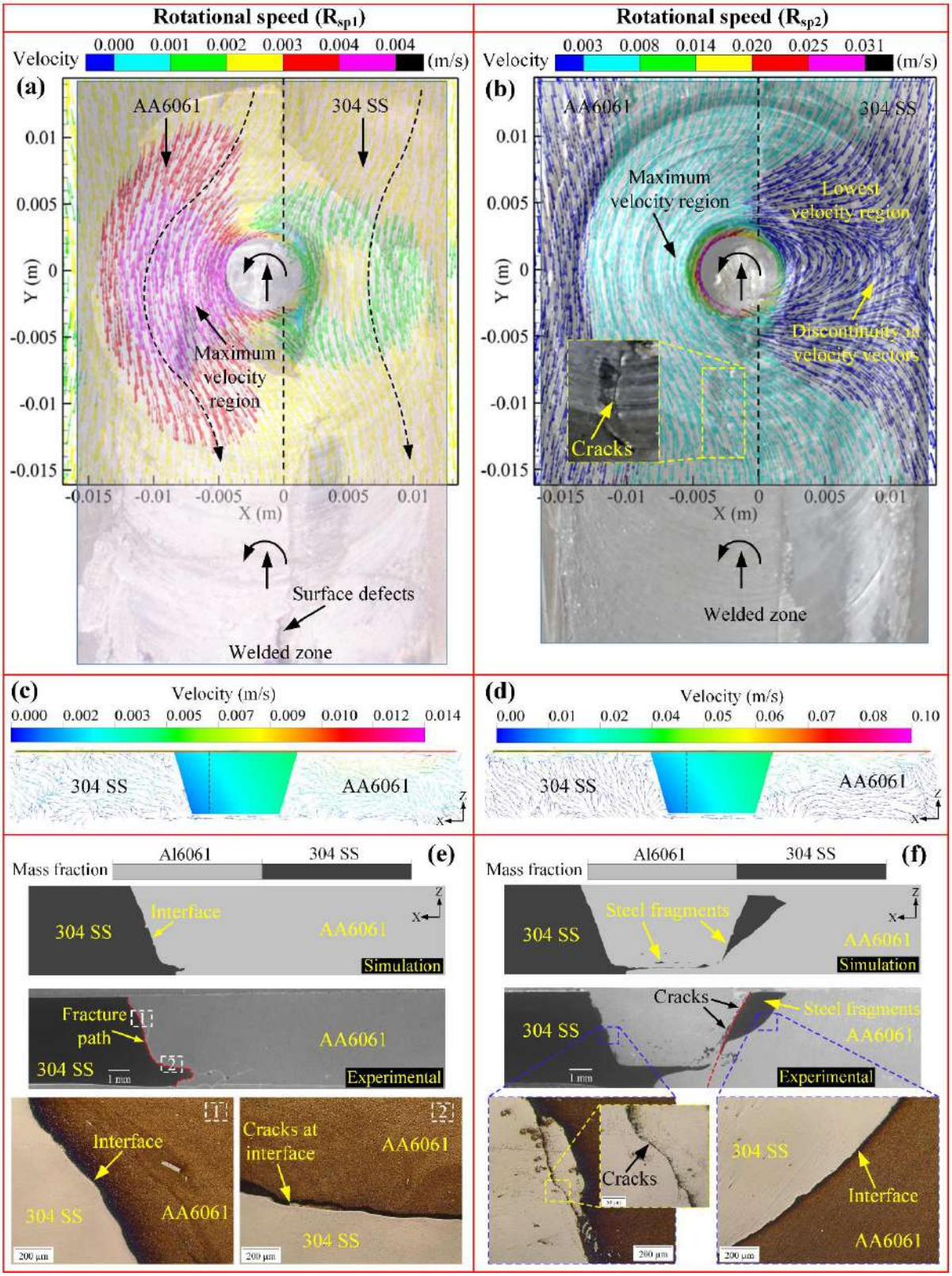

Fig. 9.11 *(a–b) Mapping of calculated velocity vectors and weld joint; (c–d) velocity vectors at V1 plane; and (e–f) calculated (STM) and experimentally obtained material distribution*

Due to the higher heat generation on the RS, the vectors revealed a substantially larger plastic deformation at the AA6061 side compared to the 304 SS side. The low rotational speeds,

i.e., R_{sp1} and R_{sp2} produced the discontinuity in velocity vectors at the PAZ caused by the comparatively low velocity at the 304 SS side. This discontinuity could produce the surface defects like weld surface cracks/grooves, as visible in Figs. 9.11(a) and 9.11(b). Figs. 9.11(e) and 9.11(f) compare the experimental and calculated material distribution around the tool in terms of the mass fraction. The STM effectively captured the steel fragments around the tool. From Fig. 9.11(a), the insufficient flow velocity made the harder material, i.e., 304 SS unable to extrude from the AS at R_{sp1}, and subsequently produced the discontinuity in the dissimilar materials flow. Hence, no steel fragments are captured in the STM and the experimental macrograph, as shown in Fig. 9.11(e). From a cross-sectional perspective, the irregular material flow and inadequate heat input resulted in the defects, such as cracks in the Al/steel boundary at R_{sp1}. Furthermore, the lowest material flow velocity at the bottom (Fig. 9.5) made it easier to generate the defects with less heat input conditions, as visible in Fig. 9.11(e). The steel fragments detached from bulk 304 SS and dispersed in the AA6061 side by enhancing the rotational speed from R_{sp1} to R_{sp2}, as shown in Fig. 9.11(f). The spreading of the steel fragments at the Al side seems to be the result of the material revolution being delayed by the material velocity at R_{sp2}. The coarse steel fragments inside the Al matrix are difficult to deform and mix since their hardness and density are greater compared to AA6061. The harder steel fragments prevented the movement of the viscous Al and generated the inappropriate material flow at their surface region, whereas the softened Al is easily deformed. As a result, the viscous Al could not fill the surface gaps between the Al matrix and the coarse steel fragments. In the AA6061 matrix, the unfilled gaps resulted in defects like tunnels/cracks (Fig. 9.11(f)) that are harmful to the strength of the weld joints.

On the other hand, the smooth weld surface is observed at R_{sp3} and R_{sp4} because the material flow is significantly improved and turned into more uniform in PAZ, as shown in Figs. 9.12(a) and 9.12(b). From Figs. 9.12(a,b) and 9.12(c,d), the velocity vectors at H2 and V1 planes showed that the greater heat generation caused the harder material to become softer, which made it easier for 304 SS to flow at a sufficient speed from AS to RS. Hence, more plasticized material in the form of a continuous steel strip is extruded from AS to RS, named a steel extruded zone (SEZ). These continuous steel strips in the AA6061 side are fairly captured by the STM and verified with the experimental macrographs, as shown in Figs. 9.12(e) and 9.12(f).

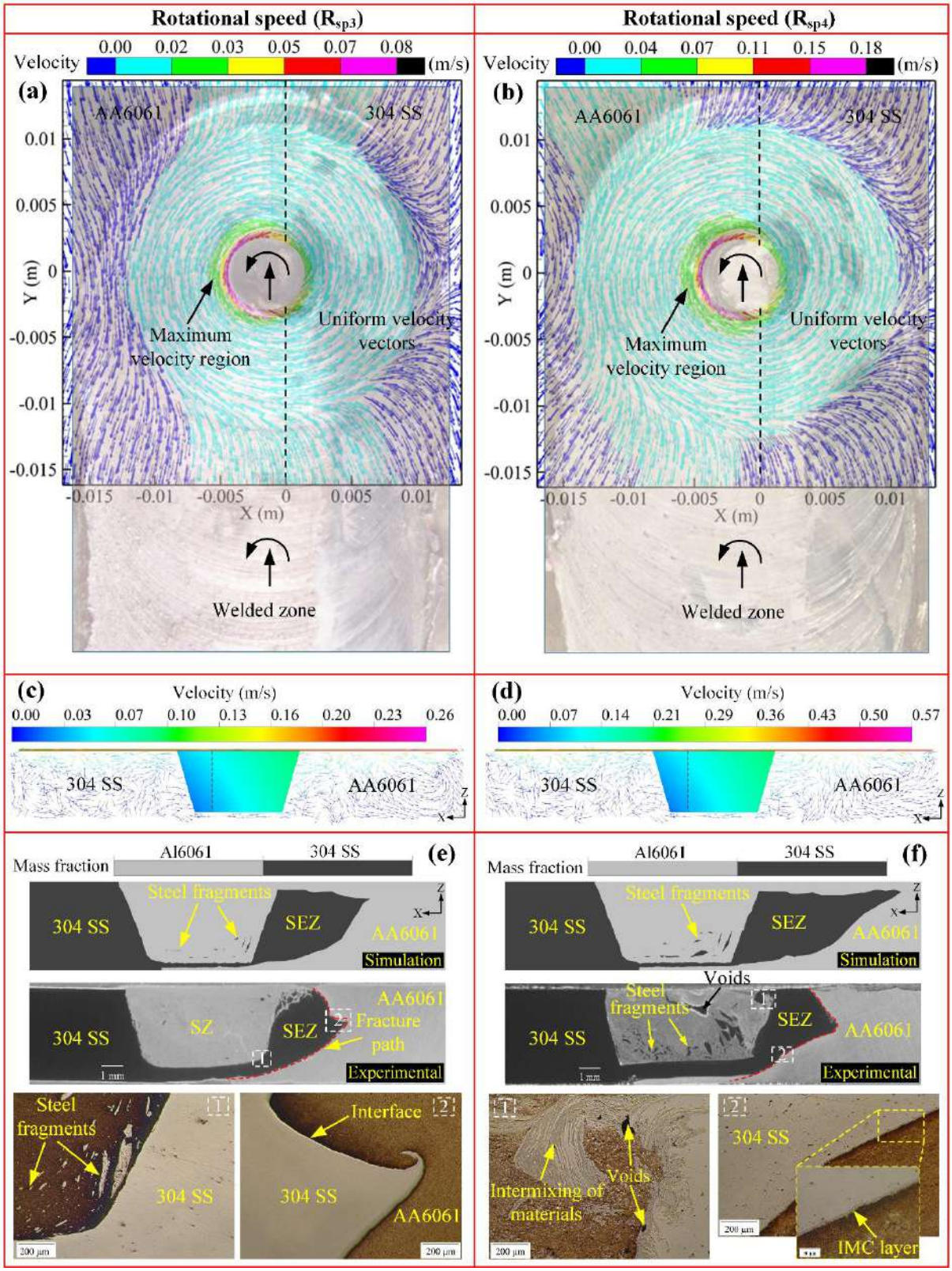

Fig. 9.12 *(a–b) Mapping of calculated velocity vectors and weld joint; (c–d) velocity vectors at V1 plane; and (e–f) calculated (STM) and experimentally obtained material distribution*

The axial pressure pushed the material downward, but the material movement stopped at the bottom due to the extrusion force provided by the backing plate. Then, the bottom steel was compressed and transported in the form of a strip to the AA6061 side through the narrow route between the backing plate and pin surface. Furthermore, the dispersion of irregularly shaped steel fragments inside the SZ is found in the calculated and experimental macrographs. Despite the uniform flow at R_{sp4}, defects like cracks and voids are also generated by the intense material mixing at lower dynamic viscosity under higher welding temperatures. The defects are clearly visible in Fig. 9.12(f). As shown in Fig. 9.12(e), no defects are found in the weld macrograph at R_{sp3} due to the uniform material flow at adequate temperature and velocity fields. Additionally, the IMCs formation at the Al/steel boundary with a different colour from base materials is clearly visible in Fig. 9.12(f). The IMC layer is typically created by the solid-state diffusion process triggered by the sequential effects of frictional heat, material extrusion, and axial forging.

9.4 EXPERIMENTAL RESULTS

In the FSW of steel and Al alloy, the IMCs formation at the interface is a major issue that can substantially influence the weld joint efficiency. The heat generation and degree of plastic deformation mainly control the formation and growth kinetics of IMCs at the Al/steel interface. In this work, the TEM and SEM equipped with an EDS system were used to conduct the phase/composition analysis of the IMC layer. Figs. 9.13(a–c) show the enlarged magnified morphology and EDS analysis of the Al/steel interface at R_{sp4}. The interface is coloured differently in EDS elemental mapping because of the coexistence of Al and Fe. In the EDS line scan, the Al/Fe concentration variations indicate the probable formation of the Al-rich IMC layer with other alloys at the interface area, which is marked by the yellow colour. To better understand the creation and composition of the IMC layer, a TEM investigation was also carried out at R_{sp4}. Typical TEM pictures of an interface at lower and higher resolution with corresponding selected area electron diffraction (SAED) patterns are shown in Fig. 9.13(a).

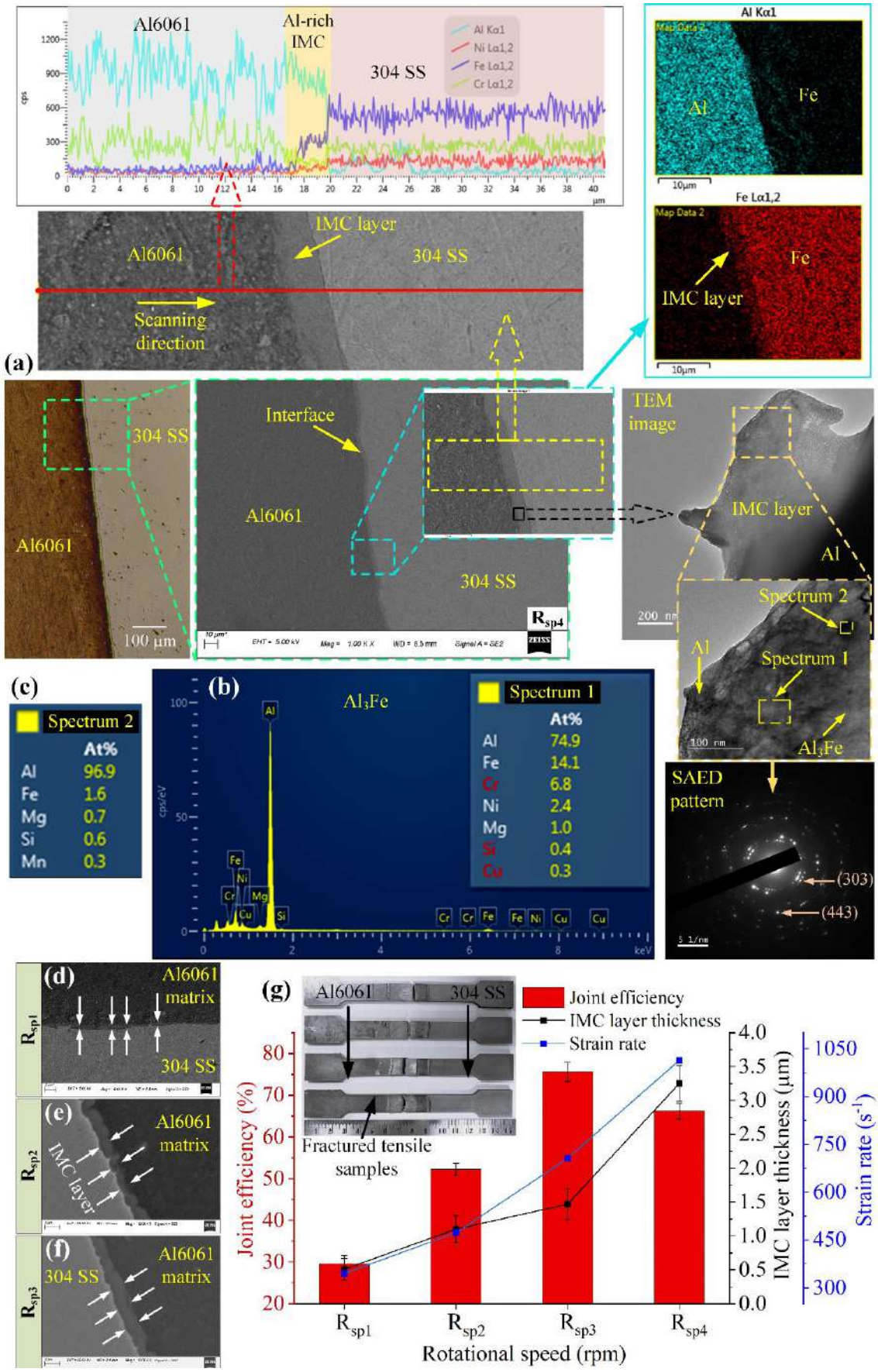

Fig. 9.13 *(a) Detailed analysis of IMC layer; (b–c) EDS elemental spectrums; (d–f) IMCs thickness at R_{sp1}–R_{sp3}; and (g) weld joint efficiency at different rotational speeds*

According to the Al–Fe phase diagram (Fig. 1.7), the atomic composition of spectrum 1 proposes the formation of Al-rich IMC, namely $FeAl_3$ at the interface. Furthermore, the EDS elemental spectrum 2 reveals the presence of an Al matrix at the interface zone. The white arrows point to the IMC layer thickness at R_{sp1}–R_{sp3} in Figs. 9.13(d–f). The IMC layer thickness enlarged with strain rate at R_{sp1}–R_{sp4}, as shown in Fig. 9.13(g). The IMC thickness is changed from 0.51 ± 0.16 μm to 3.25 ± 0.0.26 μm by increasing the rotational speed from R_{sp1} to R_{sp4}. The following parabolic and Arrhenius laws can be used to describe the diffusion-controlled phenomenon of IMC layer generation and evolution kinetics at the Al-Fe boundary [152].

$$x_t^{\,2} = \dot{k}_r t_e = \dot{k}_o t_e \, exp\left(\frac{-\dot{Q}_a}{\dot{R}T}\right) \tag{9.1}$$

where x_t, t_e, T, $\dot{Q}_a$, $\dot{k}_r$, $\dot{k}_o$, and $\dot{R}$ indicate the IMC layer thickness, exposure time, processing temperature, activation energy, rate constant, pre-exponential factor, and the universal gas constant, respectively. This equation implies that the IMC layer thickness enlarges due to an acceleration of the inter-diffusion phenomenon at a constant time (t_e) with an increase in processing temperature (T). In addition, the higher strain rate reduces the activation energy needed for the reaction-diffusion [187] and facilitates the formation of IMCs. The weld joint efficiency is significantly affected by the IMC layer thickness and defects like cracks/voids created by the inadequate material flow behaviour. When the rotational speed is increased from R_{sp1} to R_{sp3}, it is found that the joint efficiency increased; however, it is decreased by further enhancing the rotational speed from R_{sp3} to R_{sp4}, as shown in Fig. 9.13(g). At a lesser heat input, the cracks/voids reduced the joint efficiency due to discontinuous material flow and dispersion of steel fragments (Fig. 9.11). The lowest joint efficiency is observed at R_{sp1}, and a sample is fractured from the interior boundary, as shown in Fig. 9.11(e). While the tensile sample at R_{sp2} fractured at the boundary between steel fragment and AA6061 matrix, as shown in Fig. 9.11(f). Samples at R_{sp3} and R_{sp4} are fractured from the exterior interface of the steel strip, as shown in Figs. 9.12(e) and 9.12(f). The voids created by intense material mixing (Fig. 9.12(f)) and the thick IMC layer of Al_3Fe is responsible for the decrease in efficiency above 875 rpm. The stress concentration at the hard tangles of the thicker IMCs makes the cracks easy to generate and spread. In comparison to Fe-rich IMCs, the Al-rich IMCs, namely Al_3Fe, Al_5Fe_2, and Al_2Fe are also reported as more detrimental to joint efficiency [45]. The rotational speed R_{sp3} (875 rpm) produced the highest joint efficiency, which is around 75.6% of the tensile strength of AA6061. This is attributed to the consistent material flow (Fig.

9.12(a)), defect-free SZ, and mechanical interlocking offered by the continuous steel strip (SEZ).

The dispersion of some irregular-shaped particles inside the SZ is due to a higher strain rate and stirring action of the rotating tool. As shown in Fig. 9.14(a), the atomic composition of spectrum 1 and spectrum 2 revealed that these particles are probably encompassed with the Al_3Fe phase in the AA6061 matrix.

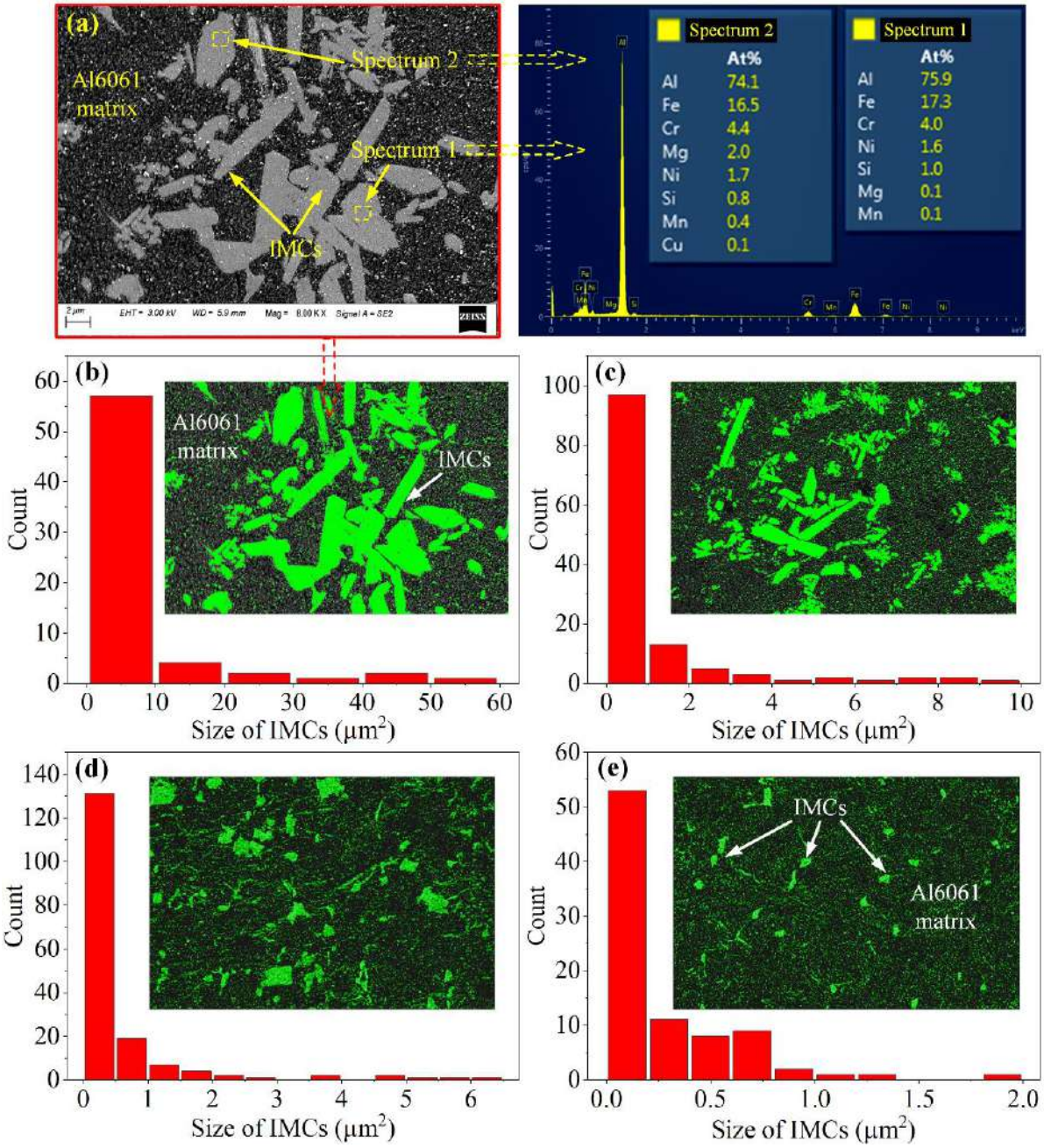

Fig. 9.14 *Quantification of IMCs in the SZ at (a) R_{sp4}; (b) R_{sp3}; (c) R_{sp2}; and (d) R_{sp1}*

The reaction-diffusion phenomena absorbed certain sheared-off steel fragments and converted them into IMCs rather than simply mixing the 304 SS fragments and AA6061 matrix. In this study, image analysis through the thresholding technique was conducted to quantify the dispersion of Al_3Fe IMCs at equivalent locations in the SZ. Figs. 9.14(a–d) show the quantification of IMCs at different rotational speeds. It is observed that when the rotational speed increased from R_{sp1} to R_{sp4}, the intensity of thicker IMCs enhanced. The thicker IMCs are produced inside the AA6061 matrix due to the reaction-diffusion phenomena, which generally accelerates with an increase in rotational speed due to higher strain rate and heat generation. The extremely large-sized IMCs could generate the voids, restrict the material movement by their pinning effect during the tensile test, and reduce the weld joint efficiency.

9.5 SUMMARY

This chapter discussed the three-dimensional coupled thermal-fluid flow analysis based on CFD for dissimilar FSW of 304 SS and AA6061. In this flow analysis, the steady-state multi-species transport model coupled with a mixture model was used for determining the material flow properties associated with the high-speed rotating tool. The developed model can capture the transversal/horizontal material features and embedded steel fragments/strips in the joints, which are also detected in macrographs from experiments under different welding conditions.

The highest strain rate and flow velocity are obtained on the outside shoulder edge caused by the lowest viscosity on the AA6061 side. Table 9.2 summarize the material flow behaviour and weld quality varying rotational speed.

Table 9.2 *Material flow behavior and weld quality at varying rotational speed*

Rotational speed (rpm)	Maximum flow velocity (m/s)	Velocity vectors	Material features	Joint quality
300	0.014	Discontinuous	Could not able to extrude steel	Defective
600	0.097	Discontinuous	Steel fragments	Defective
875	0.263	Uniform	Extruded steel strip in AA6061	Good
1200	0.573	Uniform	Extruded steel strip in AA6061	Defective

The rotational speed of 300 rpm could not extrude the steel from base 304 SS due to insufficient flow velocity, whereas the steel fragments are intermixed with the AA6061 matrix at 600 rpm. At 875 rpm and 1200 rpm, the continuous steel strips are extruded from 304 SS and deposited in AA6061 due to relatively higher heat generation and flow velocity. Furthermore, the velocity vectors revealed the discontinuous material flow at 300 rpm and 600 rpm, and it is turned into almost uniform at 875 rpm and 1200 rpm. The rotational speed of 875 rpm produced the sound weld with a maximum joint efficiency of 75.6%. In addition, the growth kinetics of Al_3Fe IMC at the interface/SZ intensified by increasing the rotational speed from 300 rpm to 1200 rpm due to higher strain rate and heat generation.

CHAPTER 10

CONCLUSIONS AND FUTURE SCOPE

To support the rapid growth of dissimilar joint applications, the current thesis work focuses on the understanding of underlying mechanisms involved in the dissimilar FSW through experimental and numerical analysis. Based on the comprehensive experimentation and numerical simulation, feasible welding conditions are investigated to produce the sound quality weld joints. This final chapter summarizes the important conclusion drawn from the study executed as part of the thesis. The possible further extension of the work is also discussed.

10.1 CONCLUSIONS

The primary objective behind the presented work is to produce the successful friction stir welds of dissimilar steels, and steel & Al alloy combinations. The underlying mechanisms affecting the weld characteristics are understood on a physical and theoretical basis to accomplish the objective. In the preview of this general theme, the concluding remarks are categorized into the following major topics addressed in the present dissertation.

10.1.1 Experimental Investigation on the FSW of Dissimilar Steels

In this work, the influence of FSW process parameters (i.e., tool rotational speed, traverse speed, and pin offset) on the temperature distribution, axial force, microstructure, and mechanical properties of the DH36 steel & AISI 1008 steel joints was investigated. This study can be drawn the following conclusions:

- The maximum peak temperature in the AS is 24.43 ^{o}C greater than the RS.
- The axial force is reduced by 13.8% with an increase in rotational speed from 300 rpm to 850 rpm.
- The axial force is reduced by 9.7% with a decrease in the traverse speed from 132 mm/min to 50 mm/min.
- The axial force decreased by 9.4% with an increase in the tool offset from 0.5 mm to 2.5 mm towards the AISI 1008 steel side.
- All the tensile test samples are fractured in the weaker material (i.e., AISI 1008 steel), and the UTS values are at least on the level of the weaker material.

- The effect of pitch ratio (ω/v_{weld}) on grain size variation is more than tool offset.
- The grain size is reduced with an increase in the pitch ratio.
- Sample S_5 (600 rpm with 90 mm/min) exhibited the finer grain size in TMAZ of DH36 steel and AISI 1008 steel.
- Sample S_5 exhibited the maximum impact toughness and hardness, which are about 103.5% and 275.5% of the AISI 1008 steel, respectively.
- The impact toughness increased by 118% with a decrease in the traverse speed from 132 mm/min to 50 mm/min.
- The impact toughness increased by increasing the rotational speed from 300 rpm to 600 rpm. The further increment generated the flash and reduced the impact toughness.
- The impact toughness is reduced by shifting the tool pin completely towards the AISI 1008 steel.
- The maximum hardness value, i.e., 234.5 HV, is observed in sample S_5 at the TMAZ of DH36 steel due to more grain refinement.

10.1.2 Numerical Investigation on the FSW of Dissimilar Steels

In this work, numerical analyses were performed to conduct the comparative study on thermal history in the FSW and PAFSW of AISI 1008 steel and DH36 steel. The influence of traverse speed, rotational speed, preheating current, and plasma offset on temperature distribution was investigated. From this study, the following conclusions can be drawn.

- The developed models for FSW and PAFSW are validated with experimental results with a maximum percentage error of 5.4% and 5.7% for peak temperature, respectively.
- The maximum peak temperature difference of 78.25 ^{o}C between FSW and PAFSW is observed at a rotational speed of 600 rpm.
- The maximum temperature difference of 86 ^{o}C between FSW and PAFSW is observed at a traverse speed of 50 mm/min.
- At a preheating current of 30 A, the maximum temperature is increased by 119.5 ^{o}C compared to normal FSW.
- The peak temperature is reduced by 48.7 ^{o}C with an increase in the plasma offset from 8 mm to 30 mm.
- The additional preheating source significantly reduced the axial force by around 15% to 20% compared to normal FSW.

- The plasma preheating assistance improved the hardness and impact toughness compared to normal FSW due to grain refinement.

10.1.3 Experimental Investigation on the FSW of Steel and AA6061

10.1.3.1 Influence of Different Tool Offsets on the Metallographic/Mechanical Characteristics of DH36 Steel and AA6061 Joints

In this work, the impact of different tool offsets towards AA6061 on macro/microstructure, IMCs formation, and mechanical behaviour of the welded joints was investigated at the constant rotational speed of 875 rpm and traverse speed of 90 mm/min. The following findings can be summarized from this study.

- The IMCs, namely Al_3Fe and Al_5Fe_2 are observed at the Al/steel interface.
- AlFe and $AlFe_3$ IMCs are observed inside the MZ at a tool offset of 0.4 mm-1.5 mm. However, the Al_2Fe with the AlFe are observed at 1.8 mm and 2.2 mm offsets.
- The average IMC layer thickness decreased with an increase in tool offset.
- The intensity and mean area of Al_3Fe inside the SZ reduced with an increase in tool offset from 0.5 mm to 2.2 mm.
- The only irregular-shaped steel fragments are distributed at a tool offset of 2.5 mm.
- The UTS and elongation increased with an increase in tool offset from 0.4 mm to 1.5 mm and then reduced by further increasing the tool offset from 1.5 mm to 2.5 mm.
- The reduction of UTS below the tool offset of 1.5 mm is attributed to the defect formation due to the thick IMC layer and higher intensity of IMCs.
- At a tool offset higher than 1.5 mm, the UTS reduced due to defects like cracks/voids created by the scattering of steel fragments in the SZ.
- At the IMC layer thickness of 4.88 ± 0.79 μm, the 1.5 mm tool offset produced the maximum UTS of about 76.16% of the AA6061 base material.
- The IMC layer and individual IMCs improved the hardness inside the SZ. The MZ acted as the hardest region due to the extensive IMCs formation in this zone.

10.1.3.2 Influence of Different Traverse Speeds on the Metallographic/Mechanical Characteristics of 304 SS and AA6061 Joints

In this work, a comprehensive study on the macro/microstructure, composition analysis, and quantification of steel fragments/IMCs inside the SZ was conducted at different traverse speeds with the constant rotational speed of 875 rpm and tool offset of 1.5 mm. Furthermore,

their coinciding effect on the mechanical properties of welded joints was also examined. The following conclusions can be drawn from this experimental investigation.

- The area fraction of steel fragments & IMCs (i.e., Al_3Fe), and the IMC layer thickness increased with a decrease in traverse speed.
- The traverse speed of 90 mm/min produced the highest elongation and weld strength around 51.6% and 75.6% of the AA6061 base material, respectively.
- At traverse speed of 90 mm/min, the IMC layer thickness is around 1.47 µm, and the area fraction of IMCs and steel fragments is about 0.023% and 6.05%, respectively.
- At a traverse speed lower than 90 mm/min, defects like cracks and voids formed due to a higher area fraction of Al_3Fe IMCs and steel fragments inside the SZ.
- The traverse speed higher than 90 mm/min produced the defects like cracks on the Al/steel interface due to a lack of intermixing between the materials.
- The grain size decreased to 52.6% and 31% in the SZ (SS 304) and SZ (AA6061) by reducing the traverse speed from 120 mm/min to 30 mm/min, respectively.
- The grain refinement resulted in a higher hardness in SZ (304 SS) than SZ (AA6061).
- The IMCs and steel fragments produced the hardness spikes inside the SZ.
- The intercalated features in the MZ acted as the hardest zone caused by the IMCs, namely Al_3Fe + AlFe at 30 mm/min–70 mm/min, and Al_3Fe + AlFe + $AlFe_3$ at 90 mm/min and 120 mm/min.

10.1.4 Numerical Investigation on the FSW of Steel and AA6061

10.1.4.1 Multiphase CFD Simulation for Thermal History and Material Flow Properties in the FSW of DH36 Steel and AA6061

In this study, VOF-based CFD simulation was performed to determine the plasticized material flow behaviour, and its subsequent impact on metallographic behaviour at different rotational speeds with the constant traverse speed of 90 mm/min and tool offset of 1.5 mm. The following main conclusions can be summarized from this study.

- The heat transmitted more rapidly on the AA6061 than the DH36 steel, which resulted in substantially wider isotherms on the Al side than on the steel side.
- The maximum velocity and strain rate are obtained at the outer edge of the shoulder on the AA6061 side due to the lowest viscosity in that region.
- The material flow velocity increased from 0.024 m/s to 0.66 m/s, and strain rate from 414.04 s^{-1} to 1105.57 s^{-1} by increasing the rotational speed from 450 rpm to 1200 rpm.

- The velocity vectors revealed the discontinuity at 450 rpm and 600 rpm due to low heat input. However, the material flow became almost uniform at 875 rpm and 1200 rpm.
- The area of IMCs and thickness of the IMC layer increased by enhancing the rotational speed due to the enhanced intermetallic reaction at higher temperature and strain rate.
- The UTS and elongation are enhanced by increasing the rotational speed from 450 rpm to 875 rpm and decreased by further increasing the rotational speed.
- The highest UTS is obtained at 875 rpm with the IMC layer thickness of 4.83 ± 0.65 μm, maximum flow velocity of 0.326 m/s, and maximum strain rate of 809.32 s^{-1}.
- The highest hardness is obtained at the intercalated features due to extensive IMCs, namely FeAl + Fe_3Al at 875 rpm and 1200 rpm and Fe_3Al at 450 rpm and 600 rpm.

10.1.4.2 Multi-species Transport CFD Simulation for Thermal History Material Flow Properties in the FSW of 304 SS and AA6061

In this study, a novel CFD-based steady-state multi-species transport model (STM) was developed to determine the material flow properties at different rotational speeds with the constant traverse speed of 90 mm/min and tool offset of 1.5 mm. From this numerical study, the following conclusions can be drawn.

- The developed model validated the calculated transversal/horizontal material features and embedded steel fragments/strips in the joints with the experimental macrographs.
- In the AA6061 side, the highest strain rate and flow velocity are observed on the outside shoulder edge caused by the lowest viscosity in that region.
- It is observed that the rotational speed of 300 rpm could not be able to separate the steel fragments from the base 304 SS due to insufficient velocity and heat generation.
- The rotational speed of 600 rpm generated the defect-prone steel fragments.
- At higher rotational speeds, i.e., 875 rpm and 1200 rpm, the continuous steel strips are captured on the AA6061 side with uniform material flow vectors.
- The uniform material flow vectors produced a smooth weld surface appearance without any internal defects at 875 rpm and 1200 rpm.
- The cross-sectional defects are generated at 1200 rpm, which is attributed to the intense material intermixing and bulky Al_3Fe IMCs.
- The rotational speed of 875 rpm produced the maximum joint efficiency at the maximum material flow velocity of 0.26 m/s, maximum strain rate of 706.3 s^{-1}, and IMC layer thickness of 1.47 ± 0.23 μm.

10.2 RECOMMENDATION FROM THE PRESENT WORK

This work addresses the comprehensive parametric investigation of the joining of dissimilar materials using a versatile, energy-efficient, and environmentally friendly FSW process. Based on the experimental and numerical study, this thesis includes the optimum process window for the FSW of dissimilar material combinations, i.e., DH36 steel & AISI 1008 steel, DH36 steel & AA6061, and 304 SS & AA6061. The selection of the tool material and geometry is a critical aspect in the joining of HMPA like steel alloys. Based on the experimental and numerical results, this thesis recommends the WC-based FSW tool with a cylindrical shoulder and a cylindrical tapered pin to successfully perform the FSW of HMPA, and dissimilar materials like HMPA to LMPA. In the current work, the plasma preheating in front of the tool significantly enhanced the welding temperature and reduced the axial force during the FSW of dissimilar steels. Therefore, this preheating technique can be utilized for FSW of other HMPA like titanium and nickel-based superalloys. In the dissimilar FSW of HMPA to LMPA, the tool life can be improved by shifting the tool pin towards the HMPA.

Based on the numerical investigation, the thesis recommends the developed & verified heat transfer modelling technique to measure the transient thermal history at different process parameters during the conventional and hybrid FSW processes. Furthermore, a thorough understanding of material flow behaviour associated with the tool–material interface substantially eradicates defects from the dissimilar weld joints. In this study, the multiphase CFD model using the volume of fluid (VOF) approach was successfully established by incorporating a modified analytical model, which can be used to understand the underlying mechanisms involved in material flow movement during the dissimilar FSW process. Furthermore, a steady-state multi-species transport model coupled with a mixture model was also established and experimentally verified for the first time. This model can be used to capture the transversal/horizontal material features and embedded material particles/strips along with the material flow properties in the dissimilar weld joints.

10.3 SCOPE OF FUTURE WORK

In the present study, the fundamental mechanisms involved in the FSW of dissimilar steel and steel-Al alloy are explored experimentally and numerically. This research opens the door for future investigators to explore the other aspects related to the dissimilar FSW. Some of the ideas to extend the experimental and modelling approach are discussed in the following subsections.

10.3.1 Experimental Prospects

In this study, an attempt was made to develop the process window for producing the successful weld joints of dissimilar steels, and steel-Al alloy. A hybrid FSW technique, i.e., PAFSW was also employed to reduce the welding forces and improve the quality of dissimilar steel weld joints. Further, an experimental study can be expanded by the following approaches.

- Development of different hybrid FSW processes, namely arc-assisted FSW and induction-assisted FSW for dissimilar materials like steel & Al alloy.
- Development of intermetallic compound mitigation techniques in steel & Al alloy dissimilar welding.

10.3.2 Numerical Prospects

In this study, the CFD-based VOF and multi-species transport models were established to investigate the material flow/intermixing during the dissimilar FSW of steel and Al alloy. Further, the following aspects can progress the modelling and simulation.

- Investigation of the material flow and intermixing during the different hybrid FSW processes, namely arc-assisted FSW and induction-assisted FSW.
- Parametric investigation on the material flow and intermixing by considering the effect of IMCs formation in the CFD-based models.

PUBLICATIONS

INTERNATIONAL JOURNALS (Published)

1. **Pardeep Pankaj**, Avinish Tiwari, Tanmoy Medhi and Pankaj Biswas, (2022) "**Multi-Species transport CFD simulation and experimental verification for material flow properties in dissimilar friction stir welding**", *Materials Today Communications*, p. 104959. (DOI: 10.1016/j.mtcomm.2022.104959)
2. **Pardeep Pankaj**, Avinish Tiwari, Lakshmi Narayan Dhara and Pankaj Biswas, (2022) "**Multiphase CFD simulation and experimental investigation of friction stir welded high strength shipbuilding steel and aluminum alloy**", *CIRP Journal of Manufacturing Science and Technology*, vol. 39, pp. 37–69. (DOI: 10.1016/j.cirpj.2022.07.001)
3. **Pardeep Pankaj**, Avinish Tiwari and Pankaj Biswas, (2022) "**Impact of varying tool position on the intermetallic compound formation, metallographic/mechanical characteristics of dissimilar DH36 steel, and aluminum alloy friction stir welds**", *Welding in the World*, vol. 66, no. 2, pp. 239–271. (DOI: 10.1007/s40194-021-01203-2)
4. **Pardeep Pankaj**, Avinish Tiwari, Lakshmi Narayan Dhara, Sanjay Raj and Pankaj Biswas, (2022) "**Investigations on the effect of sheets positioning in advancing & retreating side for dissimilar FSW of DH36 steel and aluminum alloy 6061**", *Journal of The Institution of Engineers (India): Series C*, vol. 103, no.1, pp. 5–20. (DOI: 10.1007/s40032-021-00714-7)
5. **Pardeep Pankaj**, Avinish Tiwari, Lakshmi Narayan Dhara, Tanmoy Medhi and Pankaj Biswas, (2022) "**Dissimilar friction stir joining of aluminum alloy and stainless steel: a study on the intermetallic compound formation, microstructure, and mechanical properties of the joints**", *Journal of Testing and Evaluation*, vol. 51, no. 2, p. 20210780. (DOI: 10.1520/JTE20210780)
6. **Pardeep Pankaj**, Avinish Tiwari, Pankaj Biswas and A. Gourav Rao, (2021) "**Plasma-assisted hybrid dissimilar friction stir welding for joining of DH36 steel and AISI 1008 steel: Thermal modelling and experimental analysis**", *Arabian Journal for Science and Engineering*, vol. 46, no. 8, pp. 7929–7952. (DOI: 10.1007/s13369-021-05574-y)

7. **Pardeep Pankaj**, Avinish Tiwari, Pankaj Biswas, A. Gourav Rao and Sukhomay Pal, (2020) "**A three-dimensional heat transfer modelling and experimental study on friction stir welding of dissimilar steels**", *Journal of the Brazilian Society of Mechanical Sciences and Engineering*, vol. 42, no. 9, p. 467. (DOI: 10.1007/s40430-020-02556-3)
8. **Pardeep Pankaj**, Avinish Tiwari, Pankaj Biswas, A. Gourav Rao and Sukhomay Pal, (2020) "**Experimental studies on controlling of process parameters in dissimilar friction stir welding of DH36 shipbuilding steel–AISI 1008 steel**", *Welding in the World*, vol. 64, no. 6, pp. 963–986. (DOI: 10.1007/s40194-020-00886-3)
9. **Pardeep Pankaj**, Avinish Tiwari, Pankaj Biswas and A. Gourav Rao, (2020) "**Measurement of force and torque in friction stir welding of low carbon steels**", *International Journal of Mechatronics and Manufacturing Systems*, vol. 13, no. 4, pp. 267–285. (DOI: 10.1504/IJMMS.2020.112346)
10. **Pardeep Pankaj**, Tanmoy Medhi, Lakshmi Narayan Dhara, Avinish Tiwari and Pankaj Biswas, (2023) "**Properties enhancement by utilizing external auxiliary energy systems for FSW of aluminum-steel**", *CIRP Journal of Manufacturing Science and Technology*, (Under review).

INTERNATIONAL PROCEDIA JOURNALS (Published)

1. **Pardeep Pankaj**, Pratik S. Sawarkar, Avinish Tiwari, Pankaj Biswas and Sukhomay Pal, (2021) "**Three dimensional FE thermal analysis for friction stir welding of low carbon steel**," *Materials Today: Proceedings*, vol. 41, pp. 902–907. (DOI: 10.1016/j.matpr.2020.09.484)

BOOK CHAPTERS (Published)

1. **Pardeep Pankaj**, Abhishek Bhardwaj, Avinish Tiwari, Lakshmi Narayan Dhara and Pankaj Biswas, (2021) "**Numerical Study on Material Flow Behaviour in Friction Stir Welding of Low Carbon Steel**", *In Recent Advances in Mechanical Engineering*, pp. 175–184, Springer, Singapore. (DOI: 10.1007/978-981-15-7711-6_19)
2. **Pardeep Pankaj**, Avinish Tiwari, Saurav Suman, Abhishek Kumar, Rituraj Bhattacharjee, Subhashis Majumder and Pankaj Biswas, (2020) "**Dissimilar friction stir welding of DH36 shipbuilding steel and mild steel**", *In Advances in Additive*

Manufacturing and Joining, pp. 397-408, Springer, Singapore. (DOI: 10.1007/978-981-32-9433-2_35)

INTERNATIONAL CONFERENCES

1. **Pardeep Pankaj**, Avinish Tiwari, Lakshmi Narayan Dhara, Sanjay Raj, and Pankaj Biswas, (2020) "**Investigations on the effect of sheets positioning in advancing & retreating side for dissimilar FSW of DH36 steel and aluminum alloy 6061**", 8th International Conference on Advancements and Futuristic Trends in Mechanical and Materials Engineering (AFTMME- 2020), Bathinda.
2. **Pardeep Pankaj**, Abhishek Bhardwaj, Avinish Tiwari, Lakshmi Narayan Dhara, and Pankaj Biswas, (2020) "**Numerical study on material flow behaviour in friction stir welding of low carbon steel**", International Conference on Recent Developments in Mechanical Engineering (ICRAME 2020), NIT Silchar, 2020.
3. **Pardeep Pankaj**, Pratik S. Sawarkar, Avinish Tiwari, Pankaj Biswas, and Sukhomay Pal, (2019) "**Three dimensional FE thermal analysis for friction stir welding of low carbon steel**", International Conference on Advancements and Futuristic Trends in Mechanical and Materials Engineering (AFTMME 2019), IIT Ropar.
4. **Pardeep Pankaj**, Avinish Tiwari, and Pankaj Biswas, (2019) "**Influence of tool traverse speed on the characteristics of dissimilar friction stir welded DH36 shipbuilding steel-mild steel**", International Conference on Advanced Materials and Processes for Defence Applications (ADMAT 2019), Defence Metallurgical Research Laboratory (DMRL), Hyderabad.
5. **Pardeep Pankaj**, Avinish Tiwari, Saurav Suman, Abhishek Kumar, Rituraj Bhattacharjee, Subhashis Majumder, and Pankaj Biswas, (2018) "**Dissimilar friction stir welding of DH36 shipbuilding steel and mild steel**", 7th International and 28th All India Manufacturing Technology, Design and Research Conference 2018 (AIMTDR 2018), Anna University, Chennai.
6. **Pardeep Pankaj**, Tanmoy Medhi, and Pankaj Biswas, (2022) "**Intermetallic compound formation and metallographic examination in dissimilar FSW of aluminum and steel alloys**", North-East Research Conclave (NERC 2022), Indian Institute of Technology Guwahati.

APPENDIX

A1. Specifications of FSW Machine

Power system	
Spindle	BT 40
FSW tool holder	BT 40 Arbor
Spindle motor	20 HP/440 V
Feed motor	3 HP 960 rpm
Z-axis thrust	6500 kgf/65 kN (maximum)
Feed motor	3 HP-preferably 960 rpm
Feed system	
Quill stroke	100 mm by hydraulic pressure
X-axis stroke	1000 mm (feed rate 20-300 mm/min)
X-axis feed	23-300 minimum 15-18 levels
Y-axis stroke	200 mm/manual
Z-axis stroke	300 mm (feed rate 2-50 mm/min)
Table size	1800 × 400 mm
Table surface	“T” Slot as per standard
Hydraulic system	
Hydraulic power pack motor	Minimum 5 HP/440 V
Hydraulic tank capacity	100 L
Hydraulic oil	ISO 68
Lubrication system	
Lubrication	Centralized lubrication system
Lubrication oil	SAE40
Vibration	Anti-vibration pad

A2. Specifications of Field Emission Scanning Electron Microscopy (FESEM)

Make	Zeiss
Model	Sigma
Chamber	330 mm inner diameter, 270 mm height
Magnification range	100 X to 2000 kX
Movement	X=125 mm, Y=125 mm, Z=50 mm
Specimen weight	Upto 200g
Stage	5-axis motorized Cartesian
Detector	In lens, SE-2, BSD

A3. Specifications of Field Emission Transmission Electron Microscope (TEM)

Make	JEOL
Model	2100F
Resolution	0.23 nm point to point
Probe size	0.5 nm
Camera	Gatan Orius SC200D (2k × 2k) diffraction camera
Detector	JEOL BF/HAADF STEM

A4. Specifications of Optical Microscope

Make	Carl Zeiss
Model	Axiotech-100 HD, 3D
Magnification range	5 X to 200 X
Movement	3-axis measuring system, reflecting light measuring step X=75 mm, Y=50 mm, Z=50 mm
Camera	Axio-Cam and Axiovision 4.8.2 software (inbuilt)
Lens	Binocular photo tube

A5. Specifications of Infrared Camera

Make	Testo
Model	868
Range	-30°C to 650°C
Resolution	160 ×120 pixels, 320 × 240 pixels via integrated testo SuperResolution Technology
Emissivity range	0.01 to 1
Thermal sensitivity	< 0.08 °C (80 mK)

A6. Specifications of X-Ray Diffractometer

Make	Rigaku Technologies
Model	Smartlab
Core attributes	3 kW sealed X-ray tube, CBO optics
Core dimensions	1300 mm × 1880 mm × 1300 mm
Detector	HyPix-3000 high energy resolution 2D HPAD
Stage	5-axis goniometer

REFERENCES

[1] Eyvazian, A., Hamouda, A., Tarlochan, F., Derazkola, H.A., Khodabakhshi, F., 2020, Simulation and experimental study of underwater dissimilar friction-stir welding between aluminium and steel, *J. Mater. Res. Technol.*, 9(3), 3767–3781.

[2] Haghshenas, M., Gerlich, A.P., 2018, Joining of automotive sheet materials by friction-based welding methods: A review, *Eng. Sci. Technol. an Int. J.*, 21(1), 130–148.

[3] Hussein, S.A., Hadzley, A.B., 2015, Characteristics of aluminum-to-steel joint made by friction stir welding: A review, *Mater. Today Commun.*, 5, 32–49.

[4] Wan, L., Huang, Y., 2018, Friction stir welding of dissimilar aluminum alloys and steels: a review, *Int. J. Adv. Manuf. Technol.*, 99, 1781–1811.

[5] Habibnia, M., Shakeri, M., Nourouzi, S., Givi, M.B., 2015, Microstructural and mechanical properties of friction stir welded 5050 Al alloy and 304 stainless steel plates. *Int. J. Adv. Manuf. Technol.*, 76, 819–829.

[6] Rafiei, R., Ostovari Moghaddam, A., Hatami, M.R., Khodabakhshi, F., Abdolahzadeh, A., Shokuhfar, A., 2017, Microstructural characteristics and mechanical properties of the dissimilar friction-stir butt welds between an Al–Mg alloy and A316L stainless steel, *Int. J. Adv. Manuf. Technol.*, 90, 2785–2801.

[7] Elyasi, M., Aghajani, H., Hosseinzadeh, M., 2015, Effects of friction stir welding parameters on mechanical quality of AA1100 aluminum alloy to A441 AISI steel joint, *Modares Mech. Eng.*, 15(4), 379–390.

[8] Safeen, M.W., Russo Spena, P., 2019, Main issues in quality of friction stir welding joints of aluminum alloy and steel sheets, *Metals*, 9(5), 610.

[9] Ogura, T., Nishida, T., Tanaka, Y., Nishida, H., Yoshikawa, S., Fujimoto, M., Hirose, A., 2013, Microscale evaluation of mechanical properties of friction stir welded A6061 aluminium alloy/304 stainless steel dissimilar lap joint, *Sci. Technol. Weld. Join.*, 18(2), 108–113.

[10] Karakizis, P.N., Pantelis, D.I., Dragatogiannis, D.A., Bougiouri, V.D., Charitidis, C.A., 2019, Study of friction stir butt welding between thin plates of AA5754 and mild steel for automotive applications, *Int. J. Adv. Manuf. Technol.*, 102, 3065–3076.

[11] Logan, B.P., Toumpis, A.I., Galloway, A.M., McPherson, N.A., Hambling, S.J., 2016, Dissimilar friction stir welding of duplex stainless steel to low alloy structural steel, *Sci. Technol. Weld. Join.*, 21(1), 11–19.

[12] Singh, D.K., Sahoo, G., Basu, R., Sharma, V., Mohtadi-Bonab, M.A., 2018, Investigation on the microstructure–mechanical property correlation in dissimilar steel welds of stainless steel SS 304 and medium carbon steel EN 8, *J. Manuf. Process.*, 36, 281–292.

[13] Choi, D.H., Ahn, B.W., Yeon, Y.M., Park, S.H.C., Sato, Y.S., Kokawa, H., Jung, S.B., 2011, Microstructural characterizations following friction stir welding of dissimilar alloys of low-and high-carbon steels, *Mater. Trans.*, 52(7), 1500–1505.

[14] Jang, C., Lee, J., Kim, J.S., Jin, T.E., 2008, Mechanical property variation within Inconel 82/182 dissimilar metal weld between low alloy steel and 316 stainless steel, *Int. J. Press. Vessel. Pip.*, 85(9), 635–646.

[15] Takashima, Y., Ito, Y., Lu, F., Minami, F., 2019, Fracture toughness evaluation for dissimilar steel joints by Charpy impact test. *Weld. World*, 63, 1243–1254.

[16] Jafarzadegan, M., Feng, A.H., Abdollah-Zadeh, A., Saeid, T., Shen, J., Assadi, H., 2012, Microstructural characterization in dissimilar friction stir welding between 304 stainless steel and st37 steel, *Mater. Charact.*, 74, 28–41.

[17] Boumerzoug, Z., Derfouf, C., Baudin, T., 2010, Effect of welding on microstructure and mechanical properties of an industrial low carbon steel, *Engineering*, 2(7), 502.

[18] Kumar, L., Yazar, K.U., Pramanik, S., 2019, Effect of fusion and friction stir welding techniques on the microstructure, crystallographic texture and mechanical properties of mild steel, *Mater. Sci. Eng. A*, 754, 400–410.

[19] Toumpis, A., Galloway, A., Cater, S., McPherson, N., 2014, Development of a process envelope for friction stir welding of DH36 steel–a step change, *Mater. Des.*, (1980-2015), 62, 64–75.

[20] Tiwari, A., 2021, Tool wear and weld quality characterization in friction stir welding of similar and dissimilar steel (Doctoral dissertation).

[21] Ramesh, R., Dinaharan, I., Kumar, R., Akinlabi, E.T., 2019, Microstructure and mechanical characterization of friction-stir-welded 316L austenitic stainless steels, *J. Mater. Eng. Perform.*, 28, 498–511.

[22] Feng, A.H., Chen, D.L., Ma, Z.Y., 2010, Microstructure and low-cycle fatigue of a friction-stir-welded 6061 aluminum alloy, *Metall. Mater. Trans. A Phys. Metall. Mater. Sci.*, 41, 2626–2641.

[23] Mukhopadhyay, P., 2012, Alloy designation, processing, and use of AA6XXX series aluminium alloys, *Int. Sch. Res. Notices*, 2012, 165082.

[24] Cai, W., Wang, P.C., Yang, W., 2005, Assembly dimensional prediction for self-piercing riveted aluminum panels, *Int. J. Mach. Tools Manuf.*, 45(6), 695–704.

[25] Abe, Y., Kato, T., Mori, K., 2006, Joinability of aluminium alloy and mild steel sheets by self piercing rivet, *J. Mater. Process. Technol.*, 177(1–3), 417–421.

[26] Tang, W., Yang, X., Li, S., Li, H., 2019, Microstructure and properties of CLAM/316L steel friction stir welded joints, *J. Mater. Process. Technol.*, 271, 189–201.

[27] Kuroda, S., Saida, K. and Nishimoto, K., 1999. Microstructure and properties of directly bonded joint of A6061 aluminum alloy to SUS316 stainless steel-study on diffusion bonding of aluminum alloy to stainless steel (report 1). *Q. J. Jpn. Weld. Soc.*, 17(3), 484–489.

[28] Elliott, S., ER, W., 1981, Joining aluminium to steel. I: diffusion bonding, *Met. Constr.*, 3, 167–171.

[29] Lee, W.B., Yeon, Y.M., Kim, D.U., Jung, S.B., 2003, Effect of friction welding parameters on mechanical and metallurgical properties of aluminium alloy 5052–A36 steel joint, *Mater. Sci. Technol.*, 19(6), 773–778.

[30] Yamamoto, N., 2007, Effect of interfacial layer on bond strength of friction-welded interface of Al-Mg5083 alloy to mild steel, *Q. J. Jpn. Weld. Soc.*, 23(3), 496–503.

[31] Tsujino, J., Hidai, K., Hasegawa, A., Kanai, R., Matsuura, H., Matsushima, K., Ueoka, T., 2002, Ultrasonic butt welding of aluminum, aluminum alloy and stainless steel plate specimens, *Ultrasonics*, 40(1–8), 371–374.

[32] Zhao, D., Ren, D., Zhao, K., Pan, S., Guo, X., 2017, Effect of welding parameters on tensile strength of ultrasonic spot welded joints of aluminum to steel–By experimentation and artificial neural network, *J. Manuf. Process*, 30, 63–74.

[33] Acarer, M., Demir, B., 2008, An investigation of mechanical and metallurgical properties of explosive welded aluminum–dual phase steel, *Mater. Lett.*, 62(25), 4158–4160.

[34] Han, J.H., Ahn, J.P., Shin, M.C., 2003, Effect of interlayer thickness on shear deformation behavior of AA5083 aluminum alloy/SS41 steel plates manufactured by explosive welding, *J. Mater. Sci.*, 38, 13–18.

[35] Tanaka, T., Morishige, T., Hirata, T., 2009, Comprehensive analysis of joint strength for dissimilar friction stir welds of mild steel to aluminum alloys, *Scr. Mater.*, 61(7), 756–759.

[36] Thomas, W.M., Threadgill, P.L., Nicholas, E.D., 1999, Feasibility of friction stir welding steel, *Sci. Technol. Weld. Join.*, 4(6), 365–372.

[37] Mishra, R.S., Ma, Z.Y., 2005, Friction stir welding and processing, *Mater. Sci. Eng. R Reports*, 50(1–2), 1–78.

[38] Kim, N.K., Kim, B.C., An, Y.G., Jung, B.H., Song, S.W., Kang, C.Y., 2009, The effect of material arrangement on mechanical properties in friction stir welded dissimilar A5052/A5J32 aluminum alloys, *Met. Mater. Int.*, 15, 671–675.

[39] Yan, Z., Liu, X., Fang, H., 2016, Effect of sheet configuration on microstructure and mechanical behaviors of dissimilar Al–Mg–Si/Al–Zn–Mg aluminum alloys friction stir welding joints, *J. Mater. Sci. Technol.*, 32(12), 1378–1385.

[40] Anbukkarasi, R., Kailas, S.V., 2020, Influences of shape of the new interfaces and morphology of the intermetallics on mechanical properties of aluminum AA2024–pure copper joints by friction stir welding, *Int. J. Adv. Manuf. Technol.*, 106, 5071–5083.

[41] Park, S.K., Hong, S.T., Park, J.H., Park, K.Y., Kwon, Y.J., Son, H.J., 2010, Effect of material locations on properties of friction stir welding joints of dissimilar aluminium alloys, *Sci. Technol. Weld. Join.*, 15(4), 331–336.

[42] Fu, B., Qin, G., Li, F., Meng, X., Zhang, J., Wu, C., 2015, Friction stir welding process of dissimilar metals of 6061-T6 aluminum alloy to AZ31B magnesium alloy, *J. Mater. Process. Technol.*, 218, 38–47.

[43] Firouzdor, V., Kou, S., 2009, Al-to-Mg friction stir welding: Effect of positions of Al and Mg with respect to the welding tool, *Weld. J.*, 88(11), 213–224.

[44] Sadeesh, P., Kannan, M.V., Rajkumar, V., Avinash, P., Arivazhagan, N., Ramkumar, K.D. and Narayanan, S., 2014, Studies on friction stir welding of AA 2024 and AA 6061 dissimilar metals. *Procedia Eng.*, 75, 145–149.

[45] Mehta, K.P., 2019, A review on friction-based joining of dissimilar aluminum–steel joints, *J. Mater. Res.*, 34(1), 78–96.

[46] Sunnapu, C. and Kolli, M., 2021, Tool shoulder and pin geometry's effect on friction stir welding: A study of literature, *Mater. Today Proc.*, 39, 1565–1569.

[47] Sunilkumar, D., Muthukumaran, S., Vasudevan, M., Reddy, M.G., 2020, Effect of friction stir and activated-GTA welding processes on the 9Cr–1Mo steel to 316LN stainless steel dissimilar weld joints, *Sci. Technol. Weld. Join.*, 25(4), 311–319.

[48] Rai, R., De, A., Bhadeshia, H.K.D.H., DebRoy, T., 2011, Friction stir welding tools, *Sci. Technol. Weld. Join.*, 16(4), 325–342.

[49] Lienert, T.J., Stellwag Jr, W.L., Grimmett, B.B., Warke, R.W., 2003, Friction stir welding studies on mild steel, *Weld. J.*, 82(1), 1–S.

[50] Tiwari, A., Singh, P., Pankaj, P., Biswas, P., Kore, S.D., Pal, S., 2019, Effect of tool offset and rotational speed in dissimilar friction stir welding of AISI 304 stainless steel and mild steel, *J. Mater. Eng. Perform.*, 28, 6365–6379.

[51] Choi, D.H., Lee, C.Y., Ahn, B.W., Yeon, Y.M., Park, S.H., Sato, Y.S., Kokawa, H. and Jung, S.B., 2010. Effect of fixed location variation in friction stir welding of steels with different carbon contents. *Sci. Technol. Weld. Join.*, 15(4), pp.299-304.

[52] Saeid, T., Abdollah-Zadeh, A., Assadi, H., Ghaini, F.M., 2008, Effect of friction stir welding speed on the microstructure and mechanical properties of a duplex stainless steel, *Mater. Sci. Eng. A*, 496(1–2), 262–268.

[53] Cheng, C.P., Lin, H.M., Lin, J.C., 2010, Friction stir welding of ductile iron and low carbon steel, *Sci. Technol. Weld. Join.*, 15(8), 706–711.

[54] Rahimi, S., Konkova, T.N., Violatos, I., Baker, T.N., 2019, Evolution of microstructure and crystallographic texture during dissimilar friction stir welding of duplex stainless steel to low carbon-manganese structural steel, *Metall. Mater. Trans. A Phys. Metall. Mater. Sci.*, 50, 664–687.

[55] Tiwari, A., Pankaj, P., Biswas, P., Kore, S.D., Rao, A.G., 2019, Tool performance evaluation of friction stir welded shipbuilding grade DH36 steel butt joints, *Int. J. Adv. Manuf. Technol.*, 103, 1989–2005.

[56] Fujii, H., Cui, L., Nakata, K., Nogi, K., 2008, Mechanical properties of friction stir welded carbon steel joints–Friction stir welding with and without transformation, *Weld. World*, 52, 75–81.

[57] Ipekoglu, G., Kucukomeroglu, T., Aktarer, S.M., Sekban, D.M., Cam, G., 2019, Investigation of microstructure and mechanical properties of friction stir welded dissimilar St37/St52 joints, *Mater. Res. Express*, 6(4), 046537.

[58] Kucukomeroglu, T., Aktarer, S.M., Ipekoglu, G., Cam, G., 2018, Mechanical properties of friction stir welded St 37 and St 44 steel joints, *Mater. Test.*, 60(12), 1163–1170.

[59] Wang, H., Wang, K., Wang, W., Huang, L., Peng, P., Yu, H., 2019, Microstructure and mechanical properties of dissimilar friction stir welded type 304 austenitic stainless steel to Q235 low carbon steel, *Mater. Charact.*, 155, 109803.

[60] Sharma, G., Dwivedi, D.K., 2017, Study on microstructure and mechanical properties of dissimilar steel joint developed using friction stir welding, *Int. J. Adv. Manuf. Technol.*, 88, 1299–1307.

[61] Chung, Y.D., Fujii, H., Sun, Y., Tanigawa, H., 2011, Interface microstructure evolution of dissimilar friction stir butt welded F82H steel and SUS304, Mater. Sci. Eng. A, 528(18), 5812–5821.

[62] Zheng, Q., Feng, X., Shen, Y., Huang, G., Zhao, P., 2016, Dissimilar friction stir welding of 6061 Al to 316 stainless steel using Zn as a filler metal, *J. Alloys Compd.*, 686, 693–701.

[63] Derazkola, H.A., Aval, H.J., Elyasi, M., 2015, Analysis of process parameters effects on dissimilar friction stir welding of AA1100 and A441 AISI steel, *Sci. Technol. Weld. Join.*, 20(7), 553–562.

[64] Singh, V.P., Patel, S.K., Ranjan, A., Kuriachen, B., 2020, Recent research progress in solid state friction-stir welding of aluminium–magnesium alloys: a critical review, *J. Mater. Res. Technol.*, 9(3), 6217–6256.

[65] Liu, X., Lan, S., Ni, J., 2014, Analysis of process parameters effects on friction stir welding of dissimilar aluminum alloy to advanced high strength steel, *Mater. Des.*, 59, 50–62.

[66] Murugan, B., Thirunavukarasu, G., Kundu, S., Kailas, S.V., Chatterjee, S., 2018, Interfacial microstructure and mechanical properties of friction stir welded joints of commercially pure aluminum and 304 stainless steel, *J. Mater. Eng. Perform.*, 27, 2921-2931.

[67] Chen, T., 2009, Process parameters study on FSW joint of dissimilar metals for aluminum–steel, *J. Mater. Sci.*, 44, 2573–2580.

[68] Watanabe, T., Takayama, H., Yanagisawa, A., 2006, Joining of aluminum alloy to steel by friction stir welding, *J. Mater. Process. Technol.*, 178(1–3), 342–349.

[69] Dehghani, M., Amadeh, A., Mousavi, S.A., 2013, Investigations on the effects of friction stir welding parameters on intermetallic and defect formation in joining aluminum alloy to mild steel, *Mater. Des.*, 49, 433–441.

[70] Pourali, M., Abdollah-Zadeh, A., Saeid, T., Kargar, F., 2017, Influence of welding parameters on intermetallic compounds formation in dissimilar steel/aluminum friction stir welds, *J. Alloys Compd.*, 715, 1–8.

[71] Elyasi, M., Aghajani Derazkola, H., Hosseinzadeh, M., 2016, Investigations of tool tilt angle on properties friction stir welding of A441 AISI to AA1100 aluminium, *Proc. Inst. Mech. Eng. Part B J. Eng. Manuf.*, 230(7), 1234–1241.

[72] Zhao, S., Ni, J., Wang, G., Wang, Y., Bi, Q., Zhao, Y., Liu, X., 2018, Effects of tool geometry on friction stir welding of AA6061 to TRIP steel, *J. Mater. Process. Technol.*, 261, 39-49.

[73] Xu, X., Zhang, C., Derazkola, H.A., Demiral, M., Zain, A.M., Khan, A., 2021, UFSW tool pin profile effects on properties of aluminium-steel joint, Vacuum, 192, 110460.

[74] Kumar, R., Pancholi, V., Bharti, R.P., 2018, Material flow visualization and determination of strain rate during friction stir welding, *J. Mater. Process. Tech.*, 255, 470-476.

[75] Morisada, Y., Imaizumi, T., Fujii, H., Matsushita, M., Ikeda, R., 2014, Three-dimensional visualization of material flow during friction stir welding of steel and aluminum, *J. Mater. Eng. Perform.*, 23, 4143–4147.

[76] Lee, W.B., Schmuecker, M., Mercardo, U.A., Biallas, G., Jung, S.B., 2006, Interfacial reaction in steel–aluminum joints made by friction stir welding, *Scr. Mater.*, 55(4), 355–358.

[77] Zhou, L., Yu, M., Liu, B., Zhang, Z., Liu, S., Song, X., Zhao, H., 2020, Microstructure and mechanical properties of Al/steel dissimilar welds fabricated by friction surfacing assisted friction stir lap welding, *J. Mater. Res. Technol.*, 9(1), 212–221.

[78] Coelho, R.S., Kostka, A., Dos Santos, J.F., Kaysser-Pyzalla, A., 2012, Friction-stir dissimilar welding of aluminium alloy to high strength steels: Mechanical properties and their relation to microstructure, *Mater. Sci. Eng. A*, 556, 175–183.

[79] Bang, H., Bang, H., Jeon, G., Oh, I., Ro, C., 2012, Gas tungsten arc welding assisted hybrid friction stir welding of dissimilar materials Al6061-T6 aluminum alloy and STS304 stainless steel, *Mater. Des.*, 37, 48–55.

[80] Torres Lopez, E.A., Graciano-Uribe, J.A., Marques, I.J., de Abreu Santos, T.F., 2022, Microstructural features of dissimilar thin sheets aging aluminum alloy–low carbon steel joined by friction stir welding, *Metallogr. Microstruct. Anal.*, 11(4), 617–633.

[81] Yazdipour, A., Heidarzadeh, A., 2016, Effect of friction stir welding on microstructure and mechanical properties of dissimilar Al 5083-H321 and 316L stainless steel alloy joints, *J. Alloys Compd.*, 680, 595–603.

[82] Anaman, S.Y., Cho, H.H., Das, H., Lee, J.S., Hong, S.T., 2019, Microstructure and mechanical/electrochemical properties of friction stir butt welded joint of dissimilar aluminum and steel alloys, *Mater. Charact.*, 154, 67–79.

[83] Ramachandran, K.K., Murugan, N., Kumar, S.S., 2015, Effect of tool axis offset and geometry of tool pin profile on the characteristics of friction stir welded dissimilar joints of aluminum alloy AA5052 and HSLA steel, *Mater. Sci. Eng. A*, 639, 219–233.

[84] Kaushik, P., Dwivedi, D.K., 2021, Effect of tool geometry in dissimilar Al–steel friction stir welding, *J. Manuf. Process*, 68, 198–208.

[85] Picot, F., Gueydan, A., Martinez, M., Moisy, F., Hug, E., 2018, A correlation between the ultimate shear stress and the thickness affected by intermetallic compounds in friction stir welding of dissimilar aluminum alloy–stainless steel joints. *Metals*, 8(3), 179.

[86] Rafiei, R., Ostovari Moghaddam, A., Hatami, M.R., Khodabakhshi, F., Abdolahzadeh, A., Shokuhfar, A., 2017, Microstructural characteristics and mechanical properties of the dissimilar friction-stir butt welds between an Al–Mg alloy and A316L stainless steel, *Int. J. Adv. Manuf. Technol.*, 90, 2785–2801.

[87] Girard, M., Huneau, B., Genevois, C., Sauvage, X., Racineux, G., 2010, Friction stir diffusion bonding of dissimilar metals, *Sci. Technol. Weld. Join.*, 15(8), 661–665.

[88] Mertin, C., Naumov, A., Mosecker, L., Bambach, M., Hirt, G., 2014, Influence of the process temperature on the properties of friction stir welded blanks made of mild steel and aluminum, *Key Eng. Mater.*, 611, 1429–1436.

[89] Ghosh, M., Gupta, R.K., Husain, M.M., 2014, Friction stir welding of stainless steel to Al alloy: effect of thermal condition on weld nugget microstructure, *Metall Mater Trans A*, 45, 854–863.

[90] Chen, Y., Zhang, F., 2022, Characteristics of the dissimilar AA7075 and Q235 steel joints fabricated by friction stir welding, *Metals*, 12(8), 1376.

[91] Dehghani, M., Mousavi, S.A., Amadeh, A., 2013, Effects of welding parameters and tool geometry on properties of 3003-H18 aluminum alloy to mild steel friction stir weld, *Trans. Nonferrous Met. Soc. China*, 23(7), 1957–1965.

[92] Kundu, S., Roy, D., Bhola, R., Bhattacharjee, D., Mishra, B., Chatterjee, S., 2013, Microstructure and tensile strength of friction stir welded joints between interstitial free steel and commercially pure aluminium, *Mater. Des.*, 50, 370–375.

[93] Yaduwanshi, D.K., Bag, S., Pal, S., 2016, Numerical modeling and experimental investigation on plasma-assisted hybrid friction stir welding of dissimilar materials, *Mater. Des.*, 92, 166–183.

[94] Song, K.H., Tsumura, T., Nakata, K., 2009, Development of microstructure and mechanical properties in laser–FSW hybrid welded Inconel 600, *Mater. Trans.*, 50(7), 1832–1837.

[95] Yaduwanshi, D.K., Bag, S., Pal, S., 2014, Effect of preheating in hybrid friction stir welding of aluminum alloy, *J. Mater. Eng. Perform.*, 23, 3794–3803.

[96] Zhao, X., Dong, F.B., Su, G.Y., Guo, L.J., 2012, Weld quality improvement with hybrid FSW technology assisted by preheating for copper T2/aluminium 5A06 dissimilar materials, *Appl. Mech. Mater.*, 121, 1707–1711.

[97] Alvarez, A.I., García, M., Pena, G., Sotelo, J., Verdera, D., 2014, Evaluation of an induction-assisted friction stir welding technique for super duplex stainless steels, *Surf. Interface Anal.*, 46(10–11), 892–896.

[98] Bang, H.S., Hong, S.M., Das, A., Bang, H.S., 2021, Study on the weldability and mechanical characteristics of dissimilar materials (Al5052-DP590) by TIG assisted hybrid friction stir welding, *Met. Mater. Int.*, 27, 1193–1204.

[99] Ahmad, B., Galloway, A., Toumpis, A., 2019, Numerical optimisation of laser assisted friction stir welding of structural steel, *Sci. Technol. Weld. Join.*, 24(6), 548–558.

[100] Shi, L., Wu, C.S., Liu, X.C., 2015, Modeling the effects of ultrasonic vibration on friction stir welding, *J. Mater. Process. Technol.*, 222, 91–102.

[101] Casalino, G., Campanelli, S., Ludovico, A.D., Contuzzi, N., Angelastro, A., 2012, Study of a fiber laser assisted friction stir welding process, *High Power Laser Mater. Process. Lasers, Beam Deliv. Diagnostics, Appl.*, 8239, 310–316.

[102] Merklein, M., Giera, A., 2008, Laser assisted friction stir welding of drawable steel–aluminium tailored hybrids, *Int. J. Mater. Form.*, 1(Suppl 1), 1299–1302.

[103] Sundqvist, J., Kim, K.H., Bang, H.S., Bang, H.S., Kaplan, A.F., 2018, Numerical simulation of laser preheating of friction stir welding of dissimilar metals, *Sci. Technol. Weld. Join.*, 23(4), 351–356.

[104] Yaduwanshi, D.K., Pal, S., Bag, S., 2014, Effect of preheating on mechanical properties of hybrid friction stir welded dissimilar joint, *In Proceedings of 5th International & 26th All India Manufacturing Technology, Design and Research Conference*.

[105] Bilgin, M., Karabulut, S., Ozdemir, A., 2020, Investigation of heat-assisted dissimilar friction stir welding of AA7075-T6 aluminum and AZ31B magnesium alloys, *Arab. J. Sci. Eng.*, 45, 1081–1095.

[106] Chen, G., Li, H., Wang, G., Guo, Z., Zhang, S., Dai, Q., Wang, X., Zhang, G., Shi, Q., 2018, Effects of pin thread on the in-process material flow behavior during friction stir welding: A computational fluid dynamics study, *Int. J. Mach. Tools Manuf.*, 124, 12–21.

[107] Gould, J.E., Feng, Z., 1998, Heat flow model for friction stir welding of aluminum alloys. *J. Mater. Manuf. Process.*, 7(2), 185–194.

[108] Schmidt, H., Hattel, J., Wert, J., 2003, An analytical model for the heat generation in friction stir welding, *Model. Simul. Mater. Sci. Eng.*, 12(1), 143.

[109] Kadian, A.K., Biswas, P., 2017, Effect of tool pin profile on the material flow characteristics of AA6061, *J. Manuf. Process.*, 26, 382–392.

[110] Kadian, A.K., Biswas, P., 2018, The study of material flow behaviour in dissimilar material FSW of AA6061 and Cu-B370 alloys plates, *J. Manuf. Process.*, 34, 96–105.

[111] Kadian, A.K., Biswas, P., 2015, A comparative study of material flow behavior in friction stir welding using laminar and turbulent models, *J. Mater. Eng. Perform.*, 24, 4119–4127.

[112] Dong, P., Lu, F., Hong, J.K., Cao, Z., 2001, Coupled thermomechanical analysis of friction stir welding process using simplified models, *Sci. Technol. Weld. Join.*, 6(5), 281–287.

[113] Veljic, D., Perovic, M.M., Sedmak, A., Rakin, M., Trifunovic, M.V., Bajic, N., Bajic, D., 2012, A coupled thermo-mechanical model of friction stir welding, *Therm. Sci.*, 16(2), 527–534.

[114] Grujicic, M., He, T., Arakere, G., Yalavarthy, H.V., Yen, C.F., Cheeseman, B.A., 2010, Fully coupled thermomechanical finite element analysis of material evolution during friction-stir welding of AA5083, *Proc. Inst. Mech. Eng. B J. Eng. Manuf.*, 224(4), 609–625.

[115] Ma, Z.Y., Feng, A.H., Chen, D.L., Shen, J., 2018, Recent advances in friction stir welding/processing of aluminum alloys: microstructural evolution and mechanical properties, *Crit. Rev. Solid State Mater. Sci.*, 43(4), 269–333.

[116] Deepati, A.K., Kadian, A.K., Biswas, P., 2015, Numerical and experimental study on influence of tool plunging force and shoulder size on thermal history of friction stir welding, *Int. J. Manuf. Res.*, 10(1), 64–86.

[117] Rajamanickam, N., Balusamy, V., Reddy, G.M., Natarajan, K., 2009, Effect of process parameters on thermal history and mechanical properties of friction stir welds, *Mater. Des.*, 30(7), 2726–2731.

[118] Riahi, M., Nazari, H., 2011, Analysis of transient temperature and residual thermal stresses in friction stir welding of aluminum alloy 6061-T6 via numerical simulation, *Int. J. Adv. Manuf. Technol.*, 55, 143–152.

[119] Ahmad, B., Galloway, A., Toumpis, A., 2018, Advanced numerical modelling of friction stir welded low alloy steel, *J. Manuf. Process.*, 34, 625–636.

[120] Arora, A., De, A., DebRoy, T., 2011, Toward optimum friction stir welding tool shoulder diameter, *Scr. Mater.*, 64(1), 9–12.

[121] Chao, Y.J., Qi, X., Tang, W., 2003, Heat transfer in friction stir welding–experimental and numerical studies, *J. Manuf. Sci. Eng.*, 125(1), 138–145.

[122] Nandan, R.G.G.R., Roy, G.G., Lienert, T.J., Debroy, T., 2007, Three-dimensional heat and material flow during friction stir welding of mild steel, *Acta Mater.*, 55(3), 883–895.

[123] Das, N.K., Kadian, A.K., Tiwari, A., Pankaj, P., Biswas, P., 2019, Transient thermal analysis on friction stir welding of AA6061, *In Manufacturing Engineering: Select Proceedings of CPIE 2018*, 67–82.

[124] Al-Moussawi, M., Smith, A., Young, A.E., Faraji, M., Cater, S., 2016, An advanced numerical model of friction stir welding of DH36 steel, *In: 11th International Symposium on Friction Stir Welding, TWI, Cambridge*.

[125] Yau, Y.H., Hussain, A., Lalwani, R.K., Chan, H.K., Hakimi, N., 2013, Temperature distribution study during the friction stir welding process of Al2024-T3 aluminum alloy, *Int. J. Miner. Metall. Mater.*, 20, 779–787.

[126] Darvazi, A.R., Iranmanesh, M., 2014, Prediction of asymmetric transient temperature and longitudinal residual stress in friction stir welding of 304L stainless steel, *Mater. Des.*, 55, 812–820.

[127] Hernandez, C.A., Ferrer, V.H., Mancilla, J.E., Martinez, L.C., 2017, Three-dimensional numerical modeling of the friction stir welding of dissimilar steels, *Int. J. Adv. Manuf. Technol.*, 93, 1567–1581.

[128] Zhu, X.K., Chao, Y.J., 2004, Numerical simulation of transient temperature and residual stresses in friction stir welding of 304L stainless steel, *J. Mater. Process. Technol.*,146(2), 263–272.

[129] Selvaraj, M., 2013, A temperature dependent slip factor based thermal model for friction stir welding of stainless steel, *Sadhana*, 38, 1393–1405.

[130] Camilleri, D., Micallef, D., Mollicone, P., 2015, Thermal stresses and distortion developed in mild steel DH36 friction stir-welded plates: An experimental and numerical assessment, *J. Therm. Stresses*, 38(5), 485–508.

[131] Nandan, R., Roy, G.G., Lienert, T.J., DebRoy, T., 2006, Numerical modelling of 3D plastic flow and heat transfer during friction stir welding of stainless steel, *Sci. Technol. Weld. Join.*, 11(5), 526–537.

[132] Zhang, Z., Chen, J.T., Zhang, Z.W., Zhang, H.W., 2011, Coupled thermo-mechanical model based comparison of friction stir welding processes of AA2024-T3 in different thicknesses, *J. Mater. Sci.*, 46, 5815–5821.

[133] Buffa, G., Hua, J., Shivpuri, R., Fratini, L., 2006, Design of the friction stir welding tool using the continuum based FEM model. *Mater. Sci. Eng. A*, 419(1–2), 381–388.

[134] Sadeghian, B., Taherizadeh, A., Atapour, M., 2018, Simulation of weld morphology during friction stir welding of aluminum-stainless steel joint, *J. Mater. Process. Technol.*, 259, 96–108.

[135] Liu, X., Chen, G., Ni, J., Feng, Z., 2017, Computational fluid dynamics modeling on steady-state friction stir welding of aluminum alloy 6061 to TRIP steel, *J. Manuf. Sci. Eng.*, 139(5), 051004.

[136] Yang, C., Wu, C., Shi, L., 2020, Modeling the dissimilar material flow and mixing in friction stir welding of aluminum to magnesium alloys, *J. Alloys Compd.*, 843, 156021.

[137] Gotawala, N., Shrivastava, A., 2020, Analysis of material distribution in dissimilar friction stir welded joints of Al 1050 and copper, *J. Manuf. Process.*, 57, 725–736.

[138] Akbari, M., Asadi, P., 2020, Dissimilar friction stir lap welding of aluminum to brass: Modeling of material mixing using coupled Eulerian–Lagrangian method with experimental verifications, *Proc. Inst. Mech. Eng. Pt. L J. Mater. Des. Appl.*, 234(8), 1117–1128.

[139] Ansari, M.A., Samanta, A., Behnagh, R.A., Ding, H., 2019, An efficient coupled Eulerian-Lagrangian finite element model for friction stir processing, *Int. J. Adv. Manuf. Technol.*, 101, 1495–1508.

[140] Iordache, M.D., Badulescu, C., Diakhate, M., Constantin, M.A., Nitu, E.L., Demmouche, Y., Dhondt, M., Negrea, D., 2021, A numerical strategy to identify the FSW process optimal

parameters of a butt-welded joint of quasi-pure copper plates: Modeling and experimental validation. *Int. J. Adv. Manuf. Technol.*, 115, 2505–2520.

[141] Heinze, T., Jansen, G., Galvan, B., Miller, S.A., 2016, Systematic study of the effects of mass and time scaling techniques applied in numerical rock mechanics simulations, *Tectonophysics*, 684, 4–11.

[142] Turkan, M., Karakas, O., 2021, Two different finite element models investigation of the plunge stage in joining AZ31B magnesium alloy with friction stir welding, *SN Appl. Sci.*, 3, 165.

[143] Chu, Q., Yang, X.W., Li, W.Y., Vairis, A., Wang, W.B., 2018, Numerical analysis of material flow in the probeless friction stir spot welding based on coupled Eulerian-Lagrangian approach, *J. Manuf. Process.*, 36, 181–187.

[144] Xiong, J., Peng, X., Shi, J., Wang, Y., Sun, J., Liu, X., Li, J., 2021, Numerical simulation of thermal cycle and void closing during friction stir spot welding of AA-2524 at different rotational speeds, *Mater. Charact.*, 174, 110984.

[145] Jain, R., Pal, S.K., Singh, S.B., 2017, Numerical modeling methodologies for friction stir welding process, *In Computational methods and production engineering*, 125–169.

[146] Chen, G., Zhang, S., Zhu, Y., Yang, C., Shi, Q., 2020, Thermo-mechanical analysis of friction stir welding: A review on recent advances, Acta Metall. Sin. (Engl. Lett.), 33, 3–12.

[147] Zhu, Y., Chen, G., Chen, Q., Zhang, G., Shi, Q., 2016, Simulation of material plastic flow driven by non-uniform friction force during friction stir welding and related defect prediction, *Mater. Des.*, 108, 400–410.

[148] Mohan, R., Jayadeep, U.B., Manu, R., 2021, CFD modelling of ultra-high rotational speed micro friction stir welding, *J. Manuf. Process.*, 64, 1377–1386.

[149] Pal, S., Phaniraj, M.P., 2015. Determination of heat partition between tool and workpiece during FSW of SS304 using 3D CFD modelling, *J. Mater. Process. Technol.*, 222, 280–286.

[150] Jiang, T., Wu, C., Shi, L., 2022, Effects of tool pin thread on temperature field and material mixing in friction stir welding of dissimilar Al/Mg alloys, *J. Manuf. Process.*, 74, 112–122.

[151] Nandan, R., Roy, G.G., Debroy, T., 2006, Numerical simulation of three-dimensional heat transfer and plastic flow during friction stir welding, *Metall. Mater. Trans. A Phys. Metall. Mater. Sci.*, 37, 1247–1259.

[152] Aghajani Derazkola, H., Khodabakhshi, F., 2019, Intermetallic compounds (IMCs) formation during dissimilar friction-stir welding of AA5005 aluminum alloy to St-52 steel: Numerical modeling and experimental study, *Int. J. Adv. Manuf. Technol.*, 100, 2401–2422.

[153] Tang, J., Shen, Y., 2017, Effects of preheating treatment on temperature distribution and material flow of aluminum alloy and steel friction stir welds, *J. Manuf. Process.*, 29, 29–40.

[154] Nandwani, S.K., Chakraborty, M., Gupta, S., 2019, Chemical flooding with ionic liquid and nonionic surfactant mixture in artificially prepared carbonate cores: a diffusion controlled CFD simulation, *J. Pet. Sci. Eng.*, 173, 835–843.

[155] Lin, C.X., Wang, D., Bao, A., 2013, Numerical modeling and simulation of condensation heat transfer of a flue gas in a bundle of transport membrane tubes, *Int. J. Heat Mass Transf.*, 60, 41–50.

[156] Zhang, X., Ye, J., Ye, M., Chen, K., 2021, CFD analysis on the mixing effect of orifice diameter in dxygen mixer, *J. Phys. Conf. Ser.*, 2076(1), 012108.

[157] Lee, S.Y., Dimenna, R.A., 2007, Applications of CFD method to gas mixing analysis in a large-scaled tank, *In Fluids Engineering Division Summer Meeting*, 42894, 1387–1394.

[158] Mansour, M., Khot, P., Kovats, P., Thevenin, D., Zahringer, K., Janiga, G., 2020, Impact of computational domain discretization and gradient limiters on CFD results concerning liquid mixing in a helical pipe, *Chem. Eng. J.*, 383, 123121.

[159] Thomas, J., Sinha, K., Shivkumar, G., Cao, L., Funck, M., Shang, S., Nere, N.K., 2021, A CFD digital twin to understand miscible fluid blending, *AAPS PharmSciTech*, 22, 91.

[160] Liu, X., Lan, S., Ni, J., 2015, Thermal mechanical modeling of the plunge stage during friction-stir welding of dissimilar Al 6061 to TRIP 780 steel, *J. Manuf. Sci. Eng.*, 137(5), 051017.

[161] Pankaj, P., Tiwari, A., Biswas, P., Rao, A.G., 2020, Measurement of force and torque in friction stir welding of low carbon steels, *Int. J. Mechatronics Manuf. Syst.*, 13(4), 267–285.

[162] Ericsson, M., Sandstrom, R., 2003, Influence of welding speed on the fatigue of friction stir welds, and comparison with MIG and TIG, *Int. J. Fatigue*, 25(12), 1379–1387.

[163] Pankaj, P., Tiwari, A., Dhara, L.N., Raj, S., Biswas, P., 2022, Investigations on the effect of sheets positioning in advancing & retreating side for dissimilar FSW of DH36 Steel and aluminum alloy 6061, *J. Inst. Eng. Ser. C*, 103(1), 5–20.

[164] da Silva, Y.C., Oliveira Junior, F.J., dos Santos, J.F., Marcondes, F., Silva, C., 2020, Numerical investigation of the influence of FSW parameters on the heat and mass transfer of austenitic stainless steels, Weld. World, 64, 2019–2032.

[165] Al-Moussawi, M., Smith, A.J., Young, A., Cater, S., Faraji, M., 2017, Modelling of friction stir welding of DH36 steel, *Int. J. Adv. Manuf. Technol.*, 92, 341–360.

[166] Hasan, A.F., Bennett, C.J., Shipway, P.H., Cater, S., Martin, J., 2017, A numerical methodology for predicting tool wear in friction stir welding, *J. Mater. Process. Technol.*, 241, 129–140.

[167] Shen, B., Chen, S., Cheng, L., Sun, F., 2014, The effect of the double-deck filament setup on enhancing the uniformity of temperature field on long-flute cutting tools, *Surf. Rev. Lett.*, 21(06), 1450078.

[168] Nkhoma, R.K., Siyasiya, C.W., Stumpf, W.E., 2014, Hot workability of AISI 321 and AISI 304 austenitic stainless steels, *J. Alloys Compd.*, 595, 103–112.

[169] Tiwari, A., Pankaj, P., Suman, S., Biswas, P., 2020, CFD modelling of temperature distribution and material flow investigation during FSW of DH36 shipbuilding grade steel, *Trans. Indian Inst. Met.*, 73, 2291–2307.

[170] Derazkola, H.A., Eyvazian, A., Simchi, A., 2020, Submerged friction stir welding of dissimilar joints between an Al–Mg alloy and low carbon steel: Thermo-mechanical modeling, microstructural features, and mechanical properties, J. Manuf. Process., 50, 68–79.

[171] Essa, A.R.S., Ahmed, M.M.Z., Mohamed, A.K.Y.A., El-Nikhaily, A.E., 2016, An analytical model of heat generation for eccentric cylindrical pin in friction stir welding, J. Mater. Res. Technol., 5(3), 234–240.

[172] Djurdjanovic, M.B., Mijajlovic, M.M., Milcic, D.S., Stamenkovic, D.S., 2009, Heat generation during friction stir welding process, *Tribol. Ind.*, 31(1&2), 8.

[173] Lampeas, G.N., Diamantakos, I.D., 2015, Effects of nonconventional tools on the thermo-mechanical response of friction stir welded materials, *J. Manuf. Sci. Eng.*, 137(5), 051020.

[174] Sharghi, E., Farzadi, A., 2018, Simulation of strain rate, material flow, and nugget shape during dissimilar friction stir welding of AA6061 aluminum alloy and Al-Mg_2Si composite, *J. Alloys Compd.*, 748, 953–960.

[175] Li, Y., Feng, Y.H., Zhang, X.X., Wu, C.S., 2013, An improved simulation of heat transfer and fluid flow in plasma arc welding with modified heat source model. *Int. J. Therm. Sci.*, 64, 93–104.

[176] Ceschini, L., Boromei, I., Minak, G., Morri, A., Tarterini, F., 2007, Effect of friction stir welding on microstructure, tensile and fatigue properties of the AA7005/10 vol.% Al_2O_{3p} composite, *Compos. Sci. Technol.*, 67(3–4), 605–615.

[177] Krishnan, K.N., 2002, On the formation of onion rings in friction stir welds, *Mater. Sci. Eng. A*, 327(2), 246–251.

[178] McPherson, N.A., Galloway, A.M., Cater, S.R., Hambling, S.J., 2013, Friction stir welding of thin DH36 steel plate, *Sci. Technol. Weld. Join.*, 18(5), 441–450.

[179] Samanta, A., Shen, N., Ji, H., Wang, W., Li, J., Ding, H., 2018, Cellular automaton simulation of microstructure evolution for friction stir blind riveting, *J. Manuf. Sci. Eng.*, 140(3), 031016.

[180] Asadi, P., Besharati Givi, M.K., Akbari, M., 2015, Microstructural simulation of friction stir welding using a cellular automaton method: a microstructure prediction of AZ91 magnesium alloy, *Int. J. Mech. Mater. Eng.*, 10, 20.

[181] Shojaeefard, M.H., Akbari, M., Asadi, P., 2014, Multi objective optimization of friction stir welding parameters using FEM and neural network, *Int. J. Precis. Eng. Manuf.*, 15, 2351–2356.

[182] Cho, H.H., Kang, S.H., Kim, S.H., Oh, K.H., Kim, H.J., Chang, W.S., Han, H.N., 2012, Microstructural evolution in friction stir welding of high-strength linepipe steel, *Mater. Des.*, 34, 258–267.

[183] Nemat-Nasser, S., Guo, W.G., 2003, Thermomechanical response of DH-36 structural steel over a wide range of strain rates and temperatures, *Mech. Mater.*, 35(11), 1023–1047.

[184] Khabaz-Aghdam, A., Rahmani, A., Fadaei, A., 2019, Experimental and numerical parametric study of resistance spot welding process of AISI 1008 steel sheets, *J. Theor. Appl. Mech.*, 57(4), 807–820.

[185] Sahu, P.K., Pal, S., 2018, Effect of FSW parameters on microstructure and mechanical properties of AM20 welds, *Mater. Manuf. Process.*, 33(3), 288–298.

[186] Mao, Y., Ke, L., Liu, F., Liu, Q., Huang, C., Xing, L., 2014, Effect of tool pin eccentricity on microstructure and mechanical properties in friction stir welded 7075 aluminum alloy thick plate, *Mater. Des.*, 62, 334–343.

[187] Ramachandran, K.K., Murugan, N., 2019, Influence of axial force on tensile strength and microstructural characteristics of friction stir butt welded aluminum alloy/steel joints, *Strength Mater.*, 51, 300–316.

[188] Han, K., Ohnuma, I., Kainuma, R., 2016, Experimental determination of phase equilibria of Al-rich portion in the Al–Fe binary system. *J. Alloys Compd.*, 668, 97–106.

[189] Springer, H., Kostka, A., Payton, E.J., Raabe, D., Kaysser-Pyzalla, A., Eggeler, G.J.A.M., 2011, On the formation and growth of intermetallic phases during interdiffusion between low-carbon steel and aluminum alloys, *Acta Mater.*, 59(4), 1586–1600.

[190] Mohammadi, J., Behnamian, Y., Mostafaei, A., Gerlich, A.P., 2015, Tool geometry, rotation and travel speeds effects on the properties of dissimilar magnesium/aluminum friction stir welded lap joints, *Mater. Des.*, 75, 95–112.

[191] Knibloe, J.R., Wright, R.N., Trybus, C.L., Sikka, V.K., 1993, Microstructure and mechanical properties of Fe_3Al alloys with chromium. *J. Mater. Sci.*, 28, 2040–2048.

[192] Bozzi, S., Helbert-Etter, A.L., Baudin, T., Criqui, B., Kerbiguet, J.G., 2010, Intermetallic compounds in Al 6016/IF-steel friction stir spot welds, *Mater. Sci. Eng. A.*, 527(16–17), 4505–4509.

[193] Ramachandran, K.K., Murugan, N., Kumar, S.S., 2015, Friction stir welding of aluminum alloy AA5052 and HSLA steel, Weld. J., 94(9), 291s–300s.

[194] Azimzadegan, T., Serajzadeh, S., 2010, An investigation into microstructures and mechanical properties of AA7075-T6 during friction stir welding at relatively high rotational speeds, *J. Mater. Eng. Perform.*, 19, 1256–1263.

[195] Sahu, P.K., Pal, S., 2017, Mechanical properties of dissimilar thickness aluminium alloy weld by single/double pass FSW, *J. Mater. Process. Technol.*, 243, 442–455.

[196] Memon, S., Tomków, J. and Derazkola, H.A., 2021. Thermo-mechanical simulation of underwater friction stir welding of low carbon steel. *Materials*, 14(17), p.4953.

[197] Praveen Raj Navukkarasan, A., Shanmuga Sundaram, K., Chandrasekhara Sastry, C., Muthu Manickam, M.A., 2021, Experimental investigation of dry and cryogenic friction stir welding of AA7075 aluminium alloy, *Adv. Mater. Sci. Eng.*, 2021, 9961590.

[198] Bahrami, M., Helmi, N., Dehghani, K., Givi, M.K.B., 2014, Exploring the effects of SiC reinforcement incorporation on mechanical properties of friction stir welded 7075 aluminum alloy: fatigue life, impact energy, tensile strength, *Mater. Sci. Eng. A.*, 595, 173–178.

[199] Akbari, M., Khalkhali, A., Keshavarz, S.M.E., Sarikhani, E., 2018, The effect of in-process cooling conditions on temperature, force, wear resistance, microstructural, and mechanical properties of friction stir processed A356, *Proc. Inst. Mech. Eng. Part L J. Mater. Des. Appl.*, 232(5), 429–437.

[200] Fonda, R.W., Knipling, K.E., Bingert, J.F., 2008, Microstructural evolution ahead of the tool in aluminum friction stir welds, *Scr. Mater.*, 58(5), 343–348.